

A thesis entitled

**Femtosecond LIBS Studies of Energetic
Molecules in the Near and Standoff Regimes**

Submitted to

University of Hyderabad

Towards partial fulfillment for the degree of

Doctor of Philosophy

in

Physics

by

Abdul Kalam S (13ACPA02)



Under the supervision of

Prof. Soma Venugopal Rao

Advanced Centre for Research in High Energy Materials (ACRHEM)

School of Physics, University of Hyderabad

Hyderabad 500046, Telangana, India

October 2018

Dedicated to

My grand parents

Shaik Madarbi (شيخ مداربي) &

Shaik Khadar Saheb (شيخ قادر صاحب)

&

My parents

Shaik Chand Begum (شيخ چاند بيگم) &

Shaik Abdul Gaffur (شيخ عبدالغفور)

Declaration

I, **Abdul Kalam S**, hereby declare that the work presented in this thesis entitled **“Femtosecond LIBS Studies of Energetic Molecules in the Near and Standoff Regimes”** has been carried out by me under the supervision of **Prof. Soma Venugopal Rao**, Professor in ACRHEM (School of Physics), University of Hyderabad, Hyderabad, Telangana, India, as per the Ph.D. ordinances of the University, which is also free from plagiarism. I declare, to the best of my knowledge, that no part of this thesis has been submitted for the award of a research degree of any other University. I hereby agree that my thesis can be deposited in Shodhganga/INFLIBNET.

A report on plagiarism statistics from the University Librarian is enclosed.

(Abdul Kalam S)

Reg. No: 13ACPA02

Prof. Soma Venugopal Rao

Thesis Supervisor,
ACRHEM,
School of Physics,
University of Hyderabad.

Dr. Soma Venugopal Rao

Professor

Tel.: +91-40 2313 8811

Fax: +91-40 2301 2800

E-mail: svrsp@uohyd.ernet.in

Soma_venu@yahoo.com



ACRHEM

University of Hyderabad,

Prof. C. R. Rao Road,

Gachibowli,

Hyderabad – 500 046,

Telangana, India.

Certificate

This is to certify that the thesis entitled “**Femtosecond LIBS Studies of Energetic Molecules in the Near and Standoff Regimes**” being submitted to the University of Hyderabad by **Abdul Kalam S** (Reg. No. 13ACPA02), for the award of the degree of Doctor of Philosophy in Physics, is a record of *bonafide* work carried out by him under my supervision and is free of plagiarism.

The matter embodied in this report has not been submitted to any other University or Institution for the award of any degree or diploma.

Prof. Soma Venugopal Rao
(Supervisor)

Director,
ACRHEM

Dean,
School of Physics



CERTIFICATE

This is to certify that the thesis entitled “**Femtosecond LIBS Studies of Energetic Molecules in the Near and Standoff Regimes**” submitted by **Abdul Kalam S** bearing registration number **13ACPA02** in partial fulfillment of the requirements for award of **Doctor of Philosophy in physics at ACRHEM, School of physics, University of Hyderabad** is a bonafide work carried out by him under my supervision and guidance.

This thesis is free from plagiarism and has not been submitted previously in part or in full to this or any other University or Institution for award of any degree or diploma.

Further, the student has the following publications before submission of the thesis for adjudication.

1. **S. A. Kalam**, N. L. Murthy, P. Mathi, N. Kommu, A. K. Singh, and S. V. Rao, "Correlation of molecular, atomic emissions with detonation parameters in femtosecond and nanosecond LIBS plasma of high energy materials," *J. Anal. At. Spectrom.* **32(8)**, 1535–1546 (2017), ISSN 1364-5544. [**Appears in chapter 3**].
2. **S. A. Kalam**, E.N. Rao, S. Hamad, B. Chandu, and S. Venugopal Rao, "Femtosecond laser induced breakdown spectroscopy based standoff detection of explosives and discrimination using principal component analysis," *Opt. Express* 26(7), 53–59 (2018), ISSN 1094-4087 (web). [**Appears in chapter 4**].
3. **S. A. Kalam**, Ajmathulla, S. Venugopal Rao, "Discrimination of bimetallic alloy targets using femtosecond filament-induced breakdown spectroscopy in standoff mode," *Opt. Lett.* 43(15), 18–21 (2018), ISSN 1539-4794 (web). [**Appears in chapter 4**].
4. **S. A. Kalam**, N. L. Murthy, J. R. Krishna, V. Srikanth, and Venugopal Rao Soma, "Nanoparticle Enhanced Laser Induced Breakdown Spectroscopy with Femtosecond Pulses," in *13th International Conference on Fiber Optics and Photonics* (2016), p. Th3A.89.”, [**Appears in Chapter 5**]

And has made presentations in the following conferences:

1. S. A. Kalam, and S. Venugopal Rao, “Femtosecond LIBS based Standoff Detection of Explosive Molecules”, 32nd National Symposium on Plasma Science and Technology, IPR, Ahmedabad, November 07-10, 2017 (Awarded with best oral presentation). [**National**]
2. S. Abdul Kalam, and S. Venugopal Rao, “single shot trace detection of heavy elements in water”, IC-IMPACTS summer school, 2015, University of Toronto, Canada. (Oral presentation). [**International**]

Course No.	Course offered at	Title of the Course	Credits	Pass/Fail
AC809	ACRHEM	Introduction to lasers	3	Pass
AC905	ACRHEM	Laser experiments	3	Pass
MT453	SEST	Modelling and Simulations	4	Pass
AC807	ACRHEM	Research Methodology	4	Pass
AC808	ACREHM	Non-linear Optics	4	Pass
AC810	ACRHEM	Introduction to high energy materials	4	Pass

Supervisor
Dr. Soma Venugopal Rao,
Professor,
ACRHEM, University of Hyderabad,
Hyderabad.

Director,
ACRHEM
University of Hyderabad,
Hyderabad.

Dean
School of Physics,
University of Hyderabad,
Hyderabad.

Acknowledgements

First and foremost, I convey my deepest gratitude to my thesis supervisor **Prof. Soma Venugopal Rao**, for his constant guidance and support in carrying out this constructive research work. I am grateful to him as he has been not only a continuous source of motivation, but was also more than a counsellor and a facilitator.

It is my pleasure to thank the present director, **Dr Anil Kumar Aggarwal**, and former directors **Dr Kadiyam Venkateswara Rao** and **Prof. S. P. Tewari** of ACRHEM for their support in all aspects towards completion of this work. I also thank the Dean, School of Physics (SoP), UoH, for the academic support.

I sincerely thank my doctoral committee members **Dr G Manoj Kumar** and **Dr P Prem Kiran** for their invaluable suggestions in and out of the doctoral committee meetings. I also extend my sincere thanks to **Dr P Mathi** (Scientist-G, BARC, Mumbai) for her guidance in carrying out initial LIBS experiments and writing a manuscript.

I would like to thank Defence Research and Development Organization (DRDO), India through ACRHEM for providing me the financial support all through my PhD.

I thank all the teaching staff of ACRHEM and SoP for conducting the classes and explaining the nitty-gritty things in the core subjects. I would also like to thank all the non-teaching staff of ACRHEM and SoP for their co-operation as when required.

I thank Dr Anuj Vargheese, Prof. A. K. Sahoo, and Dr K Nagarjuna from ACRHEM, UoH for providing the high energy materials. I also thank Prof. V.V.S. S. Srikanth, Dr Rama Krishna Jammula of SEST, UoH for providing nanoparticles. I thank Prof. M. Jayananda and his students for providing the geological rock samples. I thank Dr. Dibakar Das and his students Mr Sreenivas Indla, Mr Khasim, Ms Jayashree for assisting me in pelletizing the powders.

I would like to thank my seniors Dr S Sreedhar, Dr M. Ashwin Kumar, Dr E. Nageswara Rao and Mr Anubham Siva Kumar for introducing me to the LIBS technique. I also thank my other seniors Dr Debasis Swain, Dr P Gopala Krishna, Dr Syed Hamad, Dr Y Balaji, Dr Ahmed Mohiuddin, Dr Ch. Leela, Dr M Venkatesh, Dr Anusha, Dr V Rakesh, Mr E Manikanta, Dr L Vinoth, Dr Sai Shiva, Mr P Venkateshwarulu, Dr S Ummar Pasha, Dr K S Rao, Dr E Narasimha Rao, Mr Shivanagi Reddy for several fruitful discussions, which helped me in clarifying many doubts that I encountered in understanding the experimental observations.

I would like to thank my friends/roommates Mr Ajmathulla, Mr D Ganesh, Mr J Rajendhar, Mr B Chandu, Mr G Nagaraju, Mr M Mahendhar, Mr K V Sreenivasulu, and Mr G Ravi Kiran for their help in carrying out this research work, sharing their joy and my pain in these years. Without their company and help these years would have been much tougher. I would also like to thank my juniors Mrs M.S.S. Bharathi, Mr K Krishnakanth, Ms Somdatta, Mr Samuel, Mr N Linga murthy, Mrs Bindu and Mr Arjun Kidav, Mr Nagaraju Menchu and all others for their support.

My special thanks to Ajmathulla, J Rajendhar, Eshita Mal, Mss M S S Bhrarathi, Mr Sunil Mahato, Mr Arjun Kidav, for their help in proof reading the thesis chapters. I also thank my M.Sc. friends Mr B Ramesh, Mr A Shravan Kumar and my M.B.A friends Mr Shankar Narayana, Mr Kranti, Mr Bhargav swaroop, Mr. Naveen Kumar for their motivation and financial support at the hour of need.

I would also like to thank my friends and teachers from Saraswathi high School (Muddanur, Kadapa Dist) Jawahar Navodaya Vidyalaya Kadapa (JNV, Kadapa) and Regional Institute of Education, Mysore (RIE Mysore) for kindling and prospering the spirit of research in me. I offer my Special thanks all my teachers at School of Physics especially Prof. Anil K Bhatnagar (my master's thesis supervisor) and Prof. A K Kapoor for their support and motivation.

I am very lucky to have a loving and caring family. Their constant encouragement and blessings at each and every stage had made me to achieve this degree. Their patience, hard work and the moral support had taught me how to survive in this world.

Finally, I thank the almighty for bestowing me with what I deserved.

Table of contents

CHAPTER 1	1
------------------------	----------

Introduction

1.1 Introduction to high energy materials (HEMs).....	2
1.1.1 Categorization of explosive materials	2
1.2 Explosives detection	3
1.2.1 Laboratory based explosive detection techniques	3
1.2.2 Laser-based spectroscopic techniques.....	4
1.3 Laser induced breakdown spectroscopy (LIBS)	6
1.3.1 Introduction to LIBS	6
1.3.2 LIBS advantages and applications	7
1.3.3 Generation of LIP and various factors affecting LIP	8
1.3.4 Timescales of fs and ns ablation	9
1.4 LIBS for explosive detection	11
1.5 Overview of the Thesis.....	18
1.5.1 Motivation	18
1.5.2 Chapter wise summary	19
1.6 References	22

CHAPTER 2	33
------------------------	-----------

Experimental details

2.1 Introduction.....	34
2.1.1 Fast and Ultrafast lasers	34
2.1.1.a Nanosecond laser (InnoLas, SpitLight1200).....	34
2.1.1.b Ultrafast Ti: Sapphire amplifier system (Libra, M/s Coherent).....	35
2.1.1.b.i Vitesse seed laser (femtosecond oscillator)	37
2.1.1.b.ii Physics behind mode locking.....	39
2.1.1.b.iii Passive mode locking.....	39
2.1.1.b.iv Kerr-lens mode locking (KLM)	40
2.1.1.b.v Evolution pump laser	40
2.1.1.b.vi Regenerative amplifier	41
2.1.1.b.vii Absorption and emission properties of Ti: Sapphire crystal.....	41
2.1.1.b.viii Group velocity dispersion (GVD).....	42
2.1.1.b.ix Ti: Sapphire Chirped Pulse Amplifier (CPA)	43

2.1.1.c Pulse width measurements of fs pulses from Libra amplifier	44
2.1.2 Mechelle spectrograph equipped with ICCD	47
2.2 LIBS technique.....	49
2.3 fs LIBS and ns LIBS setups.....	50
2.4 Method of acquiring LIBS spectra	52
2.5 Plasma diagnostic studies of ns lead nitrate plasma plume	53
2.5.1 Introduction	53
2.5.2 Experimental details	53
2.5.3 Results and discussions	54
2.5.3.a Influence of fluence on nanosecond laser induced lead plasma	54
2.5.3.b Estimation of plasma temperature by Boltzmann plot.....	56
2.5.3.c Calculation of electron density (N_e).....	57
2.6 Conclusions.....	60
2.7 References.....	62

CHAPTER 3.....67

Influence of structural and functional groups on the LIBS data: A case study of energetic triazole derivatives with femtosecond and nanosecond pulses

3.1 Introduction.....	68
3.2 Experimental details	70
3.3 Results and Discussions	73
3.3.1 Influence of laser pulse duration on fragmentation patterns in triazole-substituted nitroarene.....	73
3.3.2 Origin of CN species and correlation studies.....	76
3.3.3 Origin of C ₂ species and correlation studies.....	80
3.3.4 Plasma chemistry of CN, C ₂ emissions	81
3.3.5 Trends in the CN, C ₂ peaks in fs-LIBS spectra for (i) para series and (ii) ortho series.....	83
3.3.6 CN and C ₂ vibrational temperatures.....	85
3.3.7 Correlation of energetic parameters	87
3.3.8 Principal Component Analysis (PCA)	94
3.3.8.a Classification of fs LIBS spectra of triazoles in air using PCA	96
3.3.8.b Classification of ns LIBS spectra of triazoles in air using PCA	97
3.3.8.c Classification of ns LIBS spectra of triazoles in argon using PCA	99

3.4 Conclusions.....	100
3.5 References.....	102

CHAPTER 4.....109

Femtosecond filament induced breakdown spectroscopy (fs FIBS) for standoff detection of high energy materials

4.1 Introduction.....	110
4.1.1 Femtosecond filament induced breakdown spectroscopy (fs FIBS).....	111
4.2 Experimental details	114
4.2.1 Schmidt-Cassegrain telescope (SCT).....	118
4.3 Results and Discussions	119
4.3.1 Standoff FIBS studies of HEMs (up to 2 m; Configuration 1)	119
4.3.1.a Estimation of fluence delivered at various standoff distances	122
4.3.1.b Classification of nitroimidazoles using PCA (up to ~2 m).....	123
4.3.2 Remote LIBS of HEMs and metals (configuration 2).....	125
4.3.3 ST-FIBS studies of metals and alloys, bimetallic strips, geological samples and energetic molecules at ~6.5 m/ ~8 m in fs ST-FIBS2 setup (configuration 3)	132
4.3.3.a ST-FIBS studies of metals and alloys (M&A).....	133
4.3.3.b Difference between ablation with tightly focused fs pulses and fs filaments	134
4.3.3.c PCA analysis of ST-FIBS spectra of M&A at different ICCD gains	136
4.3.3.d ST-FIBS studies of bimetallic targets	137
4.3.3.e ST-FIBS studies of geological samples (silicates).....	141
4.3.3.e.i Field work and sample collection.....	143
4.3.3.e.ii The mineralogy of the rock types.....	143
4.3.3.e.iii Fs ST-FIBS spectra of geological rocks.....	144
4.3.3.e.iv Classification of geological rocks using PCA in standoff mode.....	145
4.3.3.f ST-FIBS studies of RDX, HMX and TNT	146
4.3.3.g ST-FIBS studies of energetic nitroimidazoles	147
4.3.3.g.i PCA studies of nitroimidazoles.....	150
4.4 Conclusions.....	151
4.5 References.....	154

CHAPTER 5163

Nanoparticle enhanced LIBS studies towards trace detection of energetic materials using femtosecond pulses

5.1 Introduction..... 164

- 5.1.1 Nanoparticle Enhanced Laser Induced Breakdown Spectroscopy (NE-LIBS). 166
- 5.1.2 Units used for trace detection and their conversions..... 168

5.2 Experimental details 171

- 5.2.1 Materials..... 173
- 5.2.2 NPs characterization techniques..... 173
 - 5.2.2.a Ultraviolet-visible spectroscopy 173
 - 5.2.2.b Transmission Electron Microscope..... 174
- 5.2.3 Characterization of various NPs..... 174
 - 5.2.3.a Synthesis of Silver NPs by sonochemical method..... 174
 - 5.2.3.b Fabrication of gold NPs in acetone using ULAL method..... 175
 - 5.2.3.c Characterization of standard silver nanospheres (nanoXact, 0.02 mg/ml) 176

5.3 Theory 176

5.4 Results and Discussions 177

- 5.4.1 Investigation of enhancement in the proximal LIBS setup 177
 - 5.4.1.a LIBS and NE-LIBS experiments on Cu target using AgDSR NPs 177
 - 5.4.1.b LIBS and NE-LIBS experiments on Ag target using AuLAL NPs 180
 - 5.4.1.c LIBS and NE-LIBS experiments on HEM pellet using standard Ag NPs. 181
- 5.4.2 Investigation of enhancement in the LIBS signal of high energy materials in standoff configuration 182
 - 5.4.2.a FIBS and NE-FIBS experiments on bulk TNT standoff mode..... 182
 - 5.4.2.b. NE-FIBS experiments for trace detection of energetic molecule in standoff mode 183

5.5 Conclusions..... 184

5.6 References..... 185

CHAPTER 6 191

Conclusions and future scope

6.1 Conclusions..... 192

6.2 Future scope 196

6.3 References..... 199

List of figures

Figure 1.1 Time scales of ns and fs pulse energy absorption and ablation along with various processes happening during and after the laser pulse interaction. (Figure adopted from the Harilal et al. Laser-Induced Breakdown Spectroscopy, Springer. 2014, pp.143-166 [93]).	9
Figure 1.2 Various processes involved in the fs ablation and plasma formation mechanism. Figure is adopted from T. A. Labutin et al. [96] J. Anal. At. Spectrom., 2016, 31, 90-118. τ_{eq} is the equilibrium time.	10
Figure 1.3 A theoretical molecular solid with an A–B–C–D directional bonding framework towards the production of the molecular radicals. [Image adopted from Serrano et. al [99] Phys. Chem. Chem. Phys. 2016, 18, 2398-2408]	11
Figure 2.1 Femtosecond amplifier system (LIBRA) top view displaying the essential modules (i) Vitesse (seed laser), (ii) Evolution (pump laser), (iii) Regenerative amplifier region and (iv) Stretcher and compressor region [3].	35
Figure 2.2 Measurement Non-chirped pulses from Vitesse seed laser and Libra as measured by the software.	36
Figure 2.3 Beam profile of Libra output is recorded using Coherent LaserCam camera which is controlled by Beam view USB 4. 6. 3 software.	37
Figure 2.4 Internal layouts of (a) Vitesse seed laser and (b) Verdi laser layouts [3].	38
Figure 2.5 Absorption and emission spectra of Ti: Sapphire crystal in 400-1050 nm © Optical microscopy premier specialized techniques, Multiphoton Fluorescence Microscopy, Interactive Tutorials, Ti: Sapphire Mode-Locked Lasers [5].	41
Figure 2.6 Schematic diagram of a chirped pulse amplification (CPA) employed in ultrafast amplifiers. © Center for Ultrafast Optical Science, University of Michigan [9].	43
Figure 2.7 Intensity autocorrelation experimental setup to measure pulse duration of Libra Ti: Sapphire amplifier through measuring the intensity of second harmonic (SH) signal generated from BBO crystal.	45
Figure 2.8 Schematic of proximal experimental LIBS setup with the (a) femtosecond amplifier laser system (Libra, M/s Coherent Co.) and (b) the nanosecond amplifier laser system (InnoLas, SpitLight 1200). In figure M: mirror, L: lens, O.F.: optical fiber.	51
Figure 2.9 The external triggering of ICCD with gate width of 2 μ S and 100 ns gate delay. In order to view all the three signals in oscilloscope, we should trigger with channel - 3 where ICCD output is connected (pink color) or the gated LIBS experiments.	52
Figure 2.10 Stack plot of typical ns lead nitrate [Pb(NO ₃) ₂] spectra obtained at 20 mJ, 40 mJ and 60 mJ in air in the spectral region of (a) 250-450 nm and (b) 450-850 nm. Peaks are identified using NIST data base and listed in table 2.3.	54
Figure 2.11 Typical Boltzmann plot for calculating the plasma temperature of lead nitrate plasma at 60 mJ at 800 ns delay using eight Pb I atomic transitions as shown in table 2.4. The solid (red) line represent s the linear fit. I, λ , A_{ik} , E_k , g_k are the intensity, the wavelength of a transition from upper level k to lower level i, transition probability, energy of the upper state, statistical weight.	57
Figure 2.12 Decay of plasma temperature obtained from Boltzmann plots at three different fluence.	58

- Figure 2.13** Spectral intensity profile of Pb I 373.99 nm atomic transition and the Lorenz fit of intensity at different energies 20mJ (black square), 40 mJ (red circle), and 60 mJ (blue triangle at a gate delay of (a) 200 ns and (b) delay of 800 ns. The gate width is constant at 200 ns.59
- Figure 2.14** Validation of McWhirter's criterion at various fluence using lead atomic transition (Pb I) at 357.27 nm, with an energy difference of $\Delta E = 3.47$ eV..... 60
- Figure 3.1** The molecular structures of structural and functional derivatives of triazole substituted nitroarene derivatives investigated in this study. 72
- Figure 3.2** LIBS spectra of six novel HEMs with (a) fs excitation in air (b) ns excitation in air and (c) ns excitation in argon environments. Molecular (CN, C₂) and atomic emissions (C, H, N, O) and impurities (Na, Ca, Fe) are labelled in the fs/ns LIBS spectra and (d) Ratio of the molecular sum to atomic sum (MSAS), (CN+C₂)/(C+H+N+O)) in air with femtosecond (black) and nanosecond (red) excitation. 73
- Figure 3.3** Baseline correction of (a) CN molecular band ($\Delta v=0$) in the region 384-389 nm, (b) CN peak at 388.34 and (c) C₂ peak at 516.4 nm from fs LIBS spectra of A1 (recorded in air) using a MATLAB code. 77
- Figure 3.4** Correlation of CNVsum with respect to C-N linkages in air with (a) fs LIBS data (b) ns LIBS data and (c) in argon with ns LIBS data. P & O denote para & ortho isomers in all the correlation graphs..... 78
- Figure 3.5** Correlation of CN violet band emissions w.r.t C-C linkages (a-c) and O% (d-f) from the LIBS data in air obtained with fs and ns pulses and in argon with ns pulses. 78
- Figure 3.6** Correlation of C₂ emissions w.r.t C-C linkages (a-c) and O% (d-f) from the LIBS data with fs and ns pulses in air and with ns pulses in argon. 80
- Figure 3.7** Difference between theoretical fits and experimental data of CN/C₂ molecular bands obtained from NMT algorithm in (a, b) air with fs pulse excitation, (c, d) air with ns excitation and in (e, f) argon ns excitation..... 87
- Figure 3.8** Correlation of CN/C₂ emission ratio (ns LIBS, air) and with respect to energetic parameters (a-d) (a) O.B. (b) V.O.D (c) D.P. (d) Q and correlation of (CN+C₂/C+H+N+O) ratio (ns LIBS, air) with the energetic parameters (e-h) (e) O.B. (f) V.O.D (g) D.P. (h) Q. 91
- Figure 3.9** Correlation of CN/C₂ emission ratio (ns LIBS, argon) and with respect to energetic parameters (a-d) (a) O.B. (b) V.O.D (c) D.P. (d) Q and correlation of (CN+C₂/C+H+N+O) ratio (ns LIBS, argon) with the energetic parameters (e-h) (e) O.B. (f) V.O.D (g) D.P. 92
- Figure 3.10** Correlation of CN/C₂ emission ratio (fs LIBS, air) and with respect to energetic parameters (a-d) (a) O.B. (b) V.O.D (c) D.P. (d) Q and correlation of (CN+C₂/C+H+N+O) ratio (fs LIBS, air) with the energetic parameters (e-h) (e) O.B. (f) V.O.D (g) D.P. (h) Q. 93
- Figure 3.11** (a) PC score plot and (b) first three PCs of unprocessed fs LIBS spectra of triazole derivatives. (c) PC score plot and (d) first three PCs of processed (for removal of impurities such as Ca, Na, Fe) fs LIBS spectra of triazole derivatives. The variance in the data set accounted by each PC is given in parentheses. 97

- Figure 3.12** (a) PC score plot and (b) first three PCs of processed (for removal of impurities such as Ca, Na, Fe) ns LIBS spectra of triazole derivatives recorded in air. (c) PC score plot and (d) first three PCs of processed and normalized ns LIBS spectra of triazole derivatives. The variance in the data set described by each PC is given in parentheses. 98
- Figure 3.13** (a) PC score plot and (b) first three PCs of processed (for removal of impurities such as Ca, Na, Fe) ns LIBS spectra of triazole derivatives recorded in argon. (c) PC score plot and (d) first three PCs of processed and normalized ns LIBS spectra of triazole derivatives recorded in argon. The variance in the data set accounted by each PC is given in parentheses. 99
- Figure 4.1** (a) Laboratory setup of R-LIBS (configuration 2) (b) Schematic of fs ST-LIBS1 setup (up to ~2 m; configuration 1) and fs R-LIBS setup (10 m/ ~8.5 m; configuration 2). M-Mirror, A-Aperture, HWP-Half wave plate, BP-Brewster plate, L-lens, SCT-Schmidt Cassegrain telescope, P-Plasma, and T-Target. 114
- Figure 4.2 Top:** Femtosecond standoff filament induced breakdown spectroscopy (fs ST-FIBS2) setup at ~6.5 m/ ~8 m (configuration 3) at ACRHEM, University of Hyderabad. **Bottom:** Experimental schematic of fs ST-FIBS2 setup. In figure, the inset shows an fs filament of ~30 cm in length generated using two lens combination L1 [plano concave lens (PCV), f=-50 cm] and L2 [plano-concave lens (PCX), f=100 cm]. 115
- Figure 4.3** Design of the Schmidt Cassegrain telescope (SCT) used in R-LIBS (configuration 1) and ST-FIBS (configuration 2) experiments. The components 1. Schmidt corrector plate, 2. Primary mirror, 3. Secondary mirror, 4. Focusing lens, and 5. Optical fiber. 118
- Figure 4.4** Typical fs standoff LIBS spectra of nitroimidazoles at (a) 10 cm (b) 30 cm (c) 50 cm (d) 100 cm (e) 200 cm acquired in ST-LIBS (configuration 1) and (f) Stack plot of the fs standoff LIBS spectra of Al at all distances. 120
- Figure 4.5** Optical microscope images (with same scale of 500 μm) of fs filament interacted portions on Aluminum target obtained at standoff distances (a) 10 cm, (b) 30 cm, (c) 50 cm, (d) 100 cm, and (e) 200 cm in order to estimate the approximate fluence delivered at the target. 122
- Figure 4.6** PC scores plot of the processed LIBS spectra of nitroimidazoles obtained at (a) 10 cm (b) 30 cm (c) 50 cm (d) 100 cm (e) 200 cm obtained in ST-LIBS. 123
- Figure 4.7** First three PCs for the processed fs LIBS spectra of nitroimidazoles at (a) 10 cm (b) 100 cm and (c) 200 cm. 124
- Figure 4.8** Stack plots of (a) representative fs R-LIBS spectra of explosive molecules (nitroimidazoles and nitropyrazoles) and (b) metals (Aluminum, copper, brass, and stainless steel) obtained at 8.5 m away. 125
- Figure 4.9** (a) 3D PC scores plot and (b) first three PCs of processed R-LIBS spectra of explosives (nitroimidazoles and nitropyrazoles) obtained from principal component analysis. 126
- Figure 4.10** (a) PC score plots and (b) first three PCs of R-LIBS spectra of metals in 220-870 nm spectral region, (c) PC score plot and (d) first three PCs of R-LIBS spectra of metals in 350-700 nm, (e) PC score plot and (f) first three PCs of normalized R-LIBS spectra in 350-700 nm wavelength region. 130

- Figure 4.11** (a) and (b) depict the images of fs filaments obtained using lens combination 1 and lens combination 2. These photos are captured using DSLR camera with an exposure time of 30 s at 30 cm away from the filaments. 133
- Figure 4.12** Femtosecond ST-FIBS spectra of metals (Al, Cu) and alloys (brass, stainless steel) recorded in configuration 3 with ICCD gain (a) 1000 (1 k) and (b) 2500 (2.5 k). 133
- Figure 4.13** AIO/Al ratio in the obtained in R-LIBS configuration (black/square), fs ST-FIBS2 (~6.5m/ ~8 m) configuration at two different ICCD gains [1000; Red/circles and 2500; blue/triangles). The inset shows the AIO/Al ratio obtained in both the configurations. AIO/Al was unchanged when gain is switched from 1000 to 2500 in case of fs ST-FIBS spectra of Al. 135
- Figure 4.14** Estimation of plasma temperature by theoretically fitting AIO molecular band head at 484.2 nm in the spectral range of 482-485 nm in aluminum spectra obtained in (a) R-LIBS (b) ST-FIBS with ICCD gain 1000 and (c) with ICCD gain 2500, using NMT algorithm. The curves with black squares are experimental data while the curves with red circles are the theoretical fits and the curves with blue triangles are the difference between experimental data and theory. 135
- Figure 4.15** PC score plots of ST-FIBS spectra of metals with ICCD gain of (a) 1000 and (b) 2500 (c), (d) represent the principal components (PCs). 137
- Figure 4.16** Energy dispersive X-ray spectroscopy images depicting the composition and purity of Ag₂₀Au₈₀ and Ag₅₀Au₅₀ bimetallic strips. 137
- Figure 4.17** (a) ST-FIBS spectra of Ag₃₀Cu₇₀ bimetallic strips (b) Intensity variation of Ag I (520.91 nm) and Cu I (521.82 nm) peaks in bimetallic strips (c) PC score plot and (d) principal components of ST-FIBS spectra of Ag@Cu bimetallic targets obtained from PCA. 138
- Figure 4.18** (a) Representative ST-FIBS spectra of Ag₂₀Au₈₀ bimetallic strip. (b) Intensity variation of Ag I (627.81 nm) peak with variation of Ag weight percentage (c) PC score plot and (d) principal components obtained from PCA of Ag@Au bimetallic targets. 139
- Figure 4.19** (a) PC score plot of fs ST-FIBS spectra of metals and bimetallic targets (b) represents principal components (PCs). 140
- Figure 4.20** Fs ST-FIBS spectrum of tonalite rock (Rav-07) with various atomic peaks labeled using NIST atomic data base in (a) 370-600 nm and (b) 600-820 nm spectral regions. 144
- Figure 4.21** PC score plots of (a) un-normalized ST-FIBS spectra and (b) normalized fs ST-FIBS spectra of geological rocks obtained from PCA. First three principal components of (c) un-normalized ST-FIBS spectra and (b) normalized fs ST-FIBS of geological samples. 145
- Figure 4.22** (a) Y-axis offset plot representing fs ST-FIBS spectra of TNT, HMX, and RDX recorded in ST-FIBS2 setup at ~6.5 m away. The inset shows CN molecular emissions observed in TNT. (b) and (c) shows the CN molecular emissions observed in HMX and RDX fs ST-FIBS spectra. 147
- Figure 4.23** Stack plot depicting typical fs ST-FIBS spectra of Nitroimidazoles obtained in ST-FIBS2 setup in the spectral range (a) 320-880 nm and (b) 700-870 nm. 147

Figure 4.24 (a) CN ($\Delta v=0$) (b) CN ($\Delta v=-1$) and (c) C ₂ ($\Delta v=0$) band head in fs ST-FIBS spectra of all nitroimidazoles. (d) CN ($\Delta v=0$) (e) CN ($\Delta v=-1$) and (f) C ₂ ($\Delta v=0$) band head in ST-FIBS spectra of 4-NIm (only) with labelled peaks and extra peaks (in blue color). The y-axes title is Intensity (counts) for all the data presented.	149
Figure 4.25 (a) PC score plot (b) PCs of un-normalized ST-FIBS spectra of Nitroimidazoles obtained from PCA. (c) PC score plot (d) PCs of normalized ST-FIBS spectra of nitroimidazoles obtained from PCA.	150
Figure 5.1 Experimental schematic of (a) proximal LIBS (or NE-LIBS) setup and (b) ST FIBS (or ST NE-FIBS) setup. In figure P-plasma; T-target; M-Mirror; L-lens, C: Schmidt-Cassegrain telescope.	172
Figure 5.2 Molecular structure of (a) NHNO ₂ substituted aryl-tetrazole (b) TNT and (c) CL-20.	173
Figure 5.3 (a) Absorption spectra of AgDSR NPs in the wavelength region 320-650 nm and (b) TEM morphology of AgDSR NPs.	174
Figure 5.4 (a) UV-Visible absorption spectra and (b) TEM micrographs depicting the ploy dispersed nature of gold NPs synthesized using ULAL method. AuLAL1/2/3/4 represents the Au NPs synthesized using 200 μ J, 300 μ J, 400 μ J, and 500 μ J energy.	175
Figure 5.5 (a) UV-Vis extinction spectra and (b) TEM micrograph of standard 60 nm Ag nanospheres (NanoXact, 0.02 mg/ml) purchased from nanoComposix. (U.S.A.) ...	176
Figure 5.6 (a) Typical LIBS spectrum of Cu target in 220-820 nm (b) LIBS (dash/black) and NE-LIBS (solid/red) spectra of Cu in the region 505nm to 580 nm showing the enhancement of persistent Cu peaks with AgDSR NPs at 2 mm above focal point.	178
Figure 5.7 Enhancement in Copper persistent atomic transitions (a) Cu I 510.6 nm (b) Cu I 515.32 nm (c) 521.8 nm (d) Cu I 578.21 nm with increasing concentration of AgDSR NPs at 2 mm above the focal point.	178
Figure 5.8 LIBS (dashed/black) and NE-LIBS (solid/red) spectra of Cu target in the wavelength region of 505-525 and 576-582 nm showing the enhancement in persistent Cu peaks in the presence of AgDSR NPs at 4 mm above from the focal point.	179
Figure 5.9 Enhancement in Copper persistent atomic transitions (a) Cu I 510.55 nm (b) Cu I 515.32 nm (c) 521.82 nm and (d) Cu I 578.21 nm with increasing concentration of the AgDSR NPs at 4 mm above from the focal point. Labels for graphs in (b), (c), and (d) are same as represented in (a).	180
Figure 5.10 Enhancement in silver persistent atomic transitions Ag I 520.90 nm and Ag I 546.54 nm with different concentrations of the AuLAL NPs at (a) 6 mm and (b) 8 mm above the focal point.	181
Figure 5.11 Enhancement in the intensity of (a) carbon atomic transition, C I 247.80 nm and (b) CN ($\Delta v=0$) molecular band of nitroamino (NHNO ₂) substituted aryl tetrazole in the presence of standard Ag NPs (60 nm) [M/s NanoComposix] in proximal LIBS setup.	182
Figure 5.12 Enhancement in intensity of (a) CN molecular band transitions in comparison to Si I atomic peak at 390.55 nm (b) CN molecular transitions shown explicitly of TNT in standoff mode.	183
Figure 5.13 Enhancement in intensity of CN molecular band transition at 388.34 nm in the LIBS data of CL-20 and in the presence of Ag NPs.	183

List of tables

Table 1-1 Summary of various works reported in literature towards the investigation of various explosives in near and standoff mode using ns/fs LIBS techniques.....	14
Table 2-1 Specifications of Vitesse oscillator output and the Libra amplifier output.	39
Table 2-2 Parameters used in wavelength and intensity calibration of ICCD.	48
Table 2-3 Atomic and ionic transitions identified in the time integrated ns LIBS spectra of lead nitrate [Pb(NO ₃) ₂] recorded in air with 20 mJ energy.	55
Table 2-4 Spectroscopic parameters of Pb I transitions used in Boltzmann plot. A _{ki} is transition probability, E _k is the energy of upper level and g _k is the multiplicity of upper level.	57
Table 3-1 IUPAC names and molecular formula of triazole derivatives investigated in fs/ns LIBS setup.	72
Table 3-2 Atomic and bond percentages present in the triazole molecules (A1-A6). Energetic parameters of nitroimidazoles obtained from Explo5 version 6.02.	72
Table 3-3 List of atomic emission lines and molecular bands observed in the LIB spectra of triazoles obtained with fs and ns pulse excitations. Emission lines from impurities such as Ca, Na, and Fe are also tabulated.....	74
Table 3-4 The Standard enthalpy change (ΔH_r), Gibbs free energy change (ΔG_r), and equilibrium constant (K _{eq}) for the proposed reaction channels.....	82
Table 3-5 Trend of CN and C ₂ line integrated intensity ratio with fs and ns excitation in air.....	83
Table 3-6 Vibrational temperatures of CN and C ₂ molecular bands calculated using NMT algorithm with both fs (air) and ns (air, argon) excitations.....	87
Table 4-1 Details of the samples (energetic molecules, bimetallic targets and geological samples) investigated in various configurations; that were investigated in both standoff and remote configurations.	117
Table 4-2 Calculation of fluence delivered at target in different standoff positions by estimating spot size on Al target.....	123
Table 4-3 Atomic and ionic transitions identified in R-LIBS spectra of stainless steel, brass and copper and labeled using NIST atomic spectroscopic data base.	127
Table 4-4 Results from principal component analysis of R-LIBS spectra of metals (Al, Cu) and alloys (brass, stainless steel)	131
Table 4-5 Combination of lenses used to generate fs filaments at desired distances.....	132
Table 4-6 Mineralogy of geological rocks investigated in fs ST-FIBS setup.....	143
Table 4-7 Atomic transitions identified in fs ST-FIBS spectra of tonalite rock (Rav-07) in 370-820 nm spectral region.	144
Table 5-1 Recent results from various group utilizing nanoparticles for achieving enhancements in LIBS signal from NE-LIBS technique.....	169

Abbreviations

LIBS	Laser Induced Breakdown Spectroscopy
Fs/fs	Femtosecond
Ns/ns	Nanosecond
FIBS	Filament Induced Breakdown Spectroscopy
HEMs	High Energy Materials
IEDs	Improvised Explosive Devices
RDX	1,3,5-Trinitroperhydro-1,3,5-triazine ($C_3H_6N_6O_6$)
HMX	1,3,5,7-Tetranitro-1,3,5,7-tetrazocane ($C_4H_8N_8O_8$)
TNT	2-Methyl-1,3,5-trinitrobenzene ($C_7H_5N_3O_6$)
CL-20	Hexanitrohexaazaisowurtzitane ($C_6N_{12}H_6O_{12}$)
PA	2, 4, 6-Trinitrophenol ($C_6H_3N_3O_7$)
AN	Ammonium nitrate (NH_4NO_3)
CE	Capillary Electrophoresis
CEC	Capillary Electro Chromatography
HPLC	High Performance Liquid Chromatography
TOFMS	Time of Flight Mass Spectrometry
LTP-MS	Low Temperature Plasma Ambient Ionization Mass Spectrometry
PAS	Photoacoustic spectroscopy
THz	Terahertz Spectroscopy
SERS	Surface Enhanced Raman Spectroscopy
SORS	Spatial Offset Raman Spectroscopy
LIF	Laser induced fluorescence
LASER	Light Amplification by Stimulated Emission of Radiation
AIO	Aluminum Oxide molecular bands
PCA	Principal Component Analysis
k-NN	<i>k</i> Nearest Neighborhood
PLS-DA	Partial Least Squares Discriminate Analysis
SIMCA	Soft Independent Modelling Class Analogy
ANN	Artificial Neural Networks

ST	Standoff
NPs	Nanoparticles
LOD	Limit of Detection
NELIBS	Nanoparticle Enhanced Laser Induced Breakdown Spectroscopy
NEFIBS	Nanoparticle Enhanced Filament Induced Breakdown Spectroscopy
DP-LIBS	double pulse LIBS
TA-BLASER Radiation	Trace Analyzer Based on Laser Ablation and Selectively Excited
LSPR	Local Surface Plasmon Resonance
Ppm	parts per million
Ppt	parts per trillion
ULAL	Ultrafast Laser Ablation in Liquids

Chapter 1

Introduction

This chapter contains an introduction to the (a) high energy materials (the studies in this thesis are mainly confined to secondary explosives) and their primary classification based on sensitivity (b) laboratory-based techniques for explosives detection with limitations (c) laser-based spectroscopic techniques for proximal as well as standoff detection and discrimination of explosives with emphasis on laser induced breakdown spectroscopy (LIBS) technique. State-of-art of the LIBS technique in consort with its (i) history (ii) advantages and applications (iii) development of the nanosecond (ns) and femtosecond (fs) LIBS techniques and (iv) the mechanisms involved in fs/ns laser pulse interaction with matter are briefly explained. The potential of LIBS technique for analyzing and classifying explosives is deliberated through highlighting the significant results obtained by several research groups. Few important ns and fs LIBS studies (but not limited to) towards the detection and identification of energetic materials are summarized in a table. The application of fs and ns LIBS towards explosive detection with several advancements such as filament induced breakdown spectroscopy (FIBS), nanoparticle enhanced LIBS (NE-LIBS) are presented. Finally, the motivation and chapter wise discussion are included at the end to provide an overview of the thesis work.

Part of this work has been accepted for publication as a book chapter

1. S. Venugopal Rao, **S. Abdul Kalam**, and M.S.S. Bharathi, "Photonics for explosive detection," in Encyclopaedia of Applied Physics, John Wiley Inc. (**In Press**, October 2018)

1.1 Introduction to high energy materials (HEMs)

High energy materials (HEMs) are those substances which release an enormous amount of energy in a very short time-span. The energy release is usually in the form of light, heat, and sound when triggered appropriately. HEMs are broadly classified into explosives, propellants and pyrotechnics. The release of toxic gases in the explosion makes these substances hazardous for the environment as well as for living things. Remarkable efforts have been devoted to improving the essential properties of explosives such as (a) increase in the stability (b) decrease in the sensitivity (c) high velocity of detonation (d) high density (e) increased detonation performance at reduced cost and preparing environmentally friendly compositions.

1.1.1 Categorization of explosive materials

Explosives are categorized into high explosives and low explosives depending on the process of chemical explosion i.e. detonation or deflagration which they undergo while these explode [1]. Detonation of “high explosives” leads to severe damage as these possess high detonation properties (velocity of detonation ranges from 5,000 to 10,000 ms^{-1}). Propellants come under the category of low explosives where these materials release high pressure gases. The High explosives are further categorized into primary and secondary explosives depending on their sensitivity to external stimuli such as heat, shock, impact, friction, etc. Primary explosives are extremely sensitive to a small amount of heat, shock and as well as a small mechanical friction (sometimes even a scratch). Consequently, these are not safe and are difficult to handle. These are used as boosters or initiators for detonating secondary explosives in the form of blasting caps and percussion caps. An example of primary explosives is lead azide [$\text{Pb}(\text{N}_3)$]. Secondary explosives are relatively safe to handle and store since these are less sensitive to mechanical friction and heat relative to primary explosives. These explosives possess a high activation energy barrier and thus need more energy for their activation. RDX (1,3,5-Trinitroperhydro-1,3,5-triazine, $\text{C}_3\text{H}_6\text{N}_6\text{O}_6$), TNT (2-Methyl-1,3,5-trinitrobenzene, $\text{C}_7\text{H}_5\text{N}_3\text{O}_6$), HMX (1,3,5,7-Tetranitro-1,3,5,7-tetrazocane, $\text{C}_4\text{H}_8\text{N}_8\text{O}_8$) and CL-20 (2,4,6,8,10,12-Hexanitro-2,4,6,8,10,12-hexaazatetracyclododecane, $\text{C}_6\text{H}_6\text{N}_{12}\text{O}_{12}$) etc. are a few examples of secondary explosives. These are also considered as explosive fuels owing to the presence of oxygen within themselves. Explosive materials can also be categorized into military

explosives and civil explosives depending on their usage. Pyrotechnics (often indicated as commercial explosives) fall into the category of civil explosives and are used in mining and demolitions of buildings [1]. These materials undergo exothermic chemical reactions in which they produce smoke, gas, and sound, along with heat.

1.2 Explosives detection

Discrimination, labeling and identification of explosives/energetic materials within themselves as well as from non-explosive materials are of immediate concern to all for counterchecking their transport, disrupt the terrorist activities and safeguard the innocent civilians. Identification of energetic materials prior to any blast incident is concurrently important to evacuate the public places, minimize the casualties and mitigate the damage to the public in addition to private property [2]. Moreover, exploiting the capability of unrestricted chemicals such as urea (ammonium nitrate, NH_4NO_3), phenol ($\text{C}_6\text{H}_6\text{O}$) [precursor in synthesis of picric acid (2, 4, 6-Trinitrophenol, $\text{C}_6\text{H}_3\text{N}_3\text{O}_7$)] in the form of improvised explosive devices (IEDs) and homemade explosives (HMEs) by anti-social elements is a major threat. Therefore, detection of the energetic materials used in manufacturing these devices is a difficult job owing to the availability of a variety of explosives and explosives precursors.

1.2.1 Laboratory based explosive detection techniques

There are several techniques in practice to identify the high energy materials [3,4]. Mokalled et al. [5] have reviewed various electronic/chemical sensors, optical and bio-sensors for detection in the vapor phase and highlighted the advantages/disadvantages of each of these techniques. Ion mobility spectrometry (IMS) is generally used at the airports for screening explosives and hazardous chemicals [6]. Christopher et al. [7] have demonstrated the separation of 14 nitroaromatic and nitramine explosive compounds (1 $\mu\text{g}/\text{ml}$) using capillary electro chromatography (CEC) technique, which is a derived technique between high-performance liquid chromatography (HPLC) and capillary electrophoresis (CE). Trisha et al. [8] recently reported a molecular chemo-sensor for detection of RDX and PETN through enhanced fluorescence, whereas TNT was reportedly identified by fluorescence quenching as revealed by Goodpaster et al. [9]. Silver and gold nanoclusters, besides semiconducting metal-oxide nanocomposites, were

Chapter 1

utilized in detection of explosive vapors [10,11]. Although these techniques are sensitive enough for detecting trace amounts of explosives (few parts per million (ppm; 1 $\mu\text{g}/\text{ml}$) to few parts per billion (ppb; 1 ng/ml) they are not feasible to detect all explosive molecules owing to inherent issues that are associated with the molecular structure, are specific to particular bond or moiety, vapor pressure and volatility of explosives. For example, it is established that the Chemiluminescence technique cannot identify the non-nitro explosives. Furthermore, by using combination of mass spectrometry and laser ionization techniques such as Time Of Flight Mass Spectrometry (TOFMS) [12], Low Temperature Plasma Ambient Ionization Mass Spectrometry (LTP-MS) [13] etc. were also developed for explosive detection. Nevertheless, these techniques either cannot provide real-time analysis or are time consuming and often involve intricate sample preparation. Moreover, in most of these cases, a direct or close contact with the explosive molecule is essential for identification. Consequently, the safety aspect of an operator as well as the device(s) is (are) at stake. Therefore, rapid detection of these dangerous substances from a safe distance either in remote mode or in standoff mode has gained serious consideration in recent years [14–17].

1.2.2 Laser-based spectroscopic techniques

Over the past few decades, several laser-based spectroscopic techniques have been independently utilized for the identification and discrimination of explosives [15,16,18]. Raman spectroscopy, laser induced breakdown spectroscopy (LIBS), Photoacoustic spectroscopy (PAS), terahertz spectroscopy (THz) are important among them. Over the years, these are subjected to several modifications (or improvisations) in terms of their photonic components, configurations and evolved as potential spectroscopic techniques for the detection of high energy materials in noncontact standoff (safe) mode, albeit, with certain limitations. Since, Raman signal is a weak signal, as the Raman cross-section is small with one in a million photon contributes to it, other techniques were derived from Raman spectroscopy technique to enhance its capabilities such as (a) Surface Enhanced Raman Spectroscopy (SERS) (b) Spatial Offset Raman Spectroscopy (SORS) etc. SERS utilizes the electromagnetic field strength enhancement in the presence of nanoparticles or nanostructures to detect explosives ranging from few micro-molar (μM) to femtomolar (fM) [19–22]. Eliasson et al. [23] showed the capability of SORS for identification of concealed liquid explosives. The specificity of Raman spectroscopy technique towards

standoff detection of HEMs at ~50 m was demonstrated by Carter et al. [24] using a frequency doubled Nd: YAG laser. Portable and handheld Raman spectrometers have also demonstrated the capability of detecting explosives in trace amounts [25,26]. However, the lower sensitivity of Raman spectroscopy can decrease the system throughput and several acquisitions (which may take few minutes) are required to record a Raman spectrum with relatively a good signal-to-noise ratio (SNR) [18]. LIBS technique provides rapid analytical information and has proven to be a versatile technique to detect, analyze and discriminate explosives in near-field [27–29] as well as in standoff mode. Portable and standoff LIBS systems with nanosecond pulsed lasers have been utilized for standoff analysis [30–34]. However, it has to rely on traces stuck to surface or fingerprints when detecting the concealed objects and cannot interact directly with the sample if it is concealed. Its potential for the detection of organic compounds, plastics and explosives is limited because LIBS spectra are not fingerprints of any explosive molecules. Nevertheless, they can be classified and labeled by using advanced chemometric algorithms and can be successfully labeled with minimum false alarms [35–37]. Terahertz spectroscopy can be potentially employed for screening at airports as it can image hidden weapons [38] (metals reflect terahertz radiation) and objects concealed in wood case, wrapped in paper, and plastic cases as these are transparent to THz radiation. However, (a) greater attenuation of terahertz signal strength in the atmosphere due to the water absorption (b) unavailability of tunable THz radiation sources (c) further progress in developing sensitive receivers and various detection schemes limit the technique of THz spectroscopy to only near-field applications at the moment. Photoacoustic spectroscopy (PAS) also has been potentially employed for real-time recognition of explosophorous groups [39], detection of traces of post-blast explosive and hazardous materials [40]. Improvisations in mid-infrared lasers and miniaturization of PAS instrumentation should be further studied for potentially employing in the detection of explosives [41]. Recently laser induced fluorescence (LIF) has been employed for the detection of explosives [42–45]. The long-range propagation of lasers (especially fs pulses in the form of filaments [46–48]) for remote or standoff detection of the explosives is a certain advantage for laser based techniques [34,49–52]. There has been mounting interest in combining the selectivity (or specificity) of Raman spectroscopy and sensitivity of LIBS to design a hybrid Raman-LIBS spectrum owing to (i) the employment of high-intensity laser beams (ii) a single laser source can produce both

Chapter 1

scattering spectrum and the atomic emission spectrum (iii) the same spectral resolution (approximately) required by the two techniques implying the usage of same spectrographs of comparable performance [18,53]. Nevertheless, there exist several challenges for laser-based optical techniques that must overcome for the successful detection of hazardous materials such as (a) identification of explosive and non-explosive overcoming interfering effects (b) quantitative identification of explosives and precursors (c) nature and availability of traces subjected to environmental conditions (d) eliminating erroneous signal from the background (e) creation of a library etc.[54–56].

1.3 Laser induced breakdown spectroscopy (LIBS)

1.3.1 Introduction to LIBS

Light-matter interaction has been an interesting area of research since the beginning of the 20th century where several paramount theories and experiments including the photoelectric effect, Raman effect, etc. were discovered. The invention of coherent light sources (i.e. lasers), through the principle of Light Amplification by Stimulated Emission of Radiation (LASER) and their applications in various fields, has motivated several researchers for performing further investigations. Simultaneously, development of fast and ultrafast lasers has also paved the way to understand the light matter interaction at molecular, atomic as well as sub-atomic levels which mainly depends on the ablation dynamics. Lasers have now become quintessential for several analytical and spectroscopic applications. Laser Induced Breakdown Spectroscopy (LIBS) is a spectroscopic technique which utilizes the plasma emissions resulted in laser-matter interaction or from laser ablation of a sample for elemental analysis and was immediately developed after the invention of the laser in 1960. Runge et al. [57] were first ever reported the utilization of laser pulse for spectrochemical analysis of metals, where a qualitative elemental analysis was carried out. Radziemski et al. [58] have reviewed the historical development and the significant progress achieved in the LIBS technique. Similarly, Baudalet et al. [59] have comprehended the initial years of LIBS and the advancements since the early 1960's. Over the years, LIBS has evolved as a potential technique to study various materials such as organic compounds, metals, as well for geological samples, environmental and cultural heritage sites. In the beginning of 21st century miniaturized, compact and portable LIBS setups were designed with a potential

of analyzing various materials. Cremers et al. [32] and Laserna et al. [60] proposed man-portable LIBS (MP-LIBS) systems for analyzing soil, chemical and hazardous materials. Evolution of the LIBS technique from lab-based setup into a field instrument has been summarized by Yu et al. [61] and Sensi et al. [33]. Portable LIBS setups are commercially available in markets. Listed below are the few web links of such devices.

- (a) <http://www.rigaku.com/en/products/lib/katana> [62]
- (b) <http://sciaps.com/sciaps-introduces-the-z-a-high-performance-handheld-lib-analyzer/> [63]
- (c) <http://tsi.com/chemlite-portable-lib-metal-analyzer/> [64]
- (d) <http://castingssa.com/oxford-instruments-launches-vulcan-handheld-metals-analyser/> [65]
- (e) <https://hha.hitachi-hightech.com/en/product-range/products/handheld-xrf-lib-analysers/handheld-lib-analysers> [66]

Furthermore, due to the development in field-deployable instrumentation, LIBS technique has been utilized to analyze the remote samples including aerosols, molten materials, and explosive residues [30,67,68]. However, to date, ns LIBS technique has been utilized to its full potential due to the availability of a wide range of compact ns lasers at affordable prices. There has been a rapid growth, over the last decade, in studies employing fs LIBS technique for both proximal and remote/standoff applications due to several advantages associated with fs pulses [46,69,70].

1.3.2 LIBS advantages and applications

LIBS technique offers in-situ multi-elemental analysis in a single shot. LIBS is also known for its robust analysis, simple setup and doesn't mandate sample preparation. Ideally, a sample in any state i.e. solid, liquid or gaseous state can be investigated by this technique [71,72]. In-situ analysis and minimal damage occurred on the sample made LIBS suitable for the use in investigating archeological sites and cultural heritage (utensils, coins and old paintings) [73]. The potential for qualitative and quantitative analysis of LIBS made it used in analyzing rocks, alloys and concentrating ores, etc. [74–76] LIBS has also been used in investigating contaminants in food, water, fertilizers, soil analysis, pharmaceutical tablets and for biomedical applications [77,78]. Furthermore, LIBS is a potential technique for underwater, space exploration missions [79,80], standoff

Chapter 1

and remote detection of explosives [81–83]. LIBS technique is also used for isotopic analysis [84], identification and discrimination of polymers [85] and differentiating isomers [86].

1.3.3 Generation of LIP and various factors affecting LIP

LIBS technique involves the focusing an intense laser pulse (nanosecond, picosecond or femtosecond) on to the target, which vaporizes and ionizes the mass in the focal region and produces a highly dense laser induced plasma (LIP) comprising atoms, ions, electrons and nano-clusters. The optical emissions released from atoms and ions present in the plasma are utilized for several analytical and spectroscopic studies such as in LIBS technique. Thus, the composition of material is studied by diagnosing these plasma emissions using a spectrograph attached with detector [87]. The process of laser ablation i.e. the process of removal of material upon interaction of laser pulses with matter is not yet completely understood. Besides, the production and evolution of LIPs depend on several factors such as laser parameters (wavelength, pulse duration and fluence), material properties (state, hardness, conductivity and etc.), pulse focusing conditions, ambient gas properties (conductivity, reactivity and density etc.) and the ambient pressure surrounding the plasma [88,89]. Coupling of laser energy with the targets is more efficient at lower wavelengths. Cabalin et al. [90] investigated the saturation fluence of metals using visible and infrared laser radiations and reported that saturation fluence is quickly achieved at lower wavelengths. Increase in the fluence beyond the saturation fluence doesn't lead to increase in emission intensity. The numerous reactions that simultaneously occur between plasma constituents as well as those involving plasma and ambient particles make their understanding critical. Plasma diagnostics and time of flight measurements provide an insight of plasma expansion and evolution for optimizing various applications of ultrafast laser ablation such as nanoparticle generation, pulsed laser depositing, etc. [91,92]. The properties and mechanisms involved in ablation with femtosecond and nanosecond pulses are discussed in subsequent sections.

1.3.4 Timescales of fs and ns ablation

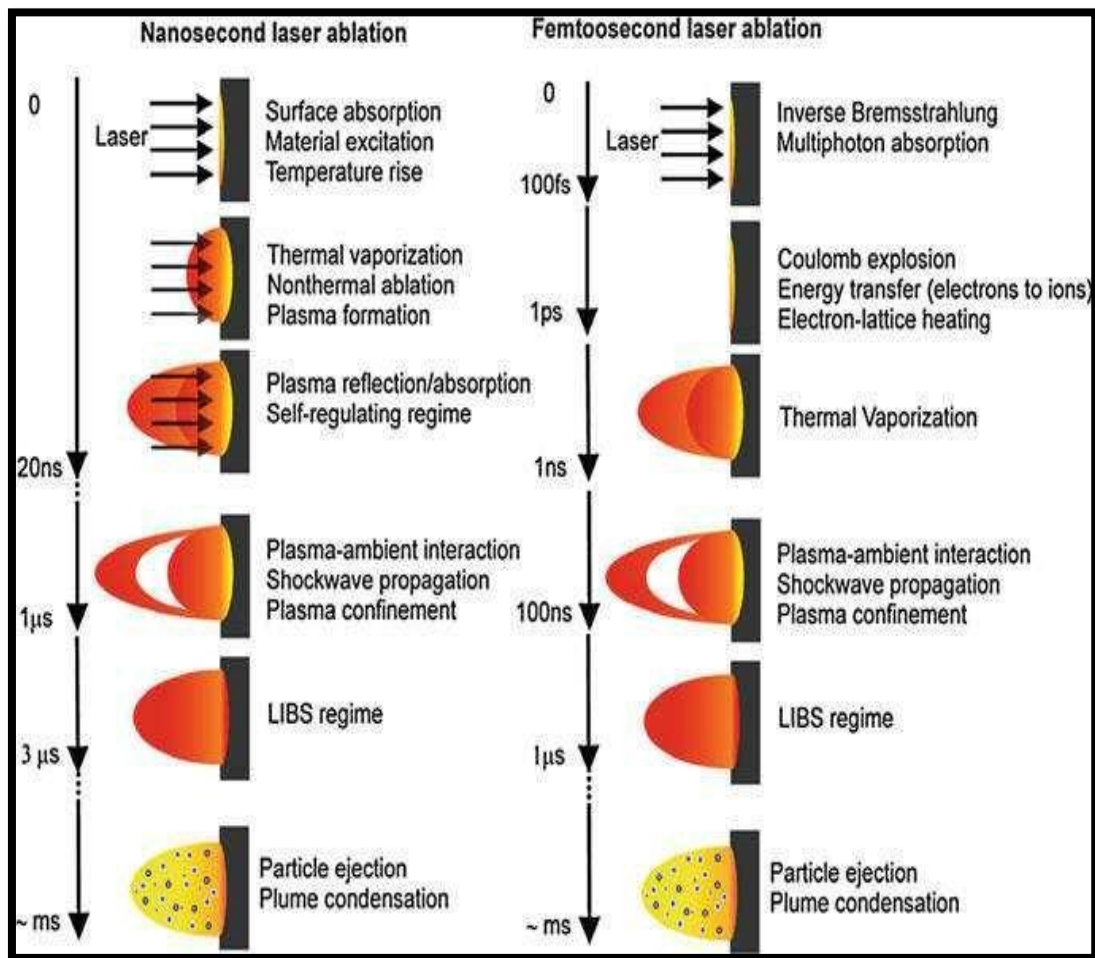


Figure 1.1 Time scales of ns and fs pulse energy absorption and ablation along with various processes happening during and after the laser pulse interaction. (Figure adopted from the Harilal et al. Laser-Induced Breakdown Spectroscopy, Springer. 2014, pp.143-166 [93]).

LIP generated with ns and fs pulses have different characteristics due to the different ablation mechanisms associated with them as illustrated in **figure 1.1**. **Figure 1.2** demonstrates the various steps in the fs ablation. Various mechanisms dominate in the process of ablation i.e. impact ionization, avalanche ionization, Coulomb explosion dominate in metals, semiconductors, and dielectrics depending on the availability of free electrons. However, these mechanisms are intensity dependent as well. As an example, Coulomb explosion is generally observed at high intensities of $\sim 10^{19} \text{ Wcm}^{-2}$ for metals, whereas for semiconductors at high intensities $> 10^{14} \text{ Wcm}^{-2}$ is still debated. Smaller sized crater formation with reduced thermal effects (negligible heat transfer from the irradiated area), the absence of plasma shielding, low ablation threshold, absence of laser-plasma interaction and minimal plasma air interaction, low continuum, low plasma temperature

Chapter 1

are advantages in fs ablation. The favoring of molecular fragments at ablation thresholds makes them more feasible for analyzing organic materials [94]. In the case of ablation with ns pulses, plasma shielding exists and the high temperature of the plasma obtained is due to the reheating of plasma with the trailing pulses. As a result, atomic emissions dominate over molecular emissions in ns plasma. However, at later times (after few μs) molecular emissions can be seen due to the recombination of ions and atoms [95].

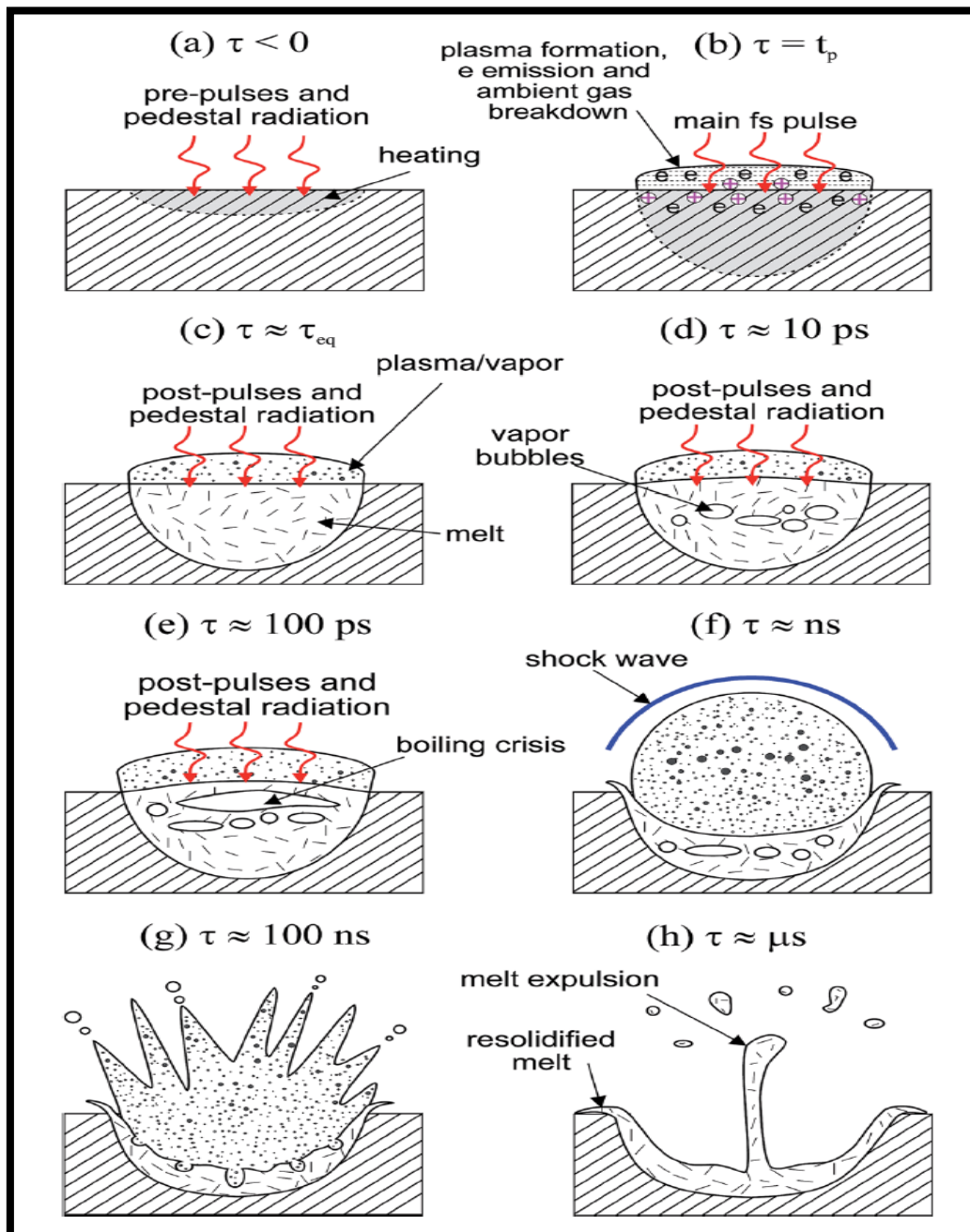


Figure 1.2 Various processes involved in the fs ablation and plasma formation mechanism. Figure is adopted from T. A. Labutin et al. [96] *J. Anal. At. Spectrom.*, 2016, 31, 90-118. τ_{eq} is the equilibrium time.

1.4 LIBS for explosive detection

In general, LIBS spectra of explosives and other common organic materials including plastics looks similar (apart from transitions of any inorganic impurities) with predominant CN, C₂ molecular emission bands as they have similar constituents of C, H, N and O [97,98]. The generation of molecular fragments enhanced the possibilities of the LIBS technique for the study of various organic materials including explosives. Several researchers studied the (i) formation of CN and C₂ species in different ways in various organic materials and explosives using fs/ns LIBS technique (ii) correlation between these emissions and their molecular structures and (c) developed several multivariate techniques in order to identify or discriminate them. **Figure 1.3** illustrates the various possible fragmentation process of molecule with A, B, C, D elements in the process of laser ablation.

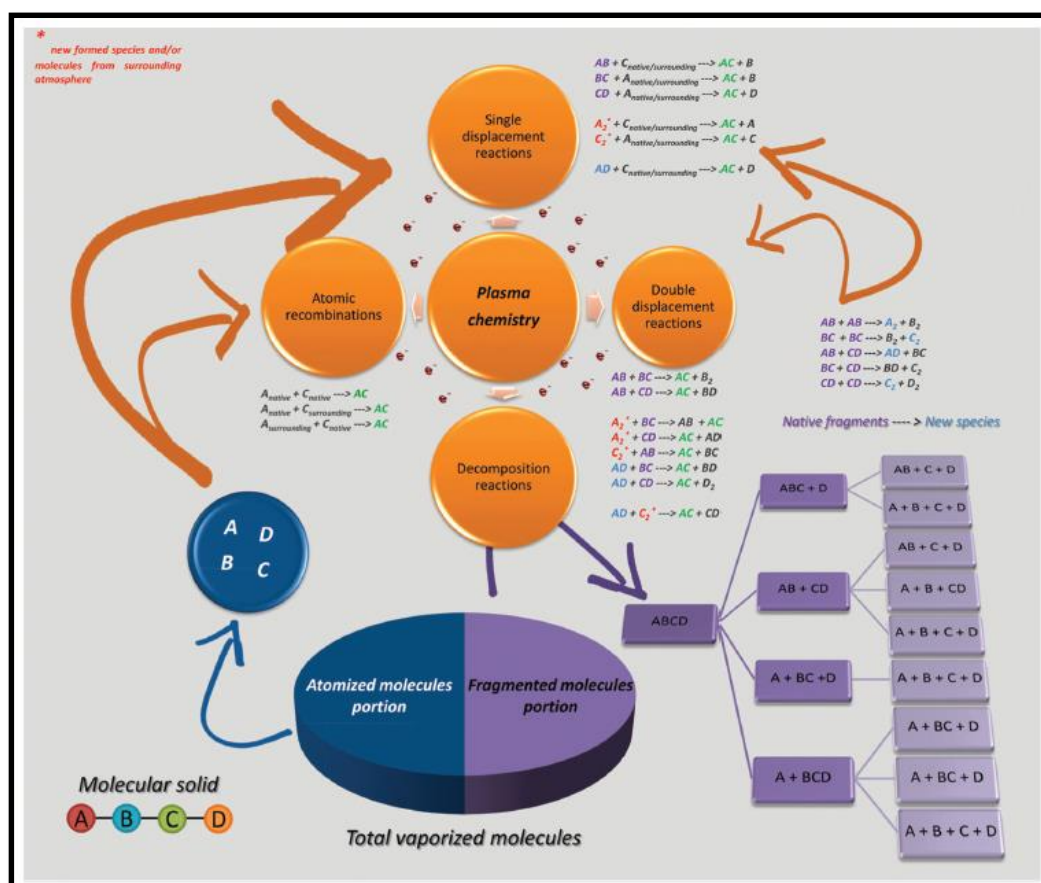


Figure 1.3 A theoretical molecular solid with an A–B–C–D directional bonding framework towards the production of the molecular radicals. [Image adopted from Serrano et. al [99] Phys. Chem. Chem. Phys. 2016, 18, 2398-2408]

Chapter 1

Grégoire et al. [100] studied the correlation between CN and C₂ emissions with native bonds present in polymeric materials using time resolved imaging.. Mousavi et al. [101] and Bravo et al. [102] had investigated the influence of molecular structure on CN and C₂ emissions for different organic materials with varying %C-C and %C=C linkages. Dong et al. [103] have experimentally studied the molecular emissions of solid materials containing C and N. Delgado et al. [104,105] had investigated several possible fragmentation pathways in organic explosives under controlled atmosphere with different background gases and at different laser fluence. Glaus et al. [106] have identified the isotopic-labelled C₂ peaks ¹²C₂, ¹²C¹³C and ¹³C₂ observed in isotopic formic acid. Few researchers have utilized table-top fs LIBS setups to study HEMs [107] as well as organic samples [108]. Rao et al. [109] have investigated the influence of varying nitro groups among nitropyrazoles on molecular emissions with fs excitation different atmospheres (air, argon, and nitrogen). Rao et al. [110] have further investigated the role of position and number of substituents on ring fragmentation pathways in nitroimidazoles using both fs and ns ablation schemes and correlated intensity ratios of molecular and atomic species between with molecular structure. Sreedhar et al. [26, 110] have investigated molecular formation dynamics of CN and C₂ in RDX, NTO, and TNT with both fs and ns excitations in different ambient gases (air, argon and nitrogen). Serrano et al. [108] have investigated the formation pathways of CH, NH, and OH diatomic radicals in fs plasmas of deuterated isotopologues of urea, terephthalic acid, and anthracene. As the LIBS spectra of pure HEMs look similar with predominant CN, C₂ molecular emission bands, it is hard to identify them by just looking at the spectra itself. Simple ratiometric analysis (comparing intensity ratios with stoichiometric ratios) of the LIBS data cannot discriminate the materials/compounds completely. Thus, several multivariate statistical analysis techniques (supervised and unsupervised) such as principal component analysis (PCA), *k*-nearest-neighborhood (k-NN) [111], partial least squares discriminate analysis (PLS-DA), soft independent modelling class analogy (SIMCA), artificial neural networks (ANN) etc. have been used in tandem with fs/ns LIBS data to achieve discrimination [112–114]. Gottfried et al. [35] successfully demonstrated the classification of explosive residues using PLS-DA in standoff mode with enhanced discrimination. Standoff experiments are executed for robust identification and discrimination of distant samples (where persons or instruments cannot be used directly). LIBS is one such potential technique where the laser pulses can be focused onto a distant target and the constituents

can be analyzed. Nanosecond pulses have been explored not only to detect explosives but also for analyzing aerosols [37], in-situ monitoring of molten materials [115–117], atmospheric sensing, exploring ores, minerals, and heavy metals [118] at standoff distances. The major challenge in correct identification of explosives is the presence of common elements (C, N, O, and H) in all these materials, which are also present in the atmosphere and invariably on-field detection needs to be performed in open atmosphere. Two groups led by Prof. J. J. Laserna [30,68,119,120] and Prof. A.W. Miziolek [32,35,121] have performed remarkable experiments and discussed several issues in detecting trace amounts of explosives on various organic and inorganic substrates, such as interference from background, interference from other organic substances including utilization of various algorithms for classification/identification in standoff configurations and also proposed future prospects [122]. Recent studies by Laserna et al. [123] revealed that atmospheric turbulence can affect the divergence and focusing of ns beam leading to beam wandering and reduction in irradiance delivered at remote locations. Though long-range propagation of high peak power fs laser pulses has been demonstrated successfully [46,47,124], Jin et al. [69] have reported the irregular intensity distribution of fs filaments after travelling 20 m in the air (500 GW power, $\tau=60$ fs, beam diameter 30 mm). However, the same authors have concluded that fs filamentation can be controlled by adjusting the beam divergence and laser power. Likewise, Fisher et al. [125] showed that onset of filamentation of fs pulses can be controlled by the use of a vortex phase plate element. Chin et al. [126] demonstrated the elongation of plasma channel generated by temporally shaped fs pulses. Therefore, detailed studies [127–129] on the types and properties of fs filaments (in terms of stability and repeatability) towards remote detection is interesting as well as challenging to develop an efficient technique for standoff trace analysis of any material. However, only a few reports are available on the utilization of fs pulses for remote or standoff applications [124,130–132]. **Table 1.1** lists out some of the important LIBS studies on detection and identification of explosives performed using ns/fs pulses. In the standoff measurements, characteristics of the detector as well as collection optics (size, transmission and reflection range) also play a crucial role. Construction and improvisation of telescopes [133–135], miniaturized spatial heterodyne spectrometers with a wide field of view [136], development of algorithms for rigorous for analyzing ICCD images [137] are further contributing to the potential of LIBS for standoff applications.

Chapter 1

Table 1-1 Summary of various works reported in literature towards the investigation of various explosives in near and standoff mode using ns/fs LIBS techniques.

Experimental details	Technique	Material	Significant results	Ref
Nanosecond LIBS for explosive detection in proximal and standoff mode				
Double pulse LIBS, Two Nd:YAG lasers (Continuum Surelite)	Proximal ns LIBS in Argon and DP-LIBS in air (< 1 m)	Residues of RDX, Comp-B (consisting of TNT, RDX and wax in 36%, 63% and 1 % respectively), diesel fuel on Aluminum target.	Improved explosive discrimination using DP-LIBS to reduce the air entrained in plasma	[31]
InnoLas nanosecond Nd :YAG laser (532 nm, ~7 ns, 10 Hz repetition rate)	Proximal Ns LIBS	Ammonium Nitrate and Ammonium Perchlorate	Stoichiometric and ratiometric analysis	[138]
InnoLas Nd :YAG laser (second harmonic wavelength 532 nm, ~7 ns, 10 Hz) Gated spectrometer (Mechelle 5000), Non-gated spectrometer (Maya 2000)	Gated & non-gated Ns LIBS	AP; Ammonium perchlorate (NH ₄ ClO ₄), BPN; Boron potassium nitrate (BKNO ₃), AN; Ammonium nitrate (NH ₄ NO ₃)	Comparison and evolution of stoichiometric ratios gated LIBS and non-gated LIBS	[139]
InnoLas SpitLight 1200 Nd :YAG laser (532 nm, ~7 ns, 10 Hz repetition rate) Gated spectrometer (Mechelle 5000)	Ns LIBS	Ammonium perchlorate, Ammonium Nitrate, Boron potassium nitrate	Ratiometric 1D, 2D and 3D models	[140]
Two Nd: YAG lasers (Ultra Big Sky and Big Sky CFR200) providing different pulse energies	Proximal LIBS (and) Man Portable LIBS system	Chemical and biological nerve agents	First man portable (MP-LIBS) system proposed by Army Research Laboratory, (ARL), USA.	[32]
SpitLight 1200, InnoLas Laser GmbH, Germany (1.2 J @1064 nm, 10 Hz), non-gated Czerny-Turner spectrometer (MAYA 2000, Ocean Optics, USA)	Proximal LIBS (ns)	Isomers of pyrazoles (1-Nitro-Pyrazole, 3-Nitro-1H-Pyrazole, 4-Nitro-1H-Pyrazole)	Classification through ANN and PCA	[86]

Quantel Brilliant Twins laser (1064 nm, 10 Hz repetition rate, 335 mJ per pulse, ~5 ns pulse duration), UV-coated Schmidt-Cassegrain telescope (SCT) by Meade (LX200GPS), DP-ST-LIBS system	Double pulse standoff LIBS (ST-LIBS) at 20 m (ns)	Various metallic and plastic materials, bulk explosives and their residues (RDX, Composition-B), biological species (anthrax surrogate <i>Bacillus subtilis</i>), and chemical warfare simulants, nerve agents	Classification of fingerprint residues of RDX, oil, on aluminum using PCA	[141]
Twin Nd: YAG laser system (Quantel Brilliant), 1064 nm, 10 Hz, 335 mJ pulse, ~5 ns pulse width) capable of generating double pulses in collinear configuration, designed for 30m operation	Standoff DP-LIBS (ns)	Explosive residues on Al, Arizona road dust, oil residue	Multivariate analysis; class assigning by PLS-DA model	[35]
Quantel Brilliant Twins, a twin laser source operating at 1064 nm, 10 Hz, 335 mJ pulse, 5 ns pulse width, which can provide collinear double pulses,	Double pulse technique for standoff laser-induced breakdown spectroscopy (STLIBS) and PLS-DA	<i>Bacillus subtilis</i> (BG) and ovalbumin as alternatives for biological warfare agents	(2% false negatives, 0% false positives) (0% false negatives, 1% false positives)	[82]
Quantel Brilliant Twins, 1064 nm, 10 Hz, 335 mJ per pulse, ~5 ns) provide a collinear doublepulse generator,	Double pulse LIBS at 25 m in standoff configuration, PLS-DA different models	RDX residue, oil residue, Arizona dust residue on plastic, wood, cardboard, etc.	Individual PLS-DA models performed.	[121]
Quantel Brilliant Q-switched Nd:YAG laser operating at 1064 nm, 350 mJ, 20 Hz)	Single pulse ns ST-LIBS setup. Algorithm based on the peak intensity ratios used	Classification between organic samples and inorganic samples including explosives	Decision making strategy for stand-off LIB spectral analysis of energetic materials.	[30]
Two Q-Switched Nd:YAG lasers (Brilliant B, Quantel, ~5 ns, 800 mJ, 10 Hz),	ns DP-LIBS for standoff experiments at 30 m	Detection of organic explosives and inorganic explosives behind a variety of transparent glasses	Mimicking conditions of detecting explosives in the vehicles, in the industrial warehouses and inside the buildings	[142]

Chapter 1

Quantel Brilliant Twins Q-switched Nd:YAG laser (532 nm, 10 Hz, 355 mJ/pulse, ~5 ns pulse width)	Raman-LIBS integration	DNT /TNT, NaClO ₃ /KClO ₃ DNT/ Nylon , NaClO ₃ /NaCl	Enhanced discrimination of explosives by combining the Raman and LIBS response emanated from the samples	[143]
Double pulse nanosecond Nd:YAG laser system (10 Hz, 850 mJ/pulse, 5.5 ns pulse duration)	ns DP-LIBS for standoff	Chloratite, TNT, PETN, DNT, and RDX residues on Al and glass substrates.	Imaging of explosives obtained from human fingerprints	[120]
Q-switched Nd:YAG twins laser system operating at 1064 nm (10 Hz, 850 mJ pulse ⁻¹ , 5.5 ns pulse width)	Ns Standoff LIBS,	Nanosecond standoff LIBS spectra of RDX and fuel oil residues at 30-50 m.	Employing supervised learning methods for superior classification	[144]
Femtosecond LIBS for explosive detection				
Ti:Sapphire amplifier system (Coherent, Hidra-25), and Nd:YAG laser system (Big Sky, CFR400)	Ns and fs proximal LIBS,	Investigations on explosives in bulk (RDX, C-4, and Composition-B) and investigation of RDX residue on aluminum substrate	Fs pulses should be operated at very low fluence for the realization of advantages associated with fs pulses towards investigating energetic molecules	[107]
Legend Ti: Sapphire fs amplifier (2W, Coherent Co.)	Near fs LIBS	Fs LIBS spectra of energetic materials such as NTO, RDX, and HMX in argon, air and nitrogen with increasing percentage of nitrogen	Influence on formation and evolution of CN and C ₂ species was investigated. No classification studies.	[27]
Legend Ti: Sapphire fs amplifier (2W, Coherent Co.)	Proximal LIBS (fs)	A set of nitropyrazoles with different number of nitro groups	CN and C ₂ molecular emissions correlation with	[109]

			the number of nitro groups present in the molecules (No clustering)	
Ti:Sapphire fs amplifier and ns laser systems (~1.2 J @1064 nm, 10 Hz)	Proximal LIBS, and time-resolved studies	A set of nitroimidazoles varying with number of nitro groups	No classification	[110]
Legend Ti:Sapphire fs amplifier (2W, Coherent Co.), INNOLAS ns laser (1.2 J @1064 nm, 10 Hz)	Near LIBS, time-resolved studies	ns and fs LIBS spectra of NTO, RDX, and HMX in ambient atmosphere	No discrimination or classification	[145]
Legend Ti: Sapphire fs amplifier (2W, Coherent Co.)	Fs LIBS in argon ambiance	ANTA, DADNE, HMX, NTO, and RDX using fs pulses in argon atmosphere	Classification with intensity ratios and kNN technique	[111]
Remote filament induced breakdown spectroscopy	Fs filament LIBS	Chemical and biological agents, barley, corn and wheat grains, Aluminum (50 m away)	No classification	[131]
Ti:sapphire laser with a chirped pulse amplifier system, Q-switched Nd:YVO4 laser	Remote UV-filament LIBS (fs)	DNT residue and remote LIBS of DNT and AP using both UV and IR filament on Al and Cu targets.	Repeatable spectral signature for explosive compounds regardless of the underlying substrate was recorded in contrast to IR filament (No classification)	[146]
Nanosecond and femtosecond LIBS	Filament libs	Al, Brass (30 m), Military grade TNT	No classification	[147]
Remote fs filament libs (2 m focusing and 12 m collection)	Femtosecond filaments	Copper, graphite and organic sample	No classification	[148]

1.5 Overview of the Thesis

1.5.1 Motivation

LIBS is one of the potential spectroscopic techniques to identify and classify hazardous substances such as explosives at standoff distances where the data collection system and the operator are at safe distances from the proximity of analysis zone. To date, nanosecond (ns) pulses have been extensively used for remote or standoff (ST) analysis of various materials including explosive residues up to ~100 m. Despite several advantages of femtosecond ablation i.e. (a) minimal air breakdown at the focal zone (b) the absence of reheating of plasma (c) narrow expansion of plasma plume thus minimizing the interaction with ambience and (d) the propagation of fs pulses in the form of filaments delivering high intensities at remote locations, the fs pulses have not been exploited up to the potential for standoff detection and discrimination of explosives. The motivation for this thesis is to comprehend or elucidate the advantages of fs pulses and fs filaments for investigating high energy materials in proximal and standoff mode respectively. Various energetic materials such as nitroimidazoles, nitropyrazoles, and triazole derivatives were investigated in this thesis work in various configurations with both fs and ns pulses or with fs pulses only (ST mode). For realizing this, the LIBS experiments were performed with both fs and ns pulse excitation in order to critically understand the (i) various formation routes of molecular species (CN, C₂, and NH) in LIP (ii) to understand the effect of functional groups and their position (para or ortho) in the molecule on LIBS spectral signatures (iii) understand the significance of molecular structure (e.g. # of nitro groups, # of single/double bonds) on the observed LIBS signatures by correlation studies which helps in discriminating studies (iv) correlation of detonation parameters of the high energy materials with LIBS spectral signatures. Such correlation studies could be helpful in discriminating the high energy materials. Since fs filaments possess the ability to deliver high intensities at remote locations, demonstration of investigation of high energy materials using fs ST-FIBS (standoff filament induced breakdown spectroscopy) technique is the second challenge. Thus, in view of this, an fs laser-based standoff system for sensing explosive molecules up to ~6.5 m (constrained by lab dimensions) is developed. Furthermore, nanoparticle enhanced LIBS (NE-LIBS) technique was also utilized for detection of explosive traces in standoff mode by achieving the enhancements.

1.5.2 Chapter wise summary

This thesis includes 6 chapters and the content is organized as follows:

Chapter 2 (Experimental details) contains of a summary of the experimental details and the theoretical concepts of LIBS technique with ns and fs laser pulses. The laser sources, spectrograph, and the detectors employed in carrying out LIBS experiments are briefly described in this chapter. The generation of fs pulses through Kerr lens mode locking and their amplification using chirped pulse amplification (CPA) technique are discussed. The pulse width of the amplifier output was measured using intensity autocorrelation technique. The method of acquiring a LIBS spectrum is clearly explained with a timing diagram. As part of initial LIBS studies the ns laser produced plasma of lead nitrate [Pb (NO₃)₂] was studied in air and the plasma parameters viz., electron density (n_e) and plasma temperature (T) were calculated.

Chapter 3 (Fs and ns LIBS studies of triazole derivatives) summarizes the results obtained from fs and ns LIBS studies of a set of six novel energetic triazole-substituted nitroarene derivatives. The examined molecules are functional and structural isomers of triazole-substituted nitroarene derivatives and have methyl (CH₃), methoxy (OCH₃), and amino (NH₂) groups in ortho and para positions. These studies were aimed to understand the (a) influence of different functional groups and their positions, (b) effect of pulse duration (c) effect of ambience gas (air, argon) on the LIBS emission. However, in the case of fs pulses, experiment was not performed in argon due to lack of sample. The influence of functional groups and their position on CN and C₂ emissions is explained through the CN/C₂ ratio i.e. atomization-to-the-fragmentation ratio. The various formation pathways for CN and C₂ in LIBS plasma are discussed and their feasibility was explained with a thermodynamics approach. CN and C₂ vibrational temperatures from fs/ns LIBS spectra were calculated using NMT algorithm. CN and C₂ emission intensities were correlated with bond percentages %C-C+%C=C, %C-N+%C=N, and %O using the fs and ns LIBS data recorded in air and argon atmospheres. Moreover, the energetic/detonation parameters of these materials namely oxygen balance, velocity of detonation, detonation pressure and chemical energy of detonation were found to correlate well with the (CN + C₂)/ (C + H + N + O) ratio. Principal component analysis

Chapter 1

(PCA) was discussed with a briefly and later utilized to successfully discriminate the triazole derivatives investigated with fs and ns LIBS techniques.

Chapter 4 (Fs ST-FIBS Studies of metals, bimetallic targets and HEMs)

concise the results obtained obtained from development of a standoff femtosecond filament induced breakdown spectroscopy technique (fs ST-FIBS) based system (~6.5 m/~8 m) for the investigation of high energy materials (HEMs) is presented. Along with HEMs (nitroimidazoles and nitropyrazoles including the standard explosive molecules such as RDX, HMX, and TNT) several other materials including metals, bimetallic targets, and geological rocks were qualitatively investigated in the same experimental configuration. The fs LIBS experiments were carried out in three different configurations i.e. (i) ST-FIBS1 (up to 2 m), (ii) Remote-LIBS (10 cm/ ~8.5 cm) and (iii) ST-FIBS2 (~6.5 cm/ ~8 m) with the last system being superior of all the configurations. ME-OPT-0007 (M/s ANDOR) collection optics (first configuration) and Schmidt-Cassegrain Telescope [(SCT), in second and third configurations] were utilized to collect the plasma emissions. The experiments in first two configurations were primarily aimed at investigating the various aspects influencing the LIBS signal strength from standoff distances such as fluence, collection system efficiency, filament generation conditions etc. The difference between ablation with tightly focused fs pulses and fs filaments is elucidated by comparing the R-LIBS and ST-FIBS2 results of Al target. Principal component analysis (PCA) was potentially utilized in tandem with fs LIBS/FIBS data to discriminate/cluster the materials investigated in all the three configurations.

Chapter 5 (NELIBS studies towards trace detection of HEMs) comprises of initial results obtained from NELIBS studies using fs pulses. There are various techniques employed to enhance the LIBS signal such as double pulse LIBS, magnetic field confinement, etc. NELIBS is one such technique, where LIBS intensity of analyte or target is enhanced in the presence of nanoparticles. We have performed initial NELIBS studies with Ag NPs on copper target and two-fold enhancement of copper signal was achieved. Simultaneously, two-fold enhancement of explosives was also achieved in table top setup (nitroamino (NHNO₂) substituted aryl-tetrazole, C₇H₄N₈O₆) as well as in ST mode (TNT pellet, 150 mg). Finally, this technique was utilized to demonstrate trace detection of HEMs (Cl-20; 1 mg over an area of 1 cm² on Brass), through obtaining enhancement in CN band in the presence of standard Ag NPs (M/s nanoComposix,

U.S.A). Thus, the obtained results open up new avenues for LIBS technique in trace explosive detection.

Chapter 6 (Conclusions and future scope) comprehend the conclusions derived from this thesis work. Conclusions from (a) proximal fs/ns LIBS studies of energetic triazole derivatives (in different atmospheres) (b) fs standoff filament induced breakdown spectroscopic (fs ST-FIBS) studies in various configurations viz., ST-FIBS1 (up to ~2 m), R-LIBS (10 cm/ ~8.5 m), ST-FIBS2 (~6.5 m/ ~8 m) of various materials viz., metals and alloys (M&A), bimetallic targets, and energetic molecules (RDX, TNT, HMX, and nitroimidazoles) (c) nanoparticle enhanced LIBS (NELIBS) studies in proximal as well as standoff mode are summarized. Future scope of the present works includes (a) detailed studies on the types and properties of filaments produced and, consequently, their effects on the LIBS plasma (b) detection and identification of standard HEMs such as RDX, HMX, CL-20 etc. at 15-20 m using ST-FIBS (c) detection of explosives in trace level and enhancing their signal in the presence of nanoparticles using NELIBS technique in table-top setup as well as in ST mode.

1.6 References

1. S. Venugopalan, *Demystifying Explosives : Concepts in High Energy Materials*, 1st ed. (Elsevier Inc., 2015).
2. S. Al Sabah, N. Alsharqawi, and E. Al Haddad, "The aftermath of the Kuwait mosque bombing: A retrospective cohort analysis and lessons learned," *Int. J. Surg.* **56**, 15–20 (2018).
3. J. S. Caygill, F. Davis, and S. P. J. Higson, "Current trends in explosive detection techniques," *Talanta* **88**, 14–29 (2012).
4. Z. Bielecki, J. Janucki, A. Kawalec, J. Mikolajczyk, N. Palka, M. Pasternak, T. Pustelny, T. Stacewicz, and J. Wojtas, "Sensors and systems for the detection of explosive devices - An overview," *Metrol. Meas. Syst.* **19**(1), 3–28 (2012).
5. L. Mokalled, M. Al-husseini, K. Y. Kabalan, and A. El-hajj, "Sensor Review for Trace Detection of Explosives," *Int. J. Sci. Eng. Res.* **5**(6), 337–350 (2014).
6. S. Singh and M. Singh, "Explosives detection systems (EDS) for aviation security," *Signal Processing* **83**(1), 31–55 (2003).
7. C. G. Bailey and C. Yan, "Separation of Explosives Using Capillary Electrochromatography," *Anal. Chem.* **70**(15), 3275–3279 (1998).
8. T. L. Andrew and T. M. Swager, "A fluorescence turn-on mechanism to detect high explosives RDX and PETN," *J. Am. Chem. Soc.* **129**(23), 7254–7255 (2007).
9. J. V. Goodpaster and V. L. McGuffin, "Fluorescence quenching as an indirect detection method for nitrated explosives," *Anal. Chem.* **73**(9), 2004–2011 (2001).
10. A. Marchisio and J. Tulliani, "Semiconducting Metal Oxides Nanocomposites for Enhanced Detection of Explosive Vapors," *ceramics* **1**(9), 1–22 (2018).
11. S. Singh, "Sensors—an effective approach for the detection of explosives," *J. Hazard. Mater.* **144**(1–2), 15–28 (2007).
12. S. E. Prebihalo, K. L. Berrier, C. E. Freye, H. D. Bahaghighat, N. R. Moore, D. K. Pinkerton, and R. E. Synovec, "Multidimensional Gas Chromatography: Advances in Instrumentation, Chemometrics, and Applications," *Anal. Chem.* **90**(1), 505–532 (2018).
13. J. F. Garcia-Reyes, J. D. Harper, G. A. Salazar, N. A. Charipar, Z. Ouyang, and R. G. Cooks, "Detection of explosives and related compounds by low-temperature plasma ambient ionization mass spectrometry," *Anal. Chem.* **83**(3), 1084–1092 (2011).
14. D. S. Moore, "Advances in Optical Methods for Standoff Detection of Explosives," **836**, (2010).
15. S. Wallin, A. Pettersson, H. Östmark, and A. Hobro, "Laser-based standoff detection of explosives: A critical review," *Anal. Bioanal. Chem.* **395**(2), 259–274 (2009).
16. J. B. Johnson, S. D. Allen, J. Merten, L. Johnson, D. Pinkham, and S. W. Reeve, "Standoff Methods for the Detection of Threat Agents: A Review of Several Promising Laser-Based Techniques," *J. Spectrosc.* **2014**(Article ID 613435), 13 (2014).
17. D. S. Moore, "Instrumentation for trace detection of high explosives," *Rev. Sci. Instrum.* **75**(8), 2499–2512 (2004).
18. J. Moros, J. A. Lorenzo, and J. J. Laserna, "Standoff detection of explosives: Critical comparison for ensuing options on Raman spectroscopy-LIBS sensor fusion," *Anal. Bioanal. Chem.* **400**(10), 3353–3365 (2011).
19. S. V. Rao, G. K. Podagatlapalli, and S. Hamad, "Femtomolar Detection of

- Explosive Molecules using Laser Ablated Targets and SERS," in *13th International Conference on Fiber Optics and Photonics* (OSA, 2016), p. Th4D.2.
20. C. Byram, S. S. B. Moram, A. K. Shaik, and V. R. Soma, "Versatile gold based SERS substrates fabricated by ultrafast laser ablation for sensing picric acid and ammonium nitrate," *Chem. Phys. Lett.* **685**, 103–107 (2017).
 21. T. Liyanage, A. Rael, S. Shaffer, S. Zaidi, J. V Goodpaster, and R. Sardar, "Fabrication of a self-assembled and flexible SERS nanosensor for explosive detection at parts-per-quadrillion levels from fingerprints," *Analyst* **143**(9), 2012–2022 (2018).
 22. P. M. Fierro-Mercado and S. P. Hernández-Rivera, "Highly sensitive filter paper substrate for SERS trace explosives detection," *Int. J. Spectrosc.* (2012).
 23. C. Eliasson, N. A. Macleod, and P. Matousek, "Noninvasive detection of concealed liquid explosives using Raman spectroscopy," *Anal. Chem.* **79**(21), 8185–8189 (2007).
 24. J. C. Carter, S. M. Angel, M. Lawrence-Snyder, J. Scaffidi, R. E. Whipple, and J. G. Reynolds, "Standoff detection of high explosive materials at 50 meters in ambient light conditions using a small Raman instrument," *Appl. Spectrosc.* **59**(6), 769–775 (2005).
 25. A. Hakonen, F.-C. Wang, P. O. Andersson, H. Wingfors, T. Rindzevicius, M. S. Schmidt, V. R. Soma, S. Xu, Y. Li, and A. Boisen, "Handheld femtogram detection of hazardous Picric acid with hydrophobic Ag nanopillar SERS substrates and mechanism of elasto-capillarity," *ACS Sensors* **2**(2), 198–202 (2017).
 26. Agilent Technologies, *Explosives Detection Through Opaque Containers with Agilent Resolve — a Handheld SORS System* (2018).
 27. S. Sreedhar, E. Nageswara Rao, G. Manoj Kumar, S. P. Tewari, and S. Venugopal Rao, "Molecular formation dynamics of 5-nitro-2,4-dihydro-3H-1,2,4-triazol-3-one, 1,3,5-trinitroperhydro-1,3,5-triazine, and 2,4,6-trinitrotoluene in air, nitrogen, and argon atmospheres studied using femtosecond laser induced breakdown spectroscopy," *Spectrochim. Acta B* **87**, 121–129 (2013).
 28. A. H. Farhadian, M. K. Tehrani, M. H. Keshavarz, and S. M. R. Darbani, "Energetic materials identification by laser-induced breakdown spectroscopy combined with artificial neural network," *Appl. Opt.* **56**(12), 3372–3377 (2017).
 29. F. C. De Lucia, R. S. Harmon, K. L. McNesby, R. J. Winkel, and A. W. Miziolek, "Laser-induced breakdown spectroscopy analysis of energetic materials," *Appl. Opt.* **42**(30), 6148–6152 (2003).
 30. C. López-Moreno, S. Palanco, J. J. Laserna, F. DeLucia, A. W. Miziolek, J. Rose, R. A. Walters, and A. I. Whitehouse, "Test of a stand-off laser-induced breakdown spectroscopy sensor for the detection of explosive residues on solid surfaces," *J. Anal. At. Spectrom.* **21**(1), 55–60 (2006).
 31. F. C. De Lucia Jr, J. L. Gottfried, C. A. Munson, and A. W. Miziolek, "Double pulse laser-induced breakdown spectroscopy of explosives: Initial study towards improved discrimination," *Spectrochim. Acta Part B At. Spectrosc.* **62**(12), 1399–1404 (2007).
 32. F. C. DeLucia, A. C. Samuels, R. S. Harmon, R. A. Walters, K. L. McNesby, A. LaPointe, R. J. Winkel, and A. W. Miziolek, "Laser-induced breakdown spectroscopy (LIBS): A promising versatile chemical sensor technology for hazardous material detection," *IEEE Sens. J.* **5**(4), 681–689 (2005).
 33. G. S. Senesi, "Portable Hand Held Laser-induced Breakdown Spectroscopy (LIBS) Instrumentation for in-field Elemental Analysis of Geological Samples," *Int. J.*

- Earth Environ. Sci. **2**, 1–3 (2017).
34. M. Gaft and L. Nagli, "UV gated Raman spectroscopy for standoff detection of explosives," *Opt. Mater. (Amst)*. **30**(11), 1739–1746 (2008).
 35. F. C. De Lucia, J. L. Gottfried, C. a Munson, and A. W. Miziolek, "Multivariate analysis of standoff laser-induced breakdown spectroscopy spectra for classification of explosive-containing residues," *Appl. Opt.* **47**(31), G112–G121 (2008).
 36. P. Yaroshchuk, D. L. Death, and S. J. Spencer, "Comparison of principal components regression, partial least squares regression, multi-block partial least squares regression, and serial partial least squares regression algorithms for the analysis of Fe in iron ore using LIBS," *J. Anal. At. Spectrom.* **27**(1), 92–98 (2012).
 37. L. A. Álvarez-Trujillo, V. Lazic, J. Moros, and J. Javier Laserna, "Standoff monitoring of aqueous aerosols using nanosecond laser-induced breakdown spectroscopy: droplet size and matrix effects," *Appl. Opt.* **56**(13), 3773–3782 (2017).
 38. L. A. Skvortsov, "Standoff Detection of Hidden Explosives and Cold and Fire Arms by Terahertz Time-Domain Spectroscopy and Active Spectral Imaging (Review)," *J. Appl. Spectrosc.* **81**(5), 725–749 (2014).
 39. Y. H. El-sharkawy and S. Elbasuney, "Real time recognition of explosophorous group and explosive material using laser induced photoacoustic spectroscopy associated with novel algorithm for time and frequency domain analysis," *Spectrochim. Acta Part A Mol. Biomol. Spectrosc.* **204**, 25–32 (2018).
 40. R. C. Sharma, S. Kumar, S. Gautam, S. Gupta, and H. B. Srivastava, "Photoacoustic sensor for trace detection of post-blast explosive and hazardous molecules," *Sensors Actuators, B Chem.* **243**, 59–63 (2017).
 41. J. Li, W. Chen, and B. Yu, "Recent progress on infrared photoacoustic spectroscopy techniques," *Appl. Spectrosc. Rev.* **46**(6), 440–471 (2011).
 42. C. M. Wynn, S. Palmacci, R. R. Kunz, and M. Rothschild, "Noncontact detection of homemade explosive constituents via photodissociation followed by laser-induced fluorescence," *Opt. Express* **18**(6), 5399–5406 (2010).
 43. C. M. Wynn, S. Palmacci, R. R. Kunz, and M. Rothschild, "A Novel Method for Remotely Detecting Trace Explosives," *Lincoln Lab. J.* **17**(2), 27–39 (2008).
 44. A. W. Fountain III, S. D. Christesen, J. a. Guicheteau, W. F. Pearman, and T. Chyba, "Long Range Standoff Detection of Chemical, Biological and Explosive Hazards on Surfaces," in *Micro- and Nanotechnology Sensors, Systems, and Applications II* (SPIE, 2010), **7679**, p. 76790H1-13.
 45. K. L. Gares, K. T. Hufziger, S. V. Bykov, and S. A. Asher, "Review of explosive detection methodologies and the emergence of standoff deep UV resonance Raman," *J. Raman Spectrosc.* **47**(1), 124–141 (2016).
 46. M. Rodriguez, R. Bourayou, G. Méjean, J. Kasparian, J. Yu, E. Salmon, A. Scholz, B. Stecklum, J. Eislöffel, U. Laux, A. P. Hatzes, R. Sauerbrey, L. Wöste, and J. P. Wolf, "Kilometer-range nonlinear propagation of femtosecond laser pulses," *Phys. Rev. E* **69**(32), 1–7 (2004).
 47. M. Durand, A. Houard, B. Prade, A. Mysyrowicz, A. Durécu, B. Moreau, D. Fleury, O. Vasseur, H. Borchert, K. Diener, R. Schmitt, F. Théberge, M. Chateaneuf, J.-F. Daigle, and J. Dubois, "Kilometer range filamentation," *Opt. Express* **21**(22), 26836–26845 (2013).
 48. A. Couairon and A. Mysyrowicz, "Femtosecond filamentation in transparent media," *Phys. Rep.* **441**(2), 47–189 (2007).

49. S. K. Sharma, "New trends in telescopic remote Raman spectroscopic instrumentation," *Spectrochim. Acta - Part A Mol. Biomol. Spectrosc.* **68**(4), 1008–1022 (2007).
50. W. Li, X. Li, X. Li, Z. Hao, Y. Lu, and X. Zeng, "A review of remote laser-induced breakdown spectroscopy," *Appl. Spectrosc. Rev.* 1–25 (2018).
51. A. K. Misra, S. K. Sharma, D. E. Bates, and T. E. Acosta, "Compact standoff Raman system for detection of homemade explosives," in *Chemical, Biological, Radiological, Nuclear, and Explosives (CBRNE) Sensing XI* (SPIE, 2010), p. 76650U.
52. G. Mogilevsky, L. Borland, M. Brickhouse, and A. W. Fountain III, "Raman Spectroscopy for Homeland Security Applications," *Int. J. Spectrosc.* **2012**(Article ID 808079), 1–12 (2012).
53. A. Giakoumaki, I. Osticioli, and D. Anglos, "Spectroscopic analysis using a hybrid LIBS-Raman system," *Appl. Phys. A* **83**(4), 537–541 (2006).
54. S. A. Kalam, E. N. Rao, and S. V. Rao, "Standoff LIBS for explosives detection: Challenges and status," *Laser Focus World* **53**, 24–28 (2017).
55. P. Wen, M. Amin, W. D. Herzog, and R. R. Kunz, "Key challenges and prospects for optical standoff trace detection of explosives," *Trends Anal. Chem.* **100**, 136–144 (2018).
56. C. W. Van Neste, X. Liu, M. Gupta, S. Kim, Y. Tsui, and T. Thundat, "Standoff detection of explosive residues on unknown surfaces," in *Micro- and Nanotechnology Sensors, Systems, and Applications IV* (SPIE, 2012), **8373**, p. 83732F.
57. E. F. Runge, R. W. Minck, and F. R. Bryan, "Spectrochemical analysis using a pulsed laser source," *Spectrochim. Acta* **20**(4), 733–736 (1964).
58. L. J. Radziemski, "From LASER to LIBS, the path of technology development," *Spectrochim. Acta B* **57**(7), 1109–1113 (2002).
59. M. Baudelet and B. W. Smith, "The first years of laser-induced breakdown spectroscopy," *J. Anal. At. Spectrom.* **28**(5), 624–629 (2013).
60. F. J. Fortes, J. Cuñat, L. M. Cabalín, and J. J. Laserna, "In Situ Analytical Assessment and Chemical Imaging of Historical Buildings Using a Man-Portable Laser System," *Appl. Spectrosc.* **61**(5), 558–564 (2007).
61. L. I. N. Qing-Yu and D. Yi-Xiang, "Laser-Induced Breakdown Spectroscopy: From Experimental Platform to Field Instrument," *Chinese J. Anal. Chem.* **45**(9), 1405–1414 (2017).
62. "Rigaku handheld laser induced breakdown (LIBS) spectrometer," <http://www.rigaku.com/en/products/lib/katana>.
63. "SciAps Introduces the Z – a High Performance, Handheld LIBS Analyzer," <https://www.sciaps.com/sciaps-introduces-the-z-a-high-performance-handheld-lib-analyzer/>.
64. "ChemLite Laser Aluminum Analyzer (Model 4235)," <http://tsi.com/chemlite-portable-lib-metal-analyzer/>.
65. "Oxford Instruments launches Vulcan handheld metals analyser," <http://castingssa.com/oxford-instruments-launches-vulcan-handheld-metals-analyser/>.
66. "Hitachi handheld LIBS analysers - Vulcan range," <https://hha.hitachi-hightech.com/en/product-range/products/handheld-xrf-lib-analysers/handheld-lib-analysers>.
67. F. J. Fortes and J. J. Laserna, "The development of fieldable laser-induced

- breakdown spectrometer: No limits on the horizon," *Spectrochim. Acta B* **65**(12), 975–990 (2010).
68. I. Gaona, J. Serrano, J. Moros, and J. J. Laserna, "Range-Adaptive Standoff Recognition of Explosive Fingerprints on Solid Surfaces using a Supervised Learning Method and Laser- Induced Breakdown Spectroscopy," *Anal. Chem.* **86**(10), 5045–5052 (2014).
 69. Z. Jin, J. Zhang, M. H. Xu, X. Lu, Y. T. Li, Z. H. Wang, Z. Y. Wei, X. H. Yuan, and W. Yu, "Control of filamentation induced by femtosecond laser pulses propagating in air.," *Opt. Express* **13**(25), 10424–30 (2005).
 70. P. Rohwetter, K. Stelmaszczyk, L. Wöste, R. Ackermann, G. Méjean, E. Salmon, J. Kasparian, J. Yu, and J. P. Wolf, "Filament-induced remote surface ablation for long range laser-induced breakdown spectroscopy operation," *Spectrochim. Acta B* **60**, 1025–1033 (2005).
 71. D. W. Hahn and N. Omenetto, "Laser-induced breakdown spectroscopy (LIBS), part I: review of basic diagnostics and plasma–particle interactions: still-challenging issues within the analytical plasma community," *Appl. Spectrosc.* **64**(12), 335A–366A (2010).
 72. D. W. Hahn and N. Omenetto, "Laser-induced breakdown spectroscopy (LIBS), part II: review of instrumental and methodological approaches to material analysis and applications to different fields," *Appl. Spectrosc.* **66**(4), 347–419 (2012).
 73. R. Gaudiuso, M. Dell’Aglia, O. de Pascale, G. S. Senesi, and A. de Giacomo, "Laser induced breakdown spectroscopy for elemental analysis in environmental, cultural heritage and space applications: A review of methods and results," *Sensors* **10**(8), 7434–7468 (2010).
 74. R. S. Harmon, R. E. Russo, and R. R. Hark, "Applications of laser-induced breakdown spectroscopy for geochemical and environmental analysis: A comprehensive review," *Spectrochim. Acta B* **87**, 11–26 (2013).
 75. E. Tognoni, G. Cristoforetti, S. Legnaioli, and V. Palleschi, "Calibration-Free Laser-Induced Breakdown Spectroscopy: State of the art," *Spectrochim. Acta B* **65**(1), 1–14 (2010).
 76. S. K. Sharma, P. G. Lucey, M. Ghosh, H. W. Hubble, and K. A. Horton, "Stand-off Raman spectroscopic detection of minerals on planetary surfaces," *Spectrochim. Acta A* **59**(10), 2391–2407 (2003).
 77. V. K. Singh and A. K. Rai, "Prospects for laser-induced breakdown spectroscopy for biomedical applications: A review," *Lasers Med. Sci.* **26**(5), 673–687 (2011).
 78. S. J. Rehse, H. Salimnia, and A. W. Miziolek, "Laser-induced breakdown spectroscopy (LIBS): An overview of recent progress and future potential for biomedical applications," *J. Med. Eng. Technol.* **36**(2), 77–89 (2012).
 79. R. C. Wiens, S. Maurice, B. Barraclough, M. Saccoccio, W. C. Barkley, J. F. Bell, S. Bender, J. Bernardin, D. Blaney, and J. Blank, "The ChemCam instrument suite on the Mars Science Laboratory (MSL) rover: Body unit and combined system tests," *Space Sci. Rev.* **170**(1–4), 167–227 (2012).
 80. R. Francis, T. Estlin, G. Doran, S. Johnstone, D. Gaines, V. Verma, M. Burl, J. Frydenvang, S. Montaña, R. C. Wiens, S. Schaffer, O. Gasnault, L. DeFlores, D. Blaney, and B. Bornstein, "AEGIS autonomous targeting for ChemCam on Mars Science Laboratory: Deployment and results of initial science team use," *Sci. Robot.* **2**(7), ean4582 (2017).
 81. Q. Q. Wang, K. Liu, H. Zhao, C. H. Ge, and Z. W. Huang, "Detection of explosives with laser-induced breakdown spectroscopy," *Front. Phys.* **7**(6), 701–

- 707 (2012).
82. J. L. Gottfried, F. C. De Lucia, C. A. Munson, and A. W. Miziolek, "Standoff detection of chemical and biological threats using laser-induced breakdown spectroscopy," *Appl. Spectrosc.* **62**(4), 353–363 (2008).
 83. A. W. Miziolek, F. C. De Lucia, C. A. Munson, and J. L. Gottfried, "Progress in Standoff LIBS Detection and Identification of Residue Materials," in *Lasers, Sources and Related Photonic Devices* (2010), p. LWD2.
 84. S. S. Harilal, B. E. Brumfield, N. L. Lahaye, K. C. Hartig, and M. C. Phillips, "Optical spectroscopy of laser-produced plasmas for standoff isotopic analysis," *Appl. Phys. Rev.* **5**(2), 021301 (2018).
 85. S. Grégoire, M. Boudinet, F. Pelascini, F. Surma, V. Detalle, and Y. Holl, "Laser-induced breakdown spectroscopy for polymer identification," *Anal. Bioanal. Chem.* **400**(10), 3331–3340 (2011).
 86. A. K. Myakalwar, S. K. Anubham, S. K. Paidi, I. Barman, and M. K. Gundawar, "Real-time fingerprinting of structural isomers using laser induced breakdown spectroscopy," *Analyst* **141**(10), 3077–3083 (2016).
 87. R. Noll, *Laser-Induced Breakdown Spectroscopy: Fundamentals and Applications*, 1st ed. (2012).
 88. D. Díaz, A. Molina, and D. Hahn, "Effect of laser irradiance and wavelength on the analysis of gold- and silver-bearing minerals with laser-induced breakdown spectroscopy," *Spectrochim. Acta B* **145**, 86–95 (2018).
 89. K. K. Anoop, S. S. Harilal, R. Philip, R. Bruzzese, and S. Amoroso, "Laser fluence dependence on emission dynamics of ultrafast laser induced copper plasma," *J. Appl. Phys.* **120**(18), 185901 (2016).
 90. L. M. Cabalin and J. J. Laserna, "Experimental determination of laser induced breakdown thresholds of metals under nanosecond Q-switched laser operation," *Spectrochim. Acta B* **53**(5), 723–730 (1998).
 91. K. H. Rao, N. Smijesh, N. Klemke, R. Philip, I. V. Litvinyuk, and R. T. Sang, "Time-resolved optical emission spectroscopic studies of picosecond laser produced Cr plasma," *Phys. Plasmas* **25**(6), 63505 (2018).
 92. N. Smijesh, K. Chandrasekharan, J. C. Joshi, and R. Philip, "Time of flight emission spectroscopy of laser produced nickel plasma: Short-pulse and ultrafast excitations," *J. Appl. Phys.* **116**(1), 13301 (2014).
 93. S. S. Harilal, J. R. Freeman, and P. K. Diwakar, "Femtosecond laser ablation: Fundamentals and Applications," in *Laser Induced Breakdown Spectroscopy: Theory and Applications*, S. Musazzi and U. Perini, eds. (Springer Berlin Heidelberg, 2014), pp. 143–166.
 94. T. A. Labutin, V. N. Lednev, A. A. Ilyin, and A. M. Popov, "Femtosecond laser-induced breakdown spectroscopy," *J. Anal. At. Spectrom.* **31**(1), 90–118 (2016).
 95. S. S. Harilal, B. E. Brumfield, B. D. Cannon, and M. C. Phillips, "Shock Wave Mediated Plume Chemistry for Molecular Formation in Laser Ablation Plasmas," *Anal. Chem.* **88**(4), 2296–2302 (2016).
 96. T. A. Labutin, V. N. Lednev, A. A. Ilyin, and A. M. Popov, "Femtosecond laser-induced breakdown spectroscopy," *J. Anal. At. Spectrom.* **31**(1), 90–118 (2016).
 97. V. P. N. Nampoori, C. P. Girijavallabhan, S. S. Harilal, C. Riju, and C. V. Bindhu, "Optical emission studies of C₂ species in laser-produced plasma from carbon," *J. Phys. D* **30**(12), 1703 (1997).
 98. S. S. Harilal, R. C. Issac, C. V. Bindhu, V. P. N. Nampoori, and C. P. G. Vallabhan, "Temporal and spatial evolution of C₂ in laser induced plasma from graphite

- target," *J. Appl. Phys.* **80**(6), 3561–3565 (1996).
99. J. Serrano, J. Moros, and J. Javier Laserna, "Molecular signatures in femtosecond laser-induced organic plasmas: comparison with nanosecond laser ablation," *Phys. Chem. Chem. Phys.* **18**(4), 2398–2408 (2016).
 100. S. Grégoire, V. Motto-Ros, Q. L. Ma, W. Q. Lei, X. C. Wang, F. Pelascini, F. Surma, V. Detalle, and J. Yu, "Correlation between native bonds in a polymeric material and molecular emissions from the laser-induced plasma observed with space and time resolved imaging," *Spectrochim. Acta B* **74**, 31–37 (2012).
 101. S. J. Mousavi, M. H. Farsani, S. M. R. Darbani, A. Mousaviazar, M. Soltanolkotabi, and A. E. Majd, "CN and C2 vibrational spectra analysis in molecular LIBS of organic materials," *Appl. Phys. B* **122**(5), 1–16 (2016).
 102. Á. Fernández-Bravo, T. Delgado, P. Lucena, and J. J. Laserna, "Vibrational emission analysis of the CN molecules in laser-induced breakdown spectroscopy of organic compounds," *Spectrochim. Acta B* **89**, 77–83 (2013).
 103. M. Dong, J. Lu, S. Yao, Z. Zhong, J. Li, J. Li, and W. Lu, "Experimental study on the characteristics of molecular emission spectroscopy for the analysis of solid materials containing C and N," *Opt. Express* **19**(18), 17021–17029 (2011).
 104. T. Delgado, J. M. Vadillo, and J. J. Laserna, "Acting Role of Background Gas in the Emission Response of Laser-Induced Plasmas of Energetic Nitro Compounds," *Appl. Spectrosc.* **70**(8), 1364–1374 (2016).
 105. T. Delgado, J. M. Vadillo, and J. J. Laserna, "Primary and recombined emitting species in laser-induced plasmas of organic explosives in controlled atmospheres," *J. Anal. At. Spectrom.* **29**(9), 1675–1685 (2014).
 106. R. Glaus, J. Riedel, and I. Gornushkin, "Insight into the formation of molecular species in laser-induced plasma of isotopically labeled organic samples," *Anal. Chem.* **87**(19), 10131–10137 (2015).
 107. F. C. De Lucia, J. L. Gottfried, and A. W. Miziolek, "Evaluation of femtosecond laser-induced breakdown spectroscopy for explosive residue detection," *Opt. Express* **17**(2), 419–425 (2009).
 108. J. Serrano, J. Moros, and J. J. Laserna, "Exploring the formation routes of diatomic hydrogenated radicals using femtosecond laser-induced breakdown spectroscopy of deuterated molecular solids," *J. Anal. At. Spectrom.* **30**(11), 2343–2352 (2015).
 109. E. N. Rao, S. Sunku, and S. V. Rao, "Femtosecond Laser-Induced Breakdown Spectroscopy Studies of Nitropyrazoles: The Effect of Varying Nitro Groups," *Appl. Spectrosc.* **69**(11), 1342–1354 (2015).
 110. E. N. Rao, P. Mathi, S. A. Kalam, S. Sreedhar, A. K. Singh, B. N. Jagatap, and S. V. Rao, "Femtosecond and nanosecond LIBS studies of nitroimidazoles: correlation between molecular structure and LIBS data," *J. Anal. At. Spectrom.* **31**(3), 737–750 (2016).
 111. S. Sunku, E. Nageswara Rao, G. Manoj Kumar, S. P. Tewari, and S. Venugopal Rao, "Discrimination methodologies using femtosecond LIBS and correlation techniques," in *Next-Generation Spectroscopic Technologies VI* (SPIE, 2013), **8726**, p. 87260H–8.
 112. T. L. Zhang, S. Wu, H. S. Tang, K. Wang, Y. X. Duan, and H. Li, "Progress of chemometrics in laser-induced breakdown spectroscopy analysis," *Chinese J. Anal. Chem.* **43**(6), 939–948 (2015).
 113. T. Zhang, H. Tang, and H. Li, "Chemometrics in laser-induced breakdown spectroscopy," *J. Chemom.* e2983 (2018).
 114. J. Moros, J. Serrano, C. Sanchez, J. Macias, and J. J. Laserna, "New chemometrics

- in laser-induced breakdown spectroscopy for recognizing explosive residues," *J. Anal. At. Spectrom.* **27**(12), 2111–2122 (2012).
115. L. A. Álvarez-Trujillo, V. Lazic, J. Moros, and J. Javier Laserna, "Standoff monitoring of aqueous aerosols using nanosecond laser-induced breakdown spectroscopy: droplet size and matrix effects," *Appl. Opt.* **56**(13), 3773–3782 (2017).
 116. D. Girón, T. Delgado, J. Ruiz, L. M. Cabalín, and J. J. Laserna, "In-situ monitoring and characterization of airborne solid particles in the hostile environment of a steel industry using stand-off LIBS," *Measurement* **115**, 1–10 (2018).
 117. A. Ferrero, J. J. Laserna, and L. A. A., "Preliminary studies on stand-off laser induced breakdown spectroscopy detection of aerosols," *J. Anal. At. Spectrom.* **23**(6), 885–888 (2008).
 118. M. M. T. and V. K. U. and R. N. and P. D. and K. M. M. S. and V. B. K. and C. Santhosh, "Development of a Stand-off Laser Induced Breakdown Spectroscopy (ST-LIBS) system for the analysis of complex matrices," *J. Instrum.* **11**(08), P08021 (2016).
 119. P. Lucena, A. Doña, L. M. Tobaría, and J. J. Laserna, "New challenges and insights in the detection and spectral identification of organic explosives by laser induced breakdown spectroscopy," *Spectrochim. Acta Part B* **66**(1), 12–20 (2011).
 120. P. Lucena, I. Gaona, J. Moros, and J. J. Laserna, "Location and detection of explosive-contaminated human fingerprints on distant targets using standoff laser-induced breakdown spectroscopy," *Spectrochim. Acta B* **85**, 71–77 (2013).
 121. J. L. Gottfried, F. C. De Lucia Jr., and A. W. Miziolek, "Discrimination of explosive residues on organic and inorganic substrates using laser-induced breakdown spectroscopy," *J. Anal. At. Spectrom.* **24**(3), 288–296 (2009).
 122. J. L. Gottfried, F. C. De Lucia, C. A. Munson, and A. W. Miziolek, "Laser-induced breakdown spectroscopy for detection of explosives residues: A review of recent advances, challenges, and future prospects," *Anal. Bioanal. Chem.* **395**(2), 283–300 (2009).
 123. J. J. Laserna, R. F. Reyes, R. González, L. Tobaría, and P. Lucena, "Study on the effect of beam propagation through atmospheric turbulence on standoff nanosecond laser induced breakdown spectroscopy measurements," *Opt. Express* **4376**(12), 10265–10276 (2009).
 124. K. Stelmaszczyk, P. Rohwetter, G. Méjean, J. Yu, E. Salmon, J. Kasparian, R. Ackermann, J. P. Wolf, and L. Wöste, "Long-distance remote laser-induced breakdown spectroscopy using filamentation in air," *Appl. Phys. Lett.* **85**(18), 3977–3979 (2004).
 125. M. Fisher, C. Siders, E. Johnson, O. Andrusyak, C. Brown, and M. Richardson, "Control of filamentation for enhancing remote detection with laser induced breakdown spectroscopy," in *Enabling Technologies and Design of Nonlethal Weapons* (International Society for Optics and Photonics, 2006), **6219**, p. 621907.
 126. A. Chen, S. Li, H. Qi, Y. Jiang, Z. Hu, X. Huang, and M. Jin, "Elongation of plasma channel generated by temporally shaped femtosecond laser pulse," *Opt. Commun.* **383**, 144–147 (2017).
 127. S. S. Harilal, J. Yeak, B. E. Brumfield, J. D. Suter, and M. C. Phillips, "Dynamics of molecular emission features from nanosecond, femtosecond laser and filament ablation plasmas," *J. Anal. At. Spectrom.* **31**(6), 1192–1197 (2016).
 128. S. S. Harilal, J. Yeak, and M. C. Phillips, "Plasma temperature clamping in filamentation laser induced breakdown spectroscopy," *Opt. Express* **23**(21),

- 27113–27122 (2015).
129. S. S. Harilal, J. Yeak, B. E. Brumfield, and M. C. Phillips, "Consequences of femtosecond laser filament generation conditions in standoff laser induced breakdown spectroscopy," *Opt. Express* **24**(16), 17941–17949 (2016).
 130. H. L. Xu and S. L. Chin, "Femtosecond laser filamentation for atmospheric sensing," *Sensors* **11**(1), 32–53 (2011).
 131. S. L. Chin, H. L. Xu, Q. Luo, F. Théberge, W. Liu, J. F. Daigle, Y. Kamali, P. T. Simard, J. Bernhardt, S. A. Hosseini, M. Sharifi, G. Méjean, A. Azarm, C. Marceau, O. Kosareva, V. P. Kandidov, N. Aközbek, A. Becker, G. Roy, P. Mathieu, J. R. Simard, M. Châteauneuf, and J. Dubois, "Filamentation "remote" sensing of chemical and biological agents/pollutants using only one femtosecond laser source," *Appl. Phys. B* **95**(1), 1–12 (2009).
 132. K. C. Hartig, I. Ghebregziabher, and I. Jovanovic, "Standoff Detection of Uranium and its Isotopes by Femtosecond Filament Laser Ablation Molecular Isotopic Spectrometry," *Sci. Rep.* **7**, 43852 (2017).
 133. K. Bhavsar and K. E. Eseller, "Design optimization of Cassegrain telescope for remote explosive trace detection," in *Counterterrorism, Crime Fighting, Forensics, and Surveillance Technologies* (SPIE, 2017), pp. 1044103–7.
 134. W. T. Li, X. Y. Yang, X. Li, S. S. Tang, J. [space]M. Li, R. X. Yi, P. Yang, Z. Q. Hao, L. B. Guo, X. Y. Li, X. Y. Zeng, and Y. F. Lu, "A portable multi-collector system based on an artificial optical compound eye for stand-off laser-induced breakdown spectroscopy," *J. Anal. At. Spectrom.* **32**(10), 1975–1979 (2017).
 135. S. Palanco, C. Lo, and J. J. Laserna, "Design , construction and assessment of a field-deployable laser-induced breakdown spectrometer for remote elemental sensing," *Spectrochim. Acta B* **61**, 88–95 (2006).
 136. P. D. Barnett, N. Lamsal, and S. M. Angel, "Standoff Laser-Induced Breakdown Spectroscopy (LIBS) Using a Miniature Wide Field of View Spatial Heterodyne Spectrometer with Sub-Microsteradian Collection Optics," *Appl. Spectrosc.* **71**(4), 583–590 (2017).
 137. P. Pořízka, J. Klus, J. Mašek, M. Rajnoha, D. Prochazka, P. Modlitbová, J. Novotný, R. Burget, K. Novotný, and J. Kaiser, "Multivariate classification of echellograms: a new perspective in Laser-Induced Breakdown Spectroscopy analysis," *Sci. Rep.* **7**(1), 3160 (2017).
 138. S. Sreedhar, S. V. Rao, P. P. Kiran, S. P. Tewari, G. M. Kumar, and M. A. Kumar, "Stoichiometric analysis of ammonium nitrate and ammonium perchlorate with nanosecond laser induced breakdown spectroscopy," in *Chemical, Biological, Radiological, Nuclear, and Explosives (CBRNE) Sensing XI*, (2010), **7665**(1), p. 76650J–11.
 139. S. Sunku, A. K. Myakalwar, M. K. Gundawar, P. K. Paturi, S. P. Tewari, and V. R. Soma, "Stoichiometric Analysis of Inorganic Compounds Using Laser-Induced Breakdown Spectroscopy with Gated and Nongated Spectrometers," *ISRN Opt.* Article ID 631504 (2012).
 140. S. Sreedhar, M. K. Gundawar, and S. V. Rao, "Laser induced breakdown spectroscopy for classification of high energy materials using elemental intensity ratios," *Def. Sci. J.* **64**(4), 332–338 (2014).
 141. J. L. Gottfried, F. C. De Lucia, C. A. Munson, and A. W. Miziolek, "Double-pulse standoff laser-induced breakdown spectroscopy for versatile hazardous materials detection," *Spectrochim. Acta Part B* **144**, 1405–1411 (2007).
 142. R. González, P. Lucena, L. M. Tobaría, and J. J. Laserna, "Standoff LIBS detection

- of explosive residues behind a barrier," *J. Anal. At. Spectrom.* **24**(8), 1123–1126 (2009).
143. J. Moros and J. J. Laserna, "New Raman-laser-induced breakdown spectroscopy identity of explosives using parametric data fusion on an integrated sensing platform," *Anal. Chem.* **83**(16), 6275–6285 (2011).
 144. I. Gaona, J. Serrano, J. Moros, and J. J. Laserna, "Range-Adaptive Standoff Recognition of Explosive Fingerprints on Solid Surfaces using a Supervised Learning Method and Laser-Induced Breakdown Spectroscopy," *Anal. Chem.* **86**(10), 5045–5052 (2014).
 145. S. Sunku, M. K. Gundawar, A. K. Myakalwar, P. P. Kiran, S. P. Tewari, and S. V. Rao, "Femtosecond and nanosecond laser induced breakdown spectroscopic studies of NTO, HMX, and RDX," *Spectrochim. Acta B* **79–80**, 31–38 (2013).
 146. D. Mirell, O. Chalus, K. Peterson, and J.-C. Diels, "Remote sensing of explosives using infrared and ultraviolet filaments," *J. Opt. Soc. Am. B* **25**(7), B108 (2008).
 147. C. G. Brown, R. Bernath, M. Fisher, M. C. Richardson, M. Sigman, R. A. Walters, A. Miziolek, H. Bereket, and L. E. Johnson, "Remote femtosecond laser induced breakdown spectroscopy (LIBS) in a standoff detection regime," in *Enabling Technologies and Design of Nonlethal Weapons* (International Society for Optics and Photonics, 2006), **6219**, p. 62190B.
 148. M. Baudalet, M. Richardson, and M. Sigman, "Self-channeling of femtosecond laser pulses for rapid and efficient standoff detection of energetic materials," in *IEEE Conference on Technologies for Homeland Security* (2009), pp. 472–476.

Intentional blank page

Chapter 2

Experimental details

This chapter comprises an overview of the experimental details of laser induced breakdown spectroscopy (LIBS) technique with nanosecond (ns) and femtosecond (fs) laser pulses. The laser sources (Libra; Ultrafast Ti: Sapphire amplifier system and SpitLight 1200; Nd: YAG nanosecond laser system), spectrograph (Andor Mechelle 5000), and the detectors employed in carrying out the LIBS experiments are briefly described in this chapter. The generation of fs pulses through Kerr lens mode locking and their amplification using chirped pulse amplification (CPA) technique are discussed. The pulse width of the amplifier output was measured using intensity autocorrelation technique. The method of acquiring a LIB spectrum is explained with a time diagram. As part of initial LIBS studies the ns laser produced plasma of lead nitrate [Pb(NO₃)₂] was studied in air at atmospheric pressure and the plasma parameters such as electron density and plasma temperature were measured.

2.1 Introduction

In this chapter, the essential components employed in carrying out LIBS experiments, such as laser sources (ultrafast or fast lasers) and their operation, spectrometer and detector are elaborated. Femtosecond (fs) amplifier system is discussed in detail as most of the experiments were performed by it. The generation of fs pulses as well as their amplification using chirped pulse amplification technique (CPA) is discussed. The pulse width of the amplified fs pulses were measured using autocorrelation method. Methodology of acquiring LIBS signal is explained with a time diagram. Initial results from diagnostic studies on the plasma of lead nitrate [Pb(NO₃)₂] obtained using nanosecond (ns) laser pulses are discussed in the final section of this chapter.

2.1.1 Fast and Ultrafast lasers

Two pulsed lasers were employed to perform LIBS experiments, namely (a) Q-switched Nd:YAG laser delivering pulses of ~7 ns duration (InnoLas SpitLight 1200, 1.2J @1064 nm, 10 Hz) and (b) mode-locked femtosecond Ti: sapphire amplifier laser system (Libra, M/s Coherent, 4 mJ, 1 kHz). This section explains the design aspects of the mentioned solid state lasers with reference to principle of production of fast and ultrafast laser pulses.

2.1.1.a Nanosecond laser (InnoLas, SpitLight1200)

InnoLas SpitLight 1200 is the nanosecond laser system which was used for carrying out ns LIBS experiments. The laser operates at a fundamental wavelength of 1064 nm with 1.2 J per pulse at 10 Hz (repetition rate) with Nd: YAG (neodymium ions (3+) doped in yttrium aluminum garnet, Nd: Y₃Al₅O₁₂) as the gain medium and delivers a pulse of ~7 ns duration. The laser can be operated at frequency other than 10 Hz depending on the robustness of experiment. The laser has two important sections (i) oscillator and pre-amplifier section and (ii) amplifier section. In oscillator and pre-amplifier section two Nd: YAG rods (oscillator rod and pre-amplifier rod) are pumped using a single xenon flash lamp and in amplifier section one Nd: YAG rod is pumped by two xenon flash lamps to achieve population inversion and amplification. The output from oscillator and pre-amplifier section is passed through a faraday rotator which

slightly changes the polarization of beam and prevents the back reflected light to pass through the pre-amplifier section and thus avoiding the damage of rods. KD*P type I and type II crystals are used to convert 1064 nm wavelength into 532 nm by down conversion process with an conversion efficiency of 43% and 37% percent respectively. Nd: YAG laser is a four-level laser system with $^4F_{3/2}$ as upper lasing level and $^4I_{11/2}$ as lower lasing level for the emission of 1064 nm fundamental wavelength [1]. The metastable state life time of upper lasing level is $\sim 230 \mu\text{s}$. The pulses in nanosecond time scales ($\sim 7 \text{ ns}$ to $\sim 25 \text{ ns}$) are generally produced by the Q-switching technique, where an optical element or device in the cavity switches the quality of the cavity once maximum population inversion is achieved [2]. In this laser, active Q-switching is performed by Pockels cell.

2.1.1.b Ultrafast Ti: Sapphire amplifier system (Libra, M/s Coherent)

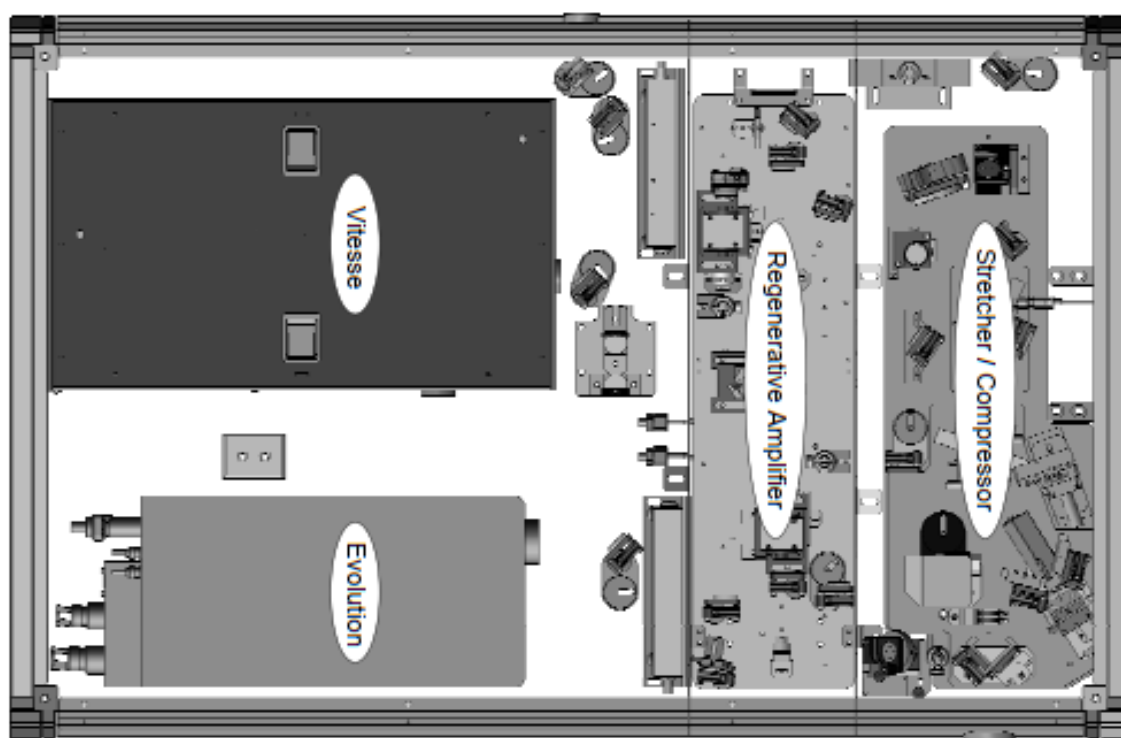


Figure 2.1 Femtosecond amplifier system (LIBRA) top view displaying the essential modules (i) Vitesse (seed laser), (ii) Evolution (pump laser), (iii) Regenerative amplifier region and (iv) Stretcher and compressor region [3].

Libra [3] is a class IV amplified Ti: Sapphire laser system (M/s Coherent, 4 mJ, 1 kHz) operating at a central wavelength of 800 nm delivers femtosecond pulses of $\sim 35 \text{ fs}$ pulse duration, and average power of 4 W at 1 kHz repetition rate. The beam diameter is $\sim 9 \text{ mm}$ ($1/e^2$ width). The Libra optical bench assembly is shown in **figure 2.1**. It consists of four modules (i) Vitesse seed laser (ii) Evolution pump laser (iii) Regenerative amplifier and

Chapter 2

(iv) Stretcher and compressor region integrated in to a single box. **Figure 2.2** represents the un-chirped transform limited output from Libra amplifier with central wavelength ~ 800 nm and its pulse duration (~ 35 fs) as measured using Ocean optics spectra suite. Likewise, **figure 2.3** shows the Gaussian beam profile (TE_{00}) of Libra output which is recorded using Coherent LaserCam camera controlled by Beam view USB 4. 6. 3.

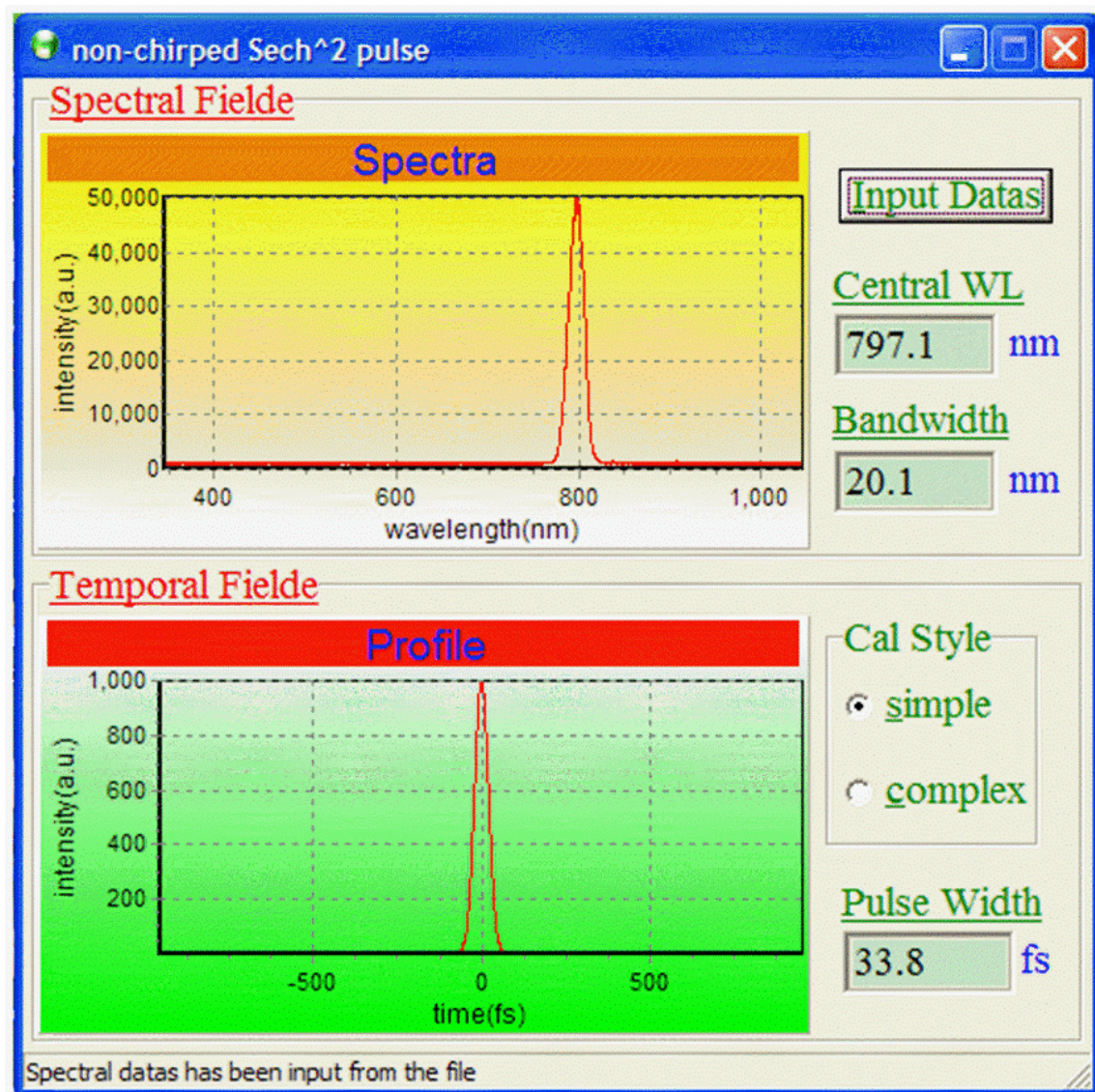


Figure 2.2 Measurement Non-chirped pulses from Vitesse seed laser and Libra as measured by the software.

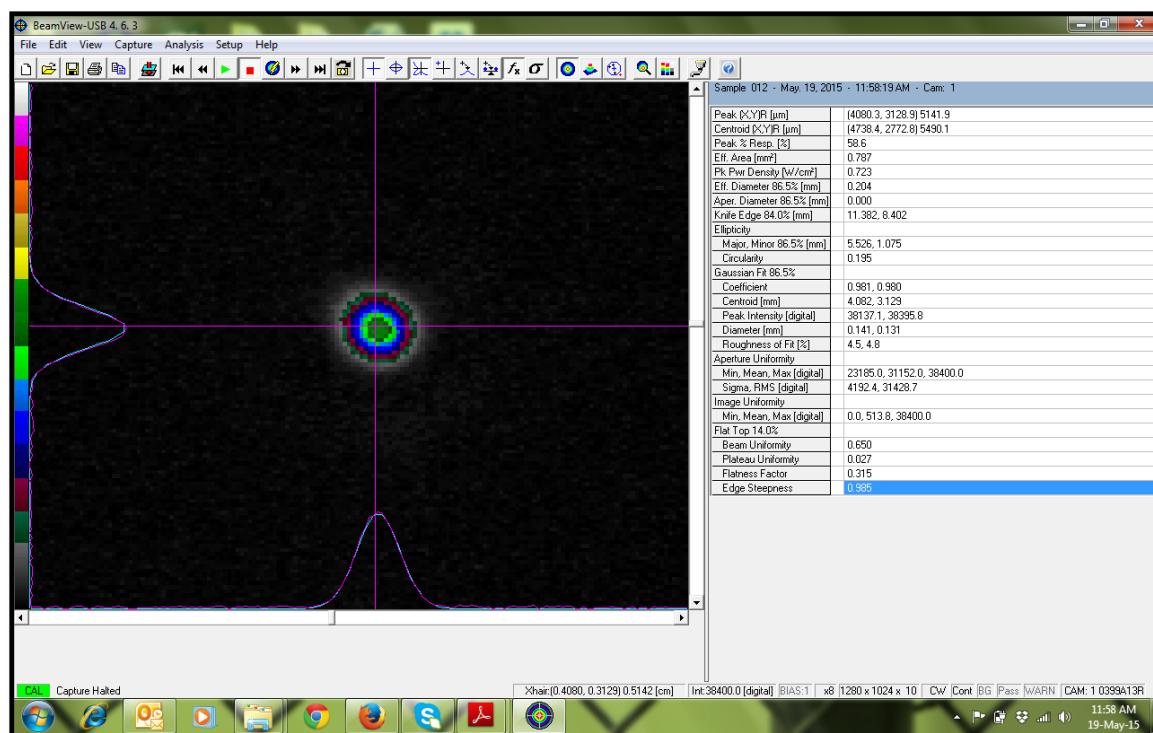


Figure 2.3 Beam profile of Libra output is recorded using Coherent LaserCam camera which is controlled by Beam view USB 4. 6. 3 software.

2.1.1.b.i Vitesse seed laser (femtosecond oscillator)

The Vitesse laser [3] is a compact Verdi-pumped ultrafast laser which serves as the seed laser (oscillator) in the Libra system. It produces modelocked, sub-100 femtosecond Gaussian pulses with an average output power of ~300 mW at 80 MHz with an optimum bandwidth of 30 nm. Vitesse laser head consists of (1) sealed Verdi laser head (2) a power track mirror, and (3) a sealed Verdi Pumped Ultra-Fast (VPUF) laser head. Both Verdi laser head and VPUF are sealed by the manufacturer to ensure best performance over the life time of the laser as shown in **figure 2.4(a)**. The schematic of Verdi laser is illustrated in **figure 2.4(b)**. Important parameters of the pulses from Vitesse seed laser and Libra amplifier are tabulated in **table 2.1**.

Verdi laser head acts as a pump laser in Vitesse laser head. It has Vanadate (Nd: YVO₄) as the gain medium which is pumped by array of diode lasers and produces a continuous laser light at 1064 nm (fundamental wavelength) with an average power of 2 W. Diode lasers offer tunable output wavelength and convert electrical energy to laser energy with high efficiency. The umbilical carries optical fiber cables (and electric cables) through which the diode laser output ($\lambda=808$ nm) is communicated to the Verdi head. The major optical components of Verdi include LBO (Lithium Triborate, LiB₃O₅)

Chapter 2

as a frequency doubling crystal (1064 nm to 532 nm), an etalon as the single-frequency optic, an optical diode, astigmatic compensator, two pump mirrors, and two end mirrors as shown in **figure 2.4(b)**. A piezo driven mirror is utilized to maintain optimum pump beam alignment into the VPUF laser head's cavity. VPUF laser head is a sealed cavity consists of Ti: Sapphire crystal and negative dispersion mirrors (NDM). The gain medium of Vitesse Oscillator i.e. Ti: Sapphire crystal which is present in VPUF laser head is pumped by second harmonic of Verdi laser (532 nm). Multiple reflections from the negative dispersion mirrors (NDMs) provide the total negative dispersion compensation which is essential to produce sub-100 fs pulses. Kerr-Lens Mode locking (KLM) [4], a passive mode locking technique, is utilized to achieve mode locking in Vitesse seed laser with an automatic starter which triggers the initiation of mode locking. Thus, the ultrashort pulses with large bandwidth, low noise with an average out power of 300 mW at repetition rate of 80 MHz are produced.

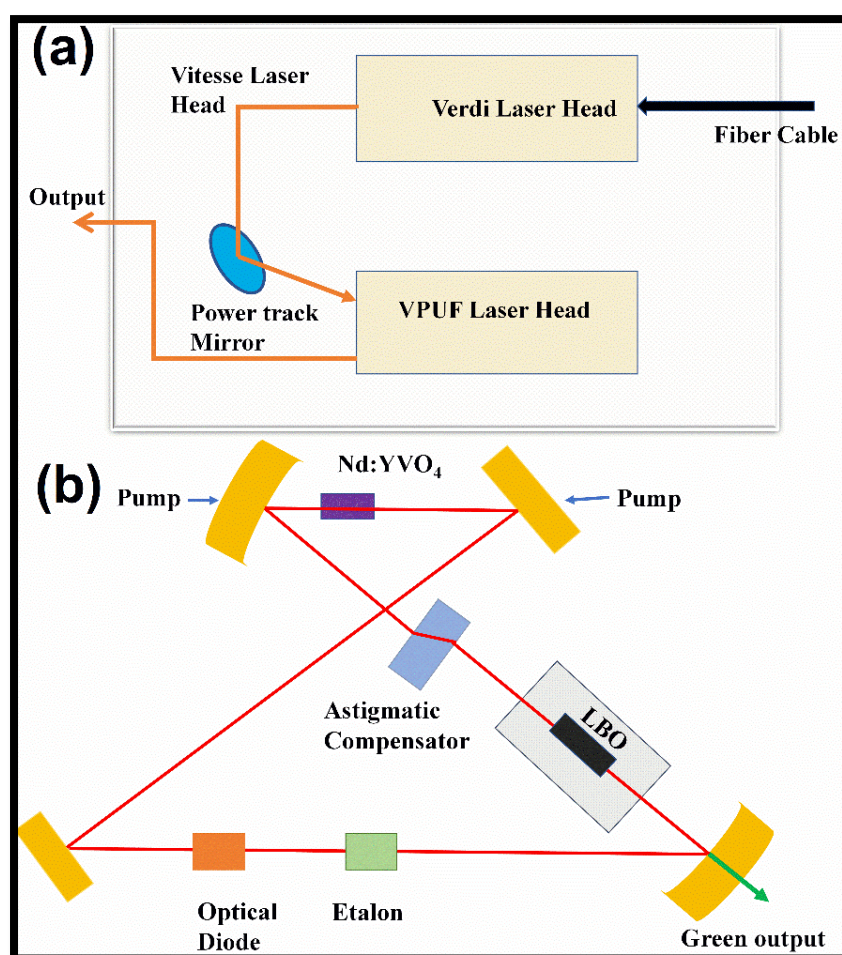


Figure 2.4 Internal layouts of (a) Vitesse seed laser and (b) Verdi laser layouts [3].

Table 2-1 Specifications of Vitesse oscillator output and the Libra amplifier output.

S.NO.	Parameters	Vitesse oscillator	Libra femtosecond amplifier
1	Pulse duration	~100 fs	~35 fs
2	Max output energy	~ 6-7 nJ	~4 mJ
3	Repetition rate	~80 MHz	1 kHz
4	Beam diameter	~ 3 mm	~9 mm (1/e ² width)
5	Polarization	Horizontal	Horizontal

2.1.1.b.ii Physics behind mode locking

Mode locking is the process in which all the optical modes oscillating in the gain bandwidth are phase locked at a given spatial location within the cavity so as to produce a total field amplitude of repetitive pulsed nature. Mode locking is the technique to generate ultrashort laser pulses (< ps) such as femtosecond pulses. Mode locking techniques are generally categorized into active mode locking and passive mode locking. In active mode locking, an externally driven component or device is placed in the laser cavity so as to obtain the mode locking. The examples are (a) electro-optic modulation (b) acousto-optic modulation (c) synchronous mode locking. The passive modelocking depends on the intrinsic properties of the materials and cannot be controlled externally. The passive modelocking is performed by using (a) saturable absorbers (b) components with non-linear absorption. Here, Vitesse employs Kerr-lens mode locking technique which is a passive technique by nature.

2.1.1.b.iii Passive mode locking

In passive mode locking externally driven devices are not used but instead saturable absorbers are used as passive mode-locking component. A saturable absorber (SA) is an optical material that absorbs energy (at the laser wavelength) till its threshold and allows the energy above its threshold energy. Thus, such materials act as passive shutters as their absorption coefficient is an intrinsic property and it cannot be controlled externally. In general, the spontaneous emission increases in laser as the pumping increases and at an instance this spontaneous emission passing down the length of the amplifier bleach through the SA and builds up the cavity. These modes are amplified in the laser medium provided if they possess high intensity. The peak part of fluctuation gets

Chapter 2

partially absorbed and the end parts are more absorbed while passing through saturable absorber therefore a pulse with high peak power can be generated within the cavity.

2.1.1.b.iv Kerr-lens mode locking (KLM)

Kerr-lens mode locking is a passive mode locking technique in which gain medium itself acts as an artificial SA based on the nonlinear effect of self-focusing (Kerr-lensing) or Kerr lens effect. When a sufficient intense pulse passes through the medium of refractive index $\eta_0(\omega)$ the intensity of the beam can alter the refractive index of the material as given by the equation 2.1;

$$\eta(\omega) = \eta_0(\omega) + \eta_{21}(\omega) * I(\omega) \quad (2.1)$$

where $\eta_0(\omega)$ is the original refractive index of the medium at the given frequency(ω) and $\eta_{21}(\omega) * I(\omega)$ is the non-linear intensity dependent term induced due to intensity of beam $I(\omega)$. The change in refractive index of the material with respect to intensity of the incident electric field is called optical Kerr effect. Gaussian beam has an intensity dependent transverse profile, where intensity reaches the maximum at its center. Thus, femtosecond pulses with sufficient intensity passing through a material induces a change in the refractive index of the material. The refractive index of material is higher at the center (for inner part of the beam at the axis) and smaller at the edges. This modified refractive index distribution then acts like a focusing lens. Due to this principle, the beam is focused or narrowed within the material. In the cavity, this effect can be used to suppress the continuous (CW) mode by using a small aperture, which produces high losses to CW mode. The relatively high intense pulse can propagate through the gain medium and can pass through the aperture due to self-focusing effect. Thus, pulses are mode-locked and CW mode is suppressed.

2.1.1.b.v Evolution pump laser

The Evolution laser provide pump power to the amplifier module. Evolution is a Nd: YLF (Nd: YLiF₄, yttrium lithium fluoride) based solid state laser, pumped by AlGaAs (Aluminum Gallium Arsenide) laser diodes. It operates at second harmonic wavelength of 527 nm (1053 nm fundamental) with a 1 kHz repetition rate. The narrow spectral emission of laser diodes allows extremely efficient pumping of laser materials where maximum light falling in the absorption band of gain medium and further reducing

the thermal losses. Low thermal lensing, long upper state life time (470 μs) and natural birefringence properties of Nd: YLF enable in achieving high powers. Acousto-optic Q-switching enables the pulse generation in Evolution pump laser. LBO crystal is employed to frequency double the laser pulses operating at non critical phase matching conditions. LBO should be maintained at particular temperature as the phase matching is temperature dependent i.e. conversion efficiency of LBO crystal (fundamental to the second harmonic) is influenced by the temperature.

2.1.1.b.vi Regenerative amplifier

The regenerative amplifier is based on the Legend EliteTM platform (M/s Coherent, USA). The amplifier is designed in a compact, enclosed module with an active cooling system, and exhibits excellent stability, reduced sensitivity to environmental temperature changes. A Synchronization and Delay Generator (SDGTM) is a sub-part of the amplifier system, which controls the functioning of pockels cells and synchronization of seed laser and pump laser respectively. The stretcher and compressor are integrated in to a single box system within a robust modular enclosure [3].

2.1.1.b.vii Absorption and emission properties of Ti: Sapphire crystal

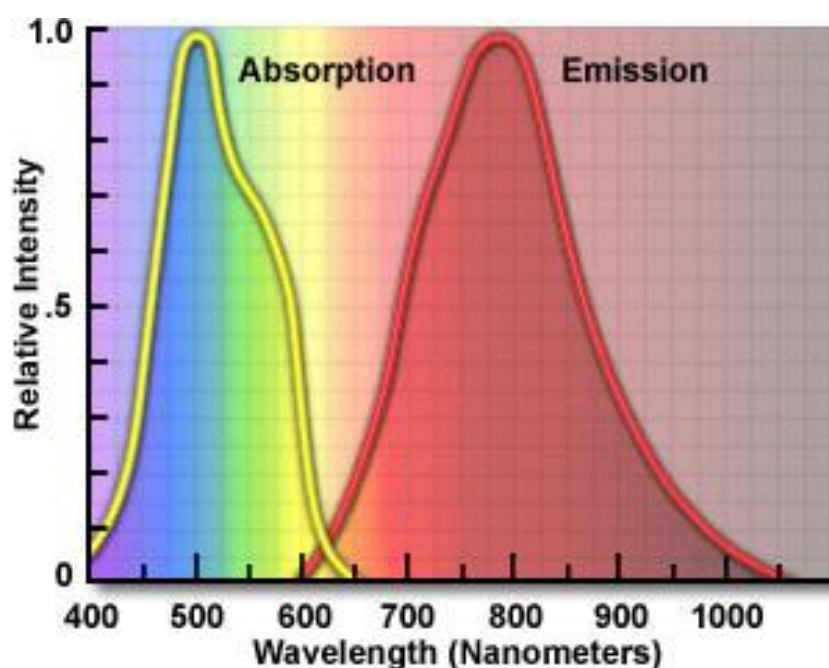


Figure 2.5 Absorption and emission spectra of Ti: Sapphire crystal in 400-1050 nm © Optical microscopy premier specialized techniques, Multiphoton Fluorescence Microscopy, Interactive Tutorials, Ti: Sapphire Mode-Locked Lasers [5].

Chapter 2

Ti: Sapphire ($\text{Ti}^+ : \text{Al}_2\text{O}_3$) is a Ti doped Al_2O_3 in which concentration of Ti ions (introducing Ti_2O_3 into a melt of Al_2O_3) is varied from 0.1-0.5%. Absorption spectra of Ti^{3+} ion doped sapphire crystal shows a broad continuous peak in 400-650 nm range [6]. The end part of the absorption band (towards higher wavelength) is overlapped with the beginning part (at shorter wavelength) of the emission band. Because of this reason, the lasing starts after 650 nm. A particular wavelength for laser emission is selected by means of an optical wedge or an etalon. In addition to this, the tuning range is influenced by losses in cavity, coating on the mirrors, quality of pump mode, input power losses and air absorption etc. The absorption and emission spectra of Ti: Sapphire crystal are illustrated in **figure 2.5**. The emission band transitions occur from the lower vibrational levels of the excited state (${}^2\text{E}$) to the upper vibrational levels of the ground state (${}^2\text{T}_2$) which is in the near infrared range of 660 nm to 1180 nm [7].

2.1.1.b.viii Group velocity dispersion (GVD)

As discussed above, fs pulses are generated by coupling the phases of oscillating modes. When an fs pulse interacts with a dispersive media having a nonlinear intensity-dependent change in refractive index, it undergoes self-phase modulation. Thus the frequency spectrum of the pulse is broadened i.e. more frequency components are added to the pulse. The effect of the dispersion properties of a material on the instantaneous frequency of the fs pulse is called chirp [8]. It is known that, fs pulses are wave packets that propagate with the group velocity (v_g) which would be different from the velocity of its components within the packet. Therefore, the fs pulse can be broadened or shortened due to the group velocity dispersion (GVD) caused by the optical elements present in laser cavity. Equation 2.2 represents group velocity (v_g) and GVD, where $k(\omega)$ is the wave vector. One can easily see that the group velocity is different for various wavelengths.

$$GVD = \frac{d}{d\omega} \left[\frac{1}{v_g} \right]; v_g = \left[\frac{dk(\omega)}{d\omega} \right]^{-1} \quad (2.2)$$

The pulse is said to be “positively chirped” when the instantaneous frequency is red shifted in a pulse front and blue shifted in trail. Similarly, the pulse is said to be “negatively chirped” when the instantaneous frequency is blue shifted in a pulse front and red shifted in trail. The dispersive medium with normal dispersion ($GVD > 0$) turns an fs

pulse into positively chirped pulse ($V_g \text{ red} > V_g \text{ blue}$) whereas the anomalous dispersion of a medium ($GVD < 0$) turns it into negatively chirped pulse ($V_g \text{ blue} > V_g \text{ red}$). The various intra-cavity components establish positive GVD and additionally, self-phase modulation (SPM) induces pulse spreading in the Ti: Sapphire crystal.

2.1.1.b.ix Ti: Sapphire Chirped Pulse Amplifier (CPA)

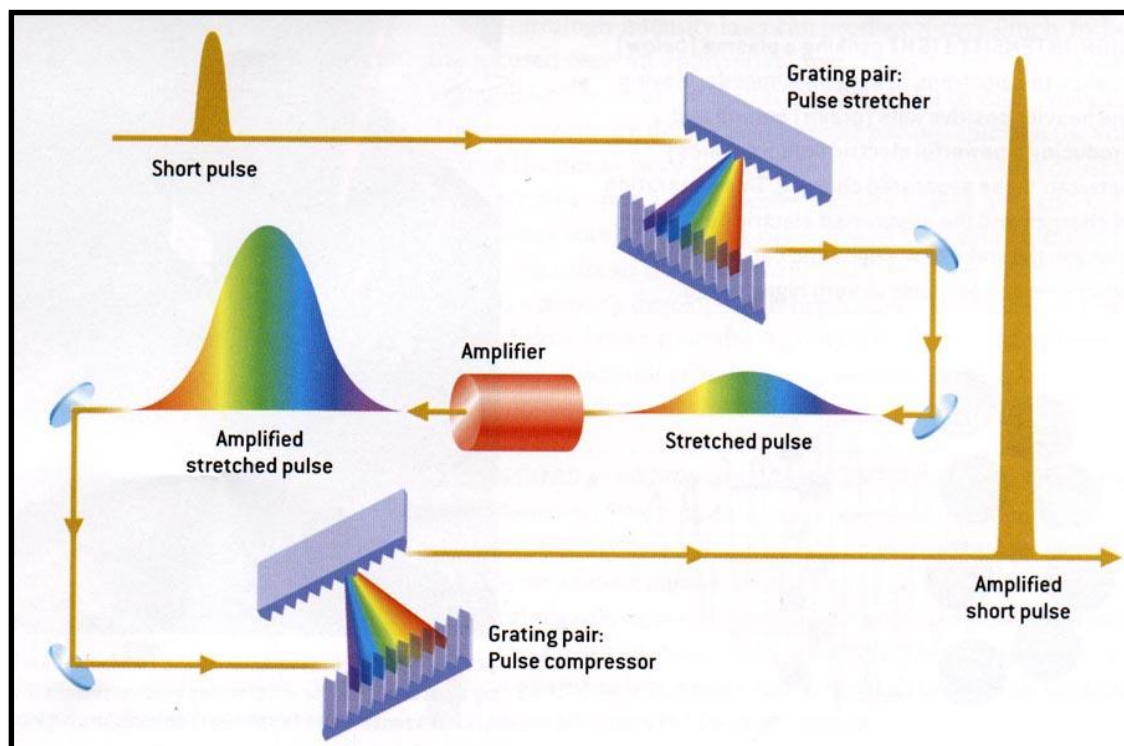


Figure 2.6 Schematic diagram of a chirped pulse amplification (CPA) employed in ultrafast amplifiers. © Center for Ultrafast Optical Science, University of Michigan [9].

Femtosecond pulses from the oscillator need to be amplified as their energy ($\sim nJ$) is not sufficient to exceed the breakdown threshold of the material and to create the plasma. Most of the LIBS experiments mandate amplified fs pulses with very high intensities. Thus, a seed pulse ($\sim nJ$) from Vitesse Ti: Sapphire oscillator is amplified ($\sim mJ$) using chirped pulse amplification (CPA) technique in the regenerative amplifier section (re-gen section) of Libra with an amplification factor of 10^6 as shown in **figure 2.6**. Re-gen section also consists Ti: sapphire crystal as gain medium because it offers large gain bandwidth which is necessary to amplify these fs pulses. Due to the self-focusing phenomenon associated with high intense fs pulses, the laser components in cavity as well as gain medium are prone to damage during the process of amplification.

Chapter 2

Thus to avoid the damage it is essential to stretch the pulse significantly so as to reduce its intensity prior to the amplification. Thus, the oscillator pulses (~ 100 fs, 80 MHz) are stretched (to ~ 100 ps, 80 MHz) in the stretcher region. Thus, CPA can effectively amplify an fs pulse without incurring any damage to the optics within the cavity.

In CPA, grating in the stretcher region is designed such that the higher frequency (blue) components of fs pulse must travel further through the stretcher than the lower frequency (red) components, resulting in the exit of lower frequency components prior to higher frequencies i.e. stretching the pulse. As the pulse is stretched from few fs to ~ 100 ps using single grating pulse stretcher the peak power (energy/ pulse duration) of pulse reduces by a factor of 10^4 . Accordingly, the power density in amplifier reaches below the damage threshold of Ti: sapphire crystal. Pockels cell, being synchronized to the RF signal generated by the seed laser, switches the oscillator pulse into the resonator. Furthermore, these Pockels cells can vary the repetition rate of amplified pulses from 10 to 1 kHz to provide maximum amplification. After amplification, the laser pulses are compressed in the compressor region. The process of pulse compression is opposite to the process of pulse stretching. Here, the gratings are arranged such that the higher frequencies travel the shortest path in order to “catch up” with the lower frequencies, thus compressing the pulse to initial time scales [3]. Thus, seed pulse energy with few \sim nJ can be amplified to ~ 4 mJ (1 kHz) in Libra amplifier system.

2.1.1.c Pulse width measurements of fs pulses from Libra amplifier

The fs pulses have several applications in physics, chemistry, biology, and engineering as these short pulses closely study several ultrafast phenomena such as excited and de-excited states of molecules which in turn demonstrate the optical properties of the material etc. They serve as measuring scales for events which occur in longer durations compared to them. Thus it is very essential to know the pulse width of the lasers. The photo detectors can measure a pulse duration ranging from few ns to ps (< 20 ps) depending on the available bandwidth. However, the existing photo detectors cannot measure the ultrashort pulse durations as the maximum bandwidth available is limited to ~ 100 GHz. Hence, self-reference techniques such as autocorrelation are used to estimate the pulse durations in ultrashort times (fs to few ps) where the pulse itself is exploited to measure it. There are two autocorrelation techniques namely, (a) intensity

autocorrelation technique as shown in **figure 2.7** and (b) interferometric autocorrelation technique performed to measure pulse duration of ultrashort pulses. Former one only illustrate the pulse duration and the latter on demonstrate the phase information as well as the pulse duration [10]. However, intensity autocorrelation method is preferred due to its simplicity.

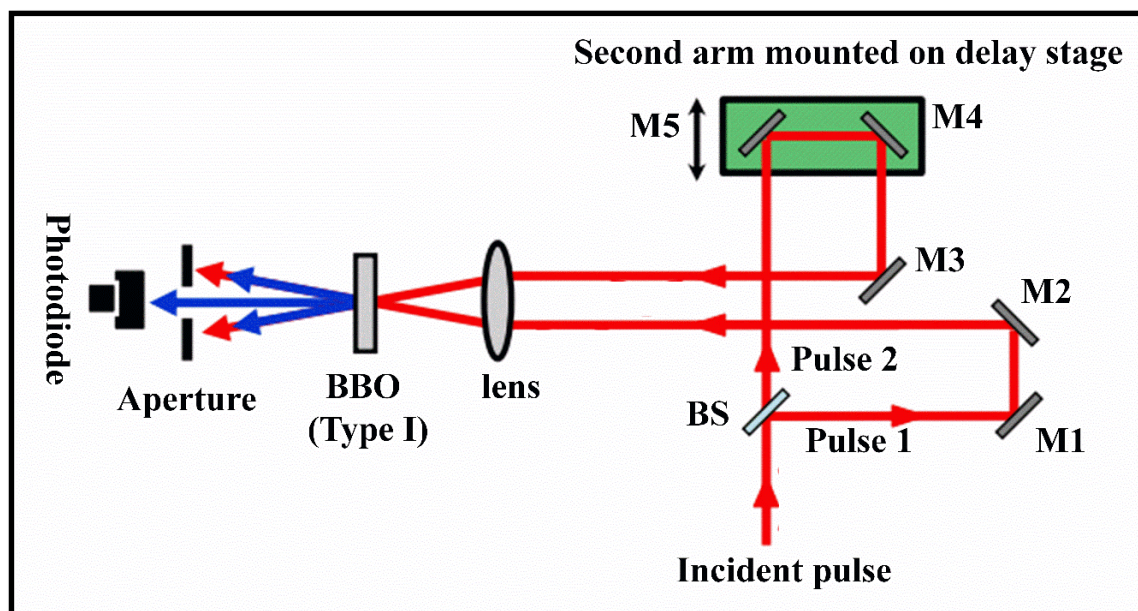


Figure 2.7 Intensity autocorrelation experimental setup to measure pulse duration of Libra Ti: Sapphire amplifier through measuring the intensity of second harmonic (SH) signal generated from BBO crystal.

The pulse duration of fs pulses from Libra (Ti: Sapphire amplifier, M/s Coherent Co.) was measured by autocorrelation technique. As discussed above, the fundamental pulse from Ti: sapphire amplifier splits in to two equally intense beams by a 1:1 beam splitter and delayed one with respect to each other by reverting them into two different arms 1 and 2 (2 is mounted on delay stage) as shown in the **figure 2.7**. The pulse is divided into two pulses with 1:1 beam splitter for better visibility of SH, where visibility is referred as $(I_{\max} - I_{\min}) / (I_{\max} + I_{\min})$. Later on these two pulses are brought together by focusing them using a plano-convex lens ($f=15$ cm) into a Type I: critically phase matched BBO crystal of 2 mm thickness. Varying the delay of second pulse with respect to the first pulse, a strong second harmonic (SH) signal was generated when the two pulses from different arms were perfectly convoluted. A photodiode connected to a lock-in amplifier (Signal Recovery, 7625) was used to record the SHG signal. Neutral density filters were used to control the SHG intensity to avoid the damage/saturation of

Chapter 2

photodiode. The pulse duration can be estimated (as the pulse shape known as Gaussian in this case) by de-convolution of the correlation function.

Equation 2.3 represents the time varying nonlinear second order polarization $P^{(2)}(t)$ induced due to the convolution of the two ultrashort laser pulses, where $E_1(t_1)$ and $E_2(t_2)$ are time dependent electric fields associated with the pulse 1 and pulse 2 .

$$P^{(2)}(t) = K \iint_{-\infty}^{+\infty} \chi^{(2)}(t - t_1, t - t_2) E_1(t_1) E_2(t_2) dt_1 dt_2 \quad (2.3)$$

Since the material response to the incident electric fields of the pulses is instantaneous, $\chi^{(2)}(t - t_1, t - t_2)$ in the above equation can be replaced by Dirac Delta function i.e. $\chi^{(2)}(\delta(t - t_1), \delta(t - t_2))$. Further, as the second pulse is delayed with respect to the first pulse their nonlinear response is nullified when these pulses are not overlapping as represented in equation 2.4.

$$P^{(2)}(t) = K * E_1(t) E_2(t - \tau) \quad (2.4)$$

Here τ is the effective time delay between the two pulses.

Simultaneously, the amount of second harmonic signal due to the convolution is given by the following equation 2.5.

$$I_{AC}(\tau) \propto \int_{-\infty}^{+\infty} |A(t) A(t - \tau)|^2 dt \quad \text{and} \\ I_{AC}(\tau) = \int_{-\infty}^{+\infty} I(t) T(t - \tau) dt \quad (2.5)$$

SHG intensity obtained as a function of delay between first and second pulse is the autocorrelation signal and its full width at half maxima (FWHM) gives the pulse duration.

An ultrashort pulse traversing in a dispersive medium of thickness “L”, the phase modification due to the influence of medium is by $\varphi(\omega)$ as shown in the equation 2.6 (i). Here, $k(\omega)$ is the propagation wave vector associated with the pulses. The expansion of propagation vector $k(\omega)$ [equation 2.6 (ii)] contains many significant terms wherein, the first term related to phase velocity, second term related to group velocity mismatch (GVM), and the third term demonstrates the variation of group velocity w.r.t the frequency i.e. group velocity dispersion (GVD) as shown in equation 2.6 (iii).

$$\varphi(\omega) = k(\omega) \times L \quad (2.6 \text{ i})$$

$$k(\omega) = k(\omega_0)L + k'(\omega_0)(\omega - \omega_0)L + \frac{1}{2}k''(\omega_0)(\omega - \omega_0)^2L + \dots \quad (2.6 \text{ ii})$$

$$k(\omega) = \frac{\omega_0}{v_\phi(\omega_0)}; \quad k'(\omega_0) = \frac{1}{v_g(\omega_0)}; \quad k''(\omega_0) = \frac{d}{d\omega} \left(\frac{1}{v_g} \right) \quad (2.6 \text{ iii})$$

However, in the present experiment, the temporal broadening of ultrashort pulses aroused due to GVD effects of dispersive media are evaluated by calculating the broadening factor (β) by the equation 2.6 (iv) [13].

$$\beta = \frac{\tau_{out}}{\tau_{in}} \quad \beta = \sqrt{\left\{ 1 + \left[4 \ln 2 \left(D_2 \times \frac{L}{\tau_{in}^2} \right)^2 \right] \right\}} \quad (2.6 \text{ iv})$$

The second order dispersion coefficients of BBO and BK-7 are $\sim 75 \text{ fs}^2/\text{mm}$ and $\sim 45 \text{ fs}^2/\text{mm}$ at 800 nm respectively. If the approximate thickness of BBO and the lens are considered as 2 mm and 7 mm, then the broadening factors are obtained as ~ 1.03 , ~ 1.14 , respectively. Hence their contribution towards pulse broadening can be subtracted estimated pulse duration of the fundamental pulse was $\sim 75 \text{ fs}$. The increase in the pulse duration is due to the broadening of fs pulses by the dispersive media in the experimental setup such as plano-convex lens (BK-7), and BBO crystal. An ultrashort pulse broadens as it traverses in any dispersive media due to its high non-linear intensity [3, 7-12].

2.1.2 Mechelle spectrograph equipped with ICCD

The ANDOR Mechelle spectrograph (ME 5000; based on echelle grating technology) equipped with Andor iStar ICCD (intensified charge coupled device) was utilized to carry out all the gated LIBS experiments. The iStar ICCD (DH334T-18U-E3) was equipped with Mechelle spectrometer in case of fs LIBS experiments whereas iStar ICCD (DH734-18U-03) equipped to Mechelle spectrograph in case of ns LIBS experiments owing to their triggering speeds of 1 kHz and 500 Hz respectively. Mechelle spectrographs combined with CCDs or ICCDs can be utilized for field applications as they are rugged and have no movable parts within them. The spectral resolving power of Mechelle is ~ 5000 , 0.05 nm @500 nm as an example. The focal length of spectrometer is 195 mm. Mechelle spectrographs are widely used in analyzing laser induced plasmas

Chapter 2

(LIP) as they offer multi-elemental analysis of any sample by providing the wide spectral range over ultra-violet (UV) to near infra-red (IR) region including visible region (200 to 900 nm) in a single acquisition. The patented echelle grating system which employs a special type of double prism combination provides high resolution for Mechelle spectrograph. Furthermore, these also provide low cross talks between the wavelength orders. The Mechelle spectrograph calibration was performed using standard lamps viz. mercury-argon (Hg-Ar) lamp and DH-3 lamp (Deuterium-halogen Lamp). Here, Hg-Ar lamp was used for wavelength calibration and DH-3 for intensity (relative efficiency correction of grating) calibration. DH-3 lamp has two sources with first source as deuterium lamp which emits in the spectral region of 200-400 nm and the second one being tungsten halogen lamp which emits in the spectral region of 380-975 nm. Different acquisition parameters were used for these lamps as their intensity is different. The acquisition parameters used for Hg-Ar and DH-3 lamp are shown in **table 2.2**.

Table 2-2 Parameters used in wavelength and intensity calibration of ICCD.

ICCD parameters	Hg-Ar lamp	DH-3 Lamp
Gate delay	0 ns	0 ns
Exposure time	0.2 s	2.5 s
Gate width	0.13 s	2.5 s
Gain (0-4000)	700	3000

A CCD is used in non-gated LIBS experiments whereas usage of an ICCD is used in gated LIBS experiments. Intensifier amplifies the intensity of the signal. Thus there are certain advantages in employing image intensifier to CCD in investigation of very weak process such as single photon events owing to increased sensitivity. ICCD is useful in recording the plasma emissions (signal) with being synchronized to the input laser trigger and acts as a gate. With reference to incident pulse, the time after which the plasma emissions are to be recorded is called the gate delay and how far the emissions are to be recorded is referred as gate width. Thus ICCD can be used to record two types of LIBS spectra (i) time integrated spectra and (ii) time resolved spectra. Signal can be recorded in particular intervals so as to understand the evolution of plasma constituents as the plasma expands in the space over the time. This technique is called as kinetic series where time resolved emissions are acquired by optimizing signal-to-background ratio in order to

study the transient LIPs to understand various atomic and molecular formation pathways. Further ICCDs have been utilized in time resolved plasma imaging, Raman spectroscopy and several other spectroscopic and imaging techniques.

2.2 LIBS technique

As described in chapter 1, laser induced breakdown spectroscopy (LIBS) is a potential spectroscopic technique to study variety of materials in their original state incurring no or minimal damage on the sample while investigation. This technique also offers real-time analysis by rapidly analyzing the constituting elements often in a single shot by analyzing the optical emissions produced during the laser matter interaction [11,12]. LIBS is being used from the past four to five decades and in the past two decades, the applications of LIBS are expanded enormously due to the commercialization of miniaturized nanosecond lasers. The amount of work being profoundly published in the form of books [13–16], review articles [17–21], conference issues and journal articles implies the active research of LIBS community. Examining the composition of alloys and metals (industrial application) [22], food analysis (checking the food adulterity) [23], soil and ore analysis (checking the nutrients and minerals percentages) [24,25] and water contamination analysis (checking for heavy elements and hazardous chemicals) [26,27], drug and pharmaceutical industry (quality and composition) , biological and medicinal research (analyzing blood, various tissues and organs) [28–32], cultural heritage investigation (studying paints, coins and utensils) [33–35], geological studies (studying composition of rocks and their origin) [36–39], environmental research (identifying plastics and hazardous substances such as explosives) [40,41] and underwater explorations [42] as well as space missions (LIBS rover on Mars and moon) [43,44] are few, but not limited, applications of LIBS. The feasibility of focusing laser pulses (both fs and ns) to long distances and the recent advancements in field deployable instruments has equipped the laser LIBS technique for investigating of various materials including energetic molecules in standoff mode also [40]. Further, the development of calibration free LIBS technique (CF-LIBS) to evaluate the composition of materials quantitatively is an attractive feature of LIBS [45]. Though the accuracy and sensitivity of LIBS is moderate when compared to other spectro-chemical analytical techniques such as the ICP-MS or Raman technique, the continuous efforts are inclined towards improving the analytical figure of merit of LIBS technique. Furthermore, developing various

Chapter 2

multivariate analytical methods such as PCA, SIMCA, PLSDA, ANN and several other techniques has led to enhanced specificity in discriminating soil, pharmaceuticals and explosives with few false alarms.

2.3 fs LIBS and ns LIBS setups

The lasers (fast and ultrafast), spectrometers and detectors are quintessential parts of the LIBS system. Simultaneously, beam focusing or delivering optics and collection optics do play a prominent role in LIBS experiments. **Figures 2.8(a)** and **2.8(b)** depict the schematic of proximal/near-field fs LIBS and ns LIBS laboratory setups. The fs and ns lasers, spectrograph and ICCD employed in carrying out LIBS experiments were already discussed. LIBS experiments using ns laser were performed at 532 nm wavelength. A 100 mm focal length lens fixed on a translational stage was used in both the cases for focusing and precise interrogation of laser pulses with the sample (pellet/ metal sheet) to produce laser induced plasma (LIP) in both proximal fs/ns LIBS experiments. Optical emissions were collected by Andor ME-OPT-0007 collector/collimator [46] at 15 cm away from the plasma and fed to an Andor Mechelle (ME 5000) spectrograph [section 2.1.2] equipped with ICCD transmitted through an optical fiber of 600 μm core diameter. The pellets/samples were placed on the translation stage which was controlled by a Newport ESP 300 motion controller (automated with LabView) to expose fresh locations of the samples (to avoid the damage of sample) to each pulse. Influence of surrounding atmospheres (argon) on LIBS signal was investigated with nanosecond pulses only. This is due to the shortage of sample and as well as the large consumption of sample in case of fs laser due to 1 kHz repetition rate. For experiments in argon atmosphere, the sample was purged with argon gas with the help of a nozzle at the rate of $\sim 3 \text{ L min}^{-1}$.

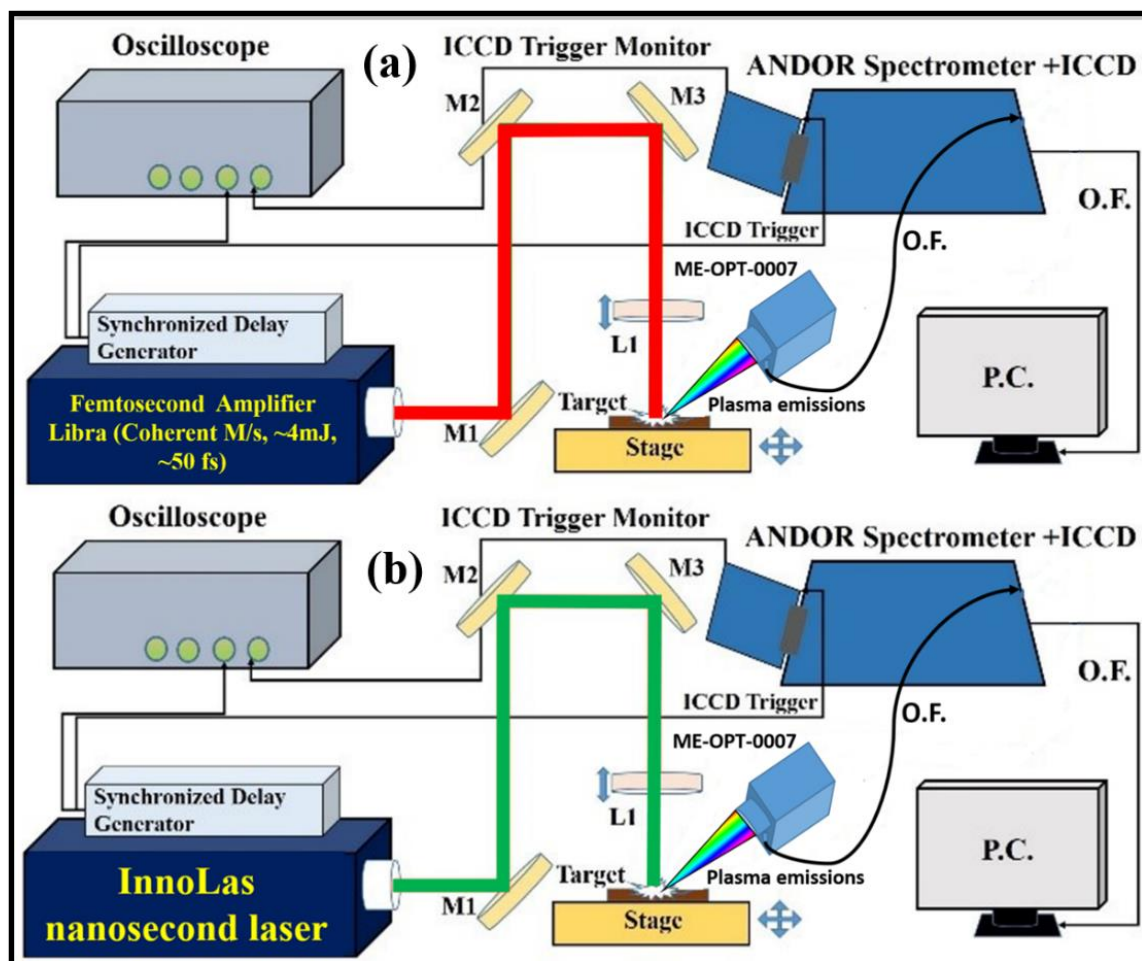


Figure 2.8 Schematic of proximal experimental LIBS setup with the (a) femtosecond amplifier laser system (Libra, M/s Coherent Co.) and (b) the nanosecond amplifier laser system (InnoLas, SpitLight 1200). In figure M: mirror, L: lens, O.F.: optical fiber.

Part of the fs LIBS data reported in chapter 3 was recorded with the LIBS setup at Radiation & Photochemistry Division, Bhabha Atomic Research Centre (RPCD, BARC), Mumbai. The laser pulses with duration of ~50 fs, delivering ~1 mJ energy at a central wavelength 800 nm were used. When fs pulses focused with a single lens ($f=50$ cm, 1 m and 2 m) or using combination of two lenses (as discussed in detail in chapter 4), the fs pulses formed into filaments of length ~10 cm to ~30 cm. The experiments performed in standoff mode using these fs filaments are reported as filament induced breakdown spectroscopy (FIBS) experiments in chapter 4. The Remote LIBS, standoff filament induced breakdown spectroscopic experiments (ST-FIBS) and nanoparticle enhanced laser induced breakdown spectroscopic (NE-LIBS) experiments were carried out only with fs laser in ambient air. The experimental details are discussed in detail in chapters 4 and 5.

2.4 Method of acquiring LIBS spectra

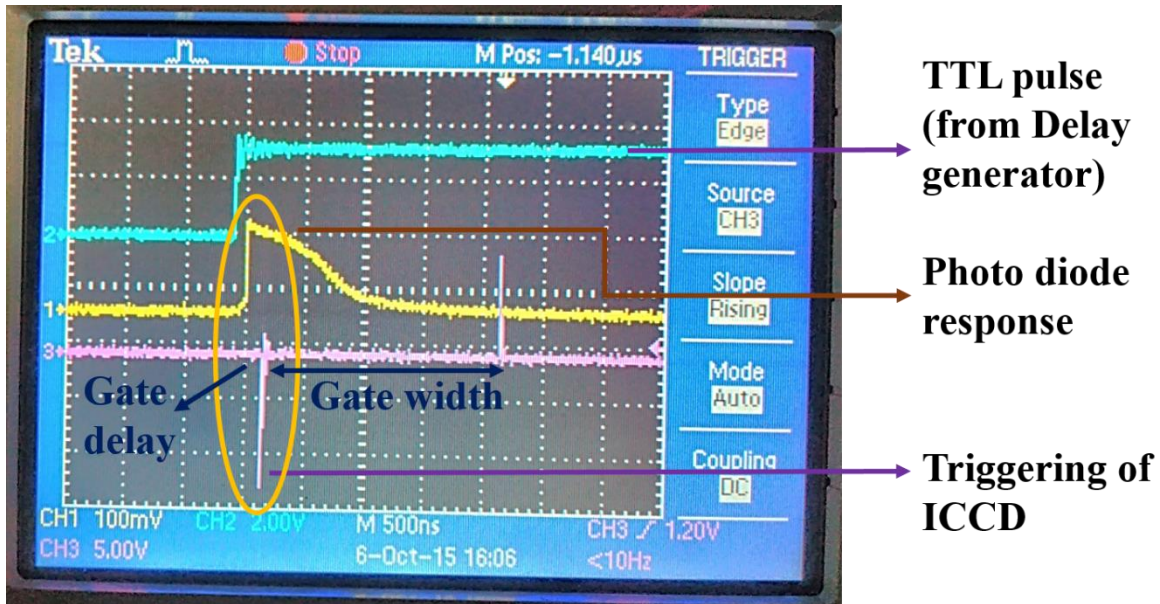


Figure 2.9 The external triggering of ICCD with gate width of 2 μs and 100 ns gate delay. In order to view all the three signals in oscilloscope, we should trigger with channel -3 where ICCD output is connected (pink color) or the gated LIBS experiments.

Figure 2.9 illustrates a typical LIBS spectral acquisition conditions in gated LIBS technique. In ns LIBS setup, the electronic pulses from the Pockels cell of the laser system were taken as the input for triggering delay generator (DG535, Stanford instruments). The DG provides a necessary pulse to trigger the ICCD. In fs LIBS setup, one of the outputs from the synchronized delay generator (SDG, Coherent M/s) is used to trigger the ICCD with respect to the ejection of fs pulse. **Figure 2.9** is a picture taken from the oscilloscope at a given gate delay of 100 ns and gate width of 2 μs at 630 V of the ns laser. The 1st signal in yellow color is the response of photodiode near to the LIBS experimental setup. The photodiode signal approximately represents the incidence of laser pulse onto the sample surface. 2nd (Blue) and 3rd (Magenta) pulses represents the DG output and ICCD gate opening signals. The time period between the laser pulse and the positive edge of intensifier on-time is referred as gate delay. The ICCD has insertion delay of 40 ns is clearly observed from the figure 2.5. Here light falls on the CCD sensor during the gate pulse width time only. The positive edge of the pulse shows the starting of the intensifier and negative edge indicate intensifier off. The period of time between positive and negative edge pulse is called as gate width. The spectra can be collected at desired gate width and gate delay with respect to the laser pulse by changing the timings of gate width and gate delay of ICCD.

2.5 Plasma diagnostic studies of ns lead nitrate plasma plume

2.5.1 Introduction

The laser induced plasmas (LIP) are complex in nature. Yet, they are good spectroscopic sources and can be exploited for quick elemental analysis of several materials. LIP contains several excited atoms and ions and they emit characteristic radiation as they de-excite and recombine. Spectroscopic emissions of LIP consists of radiation from atomic transitions, ionic transitions and continuum light which is result of free-free and free-bound transitions. The characterization of these optical emissions from the LIPs through determining electron density (n_e) and plasma temperature enables to calculate the atomic or ionic concentration present in the plasma and thus evaluating the composition and concentration of target. It is well known that the LIP characteristics are influenced by laser parameters such as pulse duration, irradiance, material properties, and atmosphere conditions etc. (buffer gases, air or vacuum and partial pressures). LIBS is a potential spectroscopic technique to detect and quantify the elements that are present in sample by examining the LIP by interrogating laser pulses with the target. LIBS provides rapid analysis and offers real-time analysis. As a part of initial experiments we have examined the plasma of lead nitrate $[\text{Pb}(\text{NO}_3)_2]$ produced with nanosecond pulses and calculated plasma temperature and electron density.

2.5.2 Experimental details

Pure lead nitrate $[\text{Pb}(\text{NO}_3)_2]$ powder was ground to fine powder in agate mortar and 200 mg of it was pressed in to pellets of 20 mm diameter at 4 tones pressure using a hydraulic press machine. The pellet was placed on a holder and moved in the plane perpendicular to the laser incidence by an ESP 500 Motion Controller which was communicated by LabView. The ns LIBS experimental setup discussed in the earlier sections has been utilized to produce LIP plasma of lead nitrate. The optical emissions from LIP were collected by collection optics (Andor ME-OPT-0007) placed at an angle of 45 degrees to the incident laser beam at 15 cm from target. The collection optics is aligned by coinciding the focused laser spot of a low intense (<5 mW) diode laser (635-650 nm) with the plasma. Optical fiber (600 μm) was used to transmit these emissions to ANDOR Mechelle 5000 spectrograph, attached with an Intensified Charge Coupled

Device (ICCD). Three different pulse energies of 20 mJ, 40 mJ, and 60 mJ were utilized to observe the effect of fluence on the persistence of plasma species in air.

2.5.3 Results and discussions

2.5.3.a Influence of fluence on nanosecond laser induced lead plasma

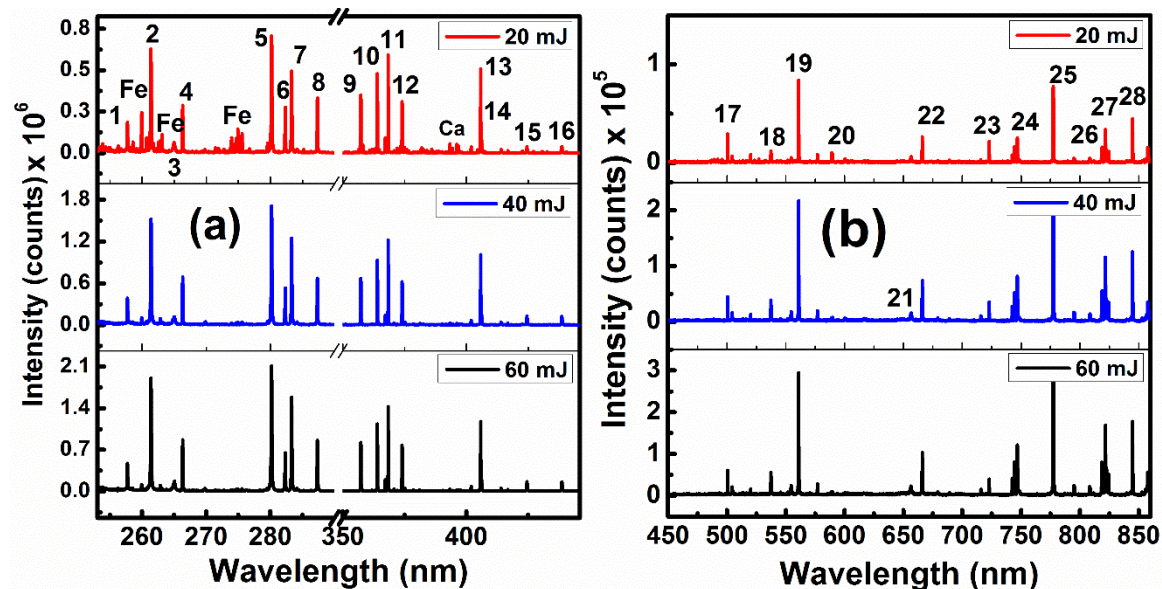


Figure 2.10 Stack plot of typical ns lead nitrate $[\text{Pb}(\text{NO}_3)_2]$ spectra obtained at 20 mJ, 40 mJ and 60 mJ in air in the spectral region of (a) 250-450 nm and (b) 450-850 nm. Peaks are identified using NIST data base and listed in table 2.3.

A typical ns LIBS spectrum of lead nitrate in the wavelength range of 250-420 nm and 450-850 nm recorded with 4 μs gate width after a gate delay of 1 μs with 20 mJ, 40 mJ and 60 mJ energy per pulse is shown in **figure 2.10(a) and 2.10(b)**. The exposure time of ICCD was 0.002 s, gain 120 (0-260) and each spectrum is a result of ten accumulations. Several atomic and ionic transitions of Pb (Pb I and Pb II), atomic emissions of O and N were observed. Along with these, few atomic and ionic transitions from impurities (Na I, Fe II, Ca II) were also identified in ns LIBS spectrum. These impurities would have entered while preparing the sample. Persistent emissions from Pb and other impurities were labeled from NIST data base and tabulated in **table 2.3**. Time resolved spectra were recorded to evaluate the persistence of species by calculating plasma temperature and electron density with an initial gate delay of 200 ns, gate width of 200 ns with step of 200 ns up to 4 μs and each spectrum was an average of 10 accumulations.

Table 2-3 Atomic and ionic transitions identified in the time integrated ns LIBS spectra of lead nitrate [Pb(NO₃)₂] recorded in air with 20 mJ energy.

Peak number	Elements and impurities	Observed Wavelength (nm)	NIST Standard wavelength (nm)
1	Fe II	257.73	257.79
2	Pb I	261.39	261.41
3	Pb I	265.01	265.71
4	Pb I	266.32	266.31
5	Pb I	280.19	280.19
6	Pb I	282.32	282.31
7	Pb I	283.32	283.30
8	Pb I	287.31	287.33
9	Pb I	357.28	357.27
10	Pb I	363.98	363.95
11	Pb I	368.36	368.34
12	Pb I	374.01	373.99
13	Pb I	405.82	405.78
14	Pb I	406.19	406.21
15	Pb II	424.52	424.49
16	Pb II	438.70	438.64
17	Pb I	500.56	500.54
18	Pb II	537.28	537.20
19	Pb II	560.90	560.88
20	Na I	589.04, 589.62	588.99, 589.59
21	H I	656.25	656.27
22	Pb II	666.04	666.02
23	Pb I	722.93	722.89
24	N I	742.50, 744.32, 746.93	742.36, 744.22, 746.83
25	O I	777.42	777.41
26	N I	818.54, 818.84	818.48, 818.80
27	N I	821.69, 822.59, 824.55	821.63, 822.31, 824.23
28	O I	844.71	844.63
	Fe II	262.58, 262.82, 263.12	262.56, 62.83, 263.13
	Fe II	271.90, 272.77	271.90, 272.75
	Fe II	273.70, 273.96	273.73, 273.95
	Fe II	274.33, 274.66	274.32, 274.64
	Ca II	393.38, 396.88	393.36, 396.84

Chapter 2

2.5.3.b Estimation of plasma temperature by Boltzmann plot

The plasma temperature was determined using Boltzmann plot method. At LTE (local thermodynamic equilibrium) conditions the intensity of plasma radiation is proportional to the relative population of the level and follow the Boltzmann distribution. The intensity of a line from a transition 'm' to 'n' can be written as shown in equation 2.7, [47,48]

$$I_{mn} = \frac{hc}{4\pi\lambda_{mn}} \frac{A_{mn}g_m N}{U(T)} \exp\left(-\frac{E_m}{k_B T}\right) \quad (2.7)$$

Where h is the Planck constant, c is the velocity of light in vacuum, U(T) is the partition function, N population density of atom, T is the plasma temperature and k_B is the Boltzmann constant. Taking logarithm of both the sides of Eq. (2.7) we get equation (2.8)

$$\ln\left(\frac{I_{mn}\lambda_{mn}}{A_{mn}g_m}\right) = -\frac{E_m}{k_B T} + \ln\left(\frac{hcN}{U(T)}\right) \quad (2.8)$$

The plot of $\ln\left(\frac{I_{mn}\lambda_{mn}}{A_{mn}g_m}\right)$ in the left hand side of the equation (2.8) versus the upper level energy (E_m) is called as the Boltzmann plot. The slope of the fitted straight line is equal to $(-1/k_B T)$ and thus the plasma temperature (T) can be evaluated without knowing the value of partition function U(T). Accuracy of temperature measurement from Boltzmann equation may be improved by involving a number of different lines. The Pb I transitions considered for estimation of plasma temperature are shown in table 2.4.

Figure 2.11 shows a typical Boltzmann plot (at 800 ns delay) for calculating the plasma temperature using the Pb atomic transitions shown in **table 2.4**. The slope from the graph (i.e. at each delay) gives the plasma temperature at a certain delay. Likewise, the plasma temperature was calculated from the slopes of the Boltzmann plots at each delay. **Figure 2.12** depicts the exponential decay of plasma temperature obtained at various fluence as the plasma evolves in time. The life time of plasma was found to be 516 ns at 20 mJ, 711 ns at 40 mJ, and 956 ns at 60 mJ. From **figure 2.12** data it is evident that at larger fluence, the plasma had longer persistence time. This could be related to the efficient ablation at higher energies. However, it could be noted that, increase in laser fluence may not always leads to increase in energy and after some threshold fluence the intensity reaches a plateau region which mainly attributed to the plasma shielding [49].

Table 2-4 Spectroscopic parameters of Pb I transitions used in Boltzmann plot. A_{ki} is transition probability, E_k is the energy of upper level and g_k is the multiplicity of upper level.

Element	Wavelength (nm)	A_{mn} (10^8)	E_m (eV)	g_m	Transitions
Pb I	261.41	1.90	5.710	5	$6d^3D_{2^{\circ}} \rightarrow 6p^2^3P_1$
Pb I	280.19	1.60	5.744	7	$6d^3F_{3^{\circ}} \rightarrow 6p^2^3P_2$
Pb I	283.30	0.58	4.375	3	$7s^3P_{1^{\circ}} \rightarrow 6p^2^3P_0$
Pb I	363.95	0.34	4.375	3	$7s^3P_{1^{\circ}} \rightarrow 6p^2^3P_1$
Pb I	368.34	1.50	4.334	1	$7s^3P_{0^{\circ}} \rightarrow 6p^2^3P_1$
Pb I	373.99	0.73	5.974	5	$7s^3P_{2^{\circ}} \rightarrow 6p^2^1D_2$
Pb I	405.78	0.89	4.375	3	$7s^3P_{1^{\circ}} \rightarrow 6p^2^3P_2$
Pb I	406.21	0.92	5.711	3	$6d^3D_{1^{\circ}} \rightarrow 6p^2^1D_2$

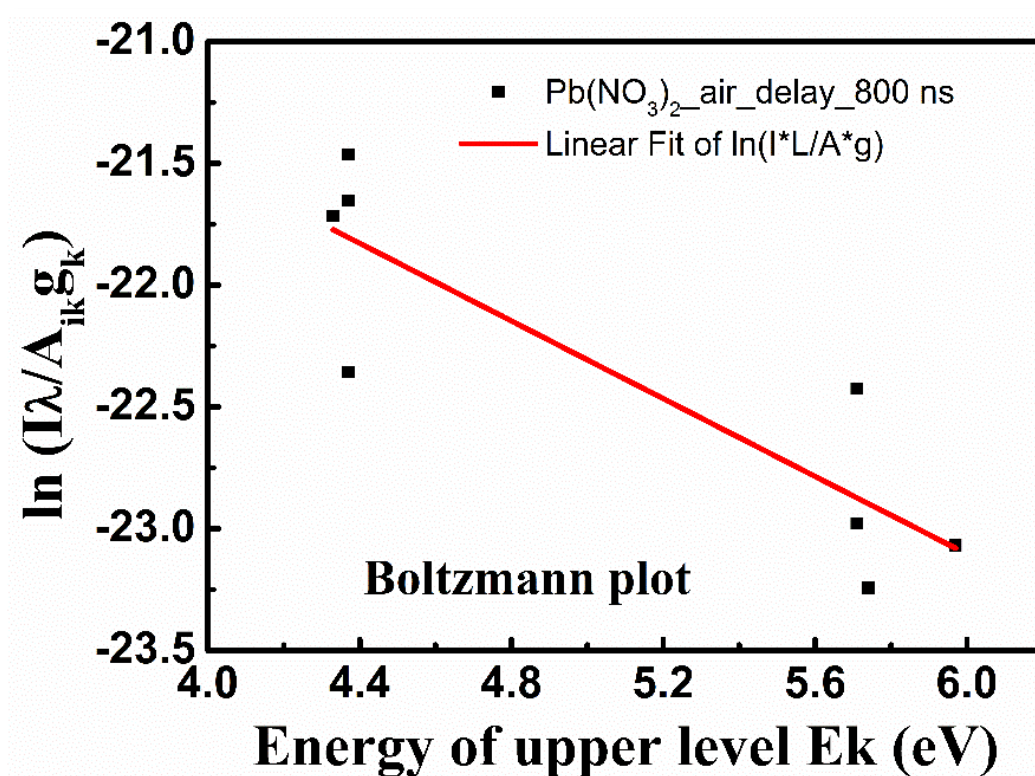


Figure 2.11 Typical Boltzmann plot for calculating the plasma temperature of lead nitrate plasma at 60 mJ at 800 ns delay using eight Pb I atomic transitions as shown in table 2.4. The solid (red) line represents the linear fit. I , λ , A_{ik} , E_k , g_k are the intensity, the wavelength of a transition from upper level k to lower level i , transition probability, energy of the upper state, statistical weight.

2.5.3.c Calculation of electron density (N_e)

The electron density of LIP was calculated using stark broadened profile of a spectral line. There are several mechanisms that contribute for broadening of an emission spectral lines that occur in plasma. They are (1) natural broadening, (2) Doppler

Chapter 2

broadening, (3) Stark-broadening. In the case of LIPs an atom is surrounded by voluminous electrons and ions. Thus, both the natural broadening and Doppler broadening are negligible in comparison with Stark broadening towards broadening of a spectral line. The width of the Stark broadened spectral lines depends on electron density of LIP [50]. For linear Stark effect (hydrogen and hydrogenic ions) the relationship between electron density and the line width is given by

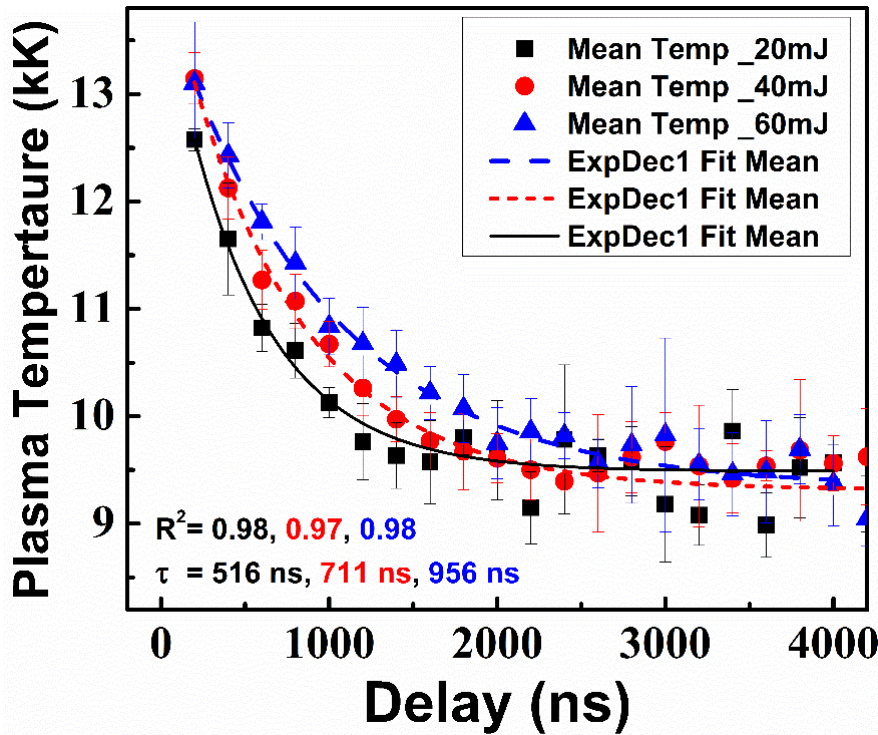


Figure 2.12 Decay of plasma temperature obtained from Boltzmann plots at three different fluence.

$$N_e = C(N_e, T_e) \Delta\lambda^{3/2}_{FWHM} \quad (2.9)$$

Where $\Delta\lambda$ is the full width at half maxima (FWHM) and the parameter C depends weakly on electron density and temperature. In case of non-hydrogen like atoms the quadratic Stark effect is dominated. Here the relation between electron density and line width is given by equation 2.10 as shown below [51,52].

$$\Delta\lambda_{FWHM} = 2\omega \left(\frac{N_e}{10^{16}} \right) + 3.5A \left(\frac{N_e}{10^{16}} \right)^{1/4} \times \left(1 - \frac{3}{4} N_D^{-1/3} \right) w \left(\frac{N_e}{10^{16}} \right) \quad (2.10)$$

The first term in brackets give the contribution from the electron broadening, and the second term arising from ion broadening. Here 'ω' is the electron broadening impact

parameter at $N_e=10^{16} \text{ cm}^{-3}$, 'A' is the ion broadening parameter, and ' N_D ' represents the number of particle in Debye sphere. The second term in the equation 2.10 is usually small (due to small A) and contributing only 5 % to the broadening [53]. Hence this term can be neglected and the equation 2.10 reduces to equation 2.11.

$$\Delta\lambda_{FWHM} = 2\omega \left(\frac{N_e}{10^{16}} \right) \quad (2.11)$$

In the present study, electron density has been determined using stark broadened profile of lead atomic transition at Pb I 373.99 nm. The stark broadening parameter (ω) is considered as 0.113 is considered from literature [54,55]. The obtained full width at half maximum obtained from fitting the atomic line profile with Lorentzian was further corrected by subtracting the resolution of spectrograph (0.05 nm). The final value is used for calculating N_e as shown in equation 2.11. **Figures 2.13(a)** and **2.13(b)** illustrate the Lorentzian fits of typical Pb I atomic transition at 373.99 nm obtained at 20 mJ, 40 mJ and 60 mJ at 200 ns and 800 ns delays respectively. A clear broadening of atomic spectral line is seen in initial times of plasma due to the continuum emission domination.

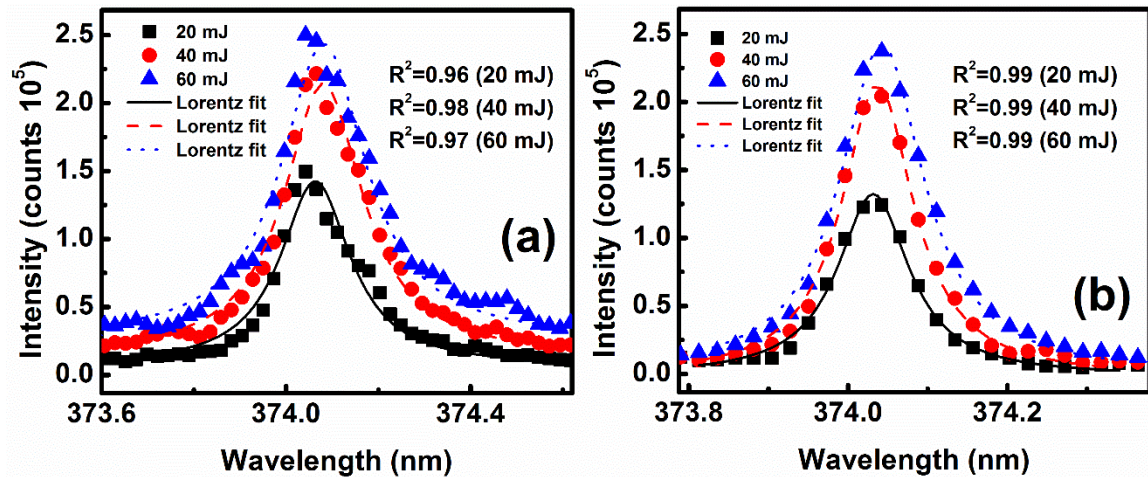


Figure 2.13 Spectral intensity profile of Pb I 373.99 nm atomic transition and the Lorentz fit of intensity at different energies 20mJ (black square), 40 mJ (red circle), and 60 mJ (blue triangle) at a gate delay of (a) 200 ns and (b) delay of 800 ns. The gate width is constant at 200 ns.

The various processes occurring in plasma are as follows: collisional ionization, photo-ionization, radiative and three-body recombination, radiative decay, collisional excitation and de-excitation, photo-excitation and bremsstrahlung process. Because of highly transient and inhomogeneous nature of LIP complete thermodynamic equilibrium is not possible to achieve inside the plasma. Thus, the concept of local thermodynamic

Chapter 2

equilibrium (LTE) is introduced. For LTE to prevail in plasma, the collisional process has to dominate over the radiative process. These conditions require a sufficiently large electron density. The lower limit of electron density for which plasma can be described in LTE is given by McWhirter's criterion. The lower limit of the electron density is given by following equation (2.10) [56]

$$N_e \geq 1.6 \times 10^{12} T^{\frac{1}{2}} (\Delta E)^3 \quad (2.10)$$

Where N_e is the electron density, $T(K)$ is the plasma temperature, $\Delta E(eV)$ is the energy differences between states which are expected to be in LTE. The Pb I peak at 357.27 nm, with an energy difference of $\Delta E = 3.47$ eV was utilized to check the McWhirter's criterion. **Figure 2.14** depicts the validation of McWhirter's criterion at various fluence.

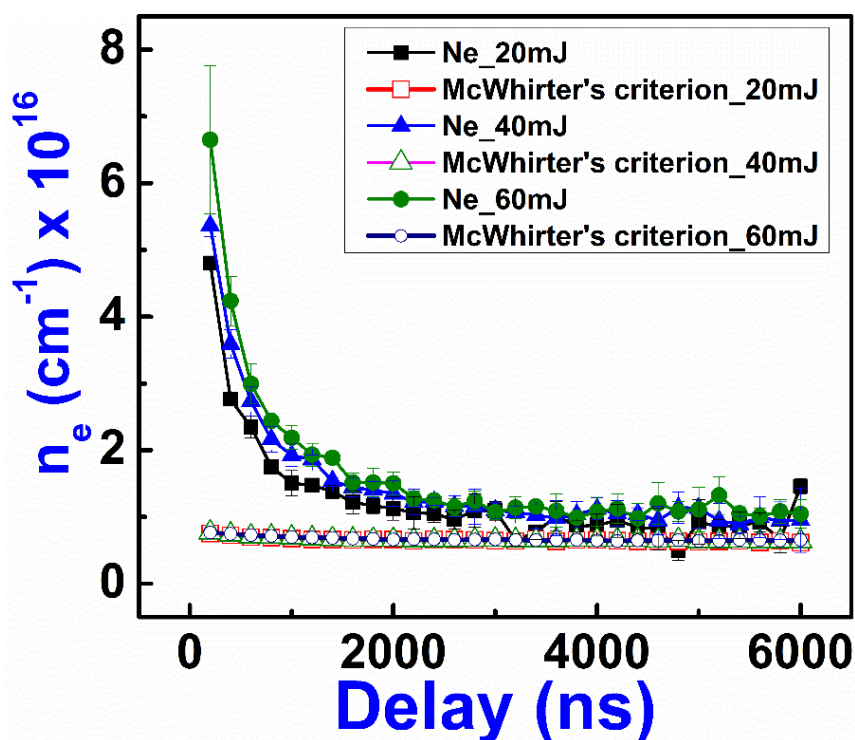


Figure 2.14 Validation of McWhirter's criterion at various fluence using lead atomic transition (Pb I) at 357.27 nm, with an energy difference of $\Delta E = 3.47$ eV.

2.6 Conclusions

Lead plasma induced by a frequency doubled pulsed Nd: YAG laser upon interaction with lead nitrate $[Pb(NO_3)_2]$ was studied in air at atmospheric pressure. The two essential parameters that characterize plasma i.e. the plasma temperature and electron density were measured by time-resolved spectroscopic studies in the time window of

200–6000 ns. Effect of fluence on these parameters was investigated in air. An echelle spectrograph attached with intensified charge coupled detector (ICCD) was used to record the plasma emissions. At each delay, Boltzmann plot method was utilized to calculate the plasma temperature and the stark widths of Pb I 373.99 nm to estimate electron density. Plasma temperature and Electron density increased with laser energy and decreases exponentially with increase in time delay. McWhirter's condition is verified for electron density calculations.

2.7 References

1. W. Koechner, *Solid State Laser Engineering*, 4th ed. (Springer-Verlag, 2006).
2. W. T. Silfvast, *Laser Fundamentals* (Cambridge University Press, 2004).
3. Coherent, *Operator's Manual: Libra Ultrafast Amplifier Laser System*, Santa Clara, CA 95054 (2013).
4. T. Brabec, C. Spielmann, P. F. Curley, and F. Krausz, "Kerr lens mode locking," *Opt. Lett.* **17**(18), 1292 (1992).
5. "Optical microscopy premier specialized techniques, Multiphoton Fluorescence Microscopy, Interactive Tutorials, Ti: Sapphire Mode-Locked Lasers," <https://micro.magnet.fsu.edu/primer/java/lasers/tsunami/index.html>.
6. S. N. Thakur and D. K. Rai, *Atom, Laser and Spectroscopy*, 2nd ed. (PHI Learning Pvt. Ltd., 2013).
7. H. Kim, "Dual-Mode Ti:Sa laser," https://www3.mpifr-bonn.mpg.de/div/submmtech/heterodyne/photonic_laser/dualmodeTiSa.html.
8. T. A. Labutin, V. N. Lednev, A. A. Ilyin, and A. M. Popov, "Femtosecond laser-induced breakdown spectroscopy," *J. Anal. At. Spectrom.* **31**(1), 90–118 (2016).
9. CUOS, "Center for Ultrafast Optical Science, University of Michigan," <https://cuos.engin.umich.edu/>.
10. K. Naganuma, K. Mogi, and H. Yamada, "General Method for Ultrashort Light Pulse Chirp Measurement," *IEEE J. Quantum Electron.* **25**(6), 1225–1233 (1989).
11. D. W. Hahn and N. Omenetto, "Laser-induced breakdown spectroscopy (LIBS), part II: Review of instrumental and methodological approaches to material analysis and applications to different fields," *Appl. Spectrosc.* **66**(4), 347–419 (2012).
12. D. W. Hahn and N. Omenetto, "Laser-induced breakdown spectroscopy (LIBS), part I: Review of basic diagnostics and plasmaparticle interactions: Still-challenging issues within the analytical plasma community," *Appl. Spectrosc.* **64**(12), 335–366 (2010).
13. J. Singh and S. Thakur, eds., *Laser Induced Breakdown Spectroscopy*, 1st ed. (Elsevier, 2007).
14. M. Baudelet, ed., *Laser Spectroscopy for Sensing Fundamentals, Techniques and Applications* (Woodhead Publishing, 2014).
15. S. Musazzi and U. Perini, eds., *Laser Induced Breakdown Spectroscopy Theory and Applications* (Springer-Verlag, 2014), **182**.
16. David A. Cremers et al, *Handbook of Laser-Induced Breakdown Spectroscopy*, 2nd ed. (John Wiley & Sons, 2013).
17. L. Radziemski and D. Cremers, "A brief history of laser-induced breakdown spectroscopy: From the concept of atoms to LIBS 2012," *Spectrochim. Acta B* **87**, 3–10 (2013).
18. J. Rakovský, P. Čermák, O. Musset, and P. Veis, "A review of the development of portable laser induced breakdown spectroscopy and its applications," *Spectrochim. Acta B* **101**, 269–287 (2014).
19. M. Baudelet and B. W. Smith, "The first years of laser-induced breakdown spectroscopy," *J. Anal. At. Spectrom.* **28**(5), 624–629 (2013).
20. L. J. Radziemski, "From LASER to LIBS, the path of technology development," *Spectrochim. Acta B* **57**(7), 1109–1113 (2002).
21. J. El Haddad, L. Canioni, and B. Bousquet, "Good practices in LIBS analysis: Review and advices," *Spectrochim. Acta B* **101**, 171–182 (2014).
22. J.-C. Diels and L. Arissian, *Lasers: The Power and Precision of Light* (Wiley-Vch,

- 2011).
23. M. Markiewicz-Keszycka, X. Cama-Moncunill, M. P. Casado-Gavaldà, Y. Dixit, R. Cama-Moncunill, P. J. Cullen, and C. Sullivan, "Laser-induced breakdown spectroscopy (LIBS) for food analysis: A review," *Trends Food Sci. Technol.* **65**, 80–93 (2017).
 24. A. M. Popov, T. A. Labutin, S. M. Zaytsev, I. V. Seliverstova, N. B. Zorov, I. A. Kal'Ko, Y. N. Sidorina, I. A. Bugaev, and Y. N. Nikolaev, "Determination of Ag, Cu, Mo and Pb in soils and ores by laser-induced breakdown spectrometry," *J. Anal. At. Spectrom.* **29**(10), 1925–1933 (2014).
 25. R. Yi, X. Yang, R. Zhou, J. Li, H. Yu, Z. Hao, and L. Guo, "Determination of Trace Available Heavy Metals in Soil Using Laser-Induced Breakdown Spectroscopy Assisted with Phase Transformation Method," *Anal. Chem.* **90**, 7080–7085 (2018).
 26. N. Saha and M. S. Rahman, "Multivariate statistical analysis of metal contamination in surface water around Dhaka export processing industrial zone, Bangladesh," *Environ. Nanotechnology, Monit. Manag.* **10**, 206–211 (2018).
 27. G. Arca, A. Ciucci, V. Palleschi, S. Rastelli, and E. Tognoni, "Trace Element Analysis in Water by the Laser-Induced Breakdown Spectroscopy Technique," *Appl. Spectrosc.* **51**(8), 1102–1105 (1997).
 28. S. J. Rehse, H. Salimnia, and A. W. Miziolek, "Laser-induced breakdown spectroscopy (LIBS): an overview of recent progress and future potential for biomedical applications," *J. Med. Eng. Technol.* **36**(2), 77–89 (2012).
 29. S. J. Rehse, H. Salimnia, and A. W. Miziolek, "Laser-induced breakdown spectroscopy (LIBS): An overview of recent progress and future potential for biomedical applications," *J. Med. Eng. Technol.* **36**(2), 77–89 (2012).
 30. V. K. Singh and A. K. Rai, "Prospects for laser-induced breakdown spectroscopy for biomedical applications: A review," *Lasers Med. Sci.* **26**(5), 673–687 (2011).
 31. V. K. Unnikrishnan, R. Nayak, S. Bhat, S. Mathew, V. B. Kartha, and C. Santhosh, "Biomedical applications of laser-induced breakdown spectroscopy (LIBS)," in *SPIE BiOS* (SPIE, 2015), p. 5.
 32. Y. Moon, J. H. Han, S. Shin, Y.-C. Kim, and S. Jeong, "Elemental analysis of tissue pellets for the differentiation of epidermal lesion and normal skin by laser-induced breakdown spectroscopy," *Biomed. Opt. Express* **7**(5), 1626–1636 (2016).
 33. R. Gaudiuso, M. Dell'Aglio, O. de Pascale, G. S. Senesi, and A. de Giacomo, "Laser induced breakdown spectroscopy for elemental analysis in environmental, cultural heritage and space applications: A review of methods and results," *Sensors* **10**(8), 7434–7468 (2010).
 34. S. Tzortzakis, D. Anglos, and D. Gray, "Ultraviolet laser filaments for remote laser-induced breakdown spectroscopy (LIBS) analysis: applications in cultural heritage monitoring," *Opt. Lett.* **31**(8), 1139 (2006).
 35. S. Awasthi, R. Kumar, G. K. Rai, and A. K. Rai, "Study of archaeological coins of different dynasties using libs coupled with multivariate analysis," *Opt. Lasers Eng.* **79**, 29–38 (2016).
 36. R. S. Harmon, R. E. Russo, and R. R. Hark, "Applications of laser-induced breakdown spectroscopy for geochemical and environmental analysis: A comprehensive review," *Spectrochim. Acta B* **87**, 11–26 (2013).
 37. R. S. Harmon, R. R. Hark, C. S. Throckmorton, C. Eugene, M. A. Wise, A. M. Somers, and L. M. Collins, "Geochemical Fingerprinting by Handheld Laser-Induced Breakdown Spectroscopy (LIBS)," *Geostand. Geoanalytical Res.* **41**(4),

Chapter 2

- 563–584 (2017).
38. B. Connors, A. Somers, and D. Day, "Application of Handheld Laser-Induced Breakdown Spectroscopy (LIBS) to Geochemical Analysis," **70**(5), 810–815 (2016).
 39. N. J. Mcmillan, S. Rees, K. Kochelek, and C. Mcmanus, "Geological Applications of Laser-Induced Breakdown Spectroscopy," *Geostand. geoanalytical Res.* **38**, 329–343 (2014).
 40. P. M. Mukhono, K. H. Angeyo, A. Dehayem-Kamadjeu, and K. A. Kaduki, "Laser induced breakdown spectroscopy and characterization of environmental matrices utilizing multivariate chemometrics," *Spectrochim. Acta B* **87**, 81–85 (2013).
 41. W. T. Y. Mohamed, "Recent advances in laser induced breakdown spectroscopy as elemental analytical technique for environmental applications and space exploration," in *Aspects of Optical Sciences and Quantum Information*, M. Abdel-Aty, ed. (Research Signpost, 2007), pp. 1–35.
 42. F. J. Fortes, S. Guirado, A. Metzinger, and J. J. Laserna, "A study of underwater stand-off laser-induced breakdown spectroscopy for chemical analysis of objects in the deep ocean," *J. Anal. At. Spectrom.* **30**(5), 1050–1056 (2015).
 43. S. Maurice, D. A. Cremers, and R. C. Wiens, "Laser-induced breakdown spectroscopy for Mars surface analysis: capabilities at stand-off distances and detection of chlorine and sulfur elements," *Spectrochim. Acta B* **59**, 1413–1422 (2004).
 44. A. Bolshakov, "LIBS at work on Mars," <https://appliedspectra.com/mars-lib.html>.
 45. E. Tognoni, G. Cristoforetti, S. Legnaioli, and V. Palleschi, "Calibration-Free Laser-Induced Breakdown Spectroscopy: State of the art," *Spectrochim. Acta B* **65**(1), 1–14 (2010).
 46. Andor Technology, *User Guide for Mechelle* (2011).
 47. S. Zhang, X. Wang, M. He, Y. Jiang, B. Zhang, W. Hang, and B. Huang, "Laser-induced plasma temperature," *Spectrochim. Acta B* **97**, 13–33 (2014).
 48. V. K. Unnikrishnan, K. Alti, V. B. Kartha, C. Santhosh, G. P. Gupta, and B. M. Suri, "Measurements of plasma temperature and electron density in laser-induced copper plasma by time-resolved spectroscopy of neutral atom and ion emissions," *Pramana - J. Phys.* **74**(6), 983–993 (2010).
 49. N. M. Shaikh, S. Hafeez, M. A. Kalyar, R. Ali, and M. A. Baig, "Spectroscopic characterization of laser ablation brass plasma," *J. Appl. Phys.* **104**(10), (2008).
 50. H. R. Griem, *Principles of Plasma Spectroscopy*, 1st ed. (Cambridge university press, 1997).
 51. G. Bekefi, *Principles of Laser Plasmas* (John Wiley, 1976).
 52. V. Milosavljević and G. Poparić, "Atomic spectral line free parameter deconvolution procedure," *Phys. Rev. E* **63**(3), 1–7 (2001).
 53. N. Konjevic, F. Physics, P. O. Box, and N. Konjevic, "Plasma broadening and shifting of non-hydrogenic spectral lines: present status and applications," *Phys. Rep.* **316**, 339–401 (1999).
 54. A. Alonso-Medina, "Experimental determination of the Stark widths of Pb I spectral lines in a laser-induced plasma," *Spectrochim. Acta B* **63**(5), 598–602 (2008).
 55. I. S. Fishman, E. V. Sarandaev, and M. K. Salakhov, "Experimental determination of the Stark parameters of PbI, PbII, and CuII spectral lines in a plasma of the pulse capillary discharge," *J. Quant. Spectrosc. Radiat. Transf.* **52**(6), 887–896 (1994).

56. R. H. Huddlestone and S. L. Leonard, *Plasma Diagnostic Techniques* (Academic Press, 1965).

Intentional blank page

Chapter 3

Influence of structural and functional groups on the LIBS data: A case study of energetic triazole derivatives with femtosecond and nanosecond pulses

In this chapter the results obtained from proximal femtosecond (fs) and nanosecond (ns) LIBS studies on a set of six energy rich triazole derivatives are presented. The major emphasis of this work is to establish the correlation between the detonation parameters of energetic molecules with their molecular and atomic emissions (from the LIBS data) and to understand the influence of various functional groups viz., methyl (CH₃), methoxy (OCH₃), and amino (NH₂) and their position (para or ortho) on the molecular formation in laser induced plumes (LIP). The CN and C₂ emission intensities from the fs (air) and ns LIBS data (air and argon) were correlated with C–N, C=N, C–C, C=C, bonds and %O. The feasibility of a few pathways in LIBS plasma leading to formation and depletion of CN and C₂ has also been addressed by considering the plasma as a thermodynamic system. The nature of functional groups and their positions in the molecular structure on the LIP emission was studied through the CN/C₂ ratio. CN and C₂ vibrational temperatures from fs/ns LIBS spectra were calculated using NMT algorithm. Further, the energetic parameters of these energetic molecules viz., oxygen balance (O.B.), velocity of detonation (V.O.D), detonation pressure (D.P.) and chemical energy of detonation (Q) were correlated with different atomic and molecular emissions. A good correlation was observed between these energetic parameters and the (CN + C₂)/(C + H + N + O) ratio from LIBS spectra. Finally, principal component analysis (PCA) was utilized in tandem with fs/ns LIBS data to discriminate these energetic molecules.

Part of this work has been accepted for publication

1. **S. A. Kalam**, N. L. Murthy, P. Mathi, N. Kommu, A. K. Singh, and S. V. Rao, "Correlation of molecular, atomic emissions with detonation parameters in femtosecond and nanosecond LIBS plasma of high energy materials," *J. Anal. At. Spectrom.* **32(8)**, 1535–1546 (2017).
2. **S. A. Kalam** and S. Venugopal Rao, "Femtosecond and nanosecond LIBS studies towards discrimination of energy rich triazoles", **Manuscript to be submitted**, 2018.

3.1 Introduction

Laser induced breakdown spectroscopy (LIBS) offers robust in-situ elemental analysis of widespread range of samples [1–3]. LIBS technique has been widely and successfully employed in a variety of fields such as drugs and pharmaceutical industry, nutrient analysis in soil, pollution monitoring, examining the cultural heritage such as buildings and coins, detection of toxic and heavy metals traces (Pb, As) in water [4–9] etc. for analytical purposes. Similarly, LIBS technique also has been successfully used for underwater and space exploration missions and in the standoff detection of explosives [10–13]. Apart from this technique several other laser-based spectroscopic techniques such as Raman spectroscopy, laser induced fluorescence, terahertz spectroscopy and photo-acoustic spectroscopy techniques, have been developed over the last decade towards the identification of explosives [14–16] at various scenarios. Simultaneously, the leverage of open path configuration and advancements in field deployable instruments has equipped LIBS for investigating various materials including energetic molecules at standoff distances [17]. Though several researchers have utilized nanosecond (ns) pulses for investigating various materials in standoff mode [7,18–20], femtosecond (fs) pulses are also promising for such applications, because of their ability to deliver high intensities over long distances ranging from few tens of meters to few kilometres through the phenomenon of filamentation [21–25]. Although the sensitivity and specificity of LIBS are moderate in comparison to other spectroscopic techniques, sustained efforts are directed towards improving these attributes. Several multivariate data analysis (MVDA) modules such as principal component analysis (PCA), Soft independent modelling of class analogies (SIMCA), partial least squares discriminant analysis (PLS-DA) have been developed and utilized in conjunction with LIBS data for improved discrimination in different fields such as soil analysis, pharmaceuticals and class labelling of explosive residues with few false alarms [26–30]. Moreover, studies of Myakalwar et al. [31] have revealed that a few LIBS spectral signatures combined with simple chemometric techniques can enhance the selectivity of LIBS towards explosive identification and can result in superior classification. Furthermore, the sensitivity of LIBS can be enhanced by achieving low limit of detection. In recent years, a derived technique of LIBS called as nanoparticle enhanced laser induced breakdown spectroscopy (NE-LIBS), based on acquiring LIBS signal in the presence of metal nanoparticles for towards the enhanced

sensitivity of analyte has been proposed by Giacomo et al. [32]. They have demonstrated the sensitivity of analyte below sub ppm level concentrations through this technique using intense nanosecond pulses at the energies near the threshold values.

The LIBS spectra of energetic molecules, plastics and other organic samples looks similar with CN, C₂ molecular emission bands and with atomic transitions of C, H, N and O owing to their similar constituents of C, H, N and O. Though LIBS is an elemental analysis technique, the molecular species formed through various complex reactions in transient laser induced plasmas enable the LIBS technique to analyse the molecular solids. However, the emission signatures in LIP from various organic materials depend on the molecular structure, constituents and the atmosphere surrounding the LIP. CN and C₂ formation pathways and their correlation with molecular structure in various organic molecules and explosives was investigated by several research groups. Some of the significant studies/results are summarized below. Grégoire et al. [33] investigated the relation between CN and C₂ emissions with native bonds present in polymeric materials using time resolved spectroscopic imaging. Mousavi et al. [34] studied aliphatic and aromatic organic molecules (13 in total) with varying %C, %H, %N, and %O and different number of aromatic rings using ns LIBS technique to understand the formation of CN and C₂ emissions. Their studies revealed that CN species are mostly formed due to recombination and C₂ species are formed due to fragmentation of the C=C dimers. The high intensity of C emissions observed in the oxygen atmosphere compared to both air and nitrogen in case of urea and thiourea revealed that C recombined with N to form CN than forming CO or CO₂ species. Bravo et al. [35] have recently investigated the influence of fluorine (F) and chlorine (Cl) present in a set of polymers on CN emission and a clear increase at 4-4, and 3-3 peaks in CN vibrational spectrum ($\Delta v=0$) of plastics with and without F and Cl. Likewise, Dong et al. [36] have studied the formation of CN and C₂ molecular radicals and their emissions in solid materials containing C and N in air and argon ambiance. Under air and argon flow conditions. Atomic carbon and C₂ molecular emission were found to be enhanced in the presence of inert argon gas due to the unavailability of N and O from air. Serrano et al. [37] have investigated the primary and secondary formation pathways of virtually unexplored diatomic hydrogenated radicals viz., CH, NH, and OH in femtosecond plasmas of deuterated isotopologues of urea, terephthalic acid and anthracene. Delgado et al. [38,39] had investigated numerous fragmentation pathways in organic explosives under controlled atmosphere i.e. with

Chapter 3

different background gases at varying pressures and at different laser fluence. They have analysed TNT and PETN simultaneously with LIBS and LIMS (laser induced mass spectrometry) technique and proposed possible fragmentation pathways. [40] In recent LIBS studies isotopic labelled C₂ peaks ¹²C₂, ¹²C¹³C and ¹³C₂ in isotopic-labelled fumaric acid were also identified. Rao et al. [41] have studied influence of varying nitro groups among nitropyrazoles on molecular emissions with fs excitation in decreasing nitrogen ambience i.e. from nitrogen, air and argon ambience. Sreedhar et al. [42,43] have investigated CN and C₂ molecular formation routes in LIBS plasma of three energetic molecules viz., RDX, TNT and NTO subjected to air and different ambient gases argon and nitrogen with both fs and ns excitations. Recently, we have investigated the role of position and number of substituents on ring fragmentation pathways in energetic nitroimidazoles using both fs and ns ablation schemes and established the correlation between molecular structure intensity ratios of molecular and atomic spectral emissions [44]. All these studies revealed that the type, position and number of substituents appear to have a strong bearing on the spectral emission signatures. To unfold and understand this phenomenon we have considered in this work a set of six energetic molecules which are structural and functional isomers of triazole substituted nitroarene derivatives [45] that possess methyl (CH₃, hereafter referred to as Me), methoxy (OCH₃, hereafter referred to as OMe) and amino (NH₂) groups at para and ortho positions. The LIBS emission spectra were recorded using fs (in ambient air) and ns (in air, argon atmospheres) pulses. The effect or influence of functional groups and their positions was examined through the trend followed by CN/C₂ ratio. Further, CN and C₂ emissions obtained from fs and ns LIBS spectra in different ambiances were correlated with %C-C+%C=C and %C-N+%C=N linkages. CN and C₂ vibrational temperature was calculated using NMT algorithm. An attempt has been made to correlate the molecular and atomic emission signatures with principal energetic parameters viz., oxygen balance (O.B.), velocity of detonation (V.O.D.), detonation pressure (D.P.), and chemical energy of detonation (Q). Finally, principal component analysis was utilized in tandem with proximal fs/ns LIBS data to classify/cluster these energetic molecules.

3.2 Experimental details

Femtosecond LIBS experiments were performed with an ultrafast Ti: Sapphire laser system (Amplitude, 3 mJ, 1 kHz) delivering ~50 fs laser pulses and operating at

central wavelength of 800 nm. The utilized fs LIBS setup is located in Radiation & Photochemistry Division of the Bhabha Atomic Research Centre, India. These experiments were carried out in ambient air using 900 μJ pulse energy. The ns ablation experiments were carried out at ACRHEM, University of Hyderabad. A Q-switched Nd:YAG laser (INNOLAS SpitLight, $\sim 1.2 \text{ J @ } 1064 \text{ nm}$, 10 Hz) operating at 532 nm wavelength and delivering $\sim 7 \text{ ns}$ pulses was employed to carry out ns experiments in air and argon with 15 mJ pulse energy. The schematic of both ns/fs proximal LIBS setups are illustrated in **Chapter 2, figure 2.8**. A 100-mm focal length lens fixed on translational stage was used in both the cases for focusing and precise interrogation of laser with sample. The plasma emissions were collected by Andor ME-OPT-007 collector/collimator at 15 cm from plasma and fed to Andor Mechelle (ME 5000) + Andor iStar ICCD (DH 334T-18U-E3) system via an optical fiber of 600 μm diameter. For experiments in argon atmosphere, the sample was purged with argon gas with the help of a nozzle at the rate of $\sim 3 \text{ L/min}$. Pellets were placed on a translation stage controlled by Newport ESP 300 motion controller to expose fresh surface to each pulse. In fs case, three spectra (only) of each sample A1-A6 were recorded in accumulation mode (6 accumulations) to obtain good signal to noise ratio, using a gate delay of 100 ns, gate width of 800 ns, exposure time of CCD is 1.5 s, and ICCD gain at 180 in air (only). Thus, a single spectrum is the result of optical emissions collected from 9000 pulses. 20-30 LIBS spectra of each sample were recorded for all samples (A1-A6) in the accumulation mode (10 accumulations) with a gate delay of 1 μs , gate width of 4 μs , exposure time of 0.002 s and ICCD gain at 120, in air and argon environments. The fs LIBS spectra could not be recorded in argon environment due to scarce sample size. The spectra were recorded in the range of 220-850 nm. The gate delays of 100 ns (fs case) and 1 μs (ns case) were chosen to avoid Continuum emissions from LIP.

Materials: Six (labelled as A1-A6) in-house synthesized energetic triazole derivatives substituted with methyl (CH_3), methoxy (OCH_3), and amino (NH_2) functional groups at ortho (A1-A3) and (A4-A6) para positions were investigated in this work. These energetic molecules were synthesized and reported by Kommu et al. [45,46]. **Figure 3.1** shows the molecular structure of the triazole derivatives (A1-A6) investigated in the present study. IUPAC names and molecular formulas of these molecules are listed in **Table 3-1**. Pellets of 2-3 mm thick and $\sim 12 \text{ mm}$ in diameter were prepared by pressing $\sim 150 \text{ mg}$ of fine ground powder at 3 tones pressure. The energetic parameters of triazole

Chapter 3

derivatives viz., oxygen balance (O.B.), velocity of detonation (V.O.D), detonation pressure (D.P.), and heat of detonation (Q) were theoretically calculated using Explo5 version 6.02. Various atomic percentages (%C, %H, %N, %O), atomic bond percentages (%C-C+%C=C, %C-N+%C=N) present in these molecules are listed in **Table 3-2**.

Table 3-1 IUPAC names and molecular formula of triazole derivatives investigated in fs/ns LIBS setup.

Label	IUPAC name	Molecular formula
A1	1-(4-methyl-3,5-dinitrophenyl)-1H-1,2,4-triazole	C ₉ H ₇ N ₅ O ₄
A2	1-(4-methoxy-3,5-dinitrophenyl)-1H-1,2,4-triazole	C ₉ H ₇ N ₅ O ₅
A3	2,6-dinitro-4-(1H-1,2,4-triazol-1-yl)aniline	C ₈ H ₆ N ₆ O ₄
A4	1-(2-methyl-3,5-dinitrophenyl)-1H-1,2,4-triazole	C ₉ H ₇ N ₅ O ₄
A5	1-(2-methoxy-3,5-dinitrophenyl)-1H-1,2,4-triazole	C ₉ H ₇ N ₅ O ₅
A6	2,4-dinitro-6-(1H-1,2,4-triazol-1-yl)aniline	C ₈ H ₆ N ₆ O ₄

Note: A1-A3 and A4-A6 are functional isomers and A1&A4, A2&A5, A3&A6 are structural isomers.

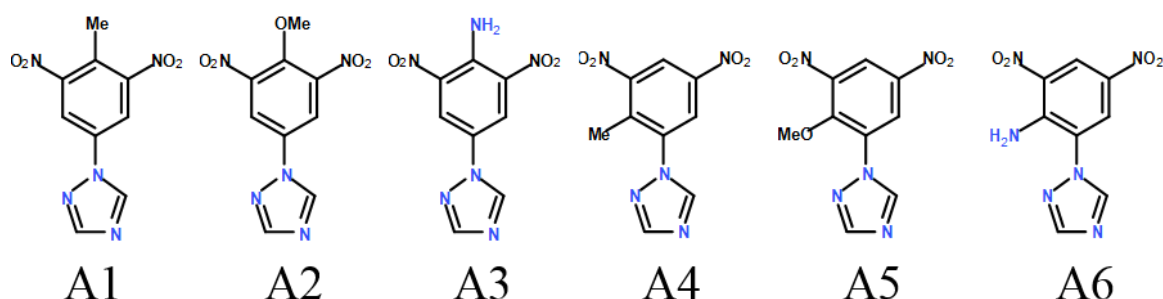


Figure 3.1 The molecular structures of structural and functional derivatives of triazole substituted nitroarene derivatives investigated in this study.

Table 3-2 Atomic and bond percentages present in the triazole molecules (A1-A6). Energetic parameters of nitroimidazoles obtained from Explo5 version 6.02.

Sample labels	C %	H %	N %	O %	C-C % + C=C %	C-N % + C=N %	V.O.D (a)	D.P. (a)	O.B. (b)	Q (b)
							(ms ⁻¹)	(G Pa)	(%)	(Cal g ⁻¹)
A1	36	28	20	16	26.5	26.7	6980	17.25	-112.369	1122.86
A2	34.6	26.9	19.2	19.2	22.1	25.4	7108	18.47	-99.555	1063.78
A3	33.3	25	25	16.6	24	32	7222	18.88	-95.9348	1024.65
A4	36	28	20	16	26.5	26.7	6980	17.13	-112.369	1115.48
A5	34.6	26.9	19.2	19.2	22.1	25.4	7008	17.77	-99.555	1053.96
A6	33.3	25	25	16.6	24	32	7167	18.51	-95.9348	1017.81

3.3 Results and Discussions

3.3.1 Influence of laser pulse duration on fragmentation patterns in triazole-substituted nitroarene

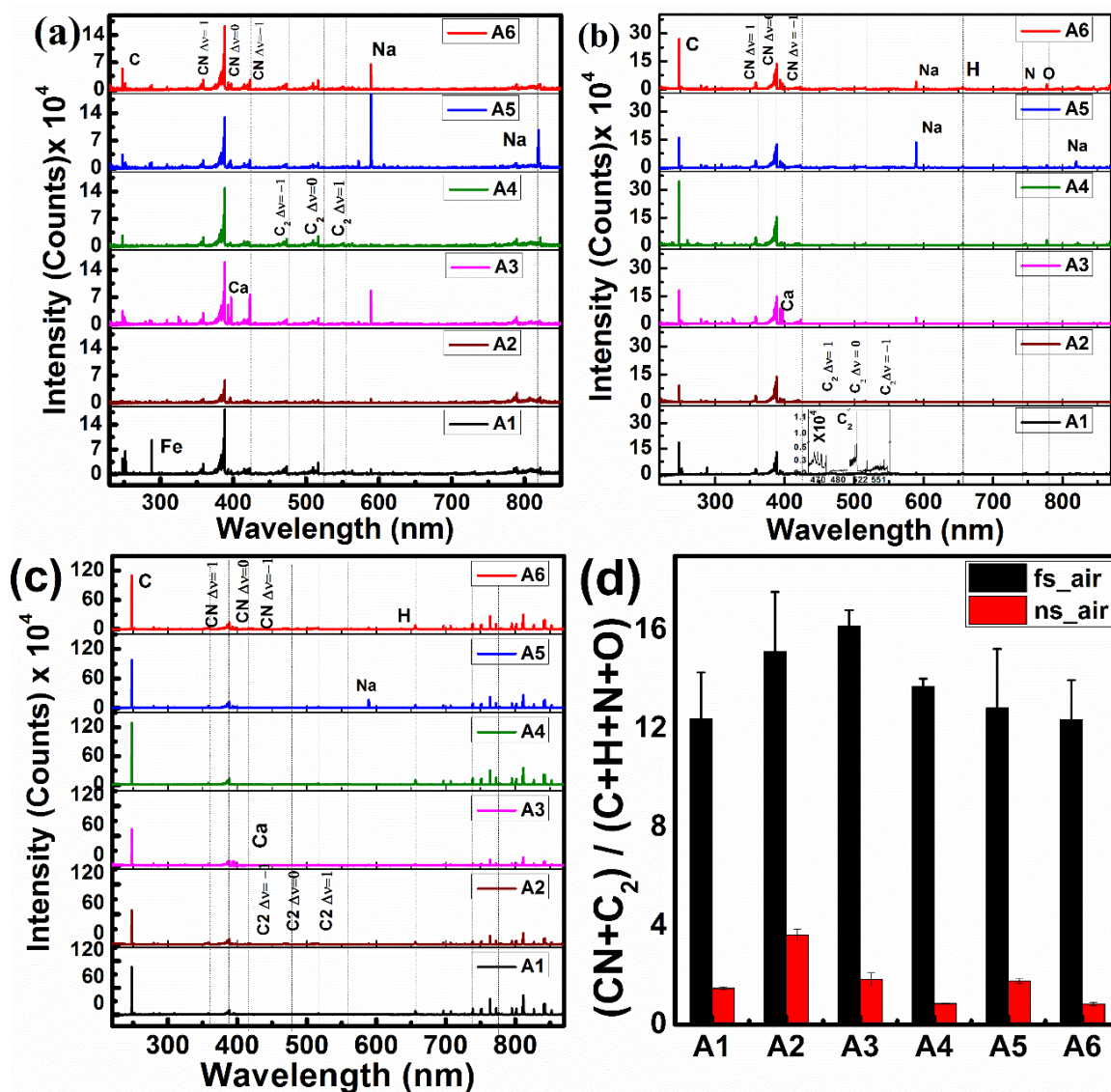


Figure 3.2 LIBS spectra of six novel HEMs with (a) fs excitation in air (b) ns excitation in air and (c) ns excitation in argon environments. Molecular (CN, C₂) and atomic emissions (C, H, N, O) and impurities (Na, Ca, Fe) are labelled in the fs/ns LIBS spectra and (d) Ratio of the molecular sum to atomic sum (MSAS), $(CN+C_2)/(C+H+N+O)$ in air with femtosecond (black) and nanosecond (red) excitation.

Chapter 3

Table 3-3 List of atomic emission lines and molecular bands observed in the LIB spectra of triazoles obtained with fs and ns pulse excitations. Emission lines from impurities such as Ca, Na, and Fe are also tabulated.

Molecular system and atomic species	Transitions observed in fs LIBS (air) (nm)	Transitions observed in ns LIBS (air) (nm)	Standard wavelengths (nm)
CN Violet ($B^2\Sigma^+-X^2\Sigma^+$)	$\Delta v=+1$: 359.03,358.61,358.4	$\Delta v=+1$: 359.04, 358.58, 358.42	359.04,358.59, 358.39
	$\Delta v=0$: 388.31, 387.11, 386.16, 385.45, 385.05	$\Delta v=0$: 388.32, 387.15, 386.17, 385.46, 385.01	388.34, 387.14, 386.19,385.47
	$\Delta v=-1$: 421.59,419.7, 417.99, 416.7, 415.71, 415.04	$\Delta v=-1$:421.52, 419.71, 418.09, 416.78, 415.72, 415.16	421.60, 419.72, 418.10, 416.78, 415.81, 415.24,
C₂ ($d^3\Pi_g \rightarrow a^3\Pi_u$)	$\Delta v=1$:473.68, 471.49, 469.71, 468.43	$\Delta v=1$: 473.71, 471.55, 469.75, 468.48, 467.84	473.71, 471.52, 469.76, 468.78, 467.86
	$\Delta v=0$: 516.46, 509.51**, 512.8	$\Delta v=0$: 516.48, 512.88	516.52, 512.93, 509.77,
	$\Delta v=-1$: 563.45,558.46, 551.49	$\Delta v=-1$: band was not observed	563.55, 558.55, 550.19
NH ($^3\Pi \rightarrow ^3\Sigma$)	336.12	336.04	336.0
O I	777.4	777.6, 844.76,	777.4,844.63
N I	746.8 *	742.41,744.28,746.89,818.44, 821.59,	742.36, 742.23, 746.83, 818.48,821.63
H I	656.4 *	656.3	656.28
C I	247.8	247.8	247.85
Na I	589.0,589.7	588.98,589.96, 818.26, 819.45	588.99, 589.59, 818.32, 819.48
Ca (I & II)	422.69,	Ca I 422.72, Ca II 393.38, Ca II 396.88,	Ca I 422.67, Ca II 393.36, Ca II 396.84,
Fe (I & II)	Fe I 251.64, Fe I 252.87, Fe II 288.18 (A1)	Fe I 251.64*, Fe II 288.19*,	Fe I 251.76, Fe I 252.91, Fe II 288.07
*weak emissions, ** observed only in fs spectra. Standard wavelengths for molecular emissions [47] and atomic transitions [48] were considered from these references.			

Figures 3.2(a) and 3.2(b) illustrate the fs and ns LIBS spectra, respectively, of six novel HEMs recorded in air. Molecular emission signatures from CN and C₂ emissions dominated in the fs LIBS spectra as compared to the ns LIBS spectra (data recorded in air). Three CN bands were observed in the spectral regions of 358-360 nm, 386-390 nm, 410-422 nm corresponding to Δv values of 1, 0, -1, respectively. Out of these, the CN violet band ($\Delta v=0$, $B^2\Sigma^+ \rightarrow X^2\Sigma^+$) had maximum intensity at band head 388.34 nm. Three C₂ bands ($\Delta v=1, 0, -1$) were observed in the spectral range of 465-475 nm, 510-518 nm, 555-565 nm with maximum intensity at C₂ Swan band ($\Delta v=0$, $d^3\Pi_g \rightarrow a^3\Pi_u$). Besides the molecular bands including NH (336.3 nm), atomic emission lines of C, H, N, O and Ca, Na, Fe (impurities) were identified and are tabulated in **Table 3-3** along with standard spectroscopic data [47,48] for comparison. Iron emissions (predominantly seen in A1, in both fs and ns cases) are possibly from an impurity which might entered during the sample preparation or the pellet preparation phase. In contrast to the fs-LIB spectra, the ns-LIB spectra recorded in air were dominated by the atomic emission lines. **Figure 3.2(c)** depicts the ns LIP spectra of six triazole molecules (A1-A6) recorded in argon. These spectra exhibited strong C, H atomic emissions and C₂ molecular emission in comparison to ns LIBS spectra recorded in air. However, feeble atomic emissions from O and N were also observed.

Figure 3.2(d) illustrates the molecular sum to the atomic sum ratio (MSAS), $[\text{CN}+\text{C}_2]/(\text{C}+\text{H}+\text{N}+\text{O})$ in air with fs (black) and ns (red) excitation. The MSAS ratio obtained from time integrated spectra using fs pulses is distinctly higher (i.e. predominantly stronger molecular emissions) than that from the corresponding ns pulses. The striking difference observed in the MSAS ratio when analyzing the LIBS spectra obtained with fs and ns pulses in air can be attributed to the difference in ablation mechanism and plasma evolution condition associated with the fs and ns pulses. The fs-plasma is relatively cooler (~7000 K) compared to ns plasma (~10,000 K). The continuum background in fs-LIB emission spectra is significantly lower than the ns-plasma due to absence of plasma re-heating, negligible plasma-atmosphere interaction due to narrower angular distribution in fs plasma expansion and, therefore, favored molecular formation [23,49–51] via associative mechanisms of atoms or ions in a laser ablation plume. The various radiative transitions of these molecular species give rise to the molecular emissions. The persistence of spectral lines is immensely dependent on the laser pulse energy, extent of laser-plasma coupling and in turn the plasma temperature. In

Chapter 3

case of ns ablation, the longer laser pulse duration and improved laser-plasma coupling results in plasmas with higher plasma temperature. Thus, the emission lines from ns-plasma possesses higher persistence times and dominate with atomic spectral lines in the initial times when compared to fs plasma. However, as the plasma cools down the atomic species recombine to form molecular species and thus delayed molecular emission is observed. The persistence of emission of spectral lines in ns-plasma is at least an order of magnitude longer than that from femtosecond plasmas [42,43]. This will certainly impact the ratio of the sum of molecular emission intensities to the sum of atomic emission intensities (MSAS), $(\text{CN}+\text{C}_2)/(\text{C}+\text{H}+\text{N}+\text{O})$, if recorded at later delay times. This MSAS ratio was later analyzed to evaluate its correlation with energetic parameters. In coming sections, the origin of CN and C_2 molecular emissions and their correlation with molecular structure (various linkages) present in the molecules is discussed.

3.3.2 Origin of CN species and correlation studies

Despite several extensive LIBS works the origin and evolution of laser induced plasma (LIP) is not clear due to the simultaneous involvement of numerous mechanisms such as heating, vaporization, shockwave generation and its collapse etc. [52,53]. The species present in surrounding environment near the focal zone may react with the species present in the plasma and result in different bond formation pathways. Serrano et al. [54] had investigated several organic compounds and proposed various pathways in which a diatomic radical can be formed by considering all dissociation and recombination processes involving single and double displacement reactions and surviving native fragments. They have also demonstrated that excitation with fs pulses better reflects the structure of the molecular solid as compared to ns excitation. Besides native CN bonds, other possible secondary sources for generation of CN species could be reaction of C_2 , C with N or N_2 , where N, N_2 could be of native origin (i.e. from the sample) or from the ambience (from air).



To establish the existence of possible channels, the correlation between CN intensities and C-N% + C=N%, C-C% + C=C%, was evaluated using fs (in air) and ns (air and argon atmosphere) pulses. In all the correlation graphs Pearson's correlation coefficient has been used to deduce the correlation in paired data sets. The value of Pearson's "r" coefficient closer to 1 or -1 indicates stronger positive or negative linear correlation between predictor variable (x) and the response (y). In all correlation graphs for ablation in air, data points corresponding to para (ortho) isomers are represented by square (circle) symbols and black color (red). Hollow symbols corresponds to the ablation in argon. Solid (dash) line represents the linear fit for para (ortho) isomers. Integrated line intensities (or area under the curve) of C, CN and C₂ emissions obtained after baseline correction using a MATLAB code were used for various correlation studies. **Figures 3.4(a)-3.4(c)** illustrate the baseline correction of CN molecular band ($\Delta\nu=0$) in the region 384-389 nm, (b) CN peak at 388.34 and (c) C₂ peak at 516.4 nm from a typical fs LIBS spectrum of A1 using a MATLAB code.

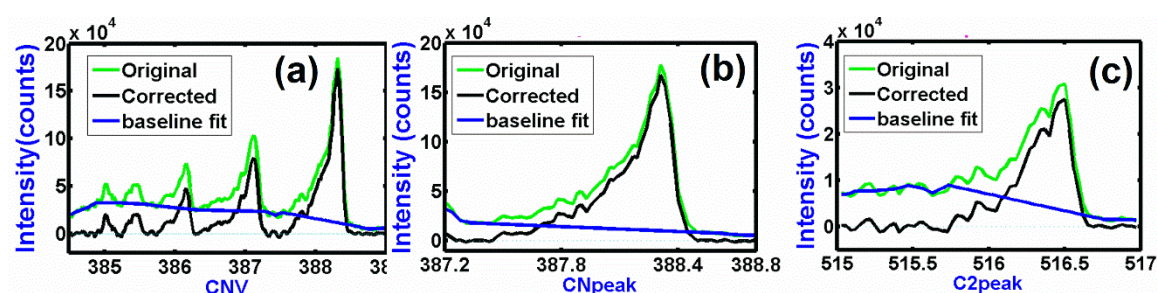


Figure 3.3 Baseline correction of (a) CN molecular band ($\Delta\nu=0$) in the region 384-389 nm, (b) CN peak at 388.34 and (c) C₂ peak at 516.4 nm from fs LIBS spectra of A1 (recorded in air) using a MATLAB code.

Figure 3.5 (a) shows the correlation of CNVsum (where CNVsum is the integrated line intensity of $\Delta\nu=0$ band for CN, in the region 384-389 nm, achieved with MATLAB program after base line correction) with respect to percentages of C-N and C=N bonds obtained from the fs LIBS data recorded in air. In contrast, the corresponding plots [**figure 3.5(b) and 3.5(c)**] obtained for the ns case demonstrates poor correlation in air [$r(P)=-0.3$]; [$r(O)=-0.68$] and argon [$r(P) = -0.17$] and [$r(O) = -0.18$]. This observation clearly suggests that CN does not originate solely from native CN bonds, but can also be formed from other secondary sources such as recombination reaction channels.

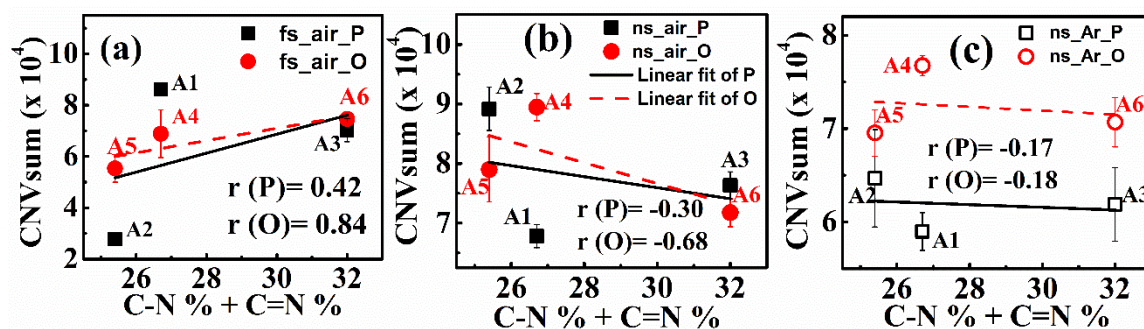


Figure 3.4 Correlation of CNVsum with respect to C-N linkages in air with (a) fs LIBS data (b) ns LIBS data and (c) in argon with ns LIBS data. P & O denote para & ortho isomers in all the correlation graphs.

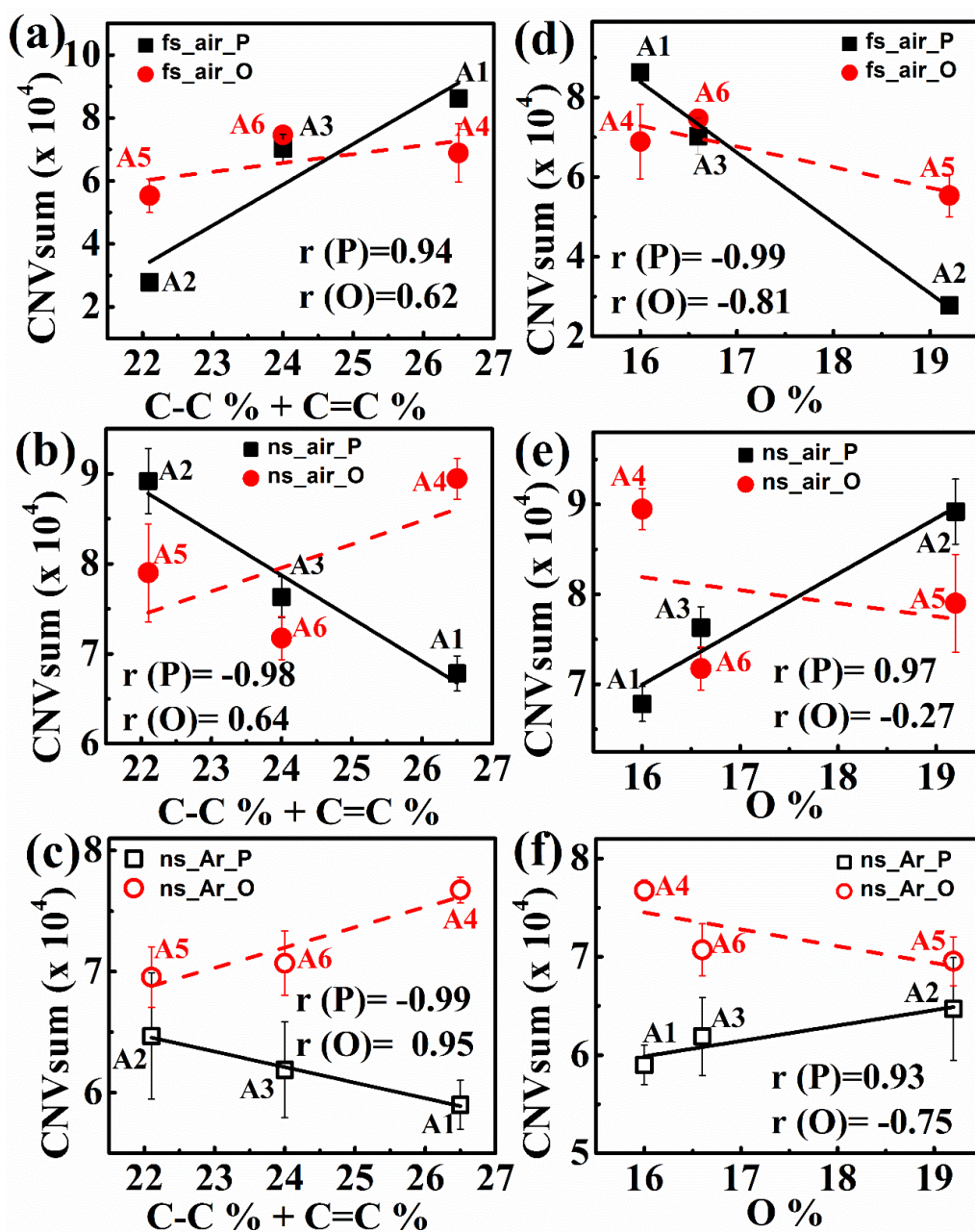


Figure 3.5 Correlation of CN violet band emissions w.r.t C-C linkages (a-c) and O% (d-f) from the LIBS data in air obtained with fs and ns pulses and in argon with ns pulses.

This can be verified by carrying out the ablation in argon atmosphere. In argon atmosphere, there is no ambient N₂ (as opposed to 80% N₂ in air medium). Therefore, in argon atmosphere, formation of CN from reaction channels (1) and (2) (using N from ambience) is not expected to take place. Hence, the CN intensity was lower compared to the corresponding signal intensities obtained for ablation in air. Further, the poor correlation with %C-N +%C=N [figure 3.5(c)] suggests the prevalence of recombination reaction channels leading to CN formation.



CN can also be formed via reaction channels 3 and 4 involving C₂ species. The latter are predominantly seen in case of ablation with fs pulses [figure 3.5(a)].

If C₂ was formed from fragmentation (i.e. C-C or C=C), a good correlation of CNV_{sum} with respect to C-C and C=C linkages [figure 3.6(a)] implies that there was not much depletion of C₂ by way of scavenging by O from air (reaction channels 5, 6) since the air in fs plasma is barely ionized and thus CN was formed via reaction channels of 3 and 4. This may not be the case for ablation with ns pulses where the surrounding air is also ionized. Under such conditions, the contribution to reaction channel 5 from “O” in the air needs to be considered. As the C₂ concentration gets depleted (by reacting with O) the formation of CN is also reduced. This is reflected as a bad correlation [figure 3.6(b)]. This aspect can be confirmed by carrying out the ablation in argon. When the ablation is carried out in argon, the reaction of C₂ with O (of air) is ruled out. In the absence of this scavenging reaction, most of the C₂ will react with N to give CN thus yielding a better correlation between CN and %C-C+%C=C linkages [figure 3.6(c)]. Furthermore, the CNV_{sum} decreased with increasing %O in the molecules [figure 3.6(d)]. This is possibly due to scavenging of C₂ by O (see above discussion), consequently there will not be much C₂ species left to react via reaction channels 3 and 4. The correlation is superior due to the absence of any contribution from O of the atmosphere as the air in fs plasma is barely ionized. However, for the case of ns ablation where the surrounding air gets ionized, the probability for scavenging of C (more C than C₂ in ns ablation) by O (from the surrounding ionized air) is high thereby resulting in a poor correlation [figure 3.6(e)]. In argon atmosphere, the interference from atmospheric O is ruled out and the correlation improves [figure 3.6(f)].

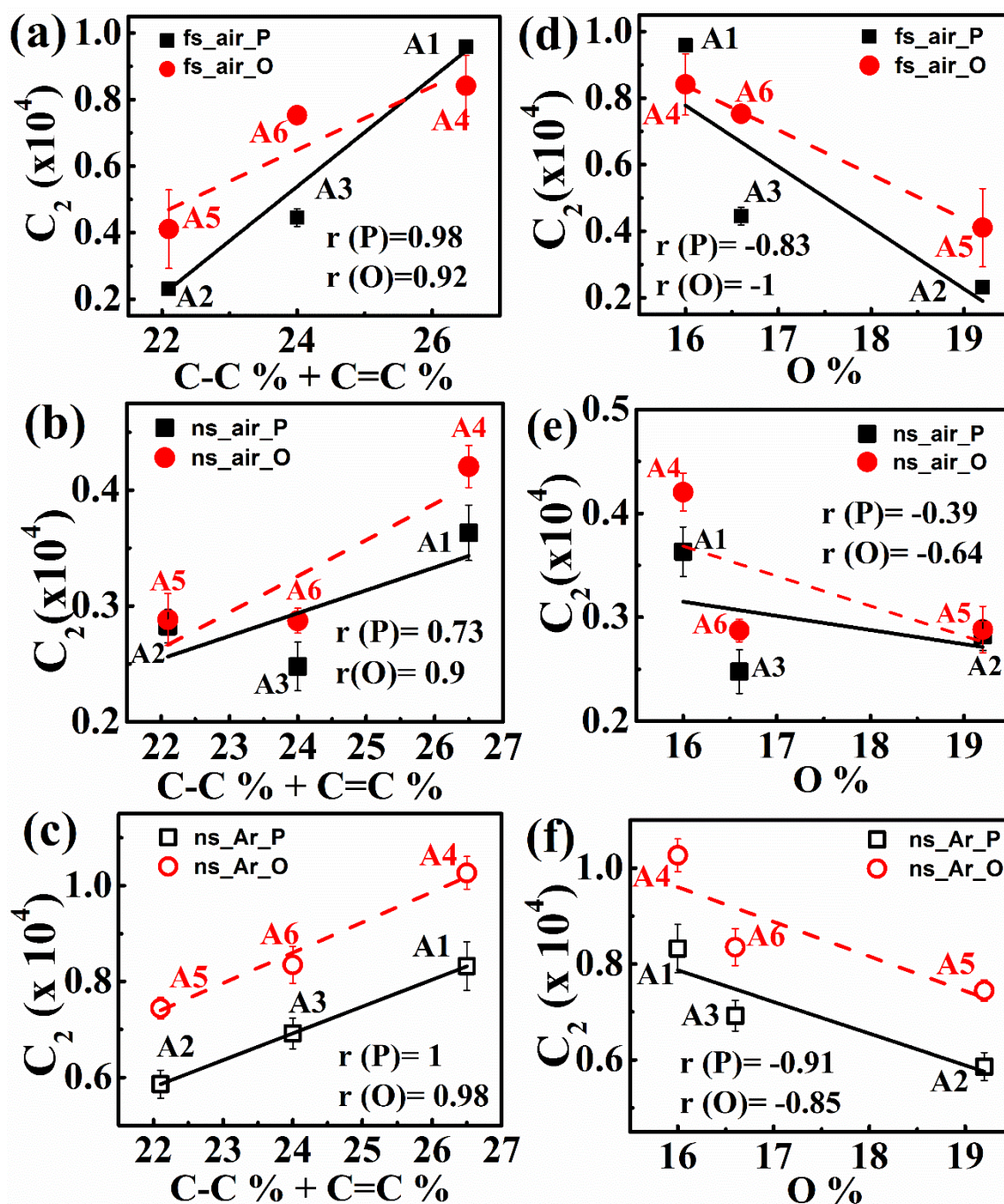
3.3.3 Origin of C₂ species and correlation studies

Figure 3.6 Correlation of C₂ emissions w.r.t C-C linkages (a-c) and O% (d-f) from the LIBS data with fs and ns pulses in air and with ns pulses in argon.

The C₂ emissions from carbon (graphite) have been extensively studied in various ambient gases [55–57], microwave discharge through CO [58]. These studies suggest that C₂ swan band emission most probably originates from electron collisional process through (i) direct excitation of C₂ molecules or (ii) formation of C₂ molecules in excited state ($d^3\Pi_g$) via dissociative or recombinative processes, where the former pathway is

favoured only when large carbon clusters are present in the plasma [59]. Anselment et al. [60] proposed that low-energy electron collisions with C_n cations ($n \geq 2$) or neutrals ($n > 2$) followed by dissociation, could result in an excited C_2 molecule. Little et al proposed another mechanism [61] for populating $d^3\pi_g$ state from the $^5\pi_g$ meta stable state via potential curve crossing. The LIBS studies on urea, thiourea, [34] RDX [42][62] molecules had linked the absence of C_2 emission bands to the lack of C=C linkage in these molecules; thereby suggesting fragmentation as the dominant mechanism for formation of C_2 . However, recombination process involving two carbon radicals can also yield C_2 species [63] according to the following reaction (7).



In our fs LIBS studies on azoles, a superior correlation [Figure 3.7(a)] was observed between the C_2 emission intensity and %C-C +%C=C bonds. This is partly due to the absence of any contribution from O of the atmosphere (reaction channel 5: scavenging reactions for C_2) since the air in fs plasma is hardly ionized. Furthermore, the superior negative correlation ($r = -0.83$, para and $r = -1$, ortho) between the C_2 intensities and O atom % in the molecules [Figure 3.7(d)] suggests that the decay of C_2 proceeds mainly by reaction channel 5, where “O” is from the molecules. With ns pulses, the correlation between C_2 emission intensity and %C-C +%C=C deteriorated ($r=0.73$, para and $r=0.9$, ortho) [Figure 3.7(b)]. This could be due to formation of C_2 by recombination channels (in addition to fragmentation) along with a concomitant loss of C_2 (scavenging reactions involving “O” from the ionized air). The latter is also responsible for the poor negative correlation between C_2 and %O [Figure 3.7(e)]. In Argon atmosphere, there is a significant improvement in the correlation [Figures 3.7(c) and 3.7(f)] largely due to the absence of scavenging reactions involving “O” from the atmosphere.

3.3.4 Plasma chemistry of CN, C_2 emissions

In thermodynamics, Gibbs free energy change (ΔG_r) and equilibrium constant (K_{eq}) play a crucial role in deciding the spontaneity and feasibility of reaction. If $\Delta G_r > 0$ the reaction is non-spontaneous; $\Delta G_r = 0$ the reaction reaches equilibrium; $\Delta G_r < 0$ the reaction is spontaneous (products are favored). Likewise, if $K_{eq} \geq 1000$, then mostly product species will be present at the equilibrium (forward reaction). If it is < 0.001 , then we expect mostly reactant species left at equilibrium (backward reaction). If the condition

Chapter 3

$0.001 < K_{eq} < 1000$ is satisfied then both reactants and products co-exist at equilibrium. Enthalpy and Gibbs free energy of reaction are state functions of a reaction and are calculated by using the equations (3.1) and (3.2). The equilibrium constant K_{eq} for a reaction at any temperature (T) is obtained from the equation (3.3) using the obtained ΔG_r

The feasibility of the above discussed reactions (irrespective of fs/ns pulse or air/argon environment) was examined by calculating equilibrium constant (K_{eq}) at two different temperatures 6000 K and 3000K using the Gibbs free energy change (ΔG_r), where the standard enthalpy of formation and Gibbs free energy of formation of reactants and products are taken from NIST-JANAF thermochemical tables [64]. **Table 3-4** lists the ΔH_r , ΔG_r and K_{eq} at 6000 K and 3000 K of the proposed reactions.

$$\Delta H_{\text{reaction}}^0 = \Sigma \Delta H_f^0(\text{products}) - \Sigma \Delta H_f^0(\text{reactants}) \quad (3.1)$$

$$\Delta G_{\text{reaction}}^0 = \Sigma \Delta G_f^0(\text{products}) - \Sigma \Delta G_f^0(\text{reactants}) \quad (3.2)$$

$$K_{eq} = e^{-\Delta G^0/RT} \quad (3.3)$$

Table 3-4 The Standard enthalpy change (ΔH_r), Gibbs free energy change (ΔG_r), and equilibrium constant (K_{eq}) for the proposed reaction channels.

Reaction	ΔH_r (kJ/mol)		ΔG_r (kJ/mol)		K_{eq}	
	6000 K	3000 K	6000 K	3000 K	6000 K	3000 K
(1)	-770.387	-769.854	930.927	-387.964	1.136	5.7E+6
(2)	218.311	195.232	210.979	169.928	0.064	0.001
(3)	-160.607	-164.126	-1090.64	-159.277	23.198	593.41
(4)	57.704	31.106	-879.658	10.651	1.485	0.652
(5)	-505.07	-490.36	-722.128	-440.189	2.2E+3	4.6E+7
(6)	-1103.26	-1072.97	528.219	-1000.41	9.8E+7	2E+17
(7)	-609.78	-605.728	2021.56	-228.687	0.048	9.6E+3

As evident from **Table 3-4**, reactions (1), (3), (5), (6) and (7) are exothermic in nature ($\Delta H_r < 0$) while the reactions (2) and (4) are endothermic in nature ($\Delta H_r > 0$). As mentioned earlier, CN is formed during the laser ablation (LA) process by collisions of C neutrals with N neutrals and N₂ molecules (from the ambience). As can be seen from Table 3, reaction (1) strongly favours the formation of CN by the recombination of C and N ($1.1 @ 6000\text{K} < K_{eq} < 5.7\text{E}+6 @ 3000\text{K}$). Reaction (3) also supports the formation of CN

with C_2 and N recombining ($23 @6000K < K_{eq} < 593 @3000K$). The reaction of C and C_2 with atmospheric nitrogen N_2 to form CN seems to be in equilibrium as their K_{eq} ranges between 0.06 to 0.001 and 1.4 to 0.65, respectively. Consequently, the formation of CN is more favourable via the reaction of C and C_2 with N. Reaction 6 is strongly exothermic ($\Delta H < 0$) and as temperature decreases from 6000 K to 3000 K, the K_{eq} increases exponentially. Similarly, reaction 5 also leads to consumption of C_2 . The formation of C_2 by recombination of C atoms with the assistance of an intermediate, is favored [K_{eq} (reaction 7) increases by 3 orders, whereas K_{eq} (reaction 6) increases by 8 orders] but the reaction (5) and (6) are competing with reaction (7). The increase in negative ΔG_r value, with decrease in temperature also shows that the reaction 7 is spontaneous and favors the formation of C_2 . Thus, the thermo-dynamical quantities play a key role in the CN and C_2 formation pathways in laser induced plasma (LIP) and emphasizes the importance of plume dynamics and plasma chemistry.

3.3.5 Trends in the CN, C_2 peaks in fs-LIBS spectra for (i) para series and (ii) ortho series

Table 3-5 Trend of CN and C_2 line integrated intensity ratio with fs and ns excitation in air.

Functional group	Para	CN/ C_2	Ortho	CN/ C_2	Para	CN/ C_2	Ortho	CN/ C_2
	Fs excitation (air)				Ns excitation (air)			
-Me	A1	5.48 ± 0.12	A4	4.94±0.28	A1	10.41±0.32	A4	11.43±0.24
-OMe	A2	8.26 ± 1.05	A5	10.34±0.03	A2	14.82±0.35	A5	15.09±0.33
-NH ₂	A3	10.36±0.35	A6	6.48±0.62	A3	17.23±0.84	A6	13.54±0.18

The molecular emission intensities can also depend on the number of substituent groups, as revealed from our earlier studies [42] on nitroimidazoles. The nitro group, by way of resonance and inductive effect (which act synergistically), drains out the electrons from the ring, making it easily susceptible to atomization. As a consequence, the CN emission intensity was higher than the C_2 intensities and the CN/ C_2 ratio was observed to increase with the number of electron withdrawing nitro groups [44]. In the present work, we attempted to understand how the nature of the substituents and their position influence the C_2 and CN emission intensities in the triazole-substituted nitroarene series. The trend in CN/ C_2 ratio (obtained with the both fs and ns excitations in air) as we move across the

Chapter 3

series A1-A3 and A4-A6, which have different functional groups (Me, OMe, NH₂) at para and ortho positions respectively, is illustrated in **Table 3-5**. It may be noted that CN/C₂ has the similar trend in both cases.

(i) Trend in CN/C₂ ratio of the para series:

The CN/C₂ emission intensity ratio within the para series followed the trend of A1 < A2 < A3 i.e. A3 had maximum tendency to atomize vis-a-vis fragmentation. This implies that there was extensive delocalization of electron density within the aromatic ring resulting in more canonical forms for A3 as compared to A2, A1. As discussed above, the delocalization of π -electrons arises primarily from the presence of electron withdrawing –NO₂ groups. All the triazole-substituted nitroarene compounds used in this study have the same number of nitro groups and only differ in the type of substituent at ortho and para positions. Therefore, it is these substituents Me, OMe, –NH₂ which play a crucial role in destabilizing the aromatic ring. The electron releasing –Me group pushes some electron density into the ring. Therefore, the pi electron cloud in the aromatic ring gets localized thus increasing the probability for fragmentation (i.e. more C₂ formation). It is the C-C and C=C bonds in the phenyl ring which will be instrumental in C₂ formation since the triazole ring is devoid of C-C or C=C linkages. When –Me is replaced by –OMe group, it is expected that the comparatively stronger electron releasing –OMe group will limit the extent of delocalization of the ring π -electron cloud. However, ‘O’ atom due to its electronegative character, pulls away the electrons leading to reduction in electron density in the phenyl ring. This facilitates delocalization of π -electrons within the ring and increases the chances of atomization leading to a higher CN/C₂ ratio. In case of the –NH₂ group (maximum electron releasing tendency amongst the three functional groups) as the substituent, it is expected that the extent of delocalization will be drastically reduced. Additionally, (as discussed above), due to the electron withdrawing effect of the N atom (less electronegative than O of OMe), a small fraction of electron density may be withdrawn towards the amino group, thereby allowing for more delocalization of the ring π -electron cloud. However, another important factor that needs to be considered here is the H-bonding (intra and inter molecular) involving the –NH₂ group and the –NO₂ groups on either side of it [45]. Since the lone pair electrons on N participate in H-bonding, they will not be available for coupling with the π -electron cloud of phenyl ring. This further promotes π -electron delocalization thereby increasing the probability of atomization.

Thus the $-\text{NH}_2$ substituted compound (A3) exhibits the highest CN/C₂ ratio among the para isomers.

(ii) Trend in CN/C₂ ratio of the ortho series:

For the ortho series, the CN/C₂ emission intensity ratio followed the trend $A4 < A6 < A5$. But for the positions of A6 and A5, this trend is like that observed in the para series. The CN/C₂ ratio for A6 which has $-\text{NH}_2$ group in ortho position is lower than A5. This can be attributed to the reduction in the extent of intramolecular H-bonding (as there is only one $-\text{NO}_2$ group adjacent to the $-\text{NH}_2$ group). Hence, unlike the para case, the lone pair electrons of N are now available for coupling with π -electron cloud of phenyl ring. The delocalization of ring π -electrons is then restricted. Furthermore, unlike the O-atom (of $-\text{OMe}$) whose electronegativity is higher than N-atom (of $-\text{NH}_2$ group), the latter cannot effectively withdraw electron density from the ring, thus further restricting delocalization. Therefore, A6 possibly exhibited greater probability of fragmentation (i.e. less atomization) compared to A5.

(iii) Trend in CN/C₂ ratio with respect to position of the substituent (para Vs ortho)

The observed variation in CN/C₂ between A1 versus A4 and A2 versus A5 could be within experimental error margin, we therefore, refrain from commenting on this. On the other hand, A3 displayed a significantly higher CN/C₂ ratio compared to A6. In other words, the presence of amino group in para position makes the molecule more vulnerable to atomization. The intra-molecular H-bonding [45] involving the lone pair electrons on $-\text{NH}_2$ group and the adjacent $-\text{NO}_2$ group (one on either side of the $-\text{NH}_2$ group) minimizes the chances of coupling of lone pair electron with the ring π -electron cloud. Since delocalization is facilitated, atomization is favored over fragmentation, thus giving rise to a higher CN/C₂ ratio for A3 as compared to A6.

3.3.6 CN and C₂ vibrational temperatures

The vibrational temperature of CN and C₂ molecular bands in the spectral region 375-390 nm and 500-520 nm respectively was calculated by using Nelder-Mead algorithm (NMT), developed by Parigger et.al, at the University of Tennessee Space Institute. This program computes theoretical spectra for the selected diatomic molecular transitions and wavelength regions (CN Violet, C₂ Swan, TiO, AlO bands) by using

Chapter 3

accurate line strengths (Hönl-London) factors, along with temperature and full-width half maximum (FWHM) values as inputs. It uses Boltzmann equilibrium spectrum program (BESP) that allows to evaluate a spectrum of free spontaneous emission from a diatomic gas in thermal equilibrium using a table of line widths for a specified diatomic transition. In the sense, out of several large number of molecules, some of the molecules are in the excited state. It assumes that there are several line transitions (either rotational or vibrational) within the spectrometer resolution (0.1 nm) and fit the spectrum by multi peak Gaussian fit. NMT uses BESP as a subroutine to fit the experimental diatomic emission spectrum by minimizing the difference between computed and experimentally recorded spectrum, in the least square sense, and provides the temperature. The calculated vibrational temperatures (with error less than 10% in most of the cases) in both the schemes are tabulated in **Table 3-6**.

Figures 3.7(a) and 3.7(b) depict the theoretical fits of CN and C₂ molecular emissions in the spectral region of 375-390 nm and 500-520 nm from a typical LIBS spectrum of A3 obtained with fs pulses in air. Likewise, **figures 3.7(c) and 3.7(d)** depict theoretical fits of CN and C₂ molecular emissions from a typical ns LIBS spectrum of A3 obtained in air and **figures 3.7(e) and 3.7(f)** in the argon environment. The figures also show the difference between experimental data and theoretical fit obtained from NMT algorithm. From the **Table 3-6** it is evident that the vibrational temperature of CN molecular emissions is least in the case of femtosecond excitation (in air) and highest in the case of ns excitation in argon environment. This could be in relation that the plasmas produced with fs pulses are cooler in comparison to plasmas produced with ns pulses. However, in the ambient air, it is observed that the vibrational temperature of C₂ molecular band is higher than vibrational temperature of CN in case of fs ablation and vice-versa in the case of ns ablation. This observation could be related to the major formation pathway of C₂ species i.e. the fragmentation as CN/C₂ ratio is more in case of fs ablation to that of ns ablation in all samples as seen from **Table 3-5**. Higher CN and C₂ vibrational temperatures in argon environment could be due to less thermal conductivity and higher density of argon gas (0.017 W m⁻¹K⁻¹, 1.66 kg/m³) in comparison to air (0.026 W m⁻¹K⁻¹, 1.18 kg/m³) [38]. The higher thermal conductivity of ambient air leads to the faster cooling of plasma owing to the higher transfer of heat. Since, argon has the low

thermal conductivity compared to air, the lifetime of plasma in argon atmosphere increases.

Table 3-6 Vibrational temperatures of CN and C₂ molecular bands calculated using NMT algorithm with both fs (air) and ns (air, argon) excitations.

Sample	Fs(air)		Ns (air)		Ns (Argon)	
	CN (K)	C ₂ (K)	CN (K)	C ₂ (K)	CN (K)	C ₂ (K)
A1	6577±73	7164±506	7429±40	5173±307	8598±158	10368±624
A2	6615±346	7398±40	8716±298	6013±158	9588±756	7327±1347
A3	6919±206	8407±764	8734±370	5940±359	10871±738	7815±152
A4	6660±111	7509±363	9275±71	6468±45	10447±502	10356±911
A5	6630±53	7864±36	8503±182	5651±232	9877±153	9986±281
A6	6460±179	7213±154	9472±247	6617±505	10552±181	9848±1017

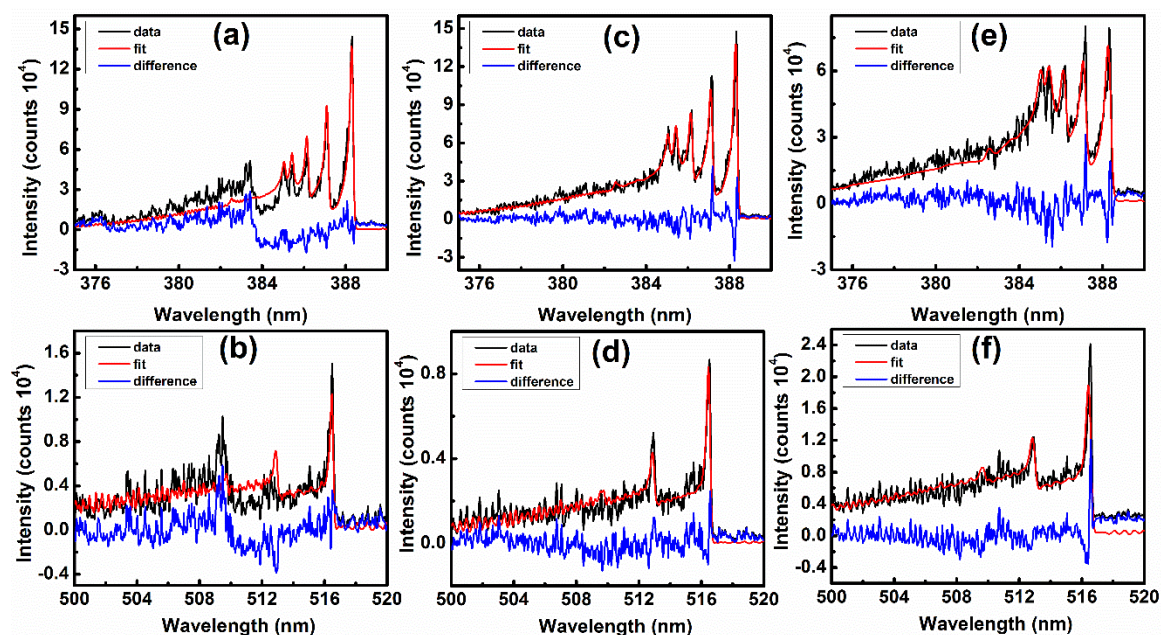


Figure 3.7 Difference between theoretical fits and experimental data of CN/C₂ molecular bands obtained from NMT algorithm in (a, b) air with fs pulse excitation, (c, d) air with ns excitation and in (e, f) argon ns excitation.

3.3.7 Correlation of energetic parameters

Globally, there is a continuous research focused on synthesis of advanced novel HEMs with increased density, diminished toxicity and increased explosive performance i.e. high positive heat of formation (H.O.F), possessing high heat of explosion (Q) resulting in high velocity of detonation (V.O.D) and detonation pressure (D.P.) [65–68]. Velocity of

Chapter 3

detonation (m/s) refers to the rate of propagation of the detonation front and detonation pressure (GPa) refers to the pressure that exists at the shock wave-medium interface as the shock wave travels through the medium. V.O.D and D.P. are linearly proportional to the density of a high energy material. A general approach for the estimation of CHNO explosives is to use Kamlet–Jacobs (K-J) equations shown in equation (3.4) and (3.5) [69].

$$D (km s^{-1}) = 1.01 (NM^{0.5}Q^{0.5})^{0.5} (1 + 1.30 \rho) \quad (3.4)$$

$$P (G Pa) = 15.58 N \rho^2 M^{0.5} Q^{0.5} \quad (3.5)$$

Where D is velocity of detonation, P is detonation pressure, ρ is the loading density, N represents the number of moles of gaseous detonation products per gram of explosive, M is the average molecular weight of the gases and Q is the heat of explosion in Cal g⁻¹. However, It is not always possible to experimentally measure V.O.D and D.P. of a new energetic sample as it requires a detonation chamber, testing apparatus and various dynamic methods based on different physical principles [70]. Therefore, a few advanced computer based algorithms such as CHEETAH, EXPLO5 were designed and are now extensively employed to predict various performance parameters of new explosive molecules as well as metal-containing explosives, which accurately predicts the detonation performance (better than the K-J equations) [71,72]. Recently, even V.O.D and D.P. used in this work were obtained using the EXPLO5 version 6.02 at standard conditions, i.e. 298 K temperature and 1 bar pressure assuming that atmospheric gases do not react with the molecule during the detonation.

The chemical energy of detonation (C.E.D.) or heat of explosion is denoted by Q. It is and defined as the energy in kcal released by 1 kg of explosive at constant volume. The heat of explosion provides information about the work capacity of the explosive. Oxygen balance is an important property of explosive which indicates the degree to which an explosive can be oxidized. A deficiency of oxygen within the molecule may end up with CO or NO gases which are toxic. Thus, there must be enough oxygen available within the sample to convert all its carbon, hydrogen and nitrogen to stable products such as carbon dioxide, water and nitrogen dioxide. In this case the molecule is said to have zero oxygen balance. In case the molecule is oxygen deficient, then it is termed as negative oxygen balanced and if oxygen is surplus to that required then the molecule is

termed as positive oxygen balanced. Oxygen balance of an explosive ($C_xH_yN_wO_z$) where total C is converted into CO_2 was calculated as per equation (3.6).

$$O.B. (\%) = \frac{1600 \left(z - 2x - \frac{y}{2} \right)}{\text{Molecular weight}} \quad (3.6)$$

For laboratory studies, the detonation products of the explosive molecules were computed using EXPLO5. C, CO, CO_2 , N_2 , H_2O etc., emerged as the major detonation products while NO, CH, HCN, NH_2 were the minor products. Products (species) observed in LIBS spectra includes C, CO, CH, CN, C_2 , N_2^+ , NO, NH, N, O, H etc. It needs to be mentioned here that in real-time detonations numerous varieties of species can be expected. However, our aim in this study is to correlate the detonation parameters of a molecule with the LIBS signals observed. Johnson et al. [73] have studied extremely short detonation interaction events in reactive materials such as aluminium, magnesium and boron with PBX-N9 pellets by simultaneous imaging and spectroscopy. Recently Farhadian et al. [74] used CN and AlO molecular band emissions to investigate the aging of high energy materials. Rezaei et al. [75] have correlated detonation parameters such as heat of formation (H.O.F), velocity of detonation (V.O.D) of aluminium based RDX explosives with Al/O ratios and shown that molecular to atomic ratios can be used to understand the trend of energetic parameters. Recently, they [76] have again utilized LIBS technique to investigate plastic-bonded explosives (PBX) with varying Al concentration and reported that, by considering CN/C_2 , PBX with Al content of 15% is found to have the optimum velocity of detonation of the RDX/Al/HTPB standard samples. To evaluate the performance of the explosives (triazole-substituted nitroarenes), we have attempted to correlate the detonation parameters viz. O.B., V.O.D., D.P. and Q with CN/C_2 and $(CN+C_2)/(C+H+N+O)$ ratios.

Figures 3.8(a)-(d) and 3.8(e)-(h) depict the correlation of energetic parameters viz., oxygen balance (O.B., %), velocity of detonation (V.O.D, ms^{-1}), detonation pressure (D.P., G Pa), and heat of detonation (Q, $Cal\ g^{-1}$) with respect to CN/C_2 ratio and MSAS ratio, $(CN+C_2)/(C+H+N+O)$ respectively in ns LIBS spectra recorded in air. The integrated intensities of C at 247.8 nm, H at 656 nm, N at 746 nm and O 777.2 nm, CN at 388.34 nm, C_2 at 516.4 nm were used to calculate CN/C_2 and $(CN+C_2)/(C+H+N+O)$ ratios. As seen in **figures 3.8(a)-3.8(d)** a strong linear correlation was observed between CN/C_2 ratio and the explosive parameters in the case of para isomers with ns excitation in

Chapter 3

air; the ortho isomers on the other hand exhibited inferior correlation. The correlation between MSAS ratio and the detonation parameters was even worsened as evident **figures 3.8(e)-3.8(h)** in the case of both para and ortho isomers with ns excitation in air. Such poor correlations could be ascribed to the intrusion of air and the uncontrolled reactions between plasma and air constituents as discussed earlier. **Figures 3.9(a)-(d) and 3.9(e)-(h)** depict the correlation of energetic parameters with respect to CN/C₂ ratio and MSAS ratio, (CN+C₂)/(C+H+N+O) respectively in ns LIBS spectra recorded in argon ambiance. As seen in **figures 3.9(a)-(d)** a moderate linear correlation was observed between CN/C₂ ratio and the explosive parameters in the case of both para and ortho isomers with ns excitation in argon. A strong linear correlation was observed between MSAS ratio and the explosive parameters in the case of para isomers with ns excitation as evident from **figures 3.9(a)-(d)**; whereas slightly moderate correlation was observed in the case of ortho isomers. **Figures 3.10(a)-(d) and 3.10(e)-(f)** depict the correlation of energetic parameters with respect to the CN/C₂ ratio and the MSAS ratio, (CN + C₂) / (C + H + N + O), respectively. A strong linear correlation was observed between the CN/C₂ ratio and the explosive parameters as observed from **figures 3.10(a)-(d)** in the case of para isomers with fs excitation in air; the ortho isomers on the other hand exhibited inferior correlation [see discussion in section 3.3.5]. As seen from **figures 3.10(e)-(h)** very good correlation of energetic parameters with the MSAS ratio, (CN + C₂) / (C + H + N + O) was obtained with fs excitation, in both the ortho and para series with a maximum of 10–15% error. This error could probably be due to the weak intensities of atomic lines corresponding to H and N. We strongly feel that such correlation would towards the evaluation/prediction of the performance of an unknown energetic material, when investigated in similar conditions. Further, the possibilities with fs pulses of delivering over long distances makes it attractive even for standoff detection. In future, we wish to utilize this correlation data along with other statistical techniques and time-resolved data concurrently to explore the possibility of unambiguous discrimination of these compounds. Our results also open a new avenue wherein the LIBS technique could possibly be used as a laboratory-scale technique to predict the energetic performance with minimal amount of the sample (~150 mg). For achieving this, comprehensive studies on standard energetic molecules and exhaustive correlation analyses are essential.

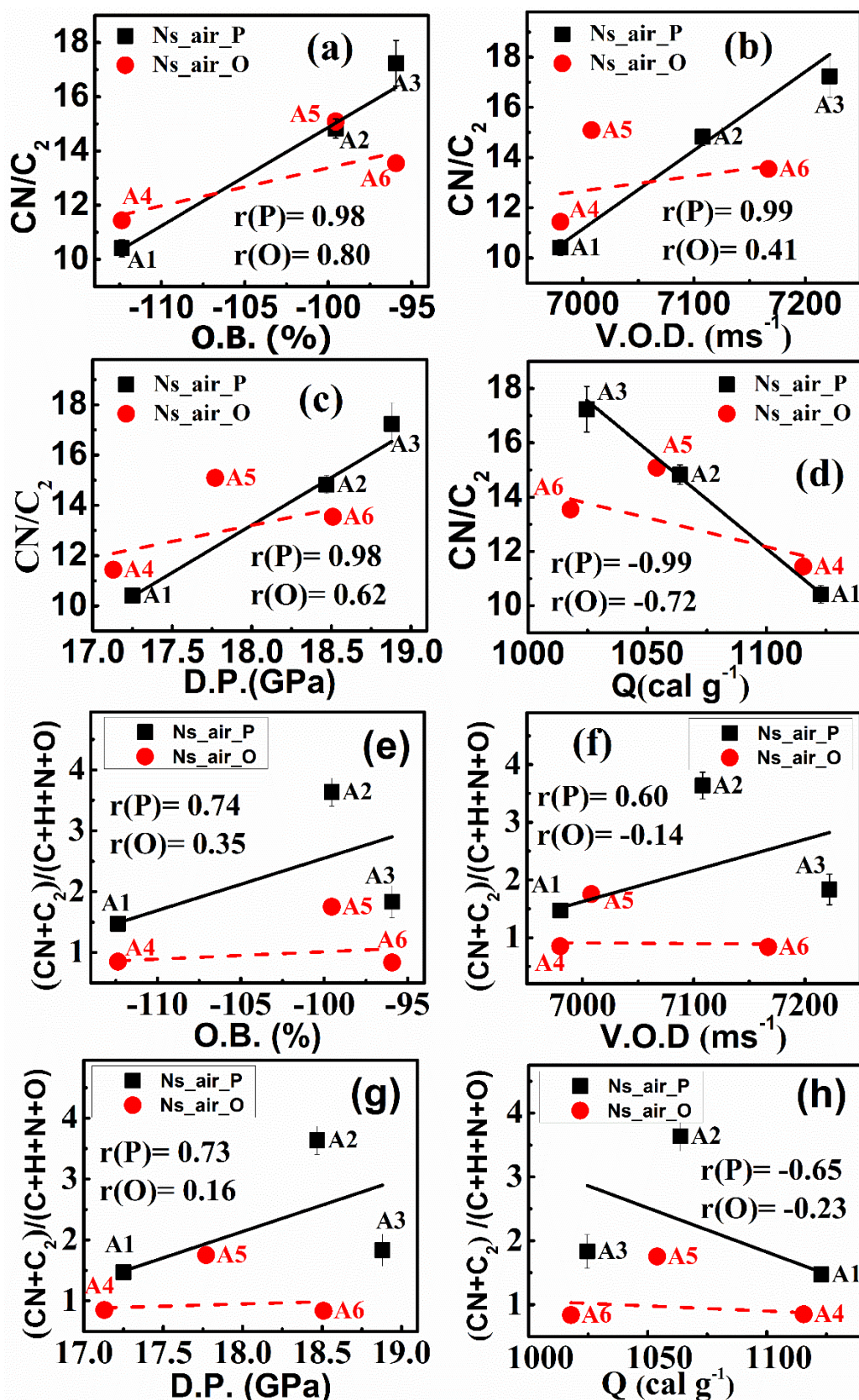


Figure 3.8 Correlation of CN/C_2 emission ratio (ns LIBS, air) and with respect to energetic parameters (a-d) (a) O.B. (b) V.O.D (c) D.P. (d) Q and correlation of $(CN+C_2)/(C+H+N+O)$ ratio (ns LIBS, air) with the energetic parameters (e-h) (e) O.B. (f) V.O.D (g) D.P. (h) Q.

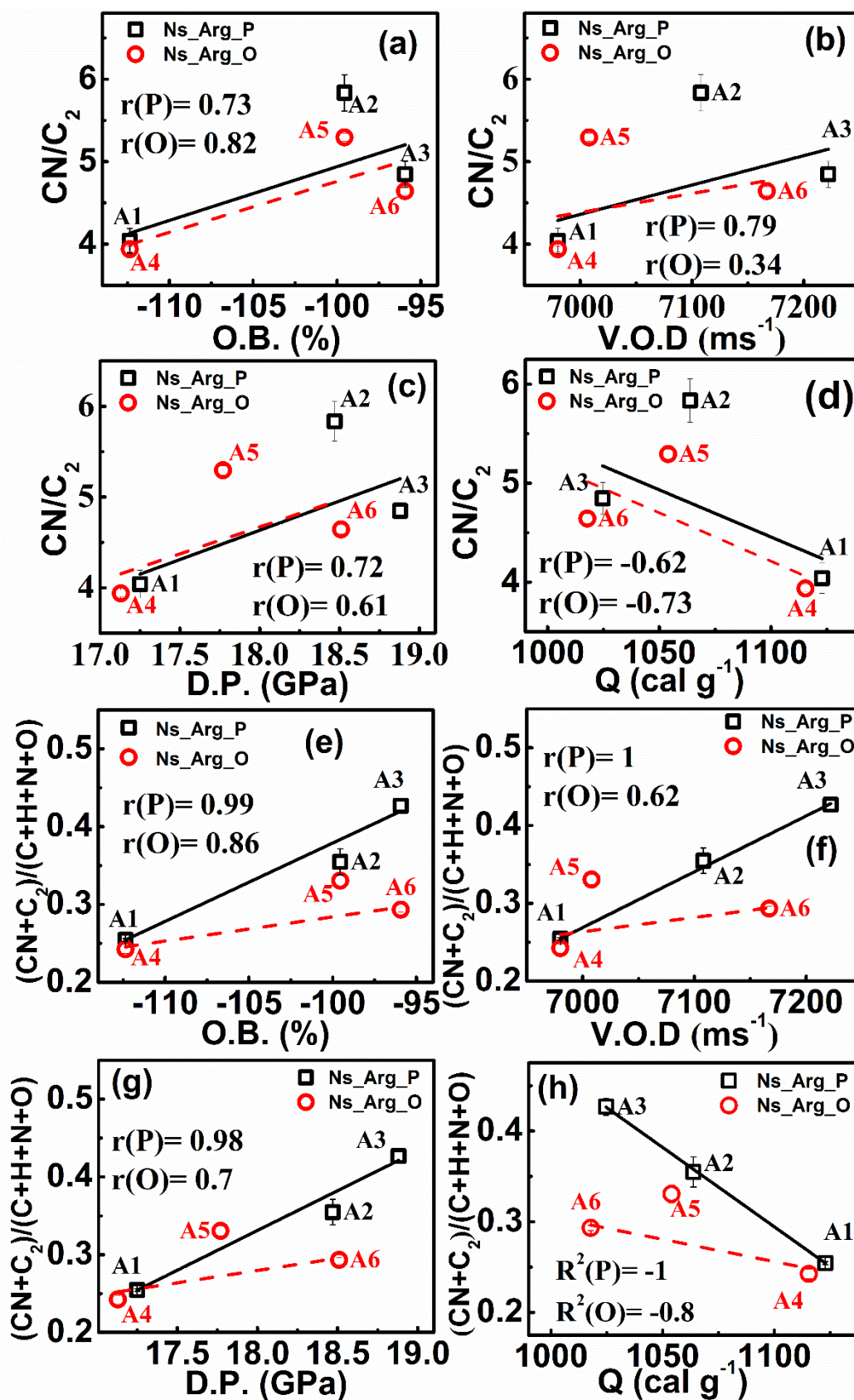


Figure 3.9 Correlation of CN/C_2 emission ratio (ns LIBS, argon) and with respect to energetic parameters (a-d) (a) O.B. (b) V.O.D (c) D.P. (d) Q and correlation of $(CN+C_2)/(C+H+N+O)$ ratio (ns LIBS, argon) with the energetic parameters (e-h) (e) O.B. (f) V.O.D (g) D.P.

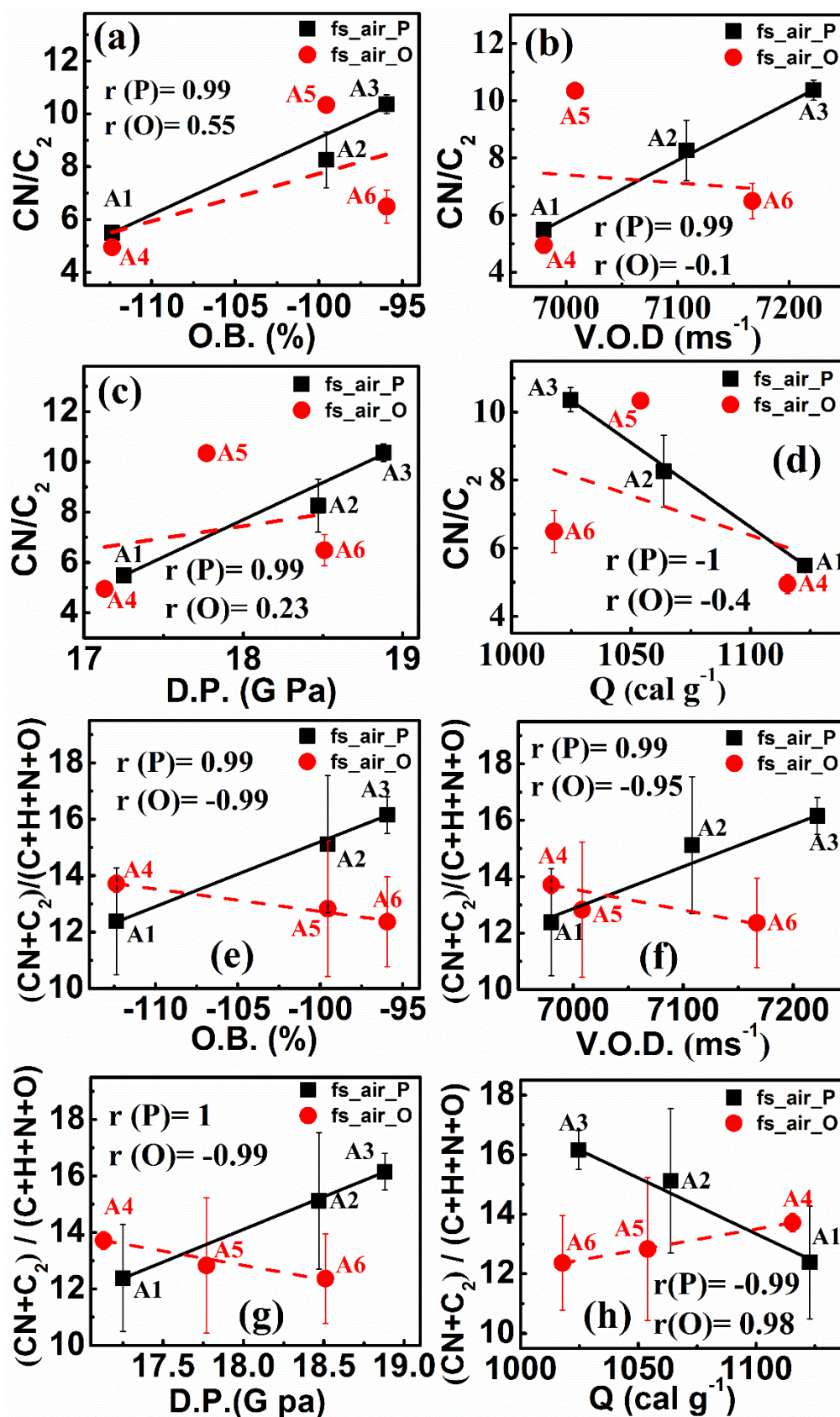


Figure 3.10 Correlation of CN/C_2 emission ratio (fs LIBS, air) and with respect to energetic parameters (a-d) (a) O.B. (b) V.O.D (c) D.P. (d) Q and correlation of $(CN+C_2)/(C+H+N+O)$ ratio (fs LIBS, air) with the energetic parameters (e-h) (e) O.B. (f) V.O.D (g) D.P. (h) Q.

3.3.8 Principal Component Analysis (PCA)

From the past decade LIBS technique has been regarded as one of a potential technique to detect trace amounts of explosives. Despite its high sensitivity the specificity or limited selectivity of this technique towards trace detection of explosives is a major concern owing to the ambiguous origin of molecular species. This leads to the non-fingerprint nature of LIBS technique towards explosive detection and further makes it challenging to classify or recognize them [77]. LIBS spectral analysis combined with chemometric techniques or multivariate data analysis (MVDA) techniques enhances the accuracy in discrimination of samples compared to the standard ratiometric approaches, where ratios of neutral and ionic species are utilized in the latter case [78]. Usage of such chemometric techniques is crucial to identify the explosive residues on organic materials such as plastics [79,80] and envelopes [77]. Principal component analysis (PCA) is a simple, unsupervised powerful chemometric technique which is capable of grouping or classifying various materials by correlating their spectral features. PCA has been used in various fields such as face recognition and image processing [81], drugs, pharmaceutical tablets analysis [4], soil analysis and explosive discrimination owing to its capability of finding patterns (the similarities and differences) in high dimensional data sets [82–85]. In this technique, original data set $X_{m \times n}$ [m observations (no. of spectra) and n variables (wavelengths)] is transformed in to a new data matrix $T (n \times m)$ through Eigen decomposition of covariance matrix of X with most of the information is stored in the first few dimensions. The eigen vectors obtained in this transformation have the essential features and referred as principal components (PCs). Each PCs represents the variance present in the data set and the amount of variance accounted by PCs decreases gradually among PCs with first PC being the highest. The representation of new matrix in the space of PCs provides us with classification or discrimination of the sample set through choosing (or looking at) an appropriate rotation (or orientation) allows us to visualize the underlying classification.

Recently, Porizka et al. [86] have summarized the progress that has been achieved by utilizing PCA by LIBS community for data analysis. They have also discussed approaches to use PCA in LIBS data processing. PCA has been used as a preprocessing technique to identify and filter the outliers as it enables to visualize the data matrix in lucid way in the space of PCs [87]. Wang et al. have used principal component analysis to

distinguish an organic explosive (TNT, trinitrotoluene) among plastics [88]. De Lucia et al. classified different explosive traces on organic explosives using PLS-DA and obtained high true classification rates (TCR) and low false classification rates (LCR) through selective data input models [89,90]. Gottfried et al. [91] demonstrated classification of *Bacillus subtilis* (a biological warfare agent) using PCA at a standoff distance of 20 m. Konstantynowski et al. [82] have utilized PCA to discriminate the response from metal oxide semiconductor gas sensor with various explosives and benign samples. PCA has also been used in conjunction with other explosive detection techniques such as laser photo acoustic spectroscopy (LPAS) [92] and Raman spectroscopy [93] to discriminate explosive traces. Though PCA accounts for total variance of the entire data set, it cannot describe the group-to-group variability and within the group variability. Moreover, being an unsupervised classification technique, the prediction and class labelling of unknown explosive materials is not possible. Therefore several other MVDA techniques such as Soft independent modelling of class analogies (SIMCA), partial least squares discriminant analysis (PLS-DA), K-nearest neighbor (KNN) [78], artificial neural network (ANN) [94] are developed and used in tandem to LIBS spectroscopy for class for classifying or class labelling of explosives. Gottfried et al. [27] have outlined various works that demonstrate the improved discrimination capability of LIBS by using the above mentioned chemometric techniques than the mere ratiometric analysis.

Throughout this thesis work, we have utilized the PCA for the dimensionality reduction of fs/ns LIBS multivariate data to cluster/group/classify various explosive molecules in near and standoff mode. Though there are several spectral normalization techniques/strategies used very often in preprocessing of LIBS data, such as mean centering, area normalization and total energy normalization etc., depending on various applications (sample matrices especially alloys and geological samples) employed by LIBS community [95,96], we have confined ourselves to the processing of impurities and normalize the spectrum with the maximum intensity. The 3D score plots in the space of first three PCs illustrate the degree of classification and the PCs represent the essential spectral features contributing for the classification. At the same time, PCA was utilized to discriminate metals and alloys, bimetallic targets and geological rocks in standoff mode using fs pulses. These results are discussed in chapter 4.

3.3.8.a Classification of fs LIBS spectra of triazoles in air using PCA

As discussed in experimental section, three fs LIBS spectra were recorded for each triazole molecule in the proximal LIBS setup. The LIBS spectra were similar with predominant CN and C₂ molecular transitions, strong C atomic transition and weak atomic transitions H, N, and O. The spectral emissions from the impurities such as Na and Ca were also identified. In the first attempt, the unprocessed fs LIBS spectra of triazoles were analyzed through PCA programme written in MATLAB code. **Figure 3.11(a)** illustrates the PC score plot illustrating the clustering/grouping of triazoles and **figure 3.11(b)** represents the first three PCs of unprocessed fs LIBS spectra of triazole derivatives obtained from PCA. PC1 (51 %), PC2 (25 %), PC3 (6 %) together accounted for 82% of the total variance present in the data set. Other PCs were neglected since the variance accounted by them was less and mostly consisted of noise. However, PC1 contributing for the classification has the Na emission lines 589.0 nm, 589.6 nm, 818.32 nm and 819.48 nm. It may also be noted that the spectral features present in the second PC (PC2) are the emission lines from other impurity elements such as Ca and Fe in addition in to the spectral features of energetic molecules. Therefore, the classification achieved in unprocessed spectra is significantly due to the emission lines from impurities. Femtosecond LIBS spectra were processed to remove the spectral emissions from impurities such as Na, Ca and Fe. The processed spectra were then analyzed using PCA program. **Figure 3.11(c)** illustrates the PC score plot and **figure 3.11(d)** represents the first three PCs of processed fs LIBS spectra of triazole derivatives obtained from PCA. First three PCs together account for 73 % (62%, 8%, and 3%) of variance. PC3 is mostly dominant with the noise and the essential spectral feature present in it is only CN. Despite the decrease in variance accounted from the first three PCs, from 82% to 73%, in the case of unprocessed to processed data, the clustering/grouping of triazoles is undoubtedly evident from **figure 3.11(c)** and importantly the significant spectral features contributing for classification are C, CN and C₂ emission lines. Thus, fs LIBS technique provides rapid identification/classification of energetic molecules when PCA was utilized in tandem.

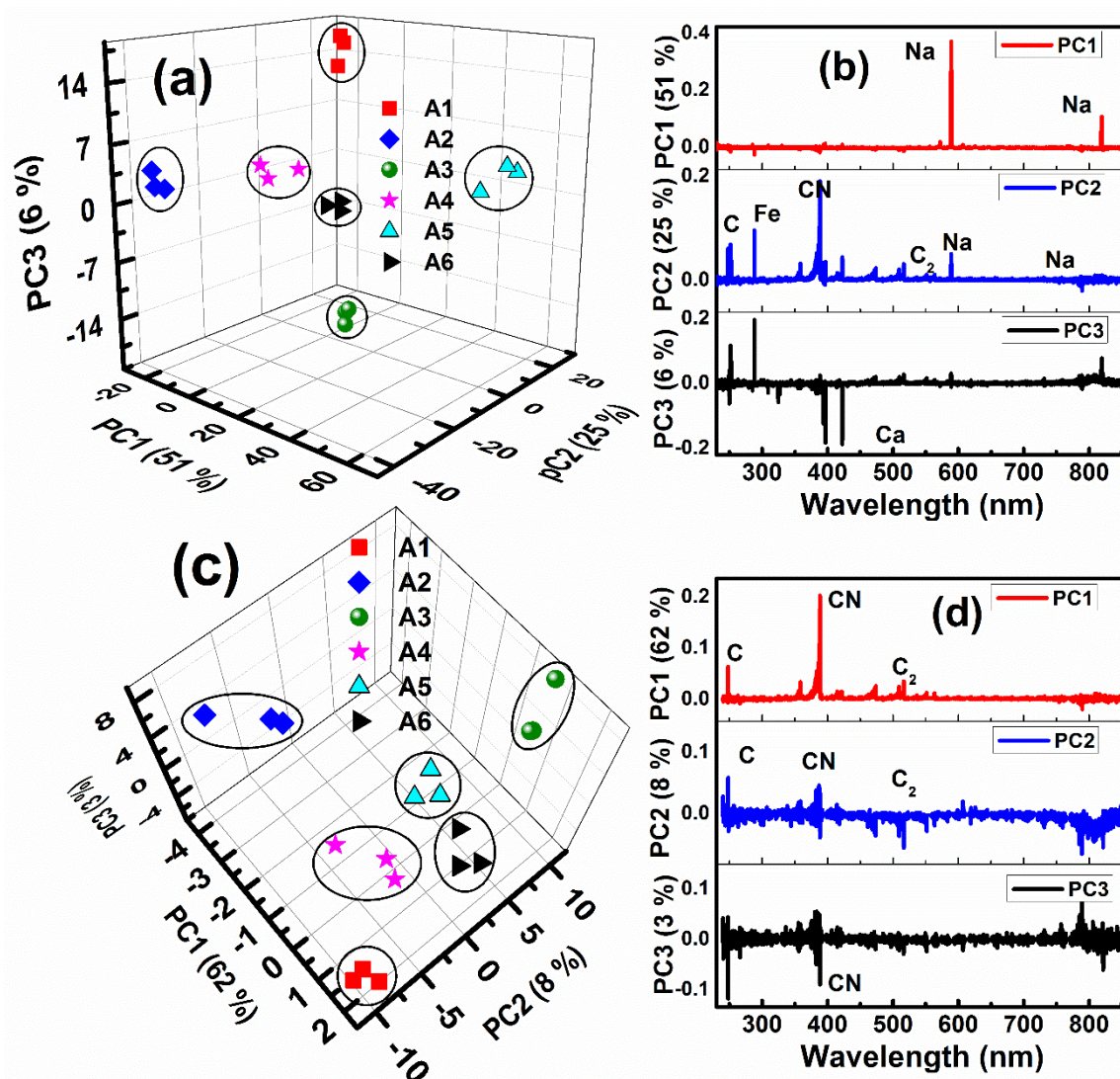


Figure 3.11 (a) PC score plot and (b) first three PCs of unprocessed fs LIBS spectra of triazole derivatives. (c) PC score plot and (d) first three PCs of processed (for removal of impurities such as Ca, Na, Fe) fs LIBS spectra of triazole derivatives. The variance in the data set accounted by each PC is given in parentheses.

3.3.8.b Classification of ns LIBS spectra of triazoles in air using PCA

A large number of LIBS spectra (20-30) of all triazole derivatives (A1-A6) were recorded in the case of ns LIBS experiments in both air and argon environments. These spectra were processed to eliminate the spectral emissions from impurities such as Na, Ca and Fe. Further the processed spectra were also normalized to the maximum intensity prior to PCA. Normalization of the spectra relatively increases the significance of weak spectral features and conduit to improved discrimination between the emission lines and the noise present in the LIB spectra. Furthermore, normalization of the spectra also mitigates of effect of signal fluctuation present in the spectrum [95].

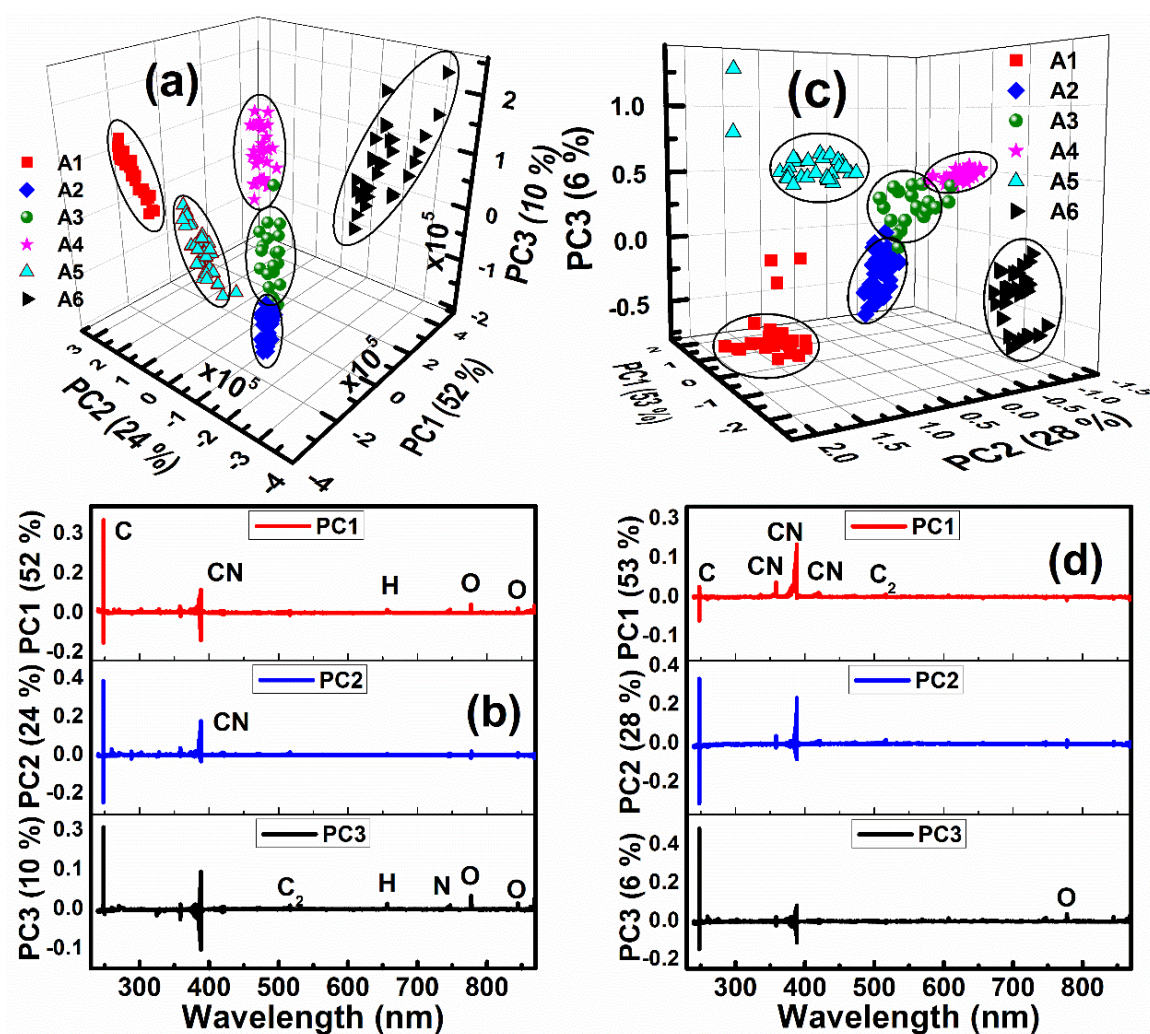


Figure 3.12 (a) PC score plot and (b) first three PCs of processed (for removal of impurities such as Ca, Na, Fe) ns LIBS spectra of triazole derivatives recorded in air. (c) PC score plot and (d) first three PCs of processed and normalized ns LIBS spectra of triazole derivatives. The variance in the data set described by each PC is given in parentheses.

Figure 3.12(a) illustrates the 3D PC score plot and **figure 3.12(b)** depicts the important spectral features contributing for the classification in the first three PCs of processed ns LIBS spectra of triazole derivatives recorded in air obtained from PCA analysis. First three PCs together accounted for 91% (PC1 52%; PC2 24%; PC3 10%) of variance present in the data. Likewise, **figure 3.12(c)** and **figure 3.12(d)** show the 3D score plot and first three PCs obtained from analyzing normalized ns LIBS spectra recorded in air with first three PCs describing the total variance of 87% (53%, 28%, and 6%) present in the data set. There was not much visual improvement as seen in 3D score plots [figures 13.2(a) and 13.2(c)]. However, the normalization has certainly led to the change in essential spectral features contributing for the classification. PC1 of un-normalized spectra (figure 13.2(b)) has spectral features from C, CN and other atomic

elements (H, N, and O) whereas PC1 of normalized spectra (figure 13.2(d)) has CN molecular emissions as dominant spectral features compared to C atomic emission.

3.3.8.c Classification of ns LIBS spectra of triazoles in argon using PCA

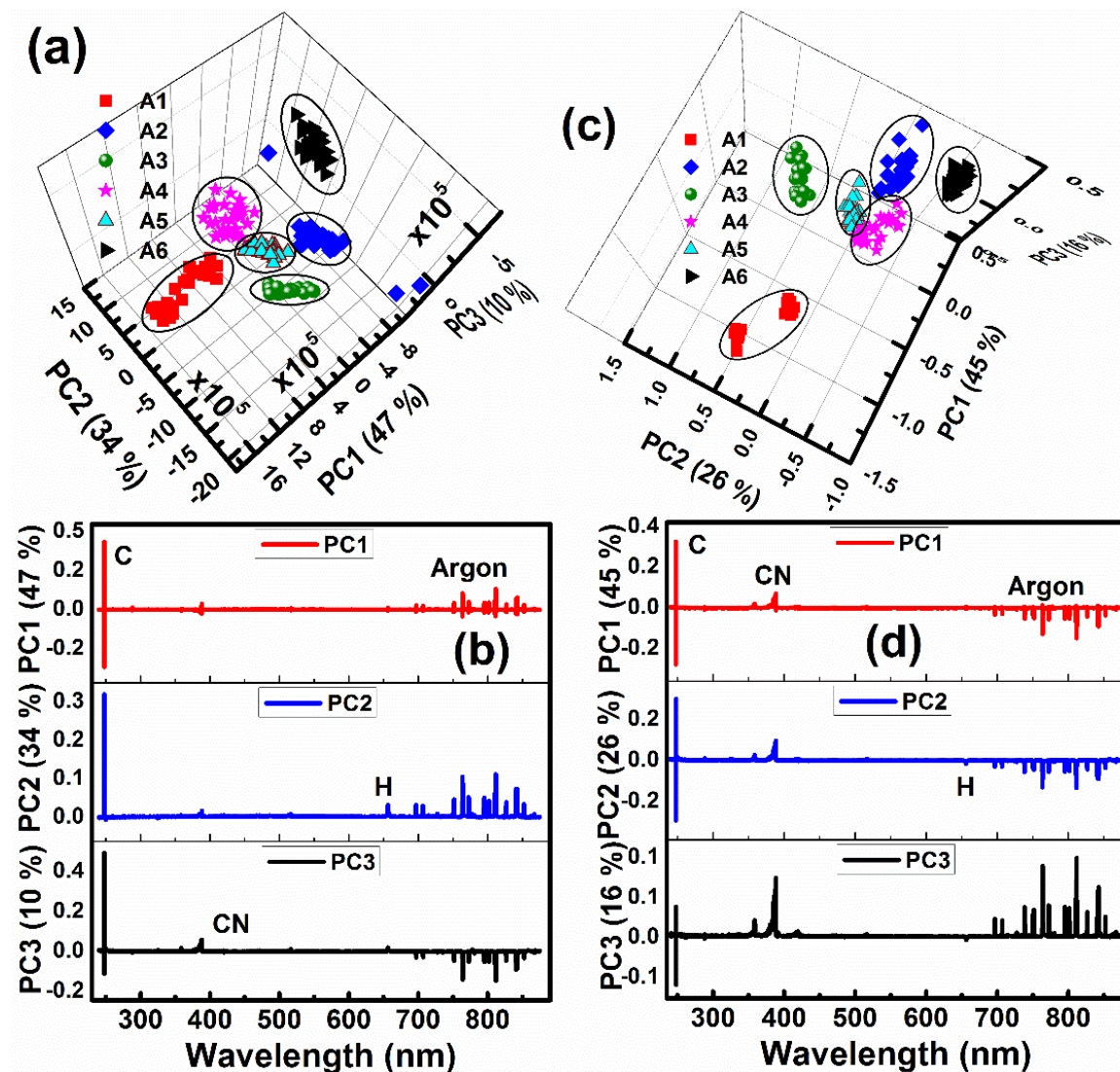


Figure 3.13 (a) PC score plot and (b) first three PCs of processed (for removal of impurities such as Ca, Na, Fe) ns LIBS spectra of triazole derivatives recorded in argon. (c) PC score plot and (d) first three PCs of processed and normalized ns LIBS spectra of triazole derivatives recorded in argon. The variance in the data set accounted by each PC is given in parentheses.

Figure 3.13(a) illustrates the 3D PC score plot and **figure 3.13(b)** depicts the first three PCs obtained from PCA analysis of processed (for removal of impurities such as Ca, Na, Fe) but un-normalized ns LIBS spectra recorded in argon. PCs represent the significant spectral features resulting in classification/discrimination. First three PCs together account for 91% (PC1 47%; PC2 34%; PC3 10 %) of variance present in the data. **Figures 3.13(c)** and **figure 3.13(d)** illustrate the PC score plot and the first three

Chapter 3

PCs obtained from PCA analysis of processed (for removal of impurities such as Ca, Na, Fe) and normalized ns LIBS spectra recorded in argon. First three PCs together accounted for 87% (PC1 45%; PC2 26%; PC3 16 %) of total variance present in the data.

3.4 Conclusions

- Novel, in-house synthesized energetic molecules (triazole-substituted nitroarene derivatives with Me, OMe, NH₂ functional groups) were investigated by fs and ns-LIBS technique with an intention to elucidate the role played by substituents on the spectral emission signatures in LIBS. CN, C₂ molecular bands were identified along with atomic lines corresponding to C, H, N and O. Molecular signatures were prominent in femtosecond LIB spectra whereas atomic emission lines dominated the ns-LIB spectra. The formation pathways for CN and C₂ species as well as the correlation of emission intensities with C-C, C=C, C-N, C=N bonds and %O were investigated using the fs and ns LIBS data recorded in air and argon. These studies revealed that in case of ablation with fs pulses, CN species were formed mostly from native CN bonds while C₂ species were formed mostly from fragmentation of C-C, C=C bonds. However, in case of ablation with ns pulses, CN and C₂ are formed from other secondary sources as well. Further, scavenging of C₂ species by O from the ambience was also evident.
- We had also investigated the trend in CN/C₂ ratio across the structural and functional isomers of triazole substituted nitroarenes, which revealed the significant impact of the type and position of substituents on the spectral emission signatures. The substituents, Me, OMe, and NH₂, in order of increasing electron releasing tendency, served to increase the electron density in the ring thus limiting the extent of delocalization of the π -electron cloud in the aromatic ring. On the other hand, the electronegative 'O' atom (in OMe) and N atom (in NH₂) pulled away the electrons leading to reduction in electron density in the aromatic ring, thus facilitating delocalization of pi electrons and increasing the chances of atomization (i.e. higher CN/C₂ ratio). Further, we concluded that the position of the -NH₂ group played a crucial role in the stability of the aromatic ring. When the -NH₂ group was in para position, the extensive H-bonding (intramolecular) with -NO₂ groups on either side, prevented the lone pair electrons on N from coupling with the π -electron cloud of

aromatic ring thus promoting π -electron delocalization and increasing the probability of atomization.

- The ratio of $(\text{CN}+\text{C}_2)/(\text{C}+\text{H}+\text{N}+\text{O})$ obtained with fs excitation in air correlated very well with energetic parameters (O.B., V.O.D, D.P., C.E.D.) for both the ortho and para series. Our detailed studies concluded that the MSAS ratio can, therefore, be a reliable performance metric for energetic compounds.
- Fs/ns LIBS data coupled with principal component analysis (PCA) was successfully exploited for the classification of energetic materials.

3.5 References

1. D. A. Cremers and A. K. Knight, *Laser- Induced Breakdown Spectroscopy* (Wiley Online Library, 2006).
2. J. P. Singh and S. N. Thakur, *Laser-Induced Breakdown Spectroscopy* (Elsevier, 2007).
3. F. J. Fortes, J. Moros, P. Lucena, L. M. Cabalín, and J. J. Laserna, "Laser-induced breakdown spectroscopy," *Anal. Chem.* **85**(2), 640–669 (2012).
4. A. K. Myakalwar, S. Sreedhar, I. Barman, N. C. Dingari, S. Venugopal Rao, P. Prem Kiran, S. P. Tewari, and G. Manoj Kumar, "Laser-induced breakdown spectroscopy-based investigation and classification of pharmaceutical tablets using multivariate chemometric analysis," *Talanta* **87**, 53–59 (2011).
5. P. Zheng, H. Liu, J. Wang, M. Shi, X. Wang, B. Zhang, and R. Yang, "Online mercury determination by laser-induced breakdown spectroscopy with the assistance of solution cathode glow discharge," *J. Anal. At. Spectrom.* **30**(4), 867–874 (2015).
6. D. W. Hahn and N. Omenetto, "Laser-induced breakdown spectroscopy (LIBS), part I: review of basic diagnostics and plasma–particle interactions: still-challenging issues within the analytical plasma community," *Appl. Spectrosc.* **64**(12), 335A–366A (2010).
7. S. J. Rehse, H. Salimnia, and A. W. Miziolek, "Laser-induced breakdown spectroscopy (LIBS): An overview of recent progress and future potential for biomedical applications," *J. Med. Eng. Technol.* **36**(2), 77–89 (2012).
8. D. W. Hahn and N. Omenetto, "Laser-induced breakdown spectroscopy (LIBS), part II: review of instrumental and methodological approaches to material analysis and applications to different fields," *Appl. Spectrosc.* **66**(4), 347–419 (2012).
9. R. Gaudiuso, M. Dell'Aglio, O. de Pascale, G. S. Senesi, and A. de Giacomo, "Laser induced breakdown spectroscopy for elemental analysis in environmental, cultural heritage and space applications: A review of methods and results," *Sensors* **10**(8), 7434–7468 (2010).
10. F. J. Fortes, S. Guirado, A. Metzinger, and J. J. Laserna, "A study of underwater stand-off laser-induced breakdown spectroscopy for chemical analysis of objects in the deep ocean," *J. Anal. At. Spectrom.* **30**(5), 1050–1056 (2015).
11. C. Lopez-Moreno, S. Palanco, J. Javier Laserna, F. DeLucia Jr, A. W. Miziolek, J. Rose, R. A. Walters, and A. I. Whitehouse, "Test of a stand-off laser-induced breakdown spectroscopy sensor for the detection of explosive residues on solid surfaces," *J. Anal. At. Spectrom.* **21**(1), 55–60 (2006).
12. P. D. Barnett, N. Lamsal, and S. M. Angel, "Standoff Laser-Induced Breakdown Spectroscopy (LIBS) Using a Miniature Wide Field of View Spatial Heterodyne Spectrometer with Sub-Microsteradian Collection Optics," *Appl. Spectrosc.* **71**(4), 583–590 (2017).
13. A. Bolshakov, "LIBS at work on Mars," <https://appliedspectra.com/mars-lib.html>.
14. J. S. Caygill, F. Davis, and S. P. J. Higson, "Current trends in explosive detection techniques," *Talanta* **88**, 14–29 (2012).
15. M. E. Farrell, E. L. Holthoff, and P. M. Pellegrino, "Laser-Based Optical Detection of Explosives," in *Laser-Based Optical Detection of Explosives* (CRC Press, 2015), pp. 1–8.
16. M. Baudelet, *Laser Spectroscopy for Sensing: Fundamentals, Techniques and Applications* (Elsevier, 2014).

17. B. Sallé, P. Mauchien, and S. Maurice, "Laser-Induced Breakdown Spectroscopy in open-path configuration for the analysis of distant objects," *Spectrochim. Acta B* **62**, 739–768 (2007).
18. R. Bogue, "Remote chemical sensing: a review of techniques and recent developments," *Sens. Rev.* **38**(4), 453–457 (2018).
19. F. J. Fortes and J. J. Laserna, "The development of fieldable laser-induced breakdown spectrometer: No limits on the horizon," *Spectrochim. Acta B* **65**(12), 975–990 (2010).
20. M. D. Aglio, J. J. Laserna, S. Longo, and A. De Giacomo, "Stand-off laser induced breakdown spectroscopy on meteorites: Calibration-free approach," *Spectrochim. Acta B* **147**, 87–92 (2018).
21. A. Couairon and A. Mysyrowicz, "Femtosecond filamentation in transparent media," *Phys. Rep.* **441**(2), 47–189 (2007).
22. S. S. Harilal, J. Yeak, B. E. Brumfield, and M. C. Phillips, "Consequences of femtosecond laser filament generation conditions in standoff laser induced breakdown spectroscopy," *Opt. Express* **24**(16), 17941–17949 (2016).
23. S. S. Harilal, J. Yeak, B. E. Brumfield, J. D. Suter, and M. C. Phillips, "Dynamics of molecular emission features from nanosecond, femtosecond laser and filament ablation plasmas," *J. Anal. At. Spectrom.* **31**(6), 1192–1197 (2016).
24. S. Tzortzakis, D. Anglos, and D. Gray, "Ultraviolet laser filaments for remote laser-induced breakdown spectroscopy (LIBS) analysis: applications in cultural heritage monitoring," *Opt. Lett.* **31**(8), 1139–1141 (2006).
25. S. S. Harilal, J. Yeak, and M. C. Phillips, "Plasma temperature clamping in filamentation laser induced breakdown spectroscopy," *Opt. Express* **23**(21), 27113 (2015).
26. J. L. Gottfried, F. C. De Lucia Jr., and A. W. Miziolek, "Discrimination of explosive residues on organic and inorganic substrates using laser-induced breakdown spectroscopy," *J. Anal. At. Spectrom.* **24**(3), 288–296 (2009).
27. J. L. Gottfried, F. C. De Lucia, C. A. Munson, and A. W. Miziolek, "Laser-induced breakdown spectroscopy for detection of explosives residues: A review of recent advances, challenges, and future prospects," *Anal. Bioanal. Chem.* **395**(2), 283–300 (2009).
28. I. Gaona, J. Serrano, J. Moros, and J. J. Laserna, "Range-Adaptive Standoff Recognition of Explosive Fingerprints on Solid Surfaces using a Supervised Learning Method and Laser-Induced Breakdown Spectroscopy," *Anal. Chem.* **86**(10), 5045–5052 (2014).
29. A. K. Myakalwar, N. C. Dingari, R. R. Dasari, I. Barman, and M. K. Gundawar, "Non-gated laser induced breakdown spectroscopy provides a powerful segmentation tool on concomitant treatment of characteristic and continuum emission," *PLoS One* **9**(8), e103546 (2014).
30. K.-Q. Yu, Y.-R. Zhao, F. Liu, and Y. He, "Laser-Induced Breakdown Spectroscopy Coupled with Multivariate Chemometrics for Variety Discrimination of Soil," *Sci. Rep.* **6**(1), 27574 (2016).
31. A. K. Myakalwar, N. Spegazzini, C. Zhang, S. Kumar Anubham, R. R. Dasari, I. Barman, and M. Kumar Gundawar, "Less is more: Avoiding the LIBS dimensionality curse through judicious feature selection for explosive detection," *Sci. Rep.* **5**, 13169 (2015).
32. A. De Giacomo, C. Koral, G. Valenza, R. Gaudiuso, and M. Dell'Aglio, "Nanoparticle enhanced laser-induced breakdown spectroscopy for microdrop

- analysis at subppm level," *Anal. Chem.* **88**(10), 5251–5257 (2016).
33. S. Grégoire, V. Motto-Ros, Q. L. Ma, W. Q. Lei, X. C. Wang, F. Pelascini, F. Surma, V. Detalle, and J. Yu, "Correlation between native bonds in a polymeric material and molecular emissions from the laser-induced plasma observed with space and time resolved imaging," *Spectrochim. Acta B* **74**, 31–37 (2012).
 34. S. J. Mousavi, M. H. Farsani, S. M. R. Darbani, A. Mousaviazar, M. Soltanolkotabi, and A. E. Majd, "CN and C2 vibrational spectra analysis in molecular LIBS of organic materials," *Appl. Phys. B* **122**(5), 1–16 (2016).
 35. Á. Fernández-Bravo, T. Delgado, P. Lucena, and J. J. Laserna, "Vibrational emission analysis of the CN molecules in laser-induced breakdown spectroscopy of organic compounds," *Spectrochim. Acta Part B* **89**, 77–83 (2013).
 36. M. Dong, J. Lu, S. Yao, Z. Zhong, J. Li, J. Li, and W. Lu, "Experimental study on the characteristics of molecular emission spectroscopy for the analysis of solid materials containing C and N," *Opt. Express* **19**(18), 17021–17029 (2011).
 37. J. Serrano, J. Moros, and J. J. Laserna, "Exploring the formation routes of diatomic hydrogenated radicals using femtosecond laser-induced breakdown spectroscopy of deuterated molecular solids," *J. Anal. At. Spectrom.* **30**(11), 2343–2352 (2015).
 38. T. Delgado, J. M. Vadillo, and J. J. Laserna, "Acting Role of Background Gas in the Emission Response of Laser-Induced Plasmas of Energetic Nitro Compounds," *Appl. Spectrosc.* **70**(8), 1364–1374 (2016).
 39. T. Delgado, J. M. Vadillo, and J. J. Laserna, "Primary and recombined emitting species in laser-induced plasmas of organic explosives in controlled atmospheres," *J. Anal. At. Spectrom.* **29**(9), 1675–1685 (2014).
 40. R. Glaus, J. Riedel, and I. Gornushkin, "Insight into the formation of molecular species in laser-induced plasma of isotopically labeled organic samples," *Anal. Chem.* **87**(19), 10131–10137 (2015).
 41. E. N. Rao, S. Sunku, and S. V. Rao, "Femtosecond Laser-Induced Breakdown Spectroscopy Studies of Nitropyrazoles: The Effect of Varying Nitro Groups," *Appl. Spectrosc.* **69**(11), 1342–1354 (2015).
 42. S. Sreedhar, E. Nageswara Rao, G. Manoj Kumar, S. P. Tewari, and S. Venugopal Rao, "Molecular formation dynamics of 5-nitro-2,4-dihydro-3H-1,2,4-triazol-3-one, 1,3,5-trinitroperhydro-1,3,5-triazine, and 2,4,6-trinitrotoluene in air, nitrogen, and argon atmospheres studied using femtosecond laser induced breakdown spectroscopy," *Spectrochim. Acta B* **87**, 121–129 (2013).
 43. S. Sunku, M. K. Gundawar, A. K. Myakalwar, P. P. Kiran, S. P. Tewari, and S. V. Rao, "Femtosecond and nanosecond laser induced breakdown spectroscopic studies of NTO, HMX, and RDX," *Spectrochim. Acta B* **79–80**, 31–38 (2013).
 44. E. N. Rao, P. Mathi, S. A. Kalam, S. Sreedhar, A. K. Singh, B. N. Jagatap, and S. V. Rao, "Femtosecond and nanosecond LIBS studies of nitroimidazoles: correlation between molecular structure and LIBS data," *J. Anal. At. Spectrom.* **31**(3), 737–750 (2016).
 45. N. Kommu, V. D. Ghule, A. S. Kumar, and A. K. Sahoo, "Triazole-Substituted Nitroarene Derivatives: Synthesis, Characterization, and Energetic Studies," *Chem. Asian J.* **9**(1), 166–178 (2014).
 46. N. Kommu, "Nitrogen Oxygen Rich 1,2,4-/1,2,3-2H-Triazole and Tetrazole Derivatives: The Thermally Stable Energetic Materials," Thesis page 51 (2015).
 47. A. G. Gaydon, *The Identification of Molecular Spectra: RWB Pearse and AG Gaydon* (Chapman and Hall, 1976).
 48. "NIST atomic spectra database," <https://www.nist.gov/pml/atomic-spectra->

- database.
49. T. A. Labutin, V. N. Lednev, A. A. Ilyin, and A. M. Popov, "Femtosecond laser-induced breakdown spectroscopy," *J. Anal. At. Spectrom.* **31**(1), 90–118 (2016).
 50. B. Zhang, M. He, W. Hang, and B. Huang, "Minimizing matrix effect by femtosecond laser ablation and ionization in elemental determination," *Anal. Chem.* **85**(9), 4507–4511 (2013).
 51. E. L. Gurevich and R. Hergenröder, "Femtosecond laser-induced breakdown spectroscopy: physics, applications, and perspectives," *Appl. Spectrosc.* **61**(10), 233A–242A (2007).
 52. S. S. Harilal, B. E. Brumfield, B. D. Cannon, and M. C. Phillips, "Shock Wave Mediated Plume Chemistry for Molecular Formation in Laser Ablation Plasmas," *Anal. Chem.* **88**(4), 2296–2302 (2016).
 53. A. De Giacomo and J. Hermann, "Laser-induced plasma emission: from atomic to molecular spectra," *J. Phys. D* **50**(18), 183002 (2017).
 54. J. Serrano, J. Moros, and J. J. Laserna, "Molecular signatures in femtosecond laser-induced organic plasmas: comparison with nanosecond laser ablation," *Phys. Chem. Chem. Phys.* **18**(4), 2398–2408 (2016).
 55. G. Dinescu, E. Aldea, M. L. De Giorgi, A. Luches, A. Perrone, and A. Zocco, "Optical emission spectroscopy of molecular species in plasma induced by laser ablation of carbon in nitrogen," *Appl. Surf. Sci.* **127**, 697–702 (1998).
 56. M. Dong, X. Mao, J. J. Gonzalez, J. Lu, and R. E. Russo, "Time-resolved LIBS of atomic and molecular carbon from coal in air, argon and helium," *J. Anal. At. Spectrom.* **27**(12), 2066–2075 (2012).
 57. V. P. N. Nampoori, C. P. Girijavallabhan, S. S. Harilal, C. Riju, and C. V Bindhu, "Optical emission studies of C₂ species in laser-produced plasma from carbon," *J. Phys. D* **30**(12), 1703 (1997).
 58. P. Caubet and G. Dorthe, "Origin of C₂ high-pressure bands observed in the products of a microwave discharge through CO," *Chem. Phys. Lett.* **218**(5–6), 529–536 (1994).
 59. S. S. Harilal, R. C. Issac, C. V Bindhu, V. P. N. Nampoori, and C. P. G. Vallabhan, "Temporal and spatial evolution of C₂ in laser induced plasma from graphite target," *J. Appl. Phys.* **80**(6), 3561–3565 (1996).
 60. M. Anselment, R. S. Smith, E. Daykin, and L. F. Dimauro, "Optical emission studies on graphite in a laser/vaporization supersonic jet cluster source," *Chem. Phys. Lett.* **134**(5), 444–449 (1987).
 61. C. E. Little and P. G. Browne, "Origin of the high-pressure bands of C₂," *Chem. Phys. Lett.* **134**(6), 560–564 (1987).
 62. F. C. De Lucia Jr and J. L. Gottfried, "Influence of molecular structure on the laser-induced plasma emission of the explosive RDX and organic polymers," *J. Phys. Chem. A* **117**(39), 9555–9563 (2013).
 63. A. Kushwaha and R. K. Thareja, "Dynamics of laser-ablated carbon plasma: formation of C₂ and CN," *Appl. Opt.* **47**(31), G65–G71 (2008).
 64. "NIST-JANAF Thermochemical Tables, <http://kinetics.nist.gov/janaf/>," (n.d.).
 65. P. F. Pagoria, G. S. Lee, A. R. Mitchell, and R. D. Schmidt, "A review of energetic materials synthesis," *Thermochim. Acta* **384**(1), 187–204 (2002).
 66. J. P. Agrawal, "Recent trends in high-energy materials," *Prog. energy Combust. Sci.* **24**(1), 1–30 (1998).
 67. P. E. Eaton, R. L. Gilardi, and M.-X. Zhang, "Polynitrocubanes: advanced high-density, high-energy materials," *Adv. Mater.* **12**(15), 1143–1148 (2000).

Chapter 3

68. J. Akhavan, *The Chemistry of Explosives* (Royal Society of Chemistry, 2011).
69. M. J. Kamlet and H. Hurwitz, "Chemistry of detonations. IV. Evaluation of a simple predictional method for detonation velocities of C–H–N–O explosives," *J. Chem. Phys.* **48**(8), 3685–3692 (1968).
70. M. Sućeska, "Experimental determination of detonation velocity," *Fragblast - Int. J. Blasting Fragmentation* **1**(3), 261–284 (1997).
71. M. H. Keshavarz, "Prediction of detonation performance of CHNO and CHNOAl explosives through molecular structure," *J. Hazard. Mater.* **166**(2), 1296–1301 (2009).
72. Y. Wang, J. Zhang, H. Su, S. Li, S. Zhang, and S. Pang, "A simple method for the prediction of the detonation performances of metal-containing explosives," *J. Phys. Chem. A* **118**(25), 4575–4581 (2014).
73. S. Johnson, M. Clemenson, and N. Glumac, "Simultaneous Imaging and Spectroscopy of Detonation Interaction in Reactive and Energetic Materials," *Appl. Spectrosc.* **71**(1), 78–86 (2017).
74. A. H. Farhadian, M. K. Tehrani, M. H. Keshavarz, M. Karimi, S. M. R. Darbani, and A. H. Rezaei, "A novel approach for investigation of chemical aging in composite propellants through laser-induced breakdown spectroscopy (LIBS)," *J. Therm. Anal. Calorim.* **124**(1), 279–286 (2016).
75. A. H. Rezaei, M. H. Keshavarz, M. K. Tehrani, S. M. R. Darbani, A. H. Farhadian, S. J. Mousavi, and A. Mousaviazar, "Approach for determination of detonation performance and aluminum percentage of aluminized-based explosives by laser-induced breakdown spectroscopy," *Appl. Opt.* **55**(12), 3233–3240 (2016).
76. A. H. Rezaei, M. H. Keshavarz, M. K. Tehrani, and S. M. R. Darbani, "Quantitative analysis for the determination of aluminum percentage and detonation performance of aluminized plastic bonded explosives by laser-induced breakdown spectroscopy," *Laser Phys.* **28**, 065605–065615 (2018).
77. J. J. Laserna, "Recognition of explosives fingerprints on objects for courier services using machine learning methods and laser-induced breakdown spectroscopy," *Talanta* **110**, 108–117 (2013).
78. S. Sunku, E. N. Rao, G. M. Kumar, S. P. Tewari, and S. V. Rao, "Discrimination methodologies using femtosecond LIBS and correlation techniques," in *SPIE Defense, Security, and Sensing* (SPIE, 2013), **8726**, p. 87260H–8.
79. V. Lazic, A. Palucci, S. Jovicevic, and M. Carpanese, "Detection of explosives in traces by laser induced breakdown spectroscopy: Differences from organic interferences and conditions for a correct classification," *Spectrochim. Acta Part B At. Spectrosc.* **66**(8), 644–655 (2011).
80. J. Serrano, J. Moros, C. Sánchez, J. Macías, and J. J. Laserna, "Advanced recognition of explosives in traces on polymer surfaces using LIBS and supervised learning classifiers," *Anal. Chim. Acta* **806**, 107–116 (2014).
81. P. K. Pandey, Y. Singh, and S. Tripathi, "Image Processing using Principle Component Analysis," *Int. J. Comput. Appl.* **15**(4), 37–40 (2011).
82. K. Konstantynowski, G. Njio, F. Börner, A. Lepcha, T. Fischer, G. Holl, and S. Mathur, "Bulk detection of explosives and development of customized metal oxide semiconductor gas sensors for the identification of energetic materials," *Sensors Actuators B Chem.* **258**, 1252–1266 (2018).
83. T. Zhang, H. Tang, and H. Li, "Chemometrics in laser-induced breakdown spectroscopy," *J. Chemom.* e2983 (2018).
84. J. Moros, J. Serrano, C. Sanchez, J. Macias, and J. J. Laserna, "New chemometrics

- in laser-induced breakdown spectroscopy for recognizing explosive residues," *J. Anal. At. Spectrom.* **27**(12), 2111–2122 (2012).
85. A. H. Farhadian, M. K. Tehrani, M. H. Keshavarz, and S. M. R. Darbani, "Energetic materials identification by laser-induced breakdown spectroscopy combined with artificial neural network," *Appl. Opt.* **56**(12), 3372–3377 (2017).
 86. P. Pořízka, J. Klus, E. Képeš, D. Prochazka, D. W. Hahn, and J. Kaiser, "On the utilization of Principal Component Analysis in Laser-Induced Breakdown Spectroscopy data analysis, a review," *Spectrochim. Acta B* **148**, 65–82 (2018).
 87. P. Pořízka, J. Klus, D. Prochazka, E. Képeš, A. Hrdlička, J. Novotný, K. Novotný, and J. Kaiser, "Laser-Induced Breakdown Spectroscopy coupled with chemometrics for the analysis of steel: The issue of spectral outliers filtering," *Spectrochim. Acta B* **123**, 114–120 (2016).
 88. Q. Q. Wang, K. Liu, H. Zhao, C. H. Ge, and Z. W. Huang, "Detection of explosives with laser-induced breakdown spectroscopy," *Front. Phys.* **7**(6), 701–707 (2012).
 89. F. C. De Lucia and J. L. Gottfried, "Classification of explosive residues on organic substrates using laser induced breakdown spectroscopy," *J. Anal. At. Spectrom.* **51**(7), 83–92 (2012).
 90. F. C. De Lucia, J. L. Gottfried, C. a Munson, and A. W. Miziolek, "Multivariate analysis of standoff laser-induced breakdown spectroscopy spectra for classification of explosive-containing residues," *Appl. Opt.* **47**(31), G112–G121 (2008).
 91. J. L. Gottfried, F. C. De Lucia, C. A. Munson, and a W. Miziolek, "Standoff detection of chemical and biological threats using laser-induced breakdown spectroscopy," *Appl. Spectrosc.* **62**(4), 353–363 (2008).
 92. G. Giubileo, F. Colao, and A. Puiu, "Identification of Standard Explosive Traces by Infrared Laser Spectroscopy : PCA on LPAS Data 1," *laser Spectrosc.* **22**(6), 1033–1037 (2012).
 93. J. Moros, J. A. Lorenzo, K. Novotný, and J. J. Laserna, "Fundamentals of stand-off Raman scattering spectroscopy for explosive fingerprinting," *J. Raman Spectrosc.* **44**(1), 121–130 (2013).
 94. A. H. Farhadian, M. K. Tehrani, M. H. Keshavarz, and S. M. R. Darbani, "Energetic materials identification by laser-induced breakdown spectroscopy combined with artificial neural network," *Appl. Opt.* **56**(12), 3372–3377 (2017).
 95. P. Pořízka, J. Klus, A. Hrdlička, J. Vrábel, P. Škarková, D. Prochazka, J. Novotný, K. Novotný, and J. Kaiser, "Impact of Laser-Induced Breakdown Spectroscopy data normalization on multivariate classification accuracy," *J. Anal. At. Spectrom.* **32**(2), 277–288 (2017).
 96. J. P. Castro and E. R. Pereira-Filho, "Twelve different types of data normalization for the proposition of classification, univariate and multivariate regression models for the direct analyses of alloys by laser-induced breakdown spectroscopy (LIBS)," *J. Anal. At. Spectrom.* **31**(10), 2005–2014 (2016).

Intentional blank page

Chapter 4

Femtosecond filament induced breakdown spectroscopy (fs FIBS) for standoff detection of high energy materials

In this chapter details of our efforts and the results obtained from development of a standoff femtosecond filament induced breakdown spectroscopy technique (fs ST-FIBS) based system (~6.5 m/~8 m) for the investigation of high energy materials (HEMs) is presented. Along with HEMs (nitroimidazoles and nitropyrazoles including the standard explosive molecules such as RDX, HMX, and TNT) several other materials including metals, bimetallic targets, and geological rocks were qualitatively investigated in the same experimental configuration. The fs LIBS experiments were carried out in three different configurations i.e. (i) ST-FIBS1 (up to 2 m) (ii) Remote-LIBS (R-LIBS; 10 cm/~8.5 m) and (iii) ST-FIBS2 (~6.5 m/ ~8 m) with the last system being superior of all the configurations. ME-OPT-0007 (ANDOR M/s) collection optics (first configuration) and Schmidt-Cassegrain Telescope [(SCT), in second and third configurations] were utilized to collect the plasma emissions. The experiments in first two configurations were primarily aimed at investigating the various aspects influencing the LIBS signal strength from standoff distances such as fluence, collection system efficiency, filament generation conditions etc. The difference between ablation with tightly focused fs pulses and fs filaments is elucidated by comparing the R-LIBS and ST-FIBS2 results of an Al target. Principal component analysis (PCA) was potentially utilized in tandem with fs LIBS/FIBS data to discriminate/cluster the materials investigated in all the three configurations.

Part of this work has been accepted for publication in

1. **S. A. Kalam**, E.N. Rao, and S. Venugopal Rao, "Standoff Spectroscopy: Standoff LIBS for explosives detection - challenges and status," *Laser Focus World*, April 2017.
2. **S. A. Kalam**, E.N. Rao, S. Hamad, B. Chandu, and S. Venugopal Rao, "Femtosecond laser induced breakdown spectroscopy based standoff detection of explosives and discrimination using principal component analysis," *Opt. Express* **26(7)**, 53–59 (2018).
3. **S. A. Kalam**, Ajmathulla, S. Venugopal Rao, "Discrimination of bimetallic alloy targets using femtosecond filament-induced breakdown spectroscopy in standoff mode," *Opt. Lett.* **43(15)**, 18–21 (2018).
4. **S.A. Kalam** and S. Venugopal Rao, "Discrimination of high energy materials using femtosecond filament-induced breakdown spectroscopy and demonstration of NE-FIBS for trace detection of explosives in standoff mode", **Submitted to Optics Letters**, 2018.

4.1 Introduction

Development of a rapid and reliable technique to anticipate the threat through real-time detection/identification of high energy materials (HEMs) and improvised explosive devices (IEDs) is of great concern for any nation to safeguard citizens. Though the existing lab-based explosive trace detection techniques (e.g. Ion mobility, Mass spectrometry) are quite sensitive, they are (i) not in-situ (ii) time-consuming and can be handy in different scenarios (e.g. post incident analysis) [1,2]. On the contrary, laser-based spectroscopic techniques such as Raman spectroscopy, laser induced breakdown spectroscopy (LIBS) and THz spectroscopy enjoy high potential for robust, real-time, remote/standoff detection of explosives, chemical/biological warfare agents and other hazardous substances [3–9]. Different lab-based techniques and laser-based spectroscopic techniques and their merits/de-merits towards explosive detection were discussed in chapter 1. LIBS technique has been extensively used in various fields, owing to its robust in-situ elemental analysis, such as space exploration, pharmaceutical, soil and nutrient analysis and identification/discrimination of explosives [10–18]. Several researchers utilized nanosecond (ns) LIBS technique in analysing aerosols [19], process control and monitoring in metallurgical industry [20], planetary missions and detection of explosive residues at standoff distances [21–24]. Initially, hand-held or man-portable LIBS systems were developed and tested for the investigation of chemical, biological threats and HEMs. However, over the last decade efforts for the development of portable LIBS systems for field applications have been multiplied by various research communities [25–28]. Lazic et al. [29] have utilized intensity ratios C/H, C/O, C/N, N/H ratios and correlation between atomic intensities with Al⁺ intensity to classify explosive trace. Gottfried et al. utilized nanosecond double pulse standoff LIBS system for detecting explosive residues and chemical warfare agents on aluminium (Al) at a distance of 20 m [21]. Further, they have utilized PLS-DA model to discriminate explosive residues on organic and inorganic substrates obtained at 25 m [30] and RDX traces on various metallic substrates in near field and suggested approaches to improve PLS-DA model as well [31]. Gottfried et al. [32] utilized principal component analysis (PCA) scores of various atomic intensities to distinguish explosives RDX, TNT, and Composition-B. Cristina et al. [33] employed a field portable co-axial ns ST-LIBS system for detection of explosive residues at 30 m away. Standoff LIBS spectra of few explosive residues, hidden behind transparent

colourless Poly(methyl methacrylate) glass (PMMA), were recorded from 30 m distance [34]. Sustained efforts are in progress to increase the sensitivity and selectivity for explosives detection by combining LIBS and Raman spectroscopy onto a single platform [35,36]. As mentioned above, several chemometric techniques were developed and utilized to analyse the LIBS data in identifying/discriminating explosive molecules, different soils, a variety of bacteria and classification of diverse polymers etc. However, there are several challenges still exist in employing the ns pulses for ST-LIBS applications such as (i) focusing ns pulses to a small spot on to the remote sample to provide necessary peak intensity (ii) minimizing the unwanted breakdown of air at the sample proximity. The laser beam can be expanded prior to focusing so as to achieve reduced spot-size and, in turn, achieve large peak intensities at standoff distances to initiate the plasma formation. The conventional long (ns) pulses suffer significantly from diffraction and beam wandering (effected by the atmospheric turbulence) which adversely affects the signal to noise ratio (SNR) because fail to deliver high peak intensities at remote locations [37]. For standoff applications, signal collection optics/system plays a vital role on par with the excitation wavelength and pulse duration of the laser. There have been several modifications implemented recently to improve the efficiency of the LIBS signal collection system [38]. Patrick et al. [39] have proposed a spatial heterodyne spectrometer for ST-LIBS measurements up to 20 m which offers a very large field of view. Recently, Li et al. [40] have shown that a multi-collector lens system could outperform the Newtonian telescope of similar dimensions for standoff LIBS measurements.

4.1.1 Femtosecond filament induced breakdown spectroscopy (fs FIBS)

Though the benefits of femtosecond (fs) pulses are well documented (when compared to ns pulses) the technique of standoff LIBS with fs pulses has not been explored to its full potential [41–44]. Femtosecond pulses are worthwhile when compared to ns pulses in LIBS studies since these ultrashort laser pulses offer lower continuum, smaller heat effected zones, lesser plasma-ambience interaction and minimal plasma and post-pulse interaction [45,46]. Owing to their high peak-peak power, fs pulses form filaments as they propagate in most of the media due to the dynamical balance between Kerr lens focusing and plasma defocusing. Couairon et al. [47] had comprehended the process of fs filamentation in various transparent media. Long range

Chapter 4

propagation of fs pulses (hundreds of meters to few kilometers) in the form filaments is advantageous for employing fs pulses for standoff applications. Fs pulses overcome the diffraction limit of conventional ns pulses and can deliver high intensities 10^{13} - 10^{14} W/cm² at remote locations which is adequate enough to generate plasma in most of the materials [48]. A first report on the usage of fs pulses, in the form of filaments, for standoff applications was demonstrated by employing a terawatt fs pulse laser by the Teramobile group [49]. Rohwetter et al. [49] reported remote LIBS analyses of Al and Cu at a distance of 25 m and simultaneously compared the advantages of fs pulses by comparing with the other short pulses in ns and ps (picosecond) regime. They found that the LIBS spectra resulting from fs pulses has shown mitigated external interference. Stelmaszczyk et al. [49] identified Cu and Fe using fs filament LIBS at 90 m. Rohwetter et al. [50] again reported investigation of metallic samples up to 180 m using terawatt laser pulses. Apart from investigating distant metal targets, fs filaments have been used in atmospheric sensing [51,52], combustion sensing [53,54], cultural heritage monitoring [55], analyzing metals [56,57], organic samples [58], chemical and biological agents [59], labeling of radioactive isotopes [60] and in detection of explosives [61]. The generation and propagation of fs filaments at distances even hundreds of meters to few kilometers [62] in air and is alluring and thus useful in remote diagnostics, LIDAR etc. [63,64]. A book chapter has been dedicated by Cremers et al. regarding usage of fs pulses for remote LIBS measurements [65]. Further Richardson et al. [66] have summarized the fundamentals of fs filaments interaction and various applications of fs filaments in a short report. Fuji et al. [63] have demonstrated in situ remote detection of salt water aerosols using fs laser pulses at 16 m. Femtosecond filaments have also shown to be affected by turbulence of air resulting in irregular intensity patterns after propagating few tens of meters depending on their initial incident energies [67,68]. Similarly, the complex focusing dynamics of fs pulse also affects the strength of LIBS signal [69]. Nevertheless, they exhibit certain advantages over ns pulses such as control of onset of filamentation, number of filaments and other properties of filaments. As reported by Jin et al.[68], the onset of filaments and their long range propagation can be controlled by varying the laser energy and divergence angle. Fischer et al. [70] recently demonstrated that fs filaments can be controlled to achieve highly stable, repeatable, spatial and temporal distributions by use of a vortex phase plate which in turn provided better signal in remote LIBS (R-LIBS) investigations. Chen et al. [71] have reported elongated plasma channels by

temporally shaping fs pulses. Effect of pulse chirp has been examined and demonstrated that detection limit can be improved by the use of chirped fs pulses, which provide better contrast compared to classical LIBS [56,72]. Polynkin et al. [73] have demonstrated that utilization of Bessel beams provide longitudinally extended and stable plasma channels in air. However, there are several challenges for explosives detection using LIBS in general, and fs pulses in particular. Baudelet et al. [74,75] have examined several polymers and graphite samples using fs filaments and reported the FIBS spectra were containing primarily molecular emission. Gottfried et al. [41] evaluated the use of fs pulses for detection of trace explosive residue on Al and reported the relative decrease in Al signal in case of fs pulses at minimal energies. Femtosecond pulses with very high energies result in large heat effected zones similar to the case of ns pulse ablation. Concurrently, employing fs pulses at low energies would sacrifice the signal intensity. Throughput of the detector, collection efficiency must be optimized in order to collect the low signal generated by small laser fluence. Detailed studies on diverse molecules using various optical configurations is essential to arrive at a field-usable instrument for unambiguous detection.

The development of fs ST-FIBS system at ACRHEM, University of Hyderabad is discussed in this chapter. Here, fs filaments were exploited (for the first time to the best of our knowledge) to investigate the energetic molecules in three different configurations i.e. (i) ST-FIBS1 (up to 2 m), (ii) Remote-LIBS (10 cm/ ~8.5 m) and (iii) ST-FIBS2 (~6.5 m/ ~8 m) with the last system being superior in all the configurations. ME-OPT-0007 (M/s ANDOR) collection optics (configuration1) and Schmidt-Cassegrain telescope (SCT) (configurations 2 and 3) were utilized to collect the plasma emissions. Experiments in the first two configurations were aimed at investigating different aspects that influence the LIBS signal strength from far distances such as intensity delivered at the target, efficiency of collection system, filament generation conditions etc. The trend observed in the LIBS emissions is discussed. The difference between the ablation with tightly focused fs pulses and with fs filaments is elucidated by comparing the results obtained from the last two configurations i.e. from R-LIBS and ST-FIBS2 on an Al target. Principal component analysis (PCA) was employed in tandem with LIBS/FIBS data to discriminate/classify all the materials obtained in all the three configurations. Results

Chapter 4

from all the configurations are compared and complexities in obtaining standoff LIBS spectra are addressed.

4.2 Experimental details

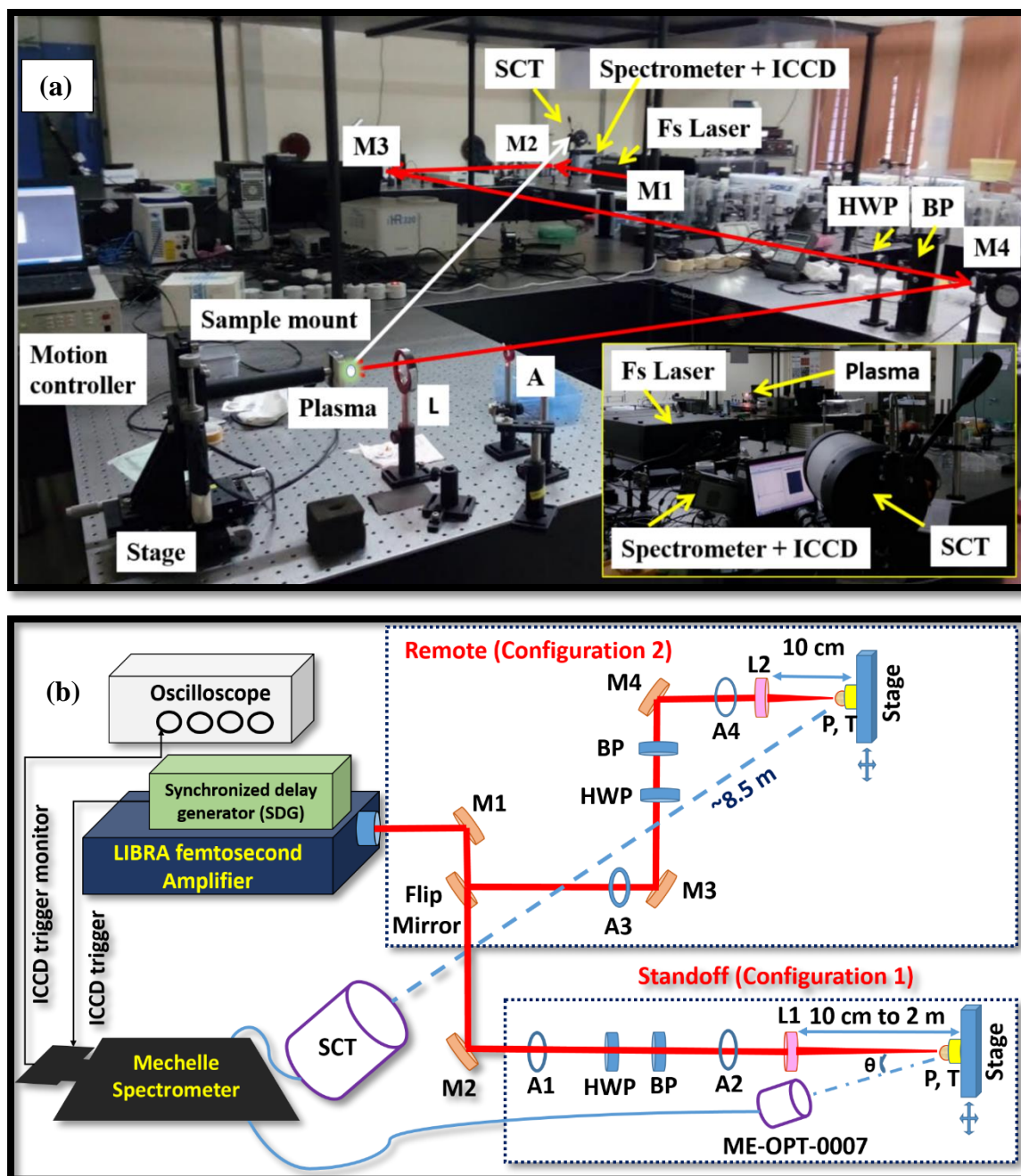


Figure 4.1 (a) Laboratory setup of R-LIBS (configuration 2) (b) Schematic of fs ST-LIBS1 setup (up to ~2 m; configuration 1) and fs R-LIBS setup (10 m / ~8.5 m; configuration 2). M-Mirror, A-Aperture, HWP-Half wave plate, BP-Brewster plate, L-lens, SCT-Schmidt Cassegrain telescope, P-Plasma, and T-Target.

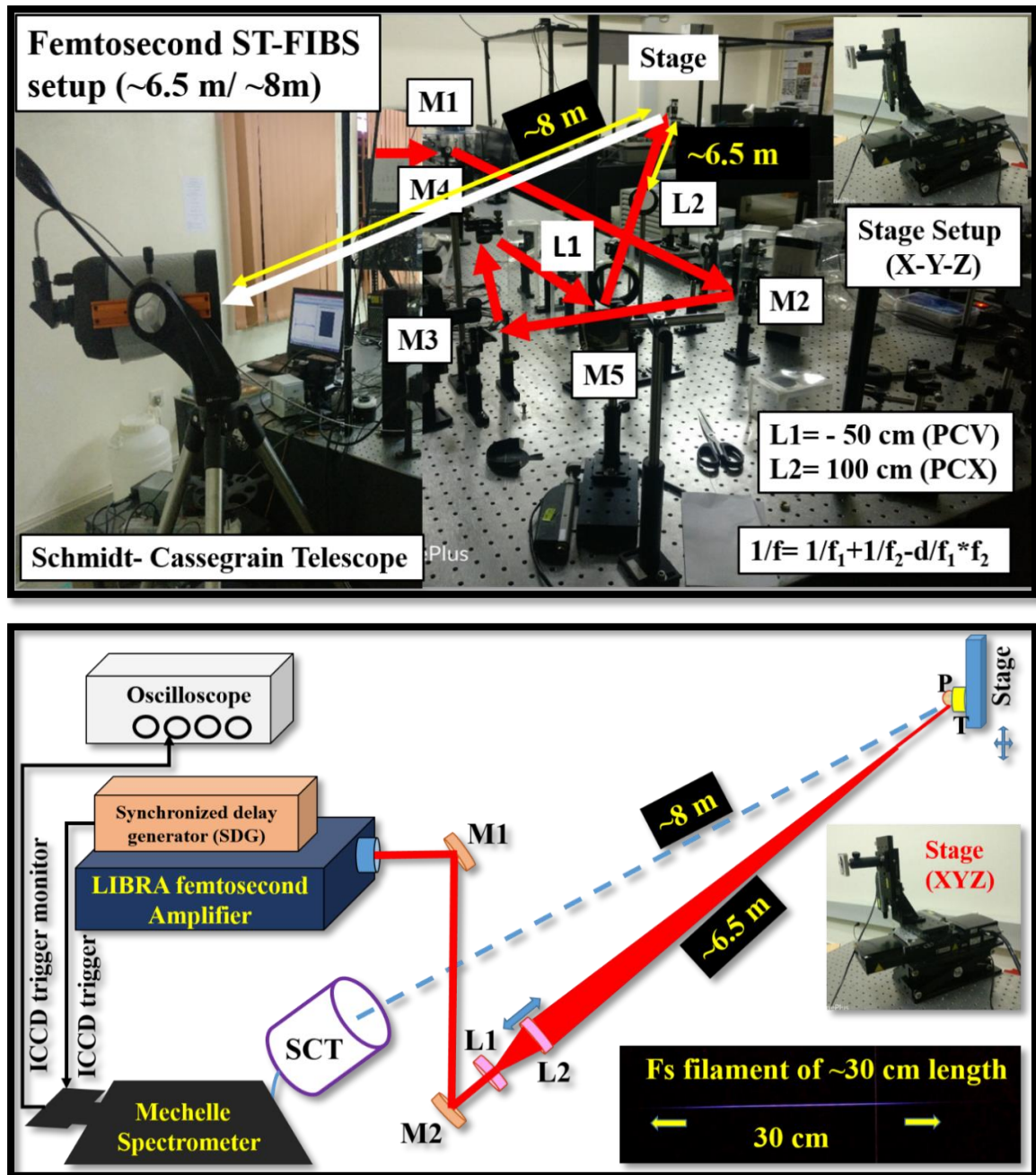


Figure 4.2 Top: Femtosecond standoff filament induced breakdown spectroscopy (fs ST-FIBS2) setup at ~6.5 m/ ~8 m (configuration 3) at ACRHEM, University of Hyderabad. **Bottom:** Experimental schematic of fs ST-FIBS2 setup. In figure, the inset shows an fs filament of ~30 cm in length generated using two lens combination L1 [plano concave lens (PCV), $f=-50$ cm] and L2 [plano-concave lens (PCX), $f=100$ cm].

An ultrafast laser system delivering ~50 fs laser pulses at 800 nm was employed to perform the fs LIBS experiments in ambient air and in all the three configurations. **Figures 4.1 and 4.2** depict the experimental schematics of three configurations used in the present work: (i) fs standoff LIBS setup (fs ST-FIBS1, up to ~2 m) (ii) fs remote LIBS setup (fs R-LIBS, 10 cm/ ~8.5 m) and (iii) fs standoff LIBS setup (fs ST-FIBS2,

Chapter 4

~6.5 m/ ~8 m). In configuration 1, ME-OPT-0007 (M/s ANDOR) was used as collection system whereas in configurations 2 and 3, a Schmidt-Cassegrain telescope (SCT) was to collect optical emissions. The experiments carried out in these three configurations explain the evolution of fs ST-LIBS experiments at ACRHEM using fs pulses and filaments. The collection optics ME-OPT-0007 [here in referred as C1 in the text] (earlier referred as CC52) [76] from M/s Andor is a patented UV-NIR achromatic collecting/collimating lens/mirror system, which is optimized to ensure that all wavelengths in the range 200-1100 nm are collected evenly into the entrance fiber. Figure 4.3 depicts the design of SCT which is explained in detail in the following section.

In fs ST-FIBS1, plano-convex lenses of five different focal lengths (10 cm, 30 cm, 50 cm, 100 cm, and 200 cm) were used to focus the fs pulses on to the sample and the optical emissions were collected by C1. The C1 position was fixed besides the focusing lens and was optimized for maximum collection at each standoff distance by tilting/adjusting it. The collection distance and the focusing distance were maintained to be equal. Beyond the focusing length of 30 cm the point plasma stretched into a filament. For example, a short filament of ~10 cm length was observed for the $f = 200$ cm focal length lens. The typical length of the filament varied from ~2 cm to ~10 cm. So, the spectra are referred as ST-FIBS spectra. Simultaneously, at each standoff position, an Al plate was probed in order to estimate the spot-size and fluence delivered. In case of R-LIBS, the plasma was produced by focusing the fs laser pulses using a 10 cm focal length lens and emissions were detected at a distance of 8.5 m away using a SCT. The incident pulse energy was ~2 mJ in both the configurations. The optical emissions collected from plasma were coupled to an ANDOR Mechelle spectrometer attached with ICCD by means of an optical fiber (600 μm of core diameter). Fs ST-LIBS spectra of a set of five HEMs (nitroimidazoles) were recorded at five standoff distances of 10, 30, 50, 100, and 200 cm. The LIBS spectra were acquired using a gate delay of 50 ns, gate width of 2 μs , gain of 4000 (gain of 3000 was used at 10 cm to avoid ICCD saturation) with 1.5 s exposure time. Each spectra is the resultant of 6 accumulations. At a given standoff distance 10-15 spectra per sample were recorded. All the acquisition conditions employed for HEMs and metals in the R-LIBS case are similar to the ST-LIBS case, except that an ICCD gain of 1000 was used in the case of metals.

Table 4-1 Details of the samples (energetic molecules, bimetallic targets and geological samples) investigated in various configurations; that were investigated in both standoff and remote configurations.

Configurations	Compound name	IUPAC name	Molecular formula
Configuration 1 Standoff FIBS1 (up to 2 m)	4-NIm	4-nitroimidazole	C ₃ H ₃ N ₃ O ₂
	1M-4NIm	1-methyl-4-nitroimidazole	C ₄ H ₅ N ₃ O ₂
	2,4-DNIm	2,4-dinitroimidazole	C ₃ H ₂ N ₄ O ₄
	1M-2,4-DNIm	1-methyl-2,4-dinitroimidazole	C ₄ H ₄ N ₄ O ₄
	2M-4(5)- NIm	2-methyl-4(5)-nitro imidazole	C ₄ H ₅ N ₃ O ₂
Configuration 2 Remote LIBS (10cm/ ~8.5 m)	4-NIm	4-nitroimidazole	C ₃ H ₃ N ₃ O ₂
	1M-2,4-DNIm	1-methyl-2,4-dinitroimidazole	C ₄ H ₄ N ₄ O ₄
	4-NPY	4-Nitropyrazole	C ₃ H ₃ N ₃ O ₂
	1,3-DNPY	1,3-dinitropyrazole	C ₃ H ₂ N ₄ O ₄
	1M-3,4,5-TNPY	1-Methyl-3,4,5-Trinitropyrazole	C ₄ H ₃ N ₅ O ₆
	Metals & Alloys	Aluminum (Al), Copper (Cu), Brass (Br), Stainless Steel (SS) (not standard samples, have impurities)	
Configuration 3 Standoff (~6.5 m/ ~8 m)	RDX	1,3,5-Trinitro-1,3,5-triazinane	C ₃ H ₆ N ₆ O ₆
	HMX	1,3,5,7-Tetranitro-1,3,5,7-tetrazocane	C ₄ H ₈ N ₈ O ₈
	TNT	2-Methyl-1,3,5-trinitrobenzene	C ₇ H ₅ N ₃ O ₆
	2-NIm	2-nitroimidazole	C ₃ H ₃ N ₃ O ₂
	4-NIm	4-nitroimidazole	C ₃ H ₃ N ₃ O ₂
	1M-4NIm	1-methyl-4-nitroimidazole	C ₄ H ₅ N ₃ O ₂
	2M-4NIm	2-methyl-4-nitroimidazole	C ₄ H ₅ N ₃ O ₂
	1,4-DNIm	1,4-dinitroimidazole	C ₃ H ₂ N ₄ O ₄
	2,4-DNIm	2,4-dinitroimidazole	C ₃ H ₂ N ₄ O ₄
	Metals & Alloys (not standard)	Aluminum (Al), Copper (Cu), Brass (Br), Stainless Steel (SS)	
	Bimetallic strips (pure targets)	Au ₂₀ Ag ₈₀ , Au ₃₀ Ag ₇₀ , Au ₄₀ Ag ₆₀ , Au ₅₀ Ag ₅₀ , Au ₆₀ Ag ₄₀ , Au ₇₀ Ag ₃₀ , and Au ₈₀ Ag ₂₀ (7 combinations) Ag ₃₀ Cu ₇₀ , Ag ₅₀ Cu ₅₀ , and Ag ₇₀ Cu ₃₀ (3 combinations)	Pure Ag @ Au Pure Ag @ Cu
	Geological rocks	Tonalitic-granodiorite gneisses (1A1), Granite (5B), Granite Gneisses (7A), Tonalite (Rav_07)	

In the case of R-LIBS, 10-15 spectra of HEMs and 20-25 spectra of metals were recorded. Pure HEMs powders (~150 mg) were ground and pressed at 3 tonnes pressure

Chapter 4

using a manual hydraulic press (Carver Co.) for 10 minutes to form pellets of typically 12 mm diameter and thickness of ~3 mm. The pellets were translated in the plane transverse to the laser incident direction (using Newport ESP 300 motion controller). **Table 4-1** lists the details of all the samples that were investigated in three configurations.

4.2.1 Schmidt-Cassegrain telescope (SCT)

Figure 4.3 depicts the design of the Schmidt-Cassegrain telescope (SCT; 6", f/10) which was utilized for R-LIBS and ST-FIBS2 (~6.5 m/~8 m) experiments. 6" is the diameter of telescope entrance and f/10 is the f-number of telescope. The incoming light passes through the Schmidt corrector lens (1; also called a corrector plate) at the anterior of telescope. It is reflected from a concave primary mirror (2) at the back of the scope that focuses the light to the front of the telescope where it is reflected again by a smaller, convex secondary mirror (3). Finally, the light travels back through a hole in the primary mirror to the rear of the SCT and coupled to an optical fiber (5) using a focusing lens (4). The length of telescope optical components is given in "mm".

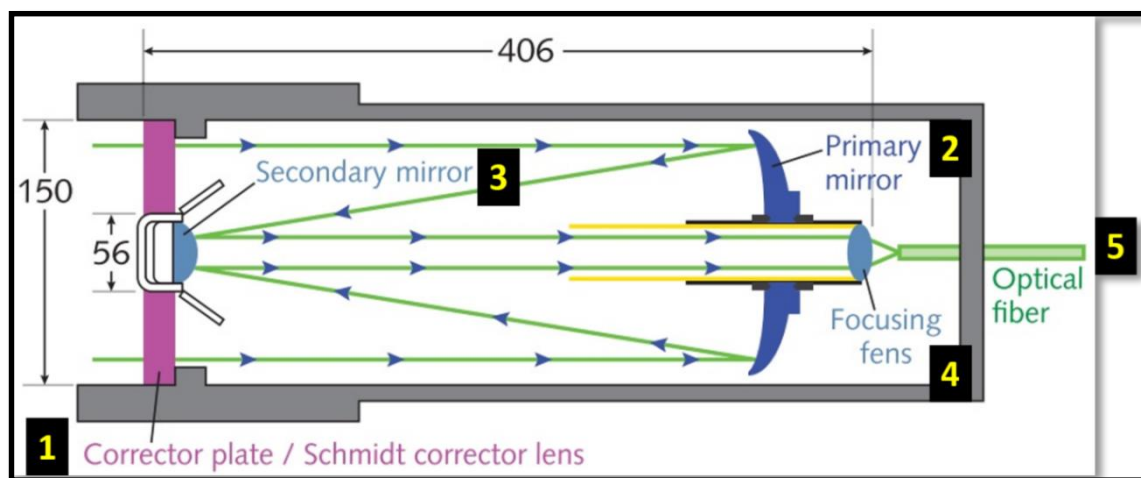


Figure 4.3 Design of the Schmidt Cassegrain telescope (SCT) used in R-LIBS (configuration 1) and ST-FIBS (configuration 2) experiments. The components 1. Schmidt corrector plate, 2. Primary mirror, 3. Secondary mirror, 4. Focusing lens, and 5. Optical fiber.

The collection capability of any telescope depends on various factors such as size of aperture, quality and transmission range of optics, contrast and alignment. Size of the aperture affects light gathering power of telescope and quality, coatings of the optics decides the reflection and transmission range of light through the telescope. Telescopes with large f-number (f/8 and above) possess high magnification capability, suffer less chromatic aberrations and deliver high power with a narrow field of view. The peak

transmission for the system is 89% at a wavelength of 520 nm. The overall system transmission is 83.5% averaged over the visible spectrum (from 400 to 750 nm) [77]. The transmission efficiency of telescope quickly drops on either of these wavelengths.

4.3 Results and Discussions

Femtosecond standoff LIBS experiments were performed in three different configurations (i) standoff FIBS1 (up to 2 m) with ME-OPT-0007 (C1) as the collection system, (ii) remote LIBS (R-LIBS; 10 cm/ ~8.5 m) and (iii) standoff (~6.5 m/ ~8 m) with SCT as the collection system. The objectives methodology and results are explained in subsequent sections.

4.3.1 Standoff FIBS studies of HEMs (up to 2 m; Configuration 1)

Figures 4.4(a)-4.4(e) illustrate the stack plots of representative fs ST-LIBS spectra of nitroimidazoles obtained at different distances (i.e. ~10, ~30, ~50, ~100 and ~200 cm). Nitroimidazoles and nitropyrazoles are nitro rich energetic molecules. Rao et al. have systematically studied and reported these molecules in near fs LIBS configuration [78,79]. The essential spectral features of these molecules are CN, C₂ molecular bands and C, H, N, O atomic emissions. Three CN bands were observed in the spectral region 358-360, 386-390 and 410-422 nm corresponding to Δv values of 1, 0, and -1 respectively. The CN violet band ($\Delta v=0$, $B^2\Sigma^+ \rightarrow X^2\Sigma^+$) had the maximum intensity. Three C₂ bands ($\Delta v = -1, 0, +1$) were observed in the spectral range of 465-475 , 510-518 , and 555-565 nm with maximum intensity at C₂ Swan band ($\Delta v=0$, $d^3\Pi_g \rightarrow a^3\Pi_u$). In the standoff spectra, CN, C₂, NH (336 nm) molecular emissions were observed along with C, H, N, O atomic emissions though their intensity decreased as the standoff/working distance increased. **Figure 4.4(f)** illustrates typical Al LIBS spectra recorded at different working distances. Few Fe I impurities were identified (305.79 , 305.90 , 386.91 and 388.71 nm) in Al along with Al I transitions at 308.2 , 309.27 , 394.40 and 396.15 nm and AlO molecular bands in the spectral region of 440-550 nm.

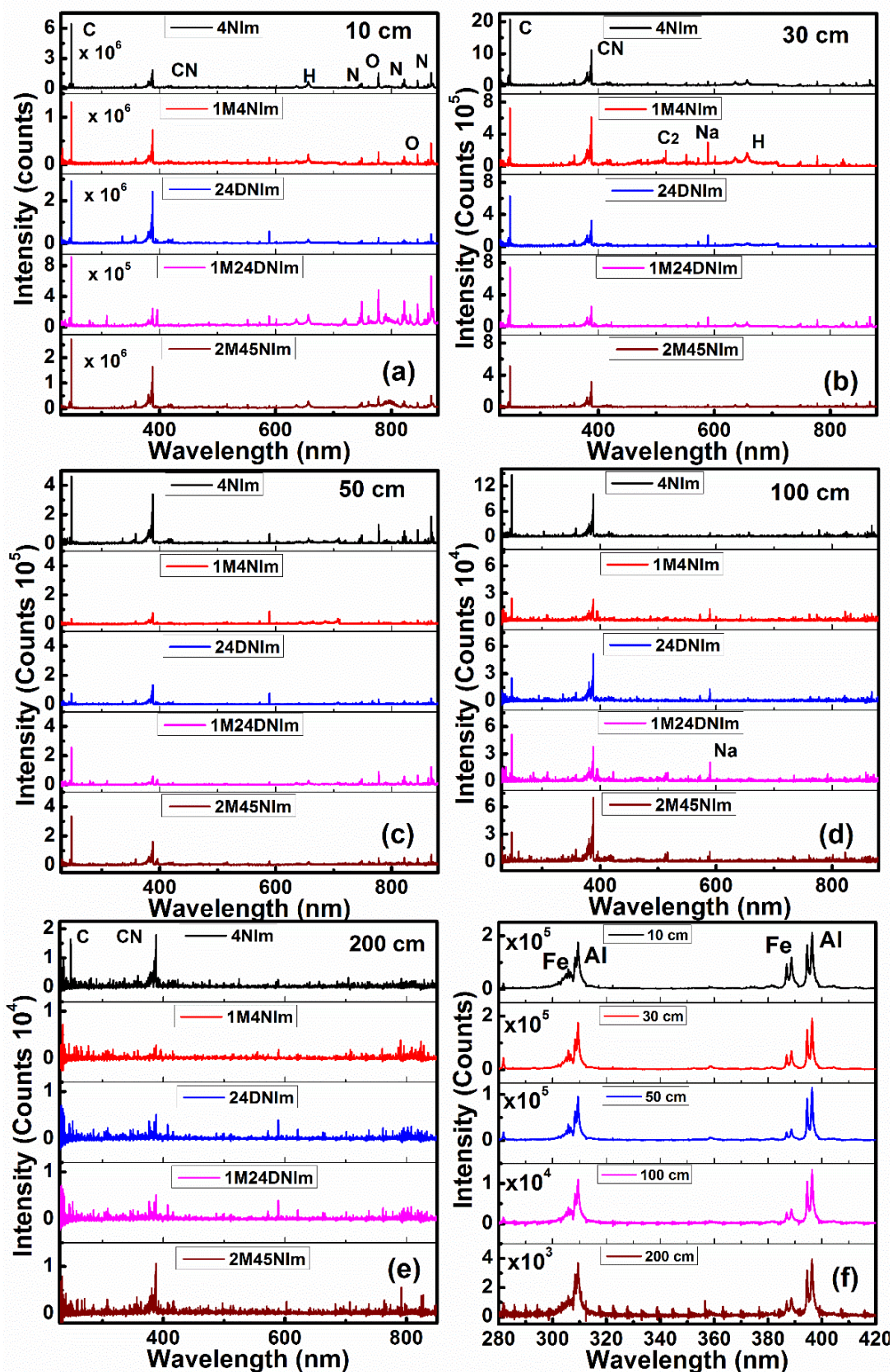


Figure 4.4 Typical fs standoff LIBS spectra of nitroimidazoles at (a) 10 cm (b) 30 cm (c) 50 cm (d) 100 cm (e) 200 cm acquired in ST-LIBS (configuration 1) and (f) Stack plot of the fs standoff LIBS spectra of Al at all distances.

From the data illustrated in **figure 4.4** it is evident that the spectral intensity of energetic molecules varied in the case of each sample at a given position. This can be attributed to their molecular structure and the complex plasma recombination reactions for a particular input energy/intensity. In laser produced plasmas (LPP) it has been clearly proved that co-existence of several reactions between excited radicles, atomic and molecular fragments from plasma as well as ambience leads to the formation or depletion of species [80,81]. In one of our earlier works we discussed and elucidated few plasma reactions and their thermodynamic feasibility through which they conduit in formation and depletion of CN and C₂ molecules in a laser induced plasma. A good correlation observed between CN spectral intensity and the %C-N, %C=N linkages of samples investigated indicates lesser intrusion of air with fs pulse interrogation than in ns case [82]. Moreover, in LPP, the input pulse duration [15] as well as the focusing conditions [83] significantly influence the persistence of plasma species. Comparative ns and fs LIBS studies of TNT residue on Al substrate by Dikmelik et al. [84] have demonstrated that a lower background signal from substrate is observed in case of fs pulses with CN and C₂ being identified as markers for explosive whereas C, H, N, O atomic lines were suggested as markers in case of ns pulses. The change in focal length affects the spot size, filament generation conditions and, hence, has significant influence in the LIBS plume emission properties. Harilal et al. [83] have recently performed several detailed experiments and identified that the filament generation conditions can significantly influence the plasma properties including (a) atomic and molecular emission features (b) persistence and (c) plasma temperature and electron density. For short focal length focusing (say $f = 10$ cm), the physical conditions of the plasma will be hotter at early times which will obscure the molecular formation. Similarly, cooler plasma will be generated when the plasma is produced using fs laser filaments and thus leading to limited persistence of plasma species.

4.3.1.a Estimation of fluence delivered at various standoff distances

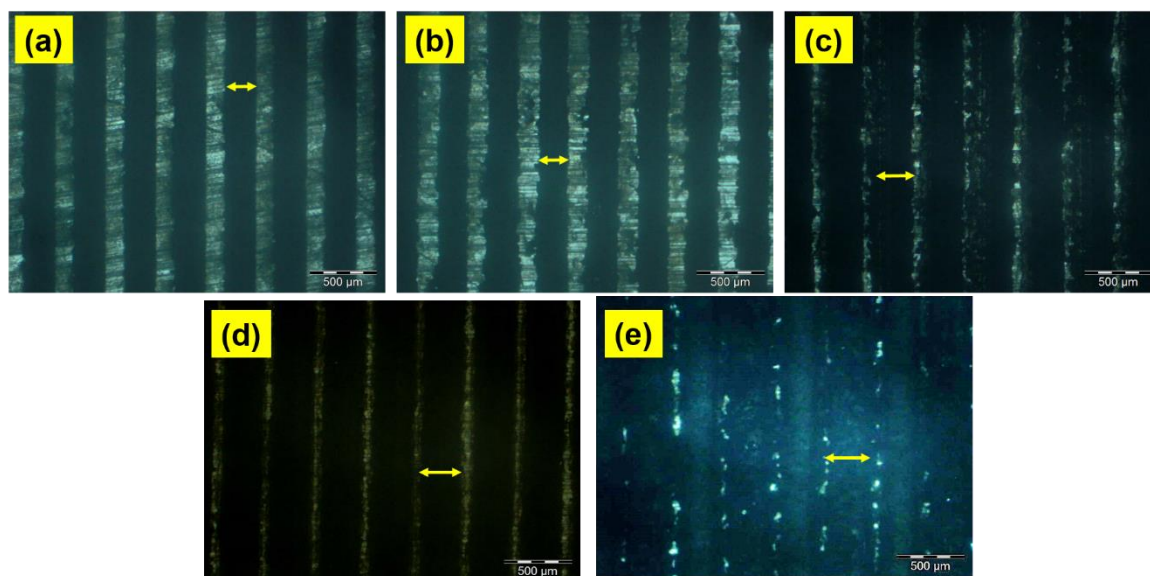


Figure 4.5 Optical microscope images (with same scale of 500 μm) of fs filament interacted portions on Aluminum target obtained at standoff distances (a) 10 cm, (b) 30 cm, (c) 50 cm, (d) 100 cm, and (e) 200 cm in order to estimate the approximate fluence delivered at the target.

As described in experimental section, an Al target was interrogated at each standoff distance to calculate the average spot size. Figures 4.5(a)-4.5(e) depict the optical microscope images of fs filament interacted portions on Al target with 10 , 30 , 50 , 100 and 200 cm focal lengths respectively. The optical images were obtained by an optical microscope (M/s Olympus instruments). Each image scale is shown in the image as 500 μm . **Table 4-2** lists out the mean spot size along with standard deviation (for 10 random measurements on the image) or the size of interacted channels estimated by analyzing these optical microscope images using ImageJ software. The average spot size observed on Al increased as the focal length of focusing lens increased. The observed spot size (diameter, $2\omega_0$) was in the range of 230-350 μm ($231.47 \pm 10 \mu\text{m}$ at 10 cm and $354 \pm 16 \mu\text{m}$ at 200 cm), which is apparently different from theoretically estimated values of 50-100 μm . This is because the repetition rate of the laser being 1 kHz, the number of pulses incident on a particular spot of the sample is more than one leading to cumulative effects thereby resulting in an increase in the observed feature size (from which the beam diameter was calculated). Simultaneously, the fluence delivered at target has decreased from 4.7 J/cm^2 to 2 J/cm^2 . This is evidently due to loose focusing of the fs pulses.

Table 4-2 Calculation of fluence delivered at target in different standoff positions by estimating spot size on Al target.

Distance (cm)	spot-size ($2\omega_0$) (μm)	Standard deviation (μm)	Fluence (J/cm^2)
10	231	10.0	4.75
30	238	6.50	4.50
50	309	9.40	2.66
100	324	9.10	2.43
120	355	16.9	2.02

4.3.1.b Classification of nitroimidazoles using PCA (up to ~2 m)

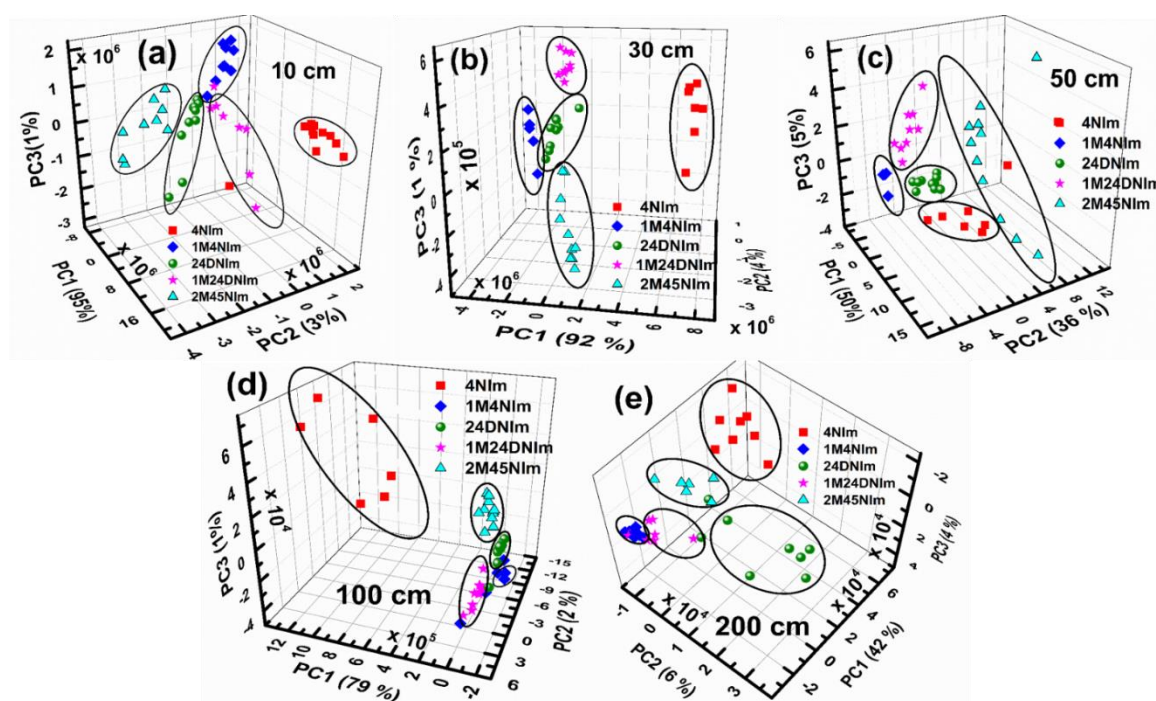


Figure 4.6 PC scores plot of the processed LIBS spectra of nitroimidazoles obtained at (a) 10 cm (b) 30 cm (c) 50 cm (d) 100 cm (e) 200 cm obtained in ST-LIBS.

The fs LIBS spectra of nitroimidazoles obtained at five different standoff distances were merged and processed for impurities such as sodium, calcium which are not the spectral signatures of HEMs and then analyzed through PCA program written in MATLAB. **Figures 4.6(a)-4.6(e)** depict the PC score plots of processed LIBS spectra of nitroimidazoles at different distances i.e. 10, 30, 50, 100, and 200 cm. First three principal components together account for 99%, 97%, 91%, 82%, and 52% of the total variance associated with in the complete data set at respective standoff distances. It is evident that as the standoff distance increases first three PCs could not account for the total variance

Chapter 4

in the data set. **Figures 4.7(a)-4.7(c)** depict the stack plots of first three PCs at 10, 100 and 200 cm respectively. The important spectral features contributing for clustering are C, CN and other atomic and molecular peaks. At farther distances, PCs could not account for the complete variance present in the data set. This could be ascribed to the decrease in signal strength and to the relative increase of noise in the FIBS spectra which deteriorates the discrimination strength of PCA model. The decrease in FIBS signal strength with the increase in standoff distance can be attributed to the following factors (a) the solid angle subtended by the collection system at the plasma (b) intensity of the laser beam (fluence/time) at the sample due to change in spot size and (c) change in filament generation conditions due to different focusing conditions, which are discussed below in detail.

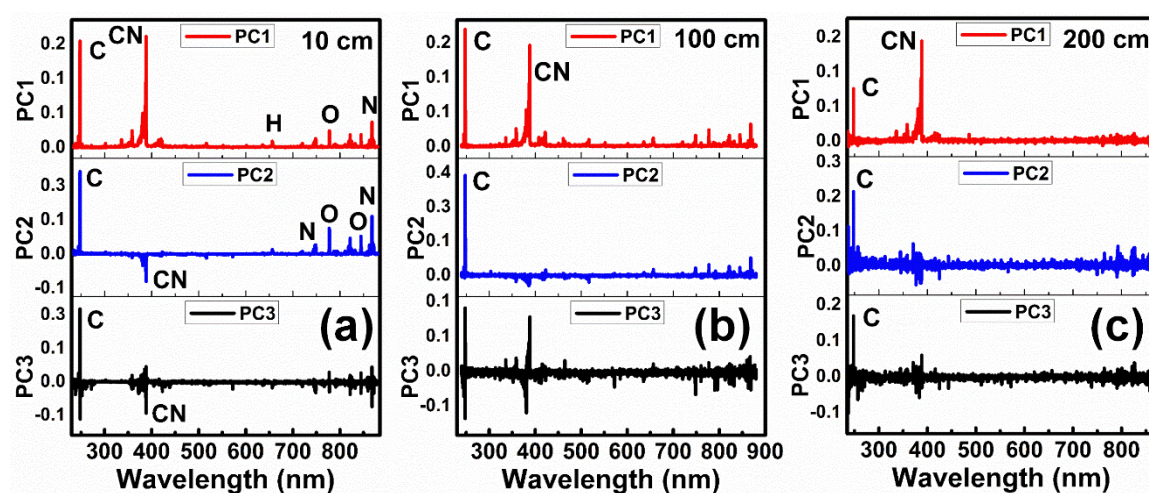


Figure 4.7 First three PCs for the processed fs LIBS spectra of nitroimidazoles at (a) 10 cm (b) 100 cm and (c) 200 cm.

The amount of plasma emissions (flux) collected can be expressed as

$$d\Phi = I \times d\Omega,$$

where 'I' is the luminous intensity of the plasma and $d\Omega = dA/(r^2)$, is the solid angle which varies square inverse with the distance, with collection area (dA) being constant.

Thus, for C1 with input aperture of 2" diameter the solid angle subtended by it at plasma source varies from 0.2 sr to 0.00051 sr from 10 cm to 200 cm, with $1/r^2$ dependence. Consequently, signal entering the collection system decreases and evidently results in decrease in signal strength. The average spot sizes at different working distances were estimated by analysing the interacted portions on an Al target using optical

microscopic data. It is well-known that the spot size (at focus) increases as the focal length of focusing lens increases and, hence, the fluence/intensity decreases (as discussed in the above section). Therefore, an increase in the spot size leads to decrease in the peak intensity. Moreover, the reduction in spectral intensity could also be due to reduced laser energy coupled to the target because of the interaction of filaments. Filaments carry a small fraction of laser energy and bulk of the laser energy is carried by the energy reservoir [85]. The ablation efficiency is governed by the filaments as well as the energy reservoir around the filaments. For lenses with larger focal lengths, especially with $f > 50$ cm, the ablation process could be due to filaments and the process can be termed as filament ablation. With increasing focal length, though the filament holds the same energy and diameter ($\sim 100 \mu\text{m}$), the energy density of the energy reservoir may change and hence the ablation efficiency along with the SNR of the LIBS spectrum is affected.

4.3.2 Remote LIBS of HEMs and metals (configuration 2)

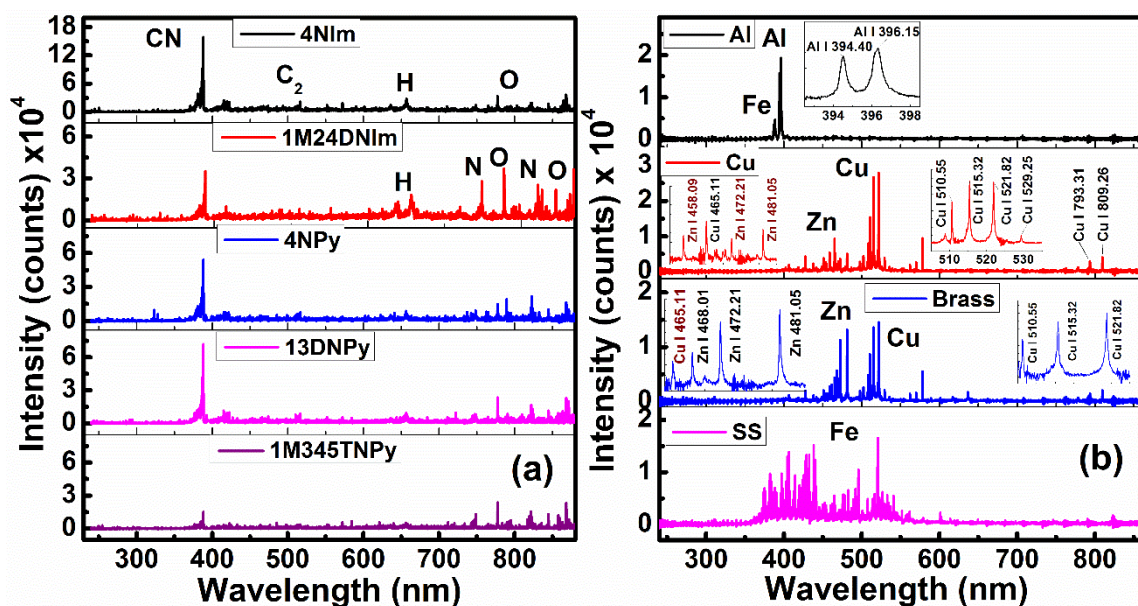


Figure 4.8 Stack plots of (a) representative fs R-LIBS spectra of explosive molecules (nitroimidazoles and nitropyrazoles) and (b) metals (Aluminum, copper, brass, and stainless steel) obtained at 8.5 m away.

As shown in **figure 4.1** and described in experimental section, metals [aluminum (Al), copper (Cu)], alloys [brass, stainless steel (SS)] and HEMs were investigated in R-LIBS setup by focusing fs pulses tightly with a 10 cm lens and using a Schmidt-Cassegrain telescope (SCT) was to collect plasma emissions at ~ 8.5 m away. The transmission range of SCT is in visible range and quickly falls off towards UV region, thus could not allowing to capture carbon emissions (C I 247.8 nm in the UV spectral

region). **Figure 4.8(a)** depicts typical R-LIBS spectra of HEMs (240-870 nm) and **figure 4.8(b)** shows the R-LIBS spectra of metals and alloys (M&A) in the wavelength region of 240-870 nm recorded at a remote distance of ~8.5 m. Few intense peaks are identified and labeled in the pictures. All HEMs exhibited CN violet ($B^2\Sigma^+ - X^2\Sigma^+$) and C_2 swan band. In CN violet band, $\Delta v=0$ band was dominantly visible compared $\Delta v=-1$ while $\Delta v=+1$ (358-359 nm) band is absent in all HEMs as the transmission of telescope falls after 400 nm and reaches ideally zero at 370 nm. In C_2 swan band ($d^3\Pi_g / a^3\Pi_u$), $\Delta v=0$ band head at 516.53 nm was observed in all HEMs. The peaks observed in Al are Al I 396.34 nm, Al I 394.52 nm, Fe I 388.69 nm, Fe I 386.93 nm. Very weak aluminum oxide (AlO; $B^2\Sigma^+ \rightarrow X^2\Sigma^+$) molecular band transitions were observed in Al R-LIBS spectra. Several copper and zinc peaks were observed in copper and brass targets and lower intensity of zinc lines in copper target implies that Zn was an impurity in copper target. **Table 4-3** lists prominent peaks identified in R-LIBS spectra of SS, brass and copper.

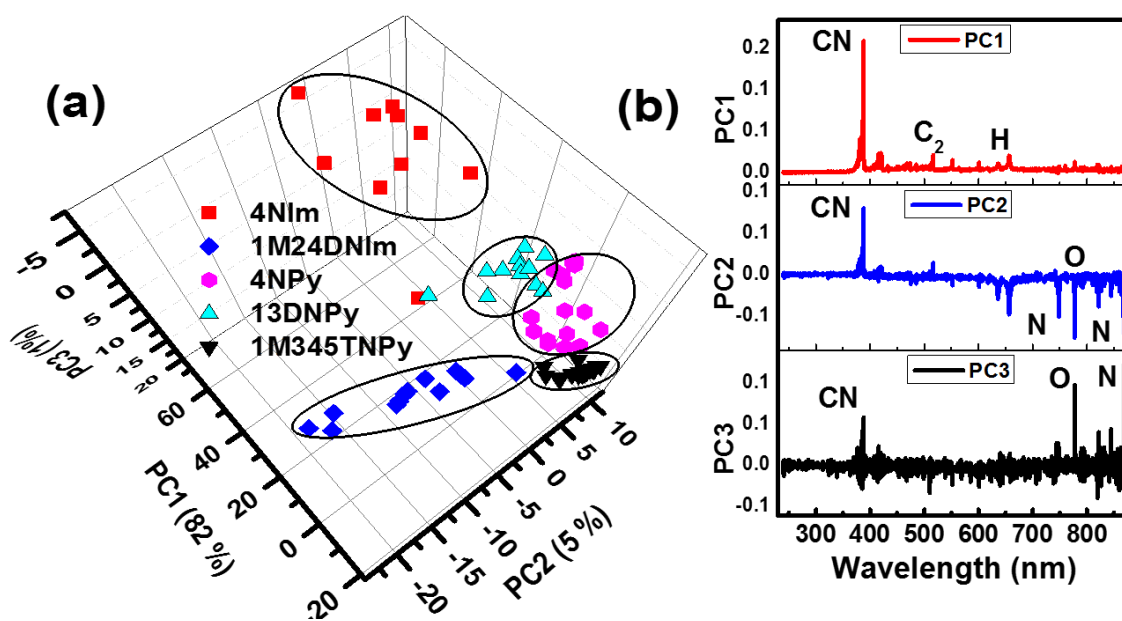


Figure 4.9 (a) 3D PC scores plot and (b) first three PCs of processed R-LIBS spectra of explosives (nitroimidazoles and nitropyrazoles) obtained from principal component analysis.

Figure 4.9(a) shows the PCs score plot of R-LIBS spectra of HEMs and **figure 4.9(b)** shows the corresponding PCs. First three principal components together accounts for 88% of the variance present in the data set, with PC1 being the strongest with 82%, followed by PC2 with 5% and PC3 with 1%. The essential spectral features in classification are C, H, N, O atomic peaks and CN, C_2 molecular bands. Major spectral

features from PC1 are CN, C₂ and hydrogen. CN, O, N, H are prominent features in PC2, whereas CN, O, and N in PC3.

Table 4-3 Atomic and ionic transitions identified in R-LIBS spectra of stainless steel, brass and copper and labeled using NIST atomic spectroscopic data base.

Elements	Observed Wavelength (nm)	NIST wavelength (nm)	Elements	Observed Wavelength (nm)	NIST wavelength (nm)
Stainless Steel					
Fe I	390.05	390.05	Cr I	390.93	390.87
Fe I	390.38	390.29	Cr I	391.56	391.62
Fe I	390.74	390.74	Cr I	391.97	391.91
Fe I	391.49	391.42	Cr I	392.83	392.86
Fe I	392.01	392.02	Cr I	397.02	396.97
Fe I	392.35	392.29	Cr I	398.46	398.43
Fe I	393.1	393.11	Cr I	400.20	400.14
Fe I	395.73	395.70	Cr I	403.97	403.90
Fe I	396.46	396.45	Cr I	404.94	404.87
Fe I	396.71	396.74	Cr I	434.04	433.97
Fe I	399.81	399.80	Cr I	434.54	343.45
Fe I	400.59	400.52	Cr I	438.44	438.49
Fe I	401.87	401.82	Cr I	439.95	439.98
Fe I	404.64	404.60	Cr I	446.28	446.27
Fe I	407.24	407.25	Cr I	446.56	446.53
Fe I	408.01	408.02	Cr I	446.72	446.75
Fe I	408.41	408.44	Cr I	450.32	450.30
Fe I	410.83	410.81	Cr I	452.71	452.64
Fe I	411.38	411.29	Cr I	452.90	452.98
Fe I	413.28	413.28	Cr I	453.16	453.12
Fe I	414.45	414.38	Cr I	453.49	453.57
Fe I	418.29	418.27	Cr I	454.11	454.10
Fe I	419.99	419.90	Cr I	454.16	454.15
Fe I	420.27	420.20	Cr I	460.17	460.10
Fe I	422.03	422.03	Cr I	461.70	461.73
Fe I	423.62	423.59	Cr I	469.95	469.95
Fe I	424.32	424.38	Cr I	464.70	464.61
Fe I	424.58	424.52	Cr I	473.79	473.73
Fe I	425.50	425.55	Cr I	475.28	475.2
Fe I	426.39	426.42	Cr I	475.52	475.51
Fe I	427.23	427.17	Cr I	475.70	475.73
Fe I	427.54	427.56	Cr I	476.72	476.72
Fe I	429.05	429.05	Cr I	482.47	482.42
Fe I	430.87	430.79	Cr I	488.77	488.70

Chapter 4

Fe I	431.59	431.50	Cr I	492.28	492.22
Fe I	431.59	432.57	Cr I	520.58	520.45
Fe I	432.68	432.67	Cr I	520.67	520.6
Fe I	433.80	433.82	Cr I	520.93	520.84
Fe I	435.24	435.27	Cr I	526.53	526.57
Fe I	436.04	436.04	Cr I	532.89	532.83
Fe I	437.20	437.29	Cr I	579.22	579.1
Fe I	440.55	440.50	-	-	-
Fe I	442.34	442.38	Mn I	397.75	397.70
Fe I	444.36	444.31	Mn I	404.20	404.13
Fe I	445.24	445.26	Mn I	406.14	406.17
Fe I	445.93	445.91	Mn I	413.54	413.50
Fe I	448.32	448.37	Mn I	414.94	414.88
Fe I	449.07	449.00	Mn I	418.85	418.99
Fe I	449.57	449.59	Mn I	423.46	423.51
Fe I	455.12	455.16	Mn I	428.12	428.11
Fe I	458.07	458.05	Mn I	431.16	431.25
Fe I	459.20	459.26	Mn I	462.70	462.65
Fe I	459.37	459.35	Mn I	470.90	470.97
Fe I	459.66	459.64	Mn I	472.83	472.74
Fe I	461.42	461.42	Mn I	601.39	601.35
Fe I	463.27	463.29	-	-	-
Fe I	463.53	463.58	Mg I	405.64	405.75
Fe I	463.81	463.80	Mg I	405.96	405.93
Fe I	466.71	466.74	Mg I	416.60	416.72
Fe I	469.02	469.01	Mg I	457.06	457.10
Fe I	471.08	471.02	Mg I	473.15	473.00
Fe I	471.20	471.21	Mg I	517.24	517.25
Fe I	477.11	477.11	-	-	-
Fe I	479.02	479.07	-	-	-
Fe I	480.24	480.28	Ni I	447.08	447.04
Fe I	484.02	484.03	Ni I	460.62	460.62
Fe I	487.20	487.21	Ni I	471.52	471.57
Fe I	492.16	492.05	Ni I	483.00	482.90
Fe I	493.96	493.96	Ni I	490.43	490.44
Fe I	495.58	495.75	Ni I	544.59	543.58
Fe I	500.38	500.40	Ni I	558.80	558.78
Fe I	501.59	501.49	Ni I	566.39	566.40
Fe I	516.82	516.88	-	-	-
Fe I	519.29	519.23	-	-	-
Fe I	522.61	522.68	-	-	-
Fe I	522.80	522.71	-	-	-
Fe I	523.25	523.29	-	-	-

Fe I	526.76	526.72	-	-	-
Fe I	527.06	527.03	-	-	-
Fe I	534.18	534.10	-	-	-
Fe I	534.94	534.97	-	-	-
Fe I	537.23	537.14	P I	507.89	507.93
Fe I	539.83	539.82	P I	510.94	510.96
Fe I	540.16	540.12	P I	534.68	534.58
Fe I	540.53	540.53	P I	547.77	547.76
Fe I	541.07	541.09	-	-	-
Fe I	546.42	546.42	Si I	500.69	500.60
Fe I	548.18	548.14	Si I	563.90	563.99
Fe I	574.79	574.79	SI I	566.00	565.99
Fe I	576.36	576.29	Si I	575.47	575.42
Fe I	581.66	581.63	-	-	-
Fe I	608.58	608.52	-	-	-
Fe I	623.21	623.26	-	-	-
Fe I	649.60	649.64	-	-	-
Brass			Copper		
Cu I	402.34	402.26	Cu I	402.32	402.26
Cu I	407.24	407.31	Cu I	406.39	406.26
Cu I	437.95	437.81	Cu I	427.60	427.51
Cu I	458.81	458.69	Cu I	448.13	448.03
Cu I	465.24	465.11	Cu I	453.18	453.07
Cu I	510.66	510.55	Cu II	454.58	454.64
Cu I	515.39	515.32	Cu I	458.78	458.69
Cu I	521.90	521.81	Cu I	465.22	465.11
Cu I	529.38	529.25	Cu I	470.56	470.45
Cu I	535.57	535.49	Cu I	510.63	510.55
Cu I	570.12	570.02	Cu I	515.39	515.32
Cu I	578.33	578.21	Cu I	521.83	521.82
Zn I	468.15	468.01	Cu I	529.34	529.25
Zn I	472.33	472.21	Cu I	570.08	570.02
Zn I	481.19	481.05	Cu I	578.29	578.21
Zn I	636.41	636.23	Zn I	468.09	468.01
Ni I	497.85	498.01	Zn I	472.33	472.21
Ni I	501.80	501.75	Zn I	481.16	481.05
Ni I	562.23	562.53	-	-	-
Sn I	617.07	617.15	-	-	-
Mn I	405.86	405.89	-	-	-
Mn I	406.36	406.35	-	-	-

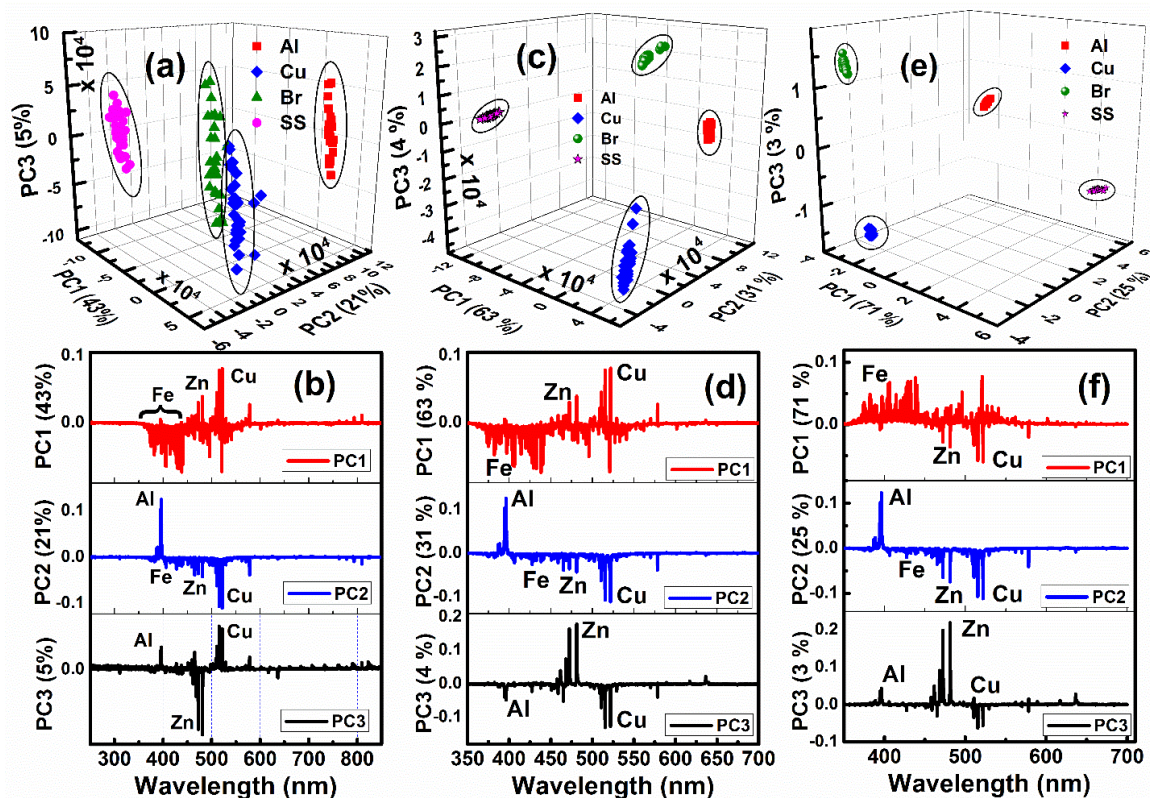


Figure 4.10 (a) PC score plots and (b) first three PCs of R-LIBS spectra of metals in 220-870 nm spectral region, (c) PC score plot and (d) first three PCs of R-LIBS spectra of metals in 350-700 nm, (e) PC score plot and (f) first three PCs of normalized R-LIBS spectra in 350-700 nm wavelength region.

Figure 4.10(a) shows the PC score plot for R-LIBS spectra of metals (Al, Cu) and alloys (brass and SS) for the entire spectral region (220 nm-870 nm). From, figure it is apparent that Al and stainless steel are well separated and easily distinguished. Brass and Copper clusters are also clearly grouped though they are slightly grouped together and this could be attributed to the low grade of copper with zinc impurities making it to similar with brass. **Figure 4.10(b)** displays the first three PCs, from the PCA analysis of R-LIBS spectra of metals and alloys, which accounted for most of the variance present in the data set. The PCs thus obtained through the analysis explain the important spectral features from various samples. The first three PCs together accounted for 69% (43%, 21%, 5%) of variance. Out of these PCs, first PC is similar to SS with transitions of Fe and has also Cu and, Zn thus indicating the spectral features of either Cu or brass, or both and SS. However, the data is dominated by SS spectral features. Second PC has lines of Al with maximum magnitude followed by Cu, Zn and Fe and, therefore, has spectral features from all the components. Thus, first and second PCs, possess spectral features of all the samples considered. The third PC has Zn lines with maximum magnitude and

followed by Cu and Al. The contribution from the spectral features of stainless steel is very feeble and thus can be ignored. Other higher PCs (fourth, fifth, etc.) are insignificant as they account for minimal variance (less than the third PC) and thus can be neglected. However the classification obtained in PCA can be improved by selectively discarding the insignificant spectral region which doesn't contribute much for the classification. However, the spectral region from 700-870 nm of R-LIBS spectra of M&A [from **figure 4.8(b)**] can be excluded as it does not contain any signature. **Figure 4.10(c)** illustrates the PC score plot and **figure 4.10(d)** shows the first three PCs of R-LIBS spectra of metals and alloys in the spectral region 350-700 nm. The first three PCs together account for 98% (63%, 31%, 4%) of variance. Consequently, copper and brass targets are well discriminated. Furthermore, normalizing the spectra slightly improved the discrimination as seen from the PC score plot **figure 4.10(e)**, where the first three PCs together accounted for 99% (71%, 25%, 3%) of variance present in the entire data set. **Figure 4.10(f)** shows the first three PCs which contain the significant spectral information contributing to the discrimination. **Table 4-4** summarizes the improved PCA results of R-LIBS spectra of M&A after removing the insignificant spectral region. Comparing the PCA results of HEMs in case of ST-LIBS (up to 2 m) with C1 and R-LIBS by SCT as collection systems (where entire spectral region was considered for analysis), 88% of variance accounted in R-LIBS is comparable with the 91% of variance accounted at 50 cm. Thus, collection optics such as telescopes with large entrance aperture and large f-number should be utilized for standoff applications. Concurrently, the discrimination results obtained from the R-LIBS spectra of metals proves the potential of R-LIBS technique for quick elemental analysis and to identify the critical spectral signatures in order to categorize the targets investigated.

Table 4-4 Results from principal component analysis of R-LIBS spectra of metals (Al, Cu) and alloys (brass, stainless steel)

R-LIBS (M&A)	PC1 (%)	PC2 (%)	PC3 (%)	Total variance (%)
220-870 nm	43	21	5	69
350-700 nm	63	31	4	98
350-700 nm (norm)	71	25	3	99

4.3.3 ST-FIBS studies of metals and alloys, bimetallic strips, geological samples and energetic molecules at ~6.5 m/ ~8 m in fs ST-FIBS2 setup (configuration 3)

After successfully recording the fs FIBS signal of energetic molecules in standoff mode (at ~2 m distance) and detecting them in R-LIBS configuration (8.5 m away), our next objective was to detect these hazardous molecules at the maximum true standoff distance possible within the laboratory conditions. Our aim is to develop a true standoff configuration to investigate and categorize various other materials such as (a) metals and alloys (low grade samples) (b) bimetallic targets (highly pure) (c) geological rocks and (d) high energy materials (HEMs) by delivering femtosecond pulses to longer distance (sample details are listed in table 1) in the form of filaments. Hence a two lens configuration was utilized to generate fs filaments and as well to focus at desired position by changing the distance between them. **Figure 4.2** depicts the experimental schematic of the fs ST-FIBS2 setup (~6.5 m/ ~8 m), where fs filaments were focused onto a target at a distance of ~6.5 m (as measured from L2) and a SCT was used to collect the optical emissions from various samples from ~8 m away. L1 is a plano-concave lens (PCV or PCC) which diverges the beam (on to L2) and L2 is a plano-convex lens (PCX) which converges or focus the beam to form forced filaments. Two such lens combinations were tried (table 4.5) to generate fs filaments and the second combination was chosen for the experiments. The advantage of this combination is the production of more intense and slightly shorter filament compared to the one obtained in the first combination as shown in the **figure 4.11(a) and 4.11(b)**. It was ensured that the beam was precisely incident on the (i) center of lenses and (ii) normal to the lenses to minimize aberration effects from lenses. The most intense part of the filament [86] was made to interact with the target's (either HEMs or metallic targets) surface normally [87].

Table 4-5 Combination of lenses used to generate fs filaments at desired distances

S. No.	PCV (L1)	PCX (L2)	Effective focal length (f_{eff})	Distance between L1 and L2 (d)
1	f= -100 cm, 2"(dia.)	f= +100 cm, 2" (dia.)	6.5 m	16 cm
2	F= -50 cm, 2"(dia.)	f= +100 cm, 2" (dia.)	6.5 m	63 cm

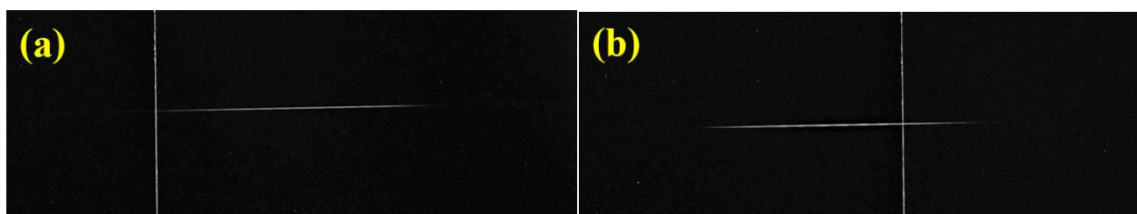


Figure 4.11 (a) and (b) depict the images of fs filaments obtained using lens combination 1 and lens combination 2. These photos are captured using DSLR camera with an exposure time of 30 s at 30 cm away from the filaments.

4.3.3.a ST-FIBS studies of metals and alloys (M&A)

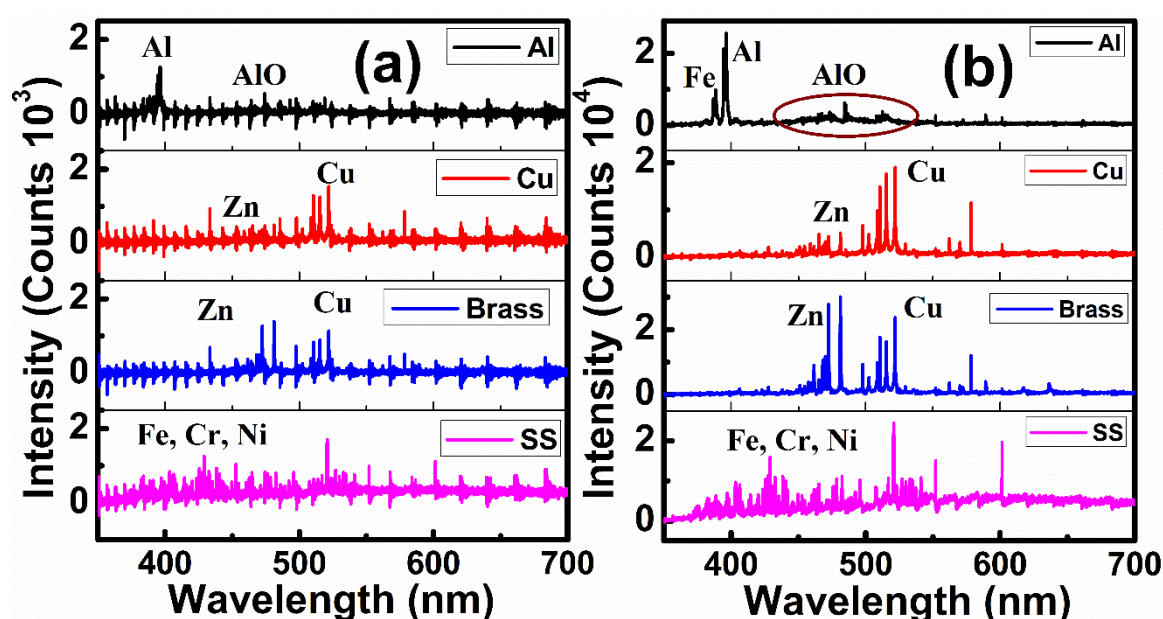


Figure 4.12 Femtosecond ST-FIBS spectra of metals (Al, Cu) and alloys (brass, stainless steel) recorded in configuration 3 with ICCD gain (a) 1000 (1 k) and (b) 2500 (or 2.5 k).

The fs ST-FIBS spectra of metals and alloys M&A were acquired using a gate delay 50 ns, gate width 2 μ s, 1.5 s exposure time at two different ICCD gains 1000 and 2500 in the fs ST-FIBS2 experimental setup (**figure 4.2**) with an intention to investigate and compare the results obtained in R-LIBS case (where ICCD gain was 1 k). Each acquired spectra is the resultant of 6 accumulations. For all M&A targets 25-30 ST-FIBS spectra per sample were recorded. **Figures 4.12(a) and 4.12(b)** represents the stack plots of fs ST-FIBS spectra of M&A obtained at \sim 6.5 m with ICCD gain 1000 and 2500. The SNR of LIBS spectra in **figure 4.12(a)** is poor and can be improved with increasing the number accumulations. However, better SNR was achieved upon increasing the ICCD gain to 2500 as demonstrated in the data of **figure 4.12(b)**. Thus, an optimum/optimized utilization of ICCD is required for better results in standoff experiments.

4.3.3.b Difference between ablation with tightly focused fs pulses and fs filaments

While comparing the R-LIBS spectra [figure 4.8(b)] and the ST-LIBS spectra [figure 4.12(a)] of M&A acquired at 1000 ICCD gain, it is evident that spectral intensities obtained in the case of fs ST-LIBS spectra are lower, though the collection distance (~8.5 m, 8 m) and collection angle were nearly same. The striking difference observed in the intensity among these two configurations could be attributed to the plasma generation conditions, where tightly focused fs pulses (using a 10 cm lens) and loosely focused filaments are the plasma generation sources in R-LIBS case and in ST-FIBS case, respectively. The fluence at the interaction zone is much higher in case of tightly focused fs pulses compared to the loosely focused filaments. Though filaments can propagate long distances (depending on energy and peak-power of fs pulses) and deliver substantial intensities at remote locations, their ablation efficiency is lower when compared to tightly focused fs pulses since the energy is distributed along the length of the filament, which is called as energy reservoir or photon reservoir [75]. Consequently, the ablation crater is also small and results in cold plasma (with less atomic, ionic and electron density and thus favors the AIO molecular formation.

AIO molecular band ($B^2\Sigma-X^2\Sigma$) is clearly observed in ST-FIBS spectra of Al recorded with an ICCD gain of 2500 [figure 4.12(b)] whereas its intensity is feeble in the R-LIBS spectra [figure 4.8(b)] as well as ST-FIBS spectra of Al recorded with an ICCD gain of 1000 [figure 4.12(a)]. However, observing the intensity ratio of AIO molecular band head at 484.2 nm to that of Al atomic transition at Al I 396.15 nm (figure 4.13) will provide an insight into the favored molecular formation in the case of fs filament ablation. The intensity ratio of AIO/Al was nearly zero (0.02) in the case of R-LIBS whereas it is 0.22 in case of fs ST-FIBS. Furthermore, it can be noticed from the inset of figure 4.13 that the AIO/Al ratio was unchanged (0.22) when gain is varied from 1000 to 2500. Thus we can conclude that AIO molecular formation is favored in the case of fs filament ablation compared to tightly focused fs pulses ablation as the AIO/Al ratio is higher in the former case. From these results it is also evident that gain of the ICCD did not affect the plasma parameters.

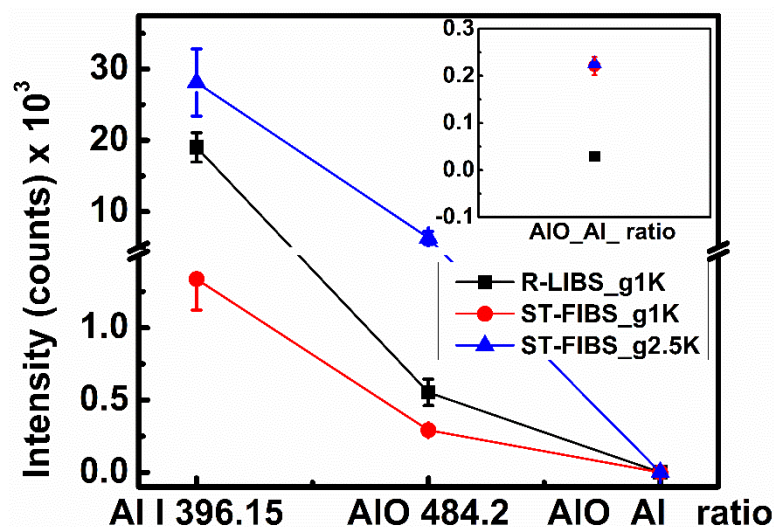


Figure 4.13 AIO/Al ratio in the obtained in R-LIBS configuration (black/square), fs ST-FIBS2 (~6.5m/ ~8 m) configuration at two different ICCD gains [1000; Red/circles and 2500; blue/triangles). The inset shows the AIO/Al ratio obtained in both the configurations. AIO/Al was unchanged when gain is switched from 1000 to 2500 in case of fs ST-FIBS spectra of Al.

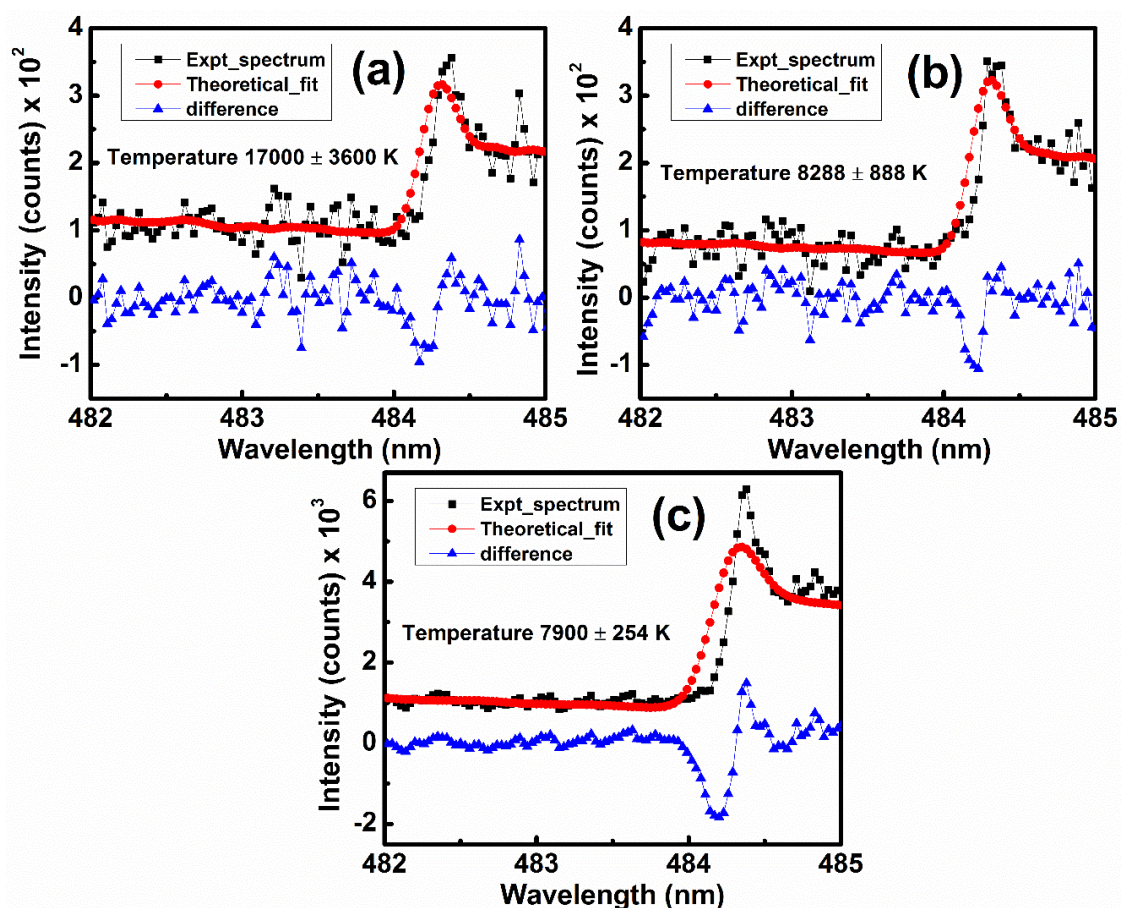


Figure 4.14 Estimation of plasma temperature by theoretically fitting AIO molecular band head at 484.2 nm in the spectral range of 482-485 nm in aluminum spectra obtained in (a) R-LIBS (b) ST-FIBS with ICCD gain 1000 and (c) with ICCD gain 2500, using NMT algorithm. The curves with black squares are experimental data while the curves with red circles are the theoretical fits and the curves with blue triangles are the difference between experimental data and theory.

Chapter 4

Further, the vibrational temperature of AIO molecular band ($B^2\Sigma^+ \rightarrow X^2\Sigma^+$ band system) in different configurations was estimated by theoretically fitting the AIO band head at 484.2 nm in the spectral region of 480-485 nm using NMT algorithm. Only AIO band head at 482.4 nm was considered for evaluating vibrational temperature as AIO bands were weak and not evolved prominently especially in the case of R-LIBS spectra of Al. **Figures 4.14(a)-4.14(c)** depict the comparison between the experimental spectrum and the theoretical fit obtained from NMT algorithm in various conditions viz. R-LIBS with gain 1000, ST-FIBS with gain 1000 and ST-FIBS with gain 2500. The average estimated temperature is 17000 ± 3600 K in the case of R-LIBS, 8288 ± 888 K and 7900 ± 254 K in the case of fs FIBS with gain 1000 and with gain 2500, respectively. From this it is evident that fs filament induced plasma is colder in nature compared to plasma produced with tightly focused pulses and, therefore, the molecular formation is favored in fs filament induced plasma.

4.3.3.c PCA analysis of ST-FIBS spectra of M&A at different ICCD gains

Figures 4.15(a) and 4.15(b) illustrate the PC score plots of normalized (to maximum intensity) fs ST-FIBS spectra of M&A at two ICCD gains of 1000, 2500 in the spectral range of 350-700 nm and **figures 4.15(c) and 4.15(d)** depict the respective principal components (PCs). First three PCs together accounted for 73% (60%, 10%, 3%) and 98% (74%, 21%, 3%) of the total variance associated, with the first PC being highest. Better grouping or clustering was achieved for the data with higher gain. This could be attributed to increased SNR, which is also evident from the first three PCs. In both the cases, PC1 and PC2 includes the spectral features from Al, Cu, brass and SS. However, PC3 (with gain 1000) resembles only few spectral features (from Zn) buried in noise compared to the one with high gain where Zn and Cu lines are clearly visible. Thus, the use of ICCDs facilitated the standoff diagnosis by offering higher gain and broadband single shot analysis.

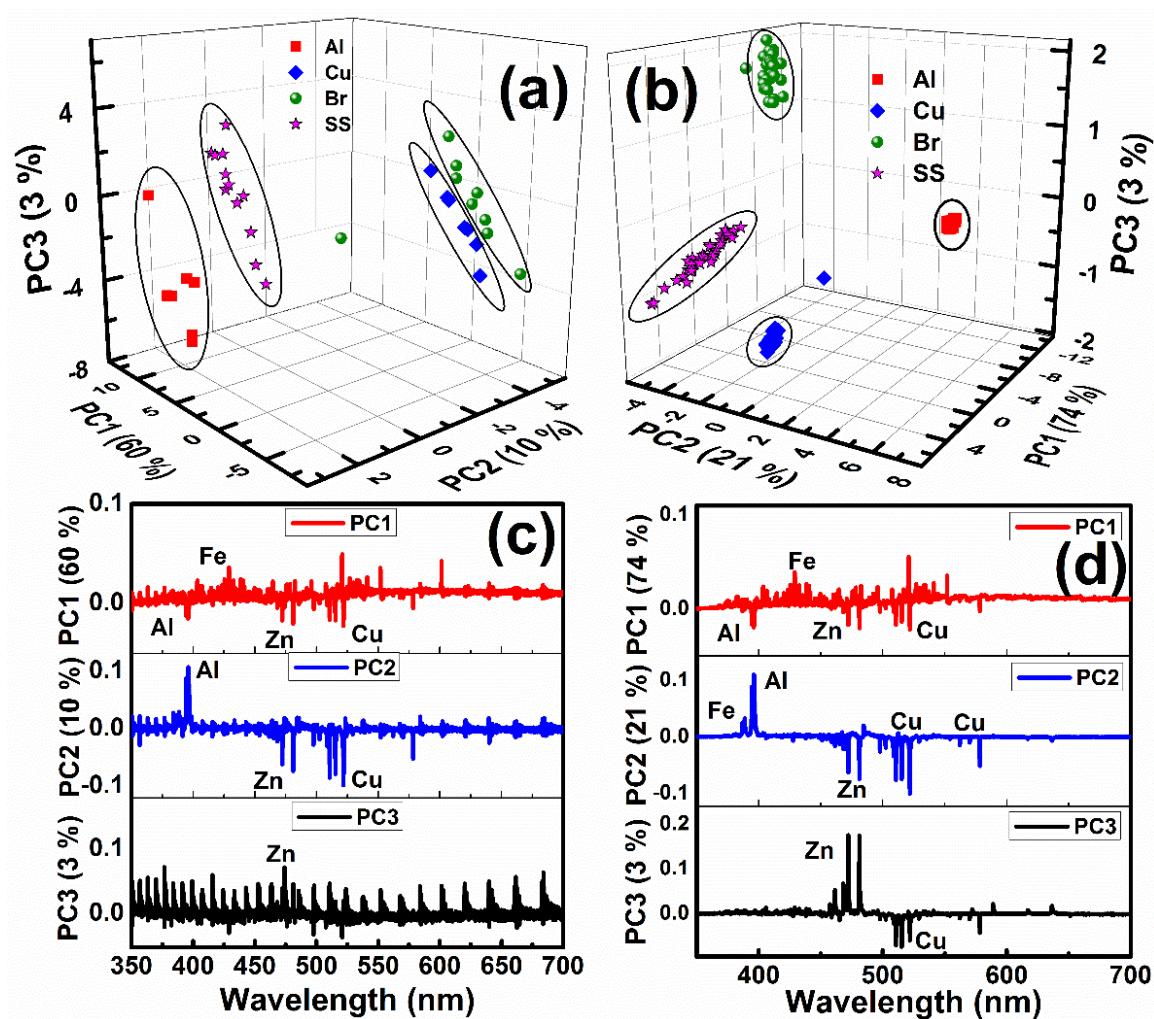


Figure 4.15 PC score plots of ST-FIBS spectra of metals with ICCD gain of (a) 1000 and (b) 2500 (c), (d) represent the principal components (PCs).

4.3.3.d ST-FIBS studies of bimetallic targets

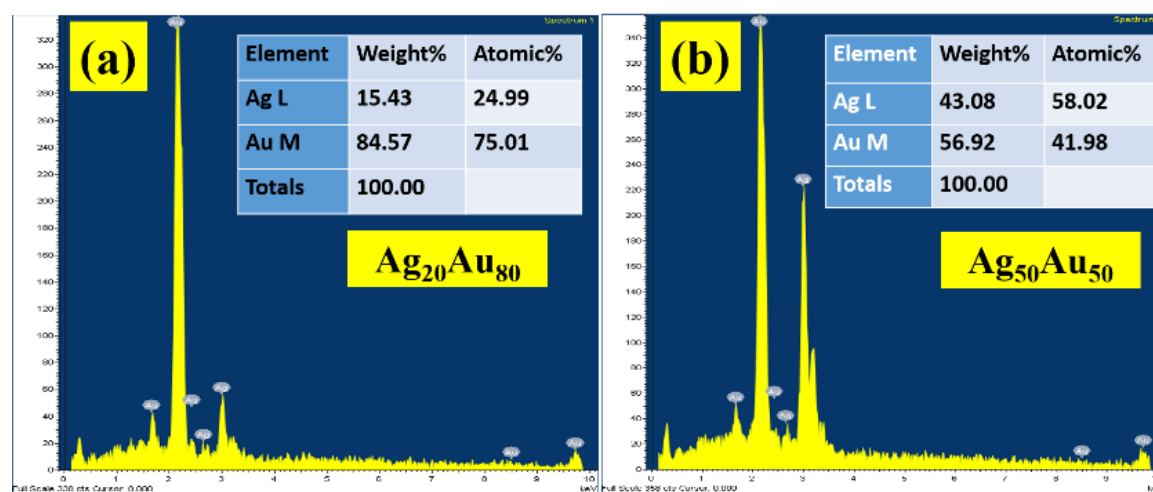


Figure 4.16 Energy dispersive X-ray spectroscopy images depicting the composition and purity of $\text{Ag}_{20}\text{Au}_{80}$ and $\text{Ag}_{50}\text{Au}_{50}$ bimetallic strips.

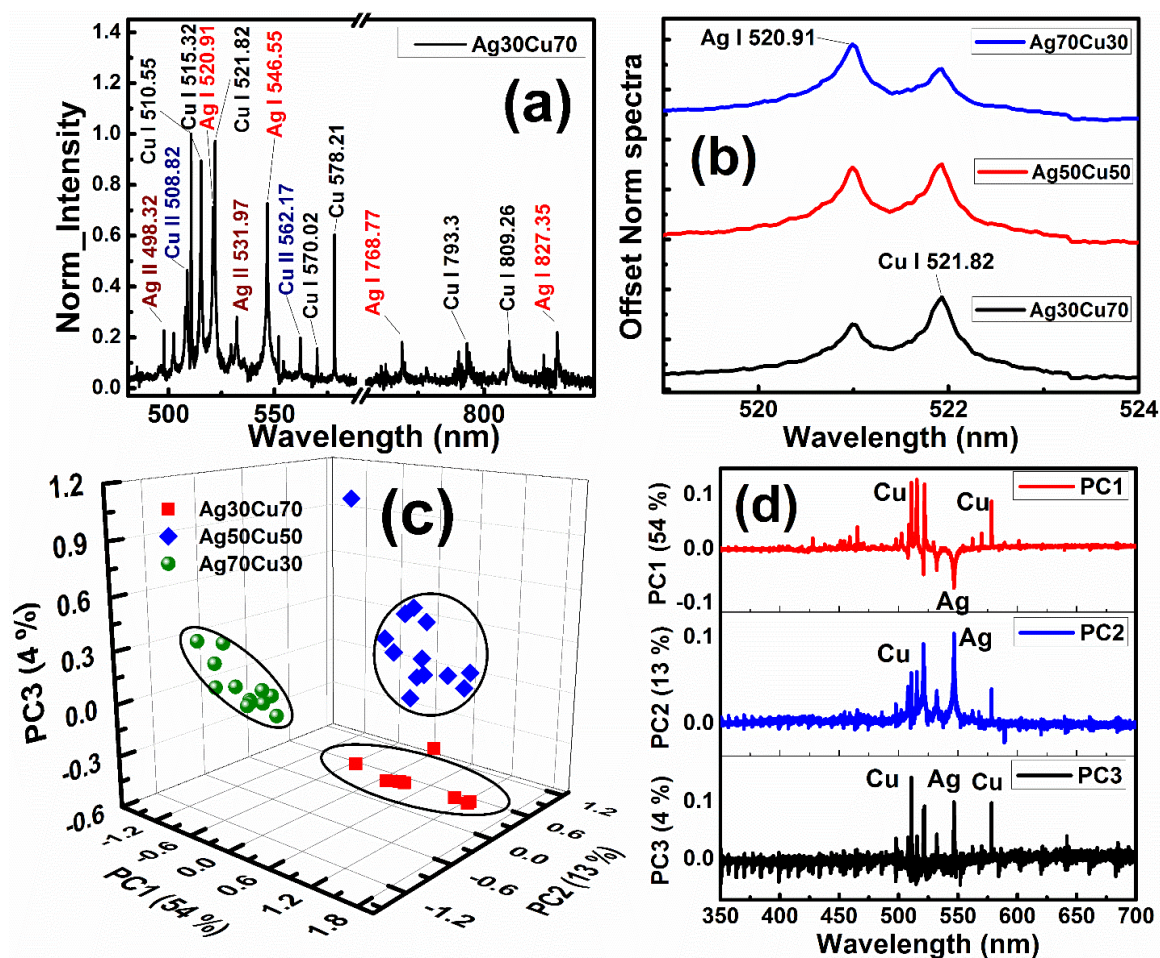


Figure 4.17 (a) ST-FIBS spectra of $\text{Ag}_{30}\text{Cu}_{70}$ bimetallic strips (b) Intensity variation of Ag I (520.91 nm) and Cu I (521.82 nm) peaks in bimetallic strips (c) PC score plot and (d) principal components of ST-FIBS spectra of Ag@Cu bimetallic targets obtained from PCA.

High purity Ag, Au and Cu metal strips were melted and mixed to fabricate two types of bimetallic strips viz., Ag@Au [$\text{Ag}_{80}\text{Au}_{20}$ up to $\text{Ag}_{20}\text{Au}_{80}$; 7 combinations] and Ag@Cu [$\text{Ag}_{30}\text{Cu}_{70}$ up to $\text{Ag}_{70}\text{Cu}_{30}$; 3 combinations] with varying weight percentage of Ag, Au and Ag, Cu at a local goldsmith shop (details are given in table 4.1). **Figures 4.16(a)-4.16(b)** represents a typical EDX spectra of $\text{Ag}_{20}\text{Au}_{80}$ and $\text{Ag}_{50}\text{Au}_{50}$ bimetallic targets displaying the purity and concentration of Ag and Au in the respective bimetallic strips. **Figure 4.17(a)** shows a typical normalized fs ST-FIBS spectra of $\text{Ag}_{30}\text{Cu}_{70}$ bimetallic strip in spectral region 480-840 nm (with break in 590-755 nm) with ionic and atomic peaks of Ag and Cu labeled with the aid of NIST data base [88]. **Figure 4.17(b)** illustrates the variation of Ag and Cu atomic peaks (Ag I 520.91 nm, Cu I 521.82 nm) with varying concentration of Ag and Cu. Normalized peak intensities exactly reflected the bimetallic weight percentage with Ag I peak intensity being highest in $\text{Ag}_{70}\text{Cu}_{30}$, equal in $\text{Ag}_{50}\text{Cu}_{50}$ and lowest in $\text{Ag}_{30}\text{Cu}_{70}$ when compared to Cu I 521.82 nm peak.

Figures 4.17(c) and 4.17(d) illustrate the PC score plot and first three PCs of normalized fs ST-FIBS spectra of Ag@Cu bimetallic targets in 470-650 nm spectral range. First three PCs accounted for 71% of total variance (54%, 13%, 4%) present in the data set. However, the classification can be improved by avoiding the spectral range which doesn't include any spectral features. The essential spectral features contributing for classification or discrimination are from both copper and silver.

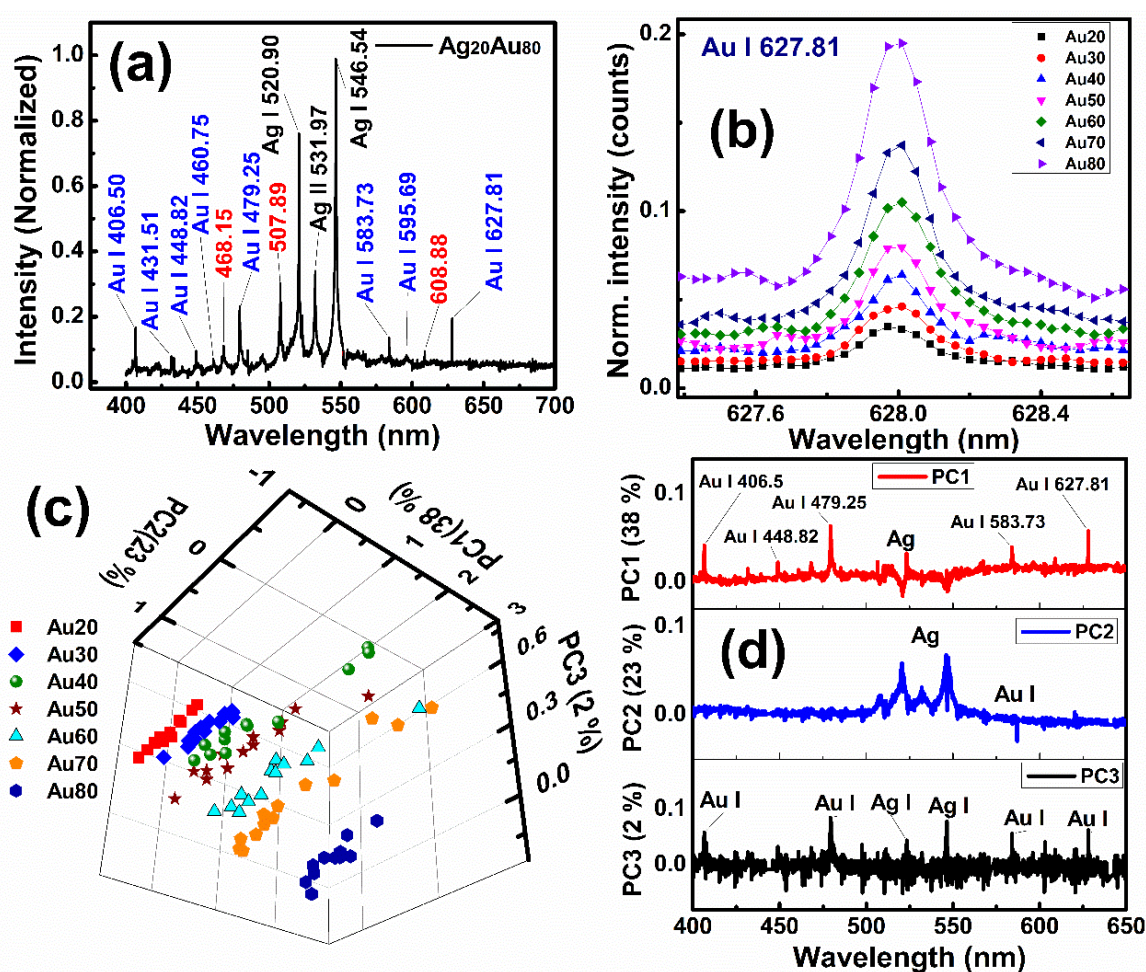


Figure 4.18 (a) Representative ST-FIBS spectra of Ag₂₀Au₈₀ bimetallic strip. (b) Intensity variation of Ag I (627.81 nm) peak with variation of Ag weight percentage (c) PC score plot and (d) principal components obtained from PCA of Ag@Au bimetallic targets.

A set of seven Ag@Au bimetallic targets (with varying weight percentages) were investigated in the same ST-FIBS configuration. Composition and purity of all the bimetallic targets was verified by recording energy dispersive X-ray spectra (EDX). **Figures 4.16(a)-4.16(b)** illustrate the EDX spectra of Ag₂₀Au₈₀ and Ag₅₀Au₅₀ bimetallic targets. **Figure 4.18(a)** depicts typical normalized ST-FIBS spectra of Ag₂₀Au₈₀ bimetallic strip in spectral region from 400-700 nm. Ag and Au transitions in FIBS

Chapter 4

spectra were identified and labeled using NIST data base [88]. Most of the persistent atomic and ionic transitions of Au lie in UV spectral region and, therefore, the observed Au transitions in visible region are weak. However, one persistent atomic transition of Au was observed at Au I 627.81 nm along with Au I 406.5 nm and Au I 479.25 nm, which are relatively strong transitions. **Figure 4.18(b)** data demonstrates that the Au I (627.81 nm) peak intensity increased linearly with increase in the weight percentage of Au (i.e. from Ag₈₀Au₂₀ to Ag₂₀Au₈₀). **Figures 4.18(c) and 4.18(d)** illustrate the PC score plot and first three PCs of normalized fs ST-FIBS spectra of Ag@Au bimetallic targets, respectively, in the 400-650 nm spectral range obtained from PCA analysis. The first three PCs accounted for 63% of total variance (38%, 23%, 2%) present in the data set. First PC depicts the essential spectral features from both Ag and Au contributing towards the discrimination. Second PC is dominated by spectral features of Ag. Even though the Au I emission intensities in ST-FIBS are relatively weaker (because of absence of persistent transitions in the visible region), the achieved classification of Ag@Au bimetallic strips using PCA was promising.

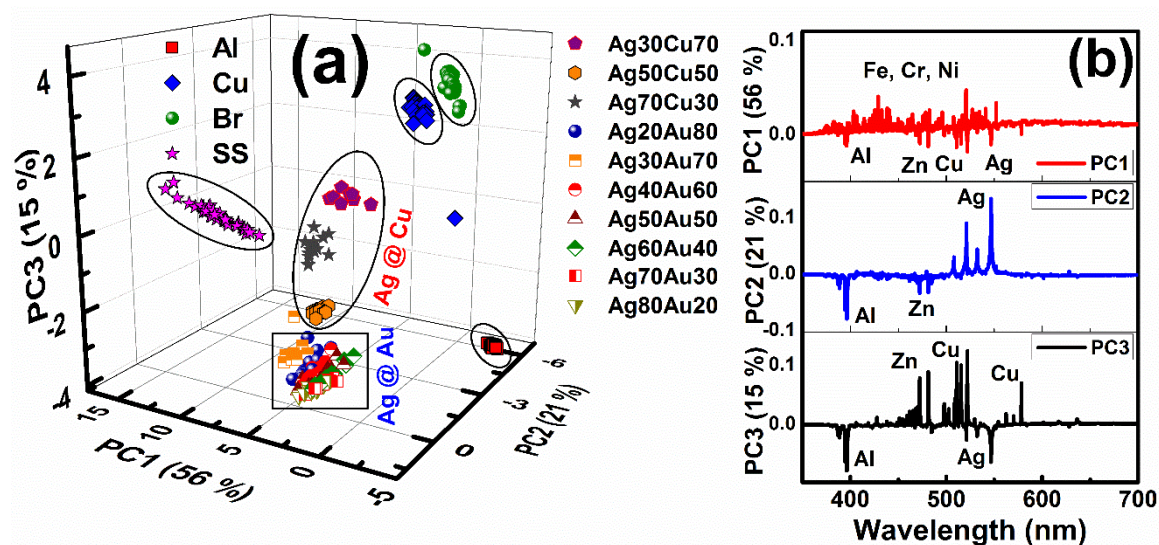


Figure 4.19 (a) PC score plot of fs ST-FIBS spectra of metals and bimetallic targets (b) represents principal components (PCs).

Finally, the classification or clustering efficiency of PCA was evaluated for all fs ST-FIBS spectra of metals and bimetallic strips in the spectral range of 350-700 nm. All the spectra were processed for minor impurities such as calcium, sodium and normalized before using for PCA analysis. **Figure 4.19(a)** represents the PC score plot of metals and bimetallic targets. The first three PCs account for 92% (56%, 21%, and 15%) of the total variance present in the data set. **Figure 4.19(b)** presents the first three PCs that contain

the essential spectral features which contribute for the classification. Out of these PCs, first PC is like SS with transitions of Fe and has Cu, Zn Al, and Ag spectral components. Second PC has spectral features from Al, Zn and Ag whereas third PC has spectral components from Al, Zn, Ag and Cu. Although Ag@Cu are well separated (encircled together in an ellipse), Ag@Au are not well resolved (shown in square). This could be attributed to the smaller contribution of weak transitions of Au I, that are present in fs ST-FIBS spectra of Ag@Au bimetallic strips, towards the total variance when all targets were analyzed together. However, supervised or generic algorithms are expected to result in superior classification. Furthermore, employing telescopes with good transmission in the UV-Visible range will support qualitative as well as quantitative measurements in the standoff mode.

4.3.3.e ST-FIBS studies of geological samples (silicates)

Petrology is a branch of geology, enumerates about different clans of rocks, igneous, metamorphic and sedimentary rocks. The identification of rock types and constituent elements is critical for understanding their origins and history in geological studies. The classification of rock types is done by two ways: 1) Modal Composition 2) Normative. The modal classification is typically a field classification specially applied to the igneous rocks of plutonic nature which can be identified by their modal mineralogy specially used to characterize the granitoids, clan of granite rocks, which has good textural characteristics with phenocryst of feldspar, quartz and biotite minerals geared with petrological microscope in laboratory and naked eye in field. Sometimes rock identification may be misleading or inappropriate, especially for those rocks that look alike with similar physical properties and mandates critical examination. In the normative composition of a rock is purely confined to the chemical determination of mineral weights by quantitative analysis and by following the guidelines down by CIPW (Cross - Iddings - Person and Washington). Though petrology has reached a microscopic level analysis using highly advanced analytical technique in which elemental composition can be determined by instruments like EPMA (Electron Probe Micro Analyzer); SEM (Scanning Electron Microscope) and laser ablation coupled techniques with mass spectroscopy [89,90], the techniques that are deployed in the preparation of the sample is quite cumbersome should take due care to avoid contamination. The process requires detailed sample preparation starting with crushing and pulverizing the rock sample to a

Chapter 4

definite size which can be further subject to the most appropriate analytical technique for quantitative and qualitative analysis for major elements, trace elements and isotopic compositions.

LIBS technique has been widely utilized by numerous researchers for investigation of various geological samples such as soils, rocks, meteorites [91–93] in various conditions [94] as it provides in-situ robust elemental analysis. LIBS based instruments in Mars Rover [10] and Chandrayaan-2 for analyzing rocks and crust compositions on mars and moon depict the potential LIBS for space exploration also [95]. A vast literature, as evident from several good reviews, is available on utilization of LIBS technique for geological applications even in standoff mode [96–99]. The development of several background removal algorithms [100] and, calibration free approaches (F-LIBS) [101] made it possible to quantify the elemental concentration. Further portable and hand-held LIBS instruments were also developed to investigate the geological samples [102–104]. Geological samples were also investigated by combined Raman-LIBS system as they provide complementary data to each other [105]. Fabre et al. [106] have also demonstrated the possibility of elemental imaging for the analysis of geological samples using LIBS technique. Various classification algorithms such as soft independent modelling of class analogy (SIMCA), partial least squares and lasso regression techniques were developed for supervised classification and labelling of rocks [107–109].

Here in, we have utilized fs ST-FIBS technique for qualitative in-situ elemental analysis of four geological rocks (silicates) and their discrimination using PCA in the same standoff configuration setup at ~6.5 m/ ~8 m. The rock samples were analyzed in same shape (in-situ) with minimal destruction of sample to obtain a preliminary result of elemental composition. Several atomic lines of Al, Fe, Ca, K, and Na were identified. Strontium atomic peak was also identified. Further, the atomic intensities from normalized fs ST-FIBS spectra were utilized to draw correlation graphs with the concentration obtained from EDX elemental analysis. However, comparison with the obtained results from the established techniques such as XRF will lead to better understanding. In future, we will be using these spectra for quantitative estimation of elemental concentration and for supervised classification.

4.3.3.e.i Field work and sample collection

The field work was carried out in the central part of Dharwar craton, Karnataka. A terrain composed predominantly of gneisses, granites and boudins of mafic rocks. These rocks are deformed, traversed by shear zones possessing phenocryst of fluorite and hornblende crystals which are attributed to the fluids interaction with the existing lithology these fluid reactions given rise to the reaction rim of biotite in the peripheral zones of mafic boudins present in the gneisses. The granites are considered to be younger components and gneisses are oldest in the field. The sampling is done to achieve spatial variability of rock samples to avoid the repetitiveness of the sample. Fresh and non-weathered samples are chosen to eliminate the chemical altered portion of the rock specimen which help us in analytical analysis to obtain the better results while quantifying the major, trace elemental data.

4.3.3.e.ii The mineralogy of the rock types

Rock sample collected from the field is dominant of gneisses following granites and small portion of mafic enclaves which are defined to be lower crustal segments, the rock types are intermediate in terms of the silica saturation, and gneisses are tonalite-granodiorite, granitic gneisses, granite and tonalitic mafic enclaves. The major elements expected to be in higher proportions in this kind of rocks are SiO_2 , Al_2O_3 , Na_2O , CaO and K_2O partially by TiO_2 , MnO , FeO , Fe_2O_3 and P_2O_5 and the trace elements occur in different proportions which is highly variably that cannot be quantified in terms of their precision and accuracy without mass spectrometry. Table 4.6 depicts the possible mineralogy of sample.

Table 4-6 Mineralogy of geological rocks investigated in fs ST-FIBS setup.

Rock (Label)	Mineralogy
Tonalite (Rav_07)	Amphiboles + Plagioclase + minor Quartz
Granite (5B)	Microcline + Orthoclase + Biotite and minor Plagioclase
Granite Gneisses (7A)	Plagioclase + Quartz + minor Microcline and Biotite
Tonalitic-granodiorite gneisses (1A1)	Plagioclase + Quartz and Amphiboles + Biotite.

4.3.3.e.iii Fs ST-FIBS spectra of geological rocks

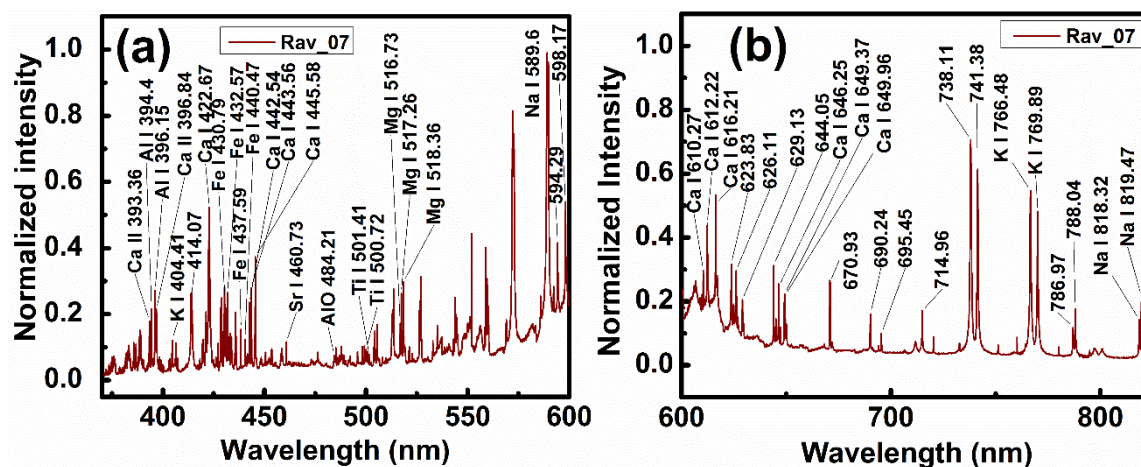


Figure 4.20 Fs ST-FIBS spectrum of tonalite rock (Rav-07) with various atomic peaks labeled using NIST atomic data base in (a) 370-600 nm and (b) 600-820 nm spectral regions.

Table 4-7 Atomic transitions identified in fs ST-FIBS spectra of tonalite rock (Rav-07) in 370-820 nm spectral region.

Observed Wavelength (nm)	NIST wavelength (nm)	element	Observed Wavelength (nm)	NIST wavelength (nm)	element
393.36	393.36	Ca II	610.43	610.27	Ca I
394.42	394.40	Al I	612.36	612.27	Ca I
396.18	396.15	Al I	614.71	614.71	Fe I
396.87	396.84	Ca II	616.35	616.37	Ca I
427.26	427.45	Ti I	626.11	626.10	Ti I
428.36	428.26	Ti I	629.72	629.77	Fe I
428.99	428.90	Ti I	645.72	645.56	Ca I
429.97	429.92	Ti I	649.12	649.17	Mn I
431.93	431.86	Ti I	646.30	646.25	Ca I
432.65	432.57	Fe I	649.24	649.37	Ca I
438.44	437.59	Fe I	649.52	649.96	Ca I
440.55	440.47	Fe I	653.39	653.90	Fe I
442.62	442.54	Ca I	657.40	657.40	Fe I
443.60	443.56	Ca I	658.13	658.13	Fe I
445.54	445.58	Ca I	668.16	670.80	V I
460.82	460.73	Sr I	732.77	732.96	V I
605.91	605.91	VI	751.23	751.28	Fe I
606.74	606.72	VI	770.09	771.03	Fe I
608.88	608.94	VI	780.16	780.99	Na I
609.83	609.96	Ti I	818.48	818.32	Na I

The fs ST-FIBS spectra of four geological sodium and potassium rich silicates were recorded at ~ 6.5 m away from the sample in the same ST-FIBS setup (configuration 3). The energy of the laser pulse was 3 mJ. The other ST-FIBS spectra acquisition parameters are exposure time of 1.5 s, accumulation 20, gate width $1\ \mu\text{s}$, gate delay 50 ns and gain 2000. **Figure 4.20(a) and 4.20(b)** depicts the typical ST-FIBS spectrum of tonalite rock (Rav-07) in (a) 370–600 nm and (b) 600–820 nm spectral regions. The observed peaks are identified (using NIST atomic database) as the atomic transitions of various constituent atoms viz., Al, Mg, Ca, Fe, K, Na, Ti, and Sr. **Table 4.7** lists out the atomic transitions observed in fs FIBS spectra.

4.3.3.e.iv Classification of geological rocks using PCA in standoff mode

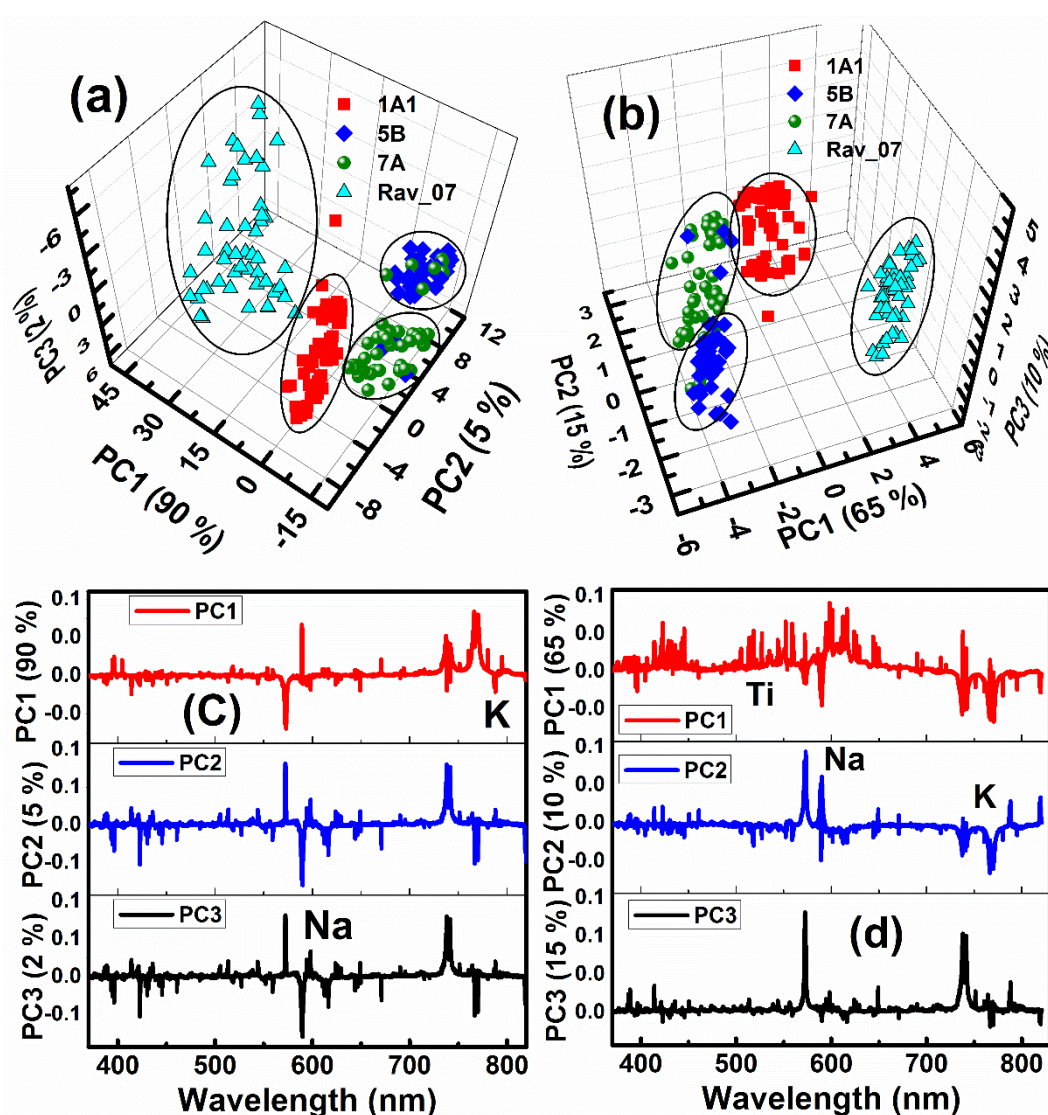


Figure 4.21 PC score plots of (a) un-normalized ST-FIBS spectra and (b) normalized fs ST-FIBS spectra of geological rocks obtained from PCA. First three principal components of (c) un-normalized ST-FIBS spectra and (b) normalized fs ST-FIBS of geological samples.

Chapter 4

Figures 4.21(a) and 4.21(b) illustrate the PC score plot of un-normalized and normalized fs ST-FIBS spectra of geological rocks in the 370-820 nm spectral range. In un-normalized case first three PCs accounted for 97% of total variance (90, 5, and 2%) present in the data set, whereas in for normalized spectra these accounted for 90% of total variance (65, 15 and 10%). **Figures 4.21(c) and 4.21(d)** depict the principal components (PCs), the essential spectral features contributing for discrimination, which include various atomic transitions from Na, K, Al, Ti, and Fe. Further detailed studies will be directed towards obtaining correlation among the atomic intensities obtained in FIBS spectrum of rock samples with concentration measurements obtained from standard ICP-MS. Detailed studies are proposed for further effective classification of rocks and their discrimination by developing supervised algorithms and imparting baseline correction as well.

4.3.3.f ST-FIBS studies of RDX, HMX and TNT

We have investigated the energetic molecules (RDX, TNT, HMX and six nitroimidazoles) in true standoff mode at a distance of ~6.5 m using fs filaments in ST-FIBS2 setup. The IUPAC names and molecular formula of investigated HEMs is provided in table 1. Each fs STFIBS spectra of HEMs is recorded with 50 ns gate delay, 1 μ s gate width, 3000 ICCD gain, exposure time of 1.5 s and 6 accumulations. Pellets were mounted on a silicon (Si) target while investigation. Only 3-4 spectra were acquired due to the scarcity of sample. **Figure 4.22(a)** depicts the stack plot of typical fs ST-FIBS spectra of RDX, HMX and TNT in the spectral region 220-880 nm obtained in ST-FIBS2 configuration. Few atomic peaks from Si and impurities (Na and K) were also observed. Though CN, C₂ molecular bands and C, H, N, O atomic emissions are the essential spectral features of these energetic molecules, only CN ($\Delta v = 0$, B² $\Sigma^+ \rightarrow$ X² Σ^+) molecular band with band head at 388.34 nm was observed in the fs ST-FIBS spectra. It is also evident that oxygen and nitrogen atomic transitions are also absent in the spectral region from 700-860 nm. Inset from the **figure 4.22(a)** shows the all five CN ($\Delta v = 0$) vibrational transitions observed in TNT. **Figure 4.22(b)** shows the only CN ($\Delta v = 0$) band head detected in the fs FIBS spectra of HMX and **figure 4.22(c)** shows the three CN ($\Delta v = 0$) band transitions observed in RDX. However, the intensity varied from one molecule to the other, which could be attributed to their molecular structure and strength of the pellet prepared. Spectral information in the wavelength region below 370 nm was lost due

to the limitation of transmitting range of collection optics utilized in SCT telescope. Thus C, CN ($\Delta v = +1$) transitions were not observed. Similarly, the atomic lines of N and O were not observed. The possible reasons for the absence of O and N atomic transitions are explained in the next section.

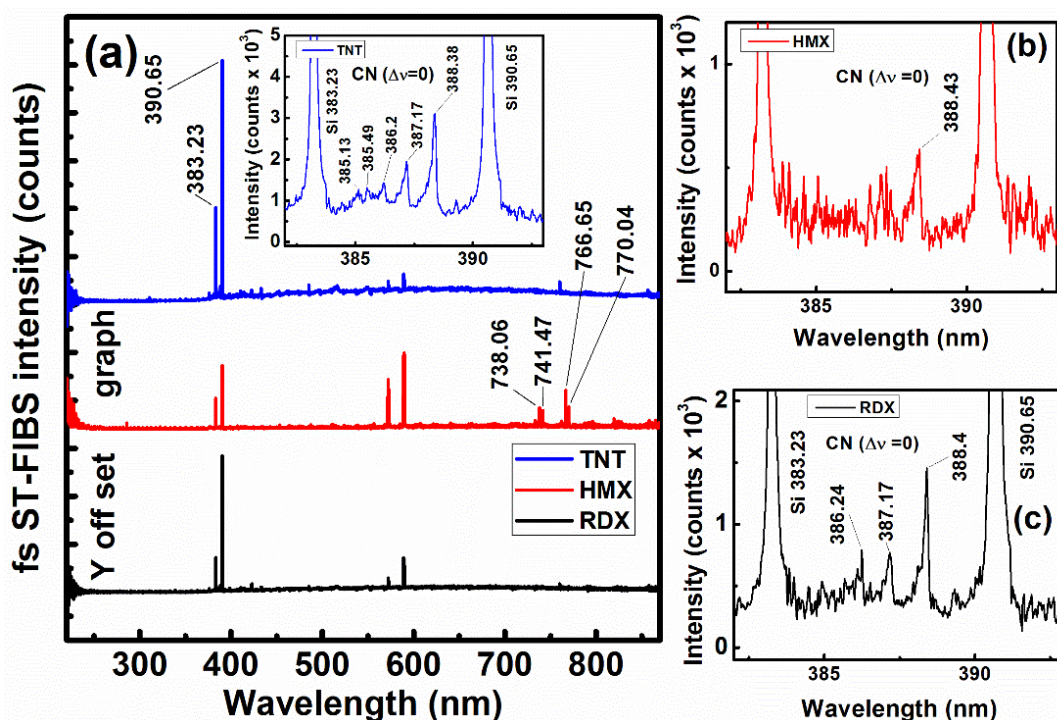


Figure 4.22 (a) Y-axis offset plot representing fs ST-FIBS spectra of TNT, HMX, and RDX recorded in ST-FIBS2 setup at ~ 6.5 m away. The inset shows CN molecular emissions observed in TNT. (b) and (c) shows the CN molecular emissions observed in HMX and RDX fs ST-FIBS spectra.

4.3.3.g ST-FIBS studies of energetic nitroimidazoles

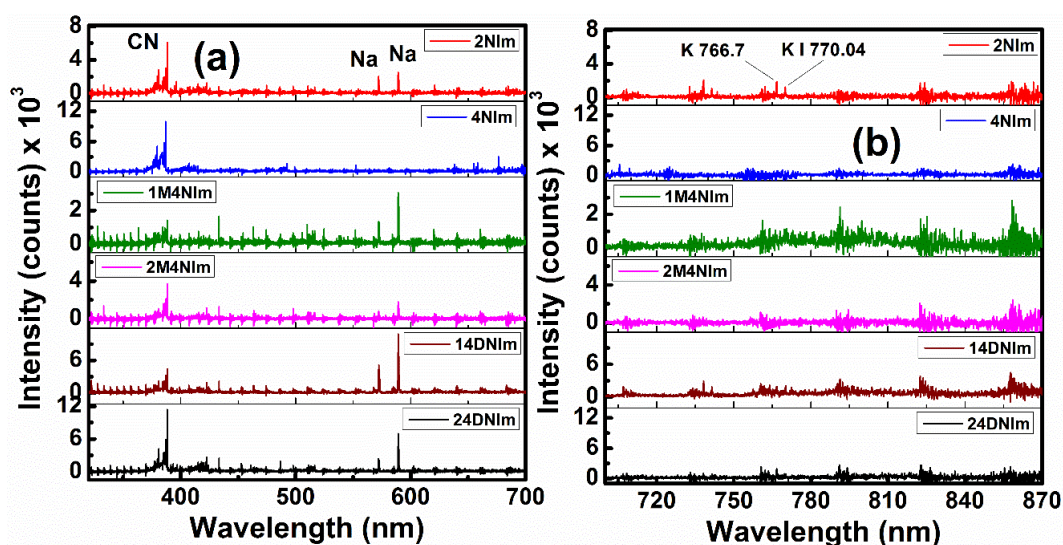


Figure 4.23 Stack plot depicting typical fs ST-FIBS spectra of Nitroimidazoles obtained in ST-FIBS2 setup in the spectral range (a) 320-880 nm and (b) 700-870 nm.

Chapter 4

Figure 4.23(a) depicts the typical fs ST-FIBS spectra of a set of six nitroimidazoles investigated in this configuration in the spectral region of 320-880 nm. **Figure 4.23(b)** shows the absence of oxygen and nitrogen in the spectral region from 700-860 nm. Two CN bands were observed in the spectral region of 386-390 nm, 410-422 nm corresponding to Δv values of 0 and -1 , respectively. The CN violet band ($\Delta v = 0$, $B^2\Sigma^+ \rightarrow X^2\Sigma^+$) had the maximum intensity. Though CN ($\Delta v=-1$) band was relatively weak compared to CN ($\Delta v=0$) band, additional peaks were observed (as shown in blue color) adjacent to it. Only the C_2 $\Delta v=0$ band head (swan band, $d^3\Pi_g \rightarrow a^3\Pi_u$) was observed at 516.42 nm. **Figures 4.24(a)-4.24(c)** depict the CN $\Delta v=0$, CN $\Delta v=-1$ and C_2 $\Delta v=0$ bands in the fs ST-FIBS spectra of all nitroimidazoles. The variation in intensity of CN and C_2 can be attributed to the molecular structure and position of the nitro groups and complex plasma reaction. Similarly, **figures 4.24(d)-4.24(f)** illustrate the CN $\Delta v=0$ and $\Delta v=-1$ and C_2 bands from fs ST-FIBS spectra of 4-NIm with few new peaks observed adjacent to both the bands. There is only a few literature discussed on these peaks and further studies are required to identify these transitions. Since the transmission range of the SCT (used to collect plasma emissions) is entirely in the visible and near IR region (370 nm- 820 nm) few essential signature of HEMs (C I 247.8 nm, CN $\Delta v=1$ 356-360 nm, NH at 336 nm) were not observed.

The absence of other atomic transitions (H, N, and O) could be attributed to the (a) fundamental principle of femtosecond ablation as well as the (b) fs filament interaction. Rohwetter et al. [50] have observed that fs LIBS (focused pulses) as well as fs FIBS (filaments) spectra of copper metal was free from ambient air species in comparison to ns LIBS spectrum and attributed these features to the fundamental difference in the ablation process associated with each pulse. In case of ns ablation, the surrounding air or gas breaks down due to diffusive mixing of the expanding hot metal vapor with ambient gas. In the case of picosecond ablation, the trailing part of pulse interacts with the surrounding atmosphere and leads to inverse Bremsstrahlung heating of the plasma plume. Especially, in the fs regime, the produced plasma plume is not enough energetic to excite ambient gas and thus minimal or no breakdown of air is observed (as we observed in the case of triazole ablation with fs and ns pulses [110]) with fs pulse ablation and thus atomic transitions of N and O are absent in the spectra. Further, the fs filament ablation

results in plasma with low temperatures and have less life time as revealed from the work of Harilal et al. [83].

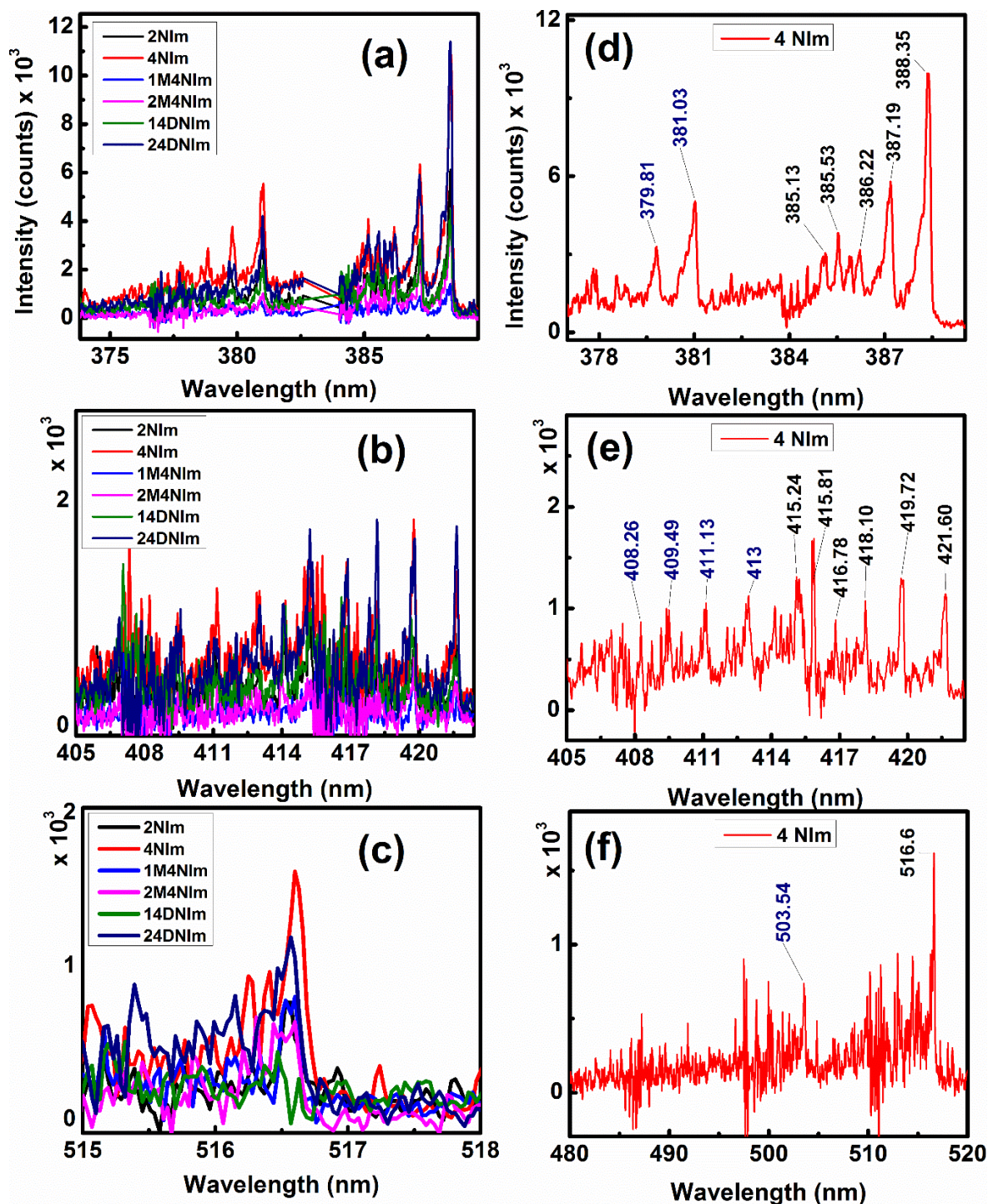


Figure 4.24 (a) CN ($\Delta v=0$) (b) CN ($\Delta v=-1$) and (c) C_2 ($\Delta v=0$) band head in fs ST-FIBS spectra of all nitroimidazoles. (d) CN ($\Delta v=0$) (e) CN ($\Delta v=-1$) and (f) C_2 ($\Delta v=0$) band head in ST-FIBS spectra of 4-NIm (only) with labelled peaks and extra peaks (in blue color). The y-axes title is Intensity (counts) for all the data presented.

Chapter 4

Moreover, the energy require to excite or promote O, N and H atoms into the excited state is difficult as it requires 10.7, 12.0, and 12.1 eV energy to be supplied [111]. Thus, the filament induced plasma temperature cannot excite or breakdown the oxygen and nitrogen further and thus these transitions are absent. However, further detailed studies on the types and properties of filaments produced and, consequently, their effects on the LIBS plasma will enable the development of an efficient technique for ST trace analysis of any material.

4.3.3.g.i PCA studies of nitroimidazoles

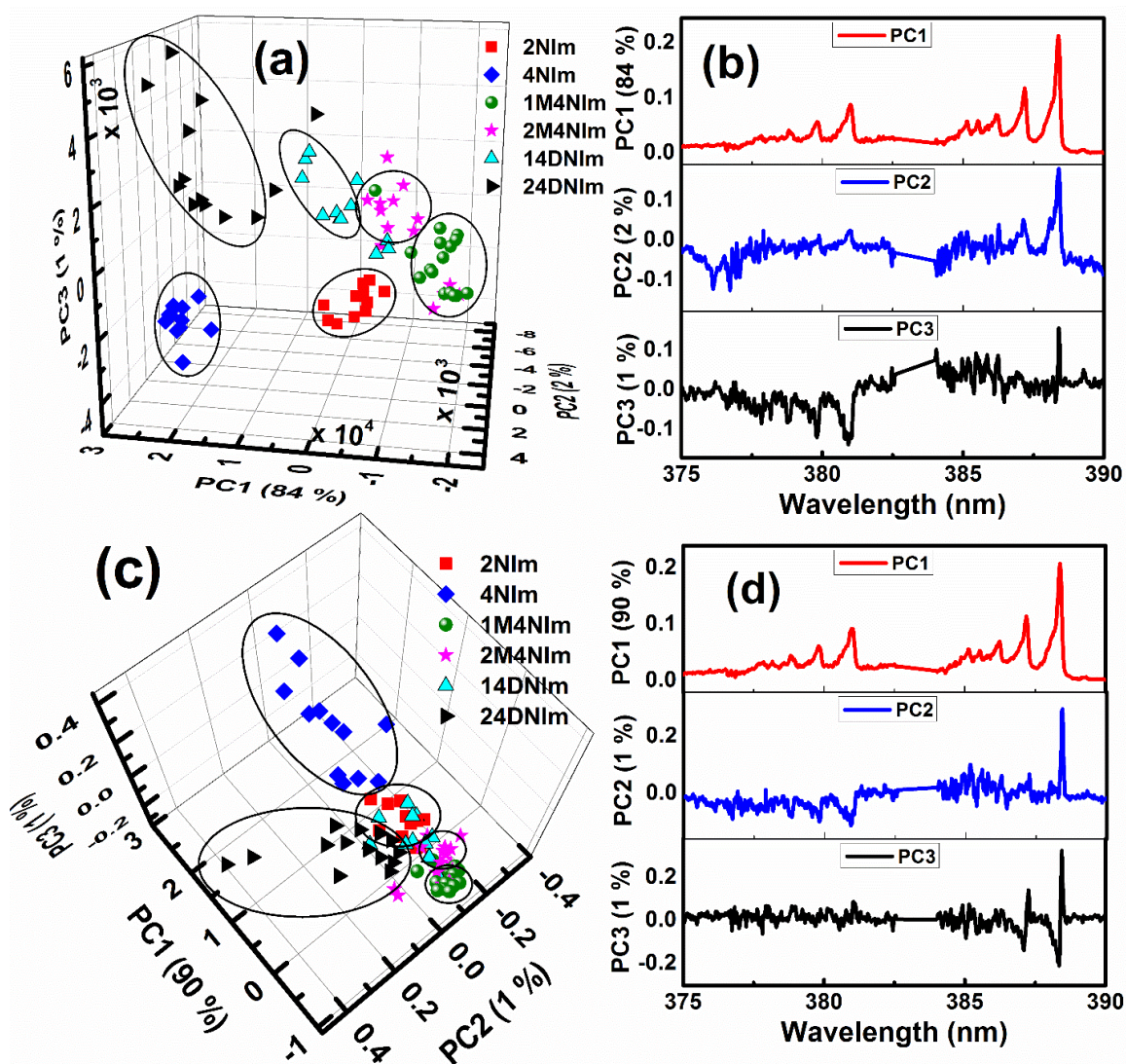


Figure 4.25 (a) PC score plot (b) PCs of un-normalized ST-FIBS spectra of Nitroimidazoles obtained from PCA. (c) PC score plot (d) PCs of normalized ST-FIBS spectra of nitroimidazoles obtained from PCA.

ST-FIBS spectra of nitroimidazoles obtained at ~ 6.5 m were clearly discriminated using principal component analysis (PCA). Only CN molecular band region (375-390

nm) was considered for PCA analysis as there are no other important spectral features present in it. **Figures 4.25(a) and 4.25(b)** show the PC score plots and first three PCs (depicting essential spectral features contributing to the discrimination) obtained after analyzing through PCA. The first three PCs together accounted for 87% (84%, 2% and 1%) of variance present in the multivariate data. Further, the ST-FIBS data in the same spectral region (375-390 nm) was normalized to the maximum intensity before analyzing with PCA program. **Figures 4.25(c) and 4.25(d)** show the PC score plots and first three PCs (depicting essential spectral features contributing to the discrimination) obtained after analyzing normalized ST-FIBS spectra in the spectral region (375-390 nm) through PCA. The first three PCs together accounted for 92% (90 1 and 1%) of variance present in the multivariate data. Though, slightly higher variance was accounted in normalized spectral analysis, the classification was not much clear. This could be attributed to weak spectral intensity of few molecules. So, normalization of data may not lead to better classification in all times [112].

4.4 Conclusions

We have successfully established the utilization of fs filament induced breakdown spectroscopy (fs FIBS) technique for standoff detection of explosives. The explosives detection is demonstrated in three configurations i.e. ST-FIBS (standoff LIBS up to 2 m), R-LIBS (at 8.5 m), and ST-FIBS (~6.5 m/ ~8 m) using sharp focused fs pulses and loose focused fs filaments. Two different collection systems i.e. ME-OPT-0007 (ANDOR) and Schmidt-Cassegrain telescope (SCT) of different size, aperture window (2", 6" diameter) and transmission capabilities [(UV-NIR), (Vis-NIR)] were used in configuration 1 and configurations 2 and 3. Finely ground powders (150 mg) of energy rich nitroimidazoles, nitropyrazoles were pressed into pellets and then used in these studies. Bimetallic targets, geological rocks were also qualitatively studied in the fs ST-FIBS setup at a distance of ~6.5 m. PCA was utilized to discriminate or cluster various materials (metals, alloys, bimetallic targets, geological rocks and high energy materials) studied in the all configurations. The prominent spectral features of HEMs i.e. C, H, N, O atomic transitions and CN, C₂, NH molecular bands were readily identified in both configuration 1 and 2, whereas only CN band was observed in configuration 3 (ST-FIBS ~6.5 m). The decrease in LIBS signal intensity with the increase in standoff distance (in configuration

Chapter 4

1) could be attributed to the decrease in solid angle subtended by the collection system at the plasma source, and thus the plasma emissions (or number of photons) reaching the collection system are decreased. PC score plots at each standoff distance showed good classification however, the contribution of first three PCs has decreased from 99% to 52%, which indicates the decrease in strength of essential spectral features. However, when the PCA was performed on R-LIBS spectra of HEMs, the first three PCs accounted for 88% of variance, which is similar to the result obtained at 50 cm standoff distance (configuration 1). The superior result was possible due to the deployment of a Schmidt-Cassegrain telescope which has large aperture (6") and improved collection arrangement. Fs pulses were focused to form filaments using a two lens combination. The distance between the lenses was varied to focus these fs filaments at desired standoff distance. Difference between ablation with tightly focused fs pulses and filaments was also discussed by comparing the Al sample R-LIBS signal and ST-FIBS signal. Bimetallic targets and geological rocks were qualitatively studied in standoff configuration and discriminated using PCA. The Quantitative elemental analysis of any material or target (bimetallic or rocks) or study of properties of filaments is not the current interest of this work and it will be studied in future. Though fs pulses are capable of delivering high energies at very long distances, they also induce structural modification such as heat affected zones similar to nanosecond pulses at very high input energies. The incident laser energy could also be decreased (optimized) to reduce the substrate interactions and substrate effects but it in turn results in deterioration of signal strength. So, the energy of the laser pulse and ICCD parameters (gate width, gate delay and gain ICCD) have to be optimized to acquire good ST-FIBS signal. Nonetheless, as demonstrated by Harilal et al. crater depth attained for fs filament ablation is smaller in comparison with fs/ns pulses and thus interaction with substrate can be greatly reduced [83]. However, at energies greater than ablation threshold, the advantage of fs pulses in comparison with ns pulses is still debated in terms of reduction in erroneous signal from background target. Further, it has also been demonstrated that either part of the LIBS spectra [113] or part of the echellograms [114] itself can be utilized in discrimination/classification studies implying the reduction in algorithm time and complexity and increase in sampling rate. Ultra-short pulse fiber lasers can also be used for portable applications owing their compact size, minimized background emission [115]. We believe that the usage of a collection system or telescope, with large input window, and large f-number are essential to obtain strong

LIBS signal with superior SNR. Thus, in conclusion, fs laser pulses can be potentially deployed in field for standoff detection provided with good collection optics or telescopes, beam delivery and an easy user interface together with superior multivariate analysis program.

We strongly believe that the future studies on fs standoff LIBS technique (including ours) should focus on

- (a) Obtaining the standoff LIBS spectra of the entire common/standard explosives.
- (b) Design and implement superior supervised algorithms (e.g. PLS-DA, ANN) for efficient and unambiguous detection.
- (c) Optimize the input laser energy to alleviate the substrate and matrix effects.
- (d) Improve the acquisition parameters (e.g. gate delay, gate width, gain of the ICCD) to enhance the SNR for each standoff position.
- (e) Advance the collection efficiency by investigating various optical configurations.
- (f) Subsequent to the success in the above fields one can then extend these studies to trace level detection. For this one also need to explore the single-shot LIBS technique with the intention of eliminating the substrate effects. With latest developments in the sources (fs) and the detectors it will not be a difficult task to make compact (portable) LIBS systems for field deployment.
- (g) Investigate some of the hybrid techniques such as LIBS-Raman technique to embrace the advantages of both the methodologies for effective explosives detection.

4.5 References

1. K. E. Brown, M. T. Greenfield, S. D. McGrane, and D. S. Moore, "Advances in explosives analysis—part I: animal, chemical, ion, and mechanical methods," *Anal. Bioanal. Chem.* **408**(1), 35–47 (2016).
2. K. E. Brown, M. T. Greenfield, S. D. McGrane, and D. S. Moore, "Advances in explosives analysis—part II: photon and neutron methods," *Anal. Bioanal. Chem.* **408**(1), 49–65 (2016).
3. J. Moros, J. A. Lorenzo, K. Novotný, and J. J. Laserna, "Fundamentals of stand-off Raman scattering spectroscopy for explosive fingerprinting," *J. Raman Spectrosc.* **44**(1), 121–130 (2013).
4. J. L. Gottfried, F. C. De Lucia, C. A. Munson, and A. W. Miziolek, "Standoff detection of chemical and biological threats using laser-induced breakdown spectroscopy," *Appl. Spectrosc.* **62**(4), 353–363 (2008).
5. S. Sreedhar, M. K. Gundawar, and S. V. Rao, "Laser induced breakdown spectroscopy for classification of high energy materials using elemental intensity ratios," *Def. Sci. J.* **64**(4), 332–338 (2014).
6. D. L. Woolard, E. R. Brown, A. C. Samuels, J. O. Jensen, T. Globus, B. Gelmont, and M. Wolski, "Terahertz-frequency remote-sensing of biological warfare agents," in *IEEE MTT-S International Microwave Symposium Digest* (2003), **2**, pp. 763–766.
7. C. M. Wynn, S. Palmacci, R. R. Kunz, and M. Rothschild, "Noncontact detection of homemade explosive constituents via photodissociation followed by laser-induced fluorescence," *Opt. Express* **18**(6), 5399–5406 (2010).
8. T. Arusi-Parpar and I. Levy, "Remote Detection of Explosives by Enhanced Pulsed Laser Photodissociation/Laser-Induced Fluorescence Method," in *Stand-Off Detection of Suicide Bombers and Mobile Subjects*, H. Schubert and A. Rimski-Korsakov, eds. (Springer Netherlands, 2006), pp. 59–68.
9. S. S. Harilal, B. E. Brumfield, M. C. Phillips, and P. Northwest, "Standoff analysis of laser-produced plasmas using laser-induced fluorescence," *Opt. Lett.* **43**(5), 2–5 (2018).
10. R. Francis, T. Estlin, G. Doran, S. Johnstone, D. Gaines, V. Verma, M. Burl, J. Frydenvang, S. Montaña, R. C. Wiens, S. Schaffer, O. Gasnault, L. DeFlores, D. Blaney, and B. Bornstein, "AEGIS autonomous targeting for ChemCam on Mars Science Laboratory: Deployment and results of initial science team use," *Sci. Robot.* **2**(7), eaan4582 (2017).
11. A. K. Myakalwar, S. Sreedhar, I. Barman, N. C. Dingari, S. Venugopal Rao, P. Prem Kiran, S. P. Tewari, and G. Manoj Kumar, "Laser-induced breakdown spectroscopy-based investigation and classification of pharmaceutical tablets using multivariate chemometric analysis," *Talanta* **87**, 53–59 (2011).
12. D. W. Hahn and N. Omenetto, "Laser-induced breakdown spectroscopy (LIBS), part II: Review of instrumental and methodological approaches to material analysis and applications to different fields," *Appl. Spectrosc.* **66**(4), 347–419 (2012).
13. J. El Haddad, L. Canioni, and B. Bousquet, "Good practices in LIBS analysis: Review and advices," *Spectrochim. Acta Part B At. Spectrosc.* **101**, 171–182 (2014).
14. F. C. De Lucia, R. S. Harmon, K. L. McNesby, R. J. Winkel, and A. W. Miziolek, "Laser-induced breakdown spectroscopy analysis of energetic materials," *Appl.*

- Opt. **42**(30), 6148–6152 (2003).
15. S. Sunku, M. K. Gundawar, A. K. Myakalwar, P. P. Kiran, S. P. Tewari, and S. V. Rao, "Femtosecond and nanosecond laser induced breakdown spectroscopic studies of NTO, HMX, and RDX," *Spectrochim. Acta Part B At. Spectrosc.* **79–80**, 31–38 (2013).
 16. C. S.-C. Yang, F. Jin, S. B. Trivedi, E. E. Brown, U. Hommerich, A. Tripathi, and A. C. Samuels, "Long-Wave Infrared (LWIR) Molecular Laser-Induced Breakdown Spectroscopy (LIBS) Emissions of Thin Solid Explosive Powder Films Deposited on Aluminum Substrates," *Appl. Spectrosc.* **71**(4), 728–734 (2017).
 17. R. S. Harmon, F. C. DeLucia, A. LaPointe, R. J. Winkel, and A. W. Miziolek, "LIBS for landmine detection and discrimination," *Anal. Bioanal. Chem.* **385**(6), 1140–1148 (2006).
 18. A. K. Myakalwar, S. K. Anubham, S. K. Paidi, I. Barman, and M. K. Gundawar, "Real-time fingerprinting of structural isomers using laser induced breakdown spectroscopy," *Analyst* **141**(10), 3077–3083 (2016).
 19. L. A. Álvarez-Trujillo, V. Lazic, J. Moros, and J. Javier Laserna, "Standoff monitoring of aqueous aerosols using nanosecond laser-induced breakdown spectroscopy: droplet size and matrix effects," *Appl. Opt.* **56**(13), 3773–3782 (2017).
 20. D. Girón, T. Delgado, J. Ruiz, L. M. Cabalín, and J. J. Laserna, "In-situ monitoring and characterization of airborne solid particles in the hostile environment of a steel industry using stand-off LIBS," *Measurement* **115**, 1–10 (2018).
 21. J. L. Gottfried, F. C. De Lucia, C. A. Munson, and A. W. Miziolek, "Double-pulse standoff laser-induced breakdown spectroscopy for versatile hazardous materials detection," *Spectrochim. Acta Part B* **144**, 1405–1411 (2007).
 22. I. Gaona, J. Serrano, J. Moros, and J. J. Laserna, "Range-Adaptive Standoff Recognition of Explosive Fingerprints on Solid Surfaces using a Supervised Learning Method and Laser-Induced Breakdown Spectroscopy," *Anal. Chem.* **86**(10), 5045–5052 (2014).
 23. J. L. Gottfried, F. C. De Lucia, C. A. Munson, and A. W. Miziolek, "Laser-induced breakdown spectroscopy for detection of explosives residues: a review of recent advances, challenges, and future prospects," *Anal. Bioanal. Chem.* **395**(2), 283–300 (2009).
 24. M. K. Gundawar, R. Junjuri, and A. K. Myakalwar, "Standoff Detection of Explosives at 1 m using Laser Induced Breakdown Spectroscopy," *Def. Sci. J.* **67**(6), 623 (2017).
 25. J. Moros, J. A. Lorenzo, P. Lucena, L. M. Tobaría, and J. J. Laserna, "Simultaneous Raman spectroscopy-laser-induced breakdown spectroscopy for instant standoff analysis of explosives using a mobile integrated sensor platform," *Anal. Chem.* **82**(4), 1389–1400 (2010).
 26. J. Moros, J. A. Lorenzo, and J. J. Laserna, "Standoff detection of explosives: Critical comparison for ensuing options on Raman spectroscopy-LIBS sensor fusion," *Anal. Bioanal. Chem.* **400**(10), 3353–3365 (2011).
 27. R. C. Wiens, S. K. Sharma, J. Thompson, A. Misra, and P. G. Lucey, "Joint analyses by laser-induced breakdown spectroscopy (LIBS) and Raman spectroscopy at stand-off distances," *Spectrochim. Acta Part A* **61**, 2324–2334 (2005).
 28. J. Moros and J. J. Laserna, "New Raman-laser-induced breakdown spectroscopy identity of explosives using parametric data fusion on an integrated sensing

- platform," *Anal. Chem.* **83**(16), 6275–6285 (2011).
29. V. Lazic, A. Palucci, S. Jovicevic, and M. Carpanese, "Detection of explosives in traces by laser induced breakdown spectroscopy: Differences from organic interferences and conditions for a correct classification," *Spectrochim. Acta Part B At. Spectrosc.* **66**(8), 644–655 (2011).
 30. J. L. Gottfried, F. C. De Lucia, and A. W. Miziolek, "Discrimination of explosive residues on organic and inorganic substrates using laser-induced breakdown spectroscopy," *J. Anal. At. Spectrom.* **24**(3), 288–296 (2009).
 31. J. L. Gottfried, "Influence of metal substrates on the detection of explosive residues with laser-induced breakdown spectroscopy," *Appl. Opt.* **52**(4), B10–B19 (2013).
 32. J. L. Gottfried, F. C. De Lucia, C. A. Munson, and A. W. Miziolek, "Strategies for residue explosives detection using laser-induced breakdown spectroscopy," *J. Anal. At. Spectrom.* **23**(2), 205–216 (2008).
 33. C. López-Moreno, S. Palanco, J. J. Laserna, F. DeLucia, A. W. Miziolek, J. Rose, R. A. Walters, and A. I. Whitehouse, "Test of a stand-off laser-induced breakdown spectroscopy sensor for the detection of explosive residues on solid surfaces," *J. Anal. At. Spectrom.* **21**(1), 55–60 (2006).
 34. R. González, P. Lucena, L. M. Tobaría, and J. J. Laserna, "Standoff LIBS detection of explosive residues behind a barrier," *J. Anal. At. Spectrom.* **24**(8), 1123–1126 (2009).
 35. J. Moros, J. A. Lorenzo, P. Lucena, L. Miguel Tobaría, and J. J. Laserna, "Simultaneous Raman Spectroscopy– Laser-Induced Breakdown Spectroscopy for instant standoff analysis of explosives using a mobile integrated sensor platform," *Anal. Chem.* **82**(4), 1389–1400 (2010).
 36. J. Moros and J. J. Laserna, "New Raman–Laser-Induced Breakdown Spectroscopy Identity of Explosives Using Parametric Data Fusion on an Integrated Sensing Platform," *Anal. Chem.* **83**(16), 6275–6285 (2011).
 37. J. J. Laserna, R. F. Reyes, R. González, L. Tobaría, and P. Lucena, "Study on the effect of beam propagation through atmospheric turbulence on standoff nanosecond laser induced breakdown spectroscopy measurements," *Opt. Express* **4376**(12), 10265–10276 (2009).
 38. K. Bhavsar and K. E. Eseller, "Design optimization of Cassegrain telescope for remote explosive trace detection," in *Counterterrorism, Crime Fighting, Forensics, and Surveillance Technologies* (SPIE, 2017), pp. 1044103–7.
 39. P. D. Barnett, N. Lamsal, and S. M. Angel, "Standoff Laser-Induced Breakdown Spectroscopy (LIBS) Using a Miniature Wide Field of View Spatial Heterodyne Spectrometer with Sub-Microsteradian Collection Optics," *Appl. Spectrosc.* **71**(4), 583–590 (2017).
 40. W. T. Li, X. Y. Yang, X. Li, S. S. Tang, J. [space]M. Li, R. X. Yi, P. Yang, Z. Q. Hao, L. B. Guo, X. Y. Li, X. Y. Zeng, and Y. F. Lu, "A portable multi-collector system based on an artificial optical compound eye for stand-off laser-induced breakdown spectroscopy," *J. Anal. At. Spectrom.* **32**(10), 1975–1979 (2017).
 41. F. C. De Lucia, J. L. Gottfried, and A. W. Miziolek, "Evaluation of femtosecond laser-induced breakdown spectroscopy for explosive residue detection," *Opt. Express* **17**(2), 419–425 (2009).
 42. C. G. Brown, R. Bernath, M. Fisher, M. C. Richardson, M. Sigman, R. A. Walters, A. Miziolek, H. Bereket, and L. E. Johnson, "Remote femtosecond laser induced breakdown spectroscopy (LIBS) in a standoff detection regime," in *Enabling Technologies and Design of Nonlethal Weapons* (International Society for Optics

- and Photonics, 2006), **6219**, p. 62190B.
43. T. A. Labutin, V. N. Lednev, A. A. Ilyin, and A. M. Popov, "Femtosecond laser-induced breakdown spectroscopy," *J. Anal. At. Spectrom.* **31**(1), 90–118 (2016).
 44. S. Sunku, E. Nageswara Rao, G. Manoj Kumar, S. P. Tewari, and S. Venugopal Rao, "Discrimination methodologies using femtosecond LIBS and correlation techniques," in *Next-Generation Spectroscopic Technologies VI* (SPIE, 2013), **8726**, p. 87260H–8.
 45. S. S. Harilal, J. Yeak, B. E. Brumfield, and M. C. Phillips, "Consequences of femtosecond laser filament generation conditions in standoff laser induced breakdown spectroscopy," *Opt. Express* **24**(16), 17941–17949 (2016).
 46. S. S. Harilal, J. Yeak, and M. C. Phillips, "Plasma temperature clamping in filamentation laser induced breakdown spectroscopy," *Opt. Express* **23**(21), 27113 (2015).
 47. A. Couairon and A. Mysyrowicz, "Femtosecond filamentation in transparent media," *Phys. Rep.* **441**(2), 47–189 (2007).
 48. J.-C. Diels and L. A. Arissian, *Lasers: The Power and Precision of Light* (Wiley-Vch, 2011).
 49. P. Rohwetter, J. Yu, G. Méjean, K. Stelmazczyk, E. Salmon, J. Kasparian, J.-P. Wolf, and L. Wöste, "Remote LIBS with ultrashort pulses: Characteristics in picosecond and femtosecond regimes," *J. Anal. At. Spectrom.* **19**(4), 437–444 (2004).
 50. P. Rohwetter, K. Stelmazczyk, L. Wöste, R. Ackermann, G. Méjean, E. Salmon, J. Kasparian, J. Yu, and J. P. Wolf, "Filament-induced remote surface ablation for long range laser-induced breakdown spectroscopy operation," *Spectrochim. Acta Part B* **60**, 1025–1033 (2005).
 51. H. L. Xu, P. T. Simard, Y. Kamali, J.-F. Daigle, C. Marceau, J. Bernhardt, J. Dubois, M. Châteauneuf, F. Théberge, G. Roy, and S. L. Chin, "Filament-induced breakdown remote spectroscopy in a polar environment," *Laser Phys.* **22**(12), 1767–1770 (2012).
 52. H. L. Xu and S. L. Chin, "Femtosecond laser filamentation for atmospheric sensing," *Sensors* **11**(1), 32–53 (2011).
 53. H. Li, W. Chu, H. Xu, Y. Cheng, S. L. Chin, K. Yamanouchi, and H. B. Sun, "Simultaneous identification of multi-combustion-intermediates of alkanol-air flames by femtosecond filament excitation for combustion sensing," *Sci. Rep.* **6**(February), 1–7 (2016).
 54. S. Li, Y. Li, Z. Shi, L. Sui, H. Li, Q. Li, A. Chen, Y. Jiang, and M. Jin, "Fluorescence emission induced by the femtosecond filament transmitting through the butane/air flame," *Spectrochim. Acta - Part A Mol. Biomol. Spectrosc.* **189**, 32–36 (2018).
 55. S. Tzortzakis, D. Anglos, and D. Gray, "Ultraviolet laser filaments for remote laser-induced breakdown spectroscopy (LIBS) analysis: applications in cultural heritage monitoring," *Opt. Lett.* **31**(8), 1139 (2006).
 56. K. Stelmazczyk, P. Rohwetter, G. Méjean, J. Yu, E. Salmon, J. Kasparian, R. Ackermann, J. P. Wolf, and L. Wöste, "Long-distance remote laser-induced breakdown spectroscopy using filamentation in air," *Appl. Phys. Lett.* **85**(18), 3977–3979 (2004).
 57. W. Liu, H. L. Xu, G. Méjean, Y. Kamali, J.-F. Daigle, A. Azarm, P. T. Simard, P. Mathieu, G. Roy, and S. L. Chin, "Efficient non-gated remote filament-induced breakdown spectroscopy of metallic sample," *Spectrochim. Acta Part B At.*

- Spectrosc. **62**(1), 76–81 (2007).
58. E. J. Judge, G. Heck, E. B. Cerkez, and R. J. Levis, "Discrimination of composite graphite samples using remote filament-induced breakdown spectroscopy," *Anal. Chem.* **81**(7), 2658–2663 (2009).
 59. S. L. Chin, H. L. Xu, Q. Luo, F. Théberge, W. Liu, J. F. Daigle, Y. Kamali, P. T. Simard, J. Bernhardt, S. A. Hosseini, M. Sharifi, G. Méjean, A. Azarm, C. Marceau, O. Kosareva, V. P. Kandidov, N. Aközbek, A. Becker, G. Roy, P. Mathieu, J. R. Simard, M. Châteauneuf, and J. Dubois, "Filamentation "remote" sensing of chemical and biological agents/pollutants using only one femtosecond laser source," *Appl. Phys. B* **95**(1), 1–12 (2009).
 60. K. C. Hartig, I. Ghebregziabher, and I. Jovanovic, "Standoff Detection of Uranium and its Isotopes by Femtosecond Filament Laser Ablation Molecular Isotopic Spectrometry," *Sci. Rep.* **7**, 43852 (2017).
 61. D. Mirell, O. Chalus, K. Peterson, and J.-C. Diels, "Remote sensing of explosives using infrared and ultraviolet filaments," *J. Opt. Soc. Am. B* **25**(7), B108–B111 (2008).
 62. M. Rodriguez, R. Bourayou, G. Méjean, J. Kasparian, J. Yu, E. Salmon, A. Scholz, B. Stecklum, J. Eislöffel, U. Laux, A. P. Hatzes, R. Sauerbrey, L. Wöste, and J. P. Wolf, "Kilometer-range nonlinear propagation of femtosecond laser pulses," *Phys. Rev. E* **69**(32), 1–7 (2004).
 63. T. Fujii, N. Goto, M. Miki, T. Nayuki, and K. Nemoto, "Lidar measurement of constituents of microparticles in air by laser-induced breakdown spectroscopy using femtosecond terawatt laser pulses," *Opt. Lett.* **31**(23), 3456–3458 (2006).
 64. J. Izawa, T. Yokozawa, T. Kurata, A. Yoshida, Y. Mastunaga, T. Somekawa, S. Eto, N. Manago, H. Horisawa, S. Yamaguchi, T. Fujii, and H. Kuze, "Stand-off detection and classification of CBRNe using a Lidar system based on a high power femtosecond laser," in *Proceedings of SPIE - The International Society for Optical Engineering* (2014), **9253**, p. 92530C.
 65. D. A. Cremers and L. J. Radziemski, "7 Remote LIBS Measurements," in *Handbook of Laser-Induced Breakdown Spectroscopy* (John Wiley & Sons, 2006).
 66. M. Richardson, *Fundamentals of Filament Interaction* (2017).
 67. Y. Hu, J. Nie, K. Sun, and L. Wang, "Filamentation of femtosecond laser pulse influenced by the air turbulence at various propagation distances," *Opt. Commun.* **383**, 281–286 (2017).
 68. Z. Jin, J. Zhang, M. H. Xu, X. Lu, Y. T. Li, Z. H. Wang, Z. Y. Wei, X. H. Yuan, and W. Yu, "Control of filamentation induced by femtosecond laser pulses propagating in air.," *Opt. Express* **13**(25), 10424–30 (2005).
 69. C. A. Zuhlke, J. Bruce III, T. P. Anderson, D. R. Alexander, and C. G. Parigger, "A fundamental understanding of the dependence of the laser-induced breakdown spectroscopy (LIBS) signal strength on the complex focusing dynamics of femtosecond laser pulses on either side of the focus," *Appl. Spectrosc.* **68**(9), 1021–1029 (2014).
 70. M. Fisher, C. Siders, E. Johnson, O. Andrusyak, C. Brown, and M. Richardson, "Control of filamentation for enhancing remote detection with laser induced breakdown spectroscopy," in *Proc. of SPIE* (2006), **6219**, p. 621907.
 71. A. Chen, S. Li, H. Qi, Y. Jiang, Z. Hu, X. Huang, and M. Jin, "Elongation of plasma channel generated by temporally shaped femtosecond laser pulse," *Opt. Commun.* **383**, 144–147 (2017).
 72. J. F. Daigle, Y. Kamali, M. Châteauneuf, G. Tremblay, F. Théberge, J. Dubois, G.

- Roy, and S. L. Chin, "Remote sensing with intense filaments enhanced by adaptive optics," *Appl. Phys. B Lasers Opt.* **97**(3), 701–713 (2009).
73. P. Polynkin, M. Kolesik, A. Roberts, D. Faccio, P. Di Trapani, and J. Moloney, "Generation of extended plasma channels in air using femtosecond Bessel beams.," *Opt. Express* **16**(20), 15733–15740 (2008).
 74. M. Weidman, M. Baudelet, M. Fisher, C. Bridge, C. Brown, M. Sigman, P. J. Dagdigian, and M. Richardson, "Molecular signal as a signature for detection of energetic materials in filament-induced breakdown spectroscopy," in *Proc. SPIE* (2009), **7304**(Chemical, Biological, Radiological, Nuclear, and Explosives (CBRNE) Sensing X), p. 73041G/1-73041G/7.
 75. M. Baudelet, M. Richardson, and M. Sigman, "Self-channeling of femtosecond laser pulses for rapid and efficient standoff detection of energetic materials," in *IEEE Conference on Technologies for Homeland Security* (2009), pp. 472–476.
 76. Andor Technology, *User Guide for Mechelle* (2011).
 77. "Celestron astronomical telescopes," <https://www.celestron.com/pages/starbright-xlt-optical-coatings>.
 78. E. N. Rao, S. Sunku, and S. V. Rao, "Femtosecond Laser-Induced Breakdown Spectroscopy Studies of Nitropyrazoles: The Effect of Varying Nitro Groups," *Appl. Spectrosc.* **69**(11), 1342–1354 (2015).
 79. E. N. Rao, P. Mathi, S. A. Kalam, S. Sreedhar, A. K. Singh, B. N. Jagatap, and S. V. Rao, "Femtosecond and nanosecond LIBS studies of nitroimidazoles: Correlation between molecular structure and LIBS data," *J. Anal. At. Spectrom.* **31**(3), (2016).
 80. S. Sreedhar, E. Nageswara Rao, G. Manoj Kumar, S. P. Tewari, and S. Venugopal Rao, "Molecular formation dynamics of 5-nitro-2,4-dihydro-3H-1,2,4-triazol-3-one, 1,3,5-trinitroperhydro-1,3,5-triazine, and 2,4,6-trinitrotoluene in air, nitrogen, and argon atmospheres studied using femtosecond laser induced breakdown spectroscopy," *Spectrochim. Acta Part B At. Spectrosc.* **87**, 121–129 (2013).
 81. J. Serrano, J. Moros, and J. J. Laserna, "Exploring the formation routes of diatomic hydrogenated radicals using femtosecond laser-induced breakdown spectroscopy of deuterated molecular solids," *J. Anal. At. Spectrom.* **30**(11), 2343–2352 (2015).
 82. S. A. Kalam, N. L. Murthy, P. Mathi, N. Kommu, A. K. Singh, and S. V. Rao, "Correlation of molecular, atomic emissions with detonation parameters in femtosecond and nanosecond LIBS plasma of high energy materials," *J. Anal. At. Spectrom.* **32**(8), 1535–1546 (2017).
 83. S. S. Harilal, J. Yeak, B. E. Brumfield, J. D. Suter, and M. C. Phillips, "Dynamics of molecular emission features from nanosecond, femtosecond laser and filament ablation plasmas," *J. Anal. At. Spectrom.* **31**(6), 1192–1197 (2016).
 84. Y. Dikmelik, C. McEnnis, and J. B. Spicer, "Femtosecond and nanosecond laser-induced breakdown spectroscopy of trinitrotoluene," *Opt. Express* **16**(8), 5332–5337 (2008).
 85. M. Mlejnek, M. Kolesik, J. V. Moloney, and E. M. Wright, "Optically turbulent femtosecond light guide in air," *Phys. Rev. Lett.* **83**(15), 2938–2941 (1999).
 86. I. Ghebregziabher, K. C. Hartig, and I. Jovanovic, "Propagation distance-resolved characteristics of filament-induced copper plasma," *Opt. Express* **24**(5), 5263 (2016).
 87. M. Weidman, M. Ramme, B. Bousquet, K. Lim, M. Durand, M. Baudelet, and M. Richardson, "Angular dependence of filament-induced plasma emission from a GaAs surface," *Opt. Lett.* **40**(19), 4548 (2015).

Chapter 4

88. "NIST atomic spectra database," <https://www.nist.gov/pml/atomic-spectra-database>.
89. A. R. Date and D. Hutchison, "Determination of Rare Earth Elements in Geological Samples by Inductively Coupled Plasma Source Mass Spectrometry," *J. Anal. At. Spectrom.* **2**(April), 269–276 (1987).
90. K. E. Jarvis and J. G. Williams, "Laser ablation inductively coupled plasma mass spectrometry (LA-ICP-MS): a rapid technique for the direct, quantitative determination of major, trace and rare-earth elements in geological samples," *Chem. Geol.* **106**(3–4), 251–262 (1993).
91. C. P. M. Roux, J. Rakovský, O. Musset, F. Monna, J. F. Buoncristiani, P. Pellenard, and C. Thomazo, "In situ Laser Induced Breakdown Spectroscopy as a tool to discriminate volcanic rocks and magmatic series, Iceland," *Spectrochim. Acta - Part B At. Spectrosc.* **103–104**, (2015).
92. P. Pořízka, A. Demidov, J. Kaiser, J. Keivanian, I. Gornushkin, U. Panne, and J. Riedel, "Laser-induced breakdown spectroscopy for in situ qualitative and quantitative analysis of mineral ores," in *Spectrochimica Acta - Part B Atomic Spectroscopy* (2014), **101**.
93. M. D. Aglio and A. De Giacomo, "Laser Induced Breakdown Spectroscopy Applications to Meteorites: Chemical Analysis and Composition Profiles," (August), (2014).
94. J. Choi, S. Choi, and J. J. Yoh, "Standoff Detection of Geological Samples of Metal, Rock, and Soil at Low Pressures Using Laser-Induced Breakdown Spectroscopy," **70**(9), 1411–1419 (2016).
95. Llibsrover, "Laser Induced Breakdown Spectrometer (LIBS) For Chandrayaan-2 Rover <https://www.prl.res.in/~rajiv/planexnews/oldarticles/Volume%20-1,%20Issue-3.16-18.pdf>," (13), 14–16 (2011).
96. N. J. Mcmillan, S. Rees, K. Kochelek, and C. Mcmanus, "Geological Applications of Laser-Induced Breakdown Spectroscopy," *Geostand. geoanalytical Res.* **38**, 329–343 (2014).
97. R. S. Harmon, R. E. Russo, and R. R. Hark, "Applications of laser-induced breakdown spectroscopy for geochemical and environmental analysis: A comprehensive review," *Spectrochim. Acta Part B* **87**, 11–26 (2013).
98. N. B. Zorov, A. M. Popov, S. M. Zaytsev, and T. A. Labutin, "Qualitative and quantitative analysis of environmental samples by laser-induced breakdown spectrometry," *Russ. Chem. Rev.* **84**(10), 1021–1050 (2015).
99. G. S. Senesi, "Laser-Induced Breakdown Spectroscopy (LIBS) applied to terrestrial and extraterrestrial analogue geomaterials with emphasis to minerals and rocks," *Earth Sci. Rev.* **139**, 231–267 (2014).
100. M. D. Dyar, S. Giguere, C. J. Carey, and T. Boucher, "Comparison of baseline removal methods for laser-induced breakdown spectroscopy of geological samples," *Spectrochim. Acta Part B* **126**, 53–64 (2016).
101. M. D. Aglio, J. J. Laserna, S. Longo, and A. De Giacomo, "Stand-off laser induced breakdown spectroscopy on meteorites: Calibration-free approach," *Spectrochim. Acta Part B At. Spectrosc.* **147**, 87–92 (2018).
102. G. S. Senesi, "Portable Hand Held Laser-induced Breakdown Spectroscopy (LIBS) Instrumentation for in-field Elemental Analysis of Geological Samples," *Int. J. Earth Environ. Sci.* **2**, 1–3 (2017).
103. R. S. Harmon, R. R. Hark, C. S. Throckmorton, E. C. Rankey, M. A. Wise, A. M. Somers, and L. M. Collins, "Geochemical Fingerprinting by Handheld Laser-

- Induced Breakdown Spectroscopy," *Geostand. Geoanalytical Res.* **41**(4), 563–584 (2017).
104. J. Rakovský, P. Čermák, O. Musset, and P. Veis, "A review of the development of portable laser induced breakdown spectroscopy and its applications," *Spectrochim. Acta - Part B At. Spectrosc.* **101**(November), 269–287 (2014).
 105. R. C. Wiens, S. K. Sharma, J. Thompson, A. Misra, and P. G. Lucey, "Joint analyses by laser-induced breakdown spectroscopy (LIBS) and Raman spectroscopy at stand-off distances," *Spectrochim. Acta Part A* **61**, 2324–2334 (2005).
 106. Fabre, Cécile, D. Devismes, S. Moncayo, F. Pelascini, F. Trichard, A. Lecomte, B. Bousquet, J. Cauzid, and V. Motto-Ros, "Elemental imaging by laser-induced breakdown spectroscopy for the geological characterization of minerals," *J. Anal. At. Spectrom.* **33**, 1345–1353 (2018).
 107. Y. Zhang, Y. Li, W. Li, Z. Sun, and Y. Bi, "Classification of Geological Samples Based on Soft Independent Modeling of Class Analogy Using Laser-Induced Breakdown Spectroscopy," **2018**, (2018).
 108. M. D. Dyar, M. L. Carmosino, E. A. Breves, M. V Ozanne, S. M. Clegg, and R. C. Wiens, "Spectrochimica Acta Part B Comparison of partial least squares and lasso regression techniques as applied to laser-induced breakdown spectroscopy of geological samples," *Spectrochim. Acta Part B At. Spectrosc.* **70**, 51–67 (2012).
 109. M. D. Dyar, C. I. Fassett, S. Giguere, K. Lepore, S. Byrne, T. Boucher, C. J. Carey, and S. Mahadevan, "Comparison of univariate and multivariate models for prediction of major and minor elements from laser-induced breakdown spectra with and without masking," *Spectrochim. Acta - Part B At. Spectrosc.* **123**, (2016).
 110. S. A. Kalam, N. L. Murthy, P. Mathi, N. Kommu, A. K. Singh, and S. V. Rao, "Correlation of molecular, atomic emissions with detonation parameters in femtosecond and nanosecond LIBS plasma of high energy materials," *J. Anal. At. Spectrom.* **32**(8), 1535–1546 (2017).
 111. J. L. Gottfried, "Laser-induced plasma chemistry of the explosive RDX with various metallic nanoparticles," **51**(7), 13–21 (2012).
 112. P. Pořízka, J. Klus, A. Hrdlička, J. Vrábel, P. Škarková, D. Prochazka, J. Novotný, K. Novotný, and J. Kaiser, "Impact of Laser-Induced Breakdown Spectroscopy data normalization on multivariate classification accuracy," *J. Anal. At. Spectrom.* **32**(2), 277–288 (2017).
 113. A. Kumar Myakalwar, N. Spegazzini, C. Zhang, S. Kumar Anubham, R. R. Dasari, I. Barman, and M. Kumar Gundawar, "Less is more: Avoiding the LIBS dimensionality curse through judicious feature selection for explosive detection," *Sci. Rep.* **5**(August), 1–10 (2015).
 114. P. Pořízka, J. Klus, J. Mašek, M. Rajnoha, D. Prochazka, P. Modlitbová, J. Novotný, R. Burget, K. Novotný, and J. Kaiser, "Multivariate classification of echellograms: a new perspective in Laser-Induced Breakdown Spectroscopy analysis," *Sci. Rep.* **7**(1), 3160 (2017).
 115. A. W. Schill, D. A. Heaps, D. N. Stratis-Cullum, B. R. Arnold, and P. M. Pellegrino, "Characterization of near-infrared low energy ultra-short laser pulses for portable applications of laser induced breakdown spectroscopy," *Opt. Express* **15**(21), 14044–14056 (2007).

Intentional blank page

Chapter 5

Nanoparticle enhanced LIBS studies towards trace detection of energetic materials using femtosecond pulses

Though LIBS is a well-established spectroscopic technique for multi-elemental analysis the limit of detection (LOD) achieved is moderate and limited to few ppm only, when compared to other analytical techniques. The sensitivity of LIBS has been a bottleneck in some of the practical applications and there have been continuous efforts from various research groups to improve it. There have been several proposed improvisations/modifications in the LIBS setup either by using many pulses or using other devices to confine plasma with the intention of achieving higher LOD. However, recent progress on the enhancement of LIBS signal using plasmonic metal nanoparticles (NPs) has attracted the attention of many researchers because of its success. The NPs deposited over the surface manifest the laser ablation process and increase the intensity of LIBS signal and in turn achieve superior LOD. Thus the technique is named as nanoparticle enhanced laser induced breakdown spectroscopy (NE-LIBS). This technique has been used here to enhance the LIBS signal of copper and silver metallic targets. Concurrently, enhancement in the LIBS signal of high energy materials (HEMs) was also investigated in proximal LIBS setup. Finally, this technique was utilized to (a) achieve enhancement in the LIBS signal of TNT (pellet; 150 mg) at a standoff distance and (b) demonstrate trace detection of HEMs (CL-20; 1 mg over an area of 1 cm² on Brass), through obtaining enhancement in the CN band. NE-LIBS results of various samples (metals and HEMs) obtained in different configurations are presented in this chapter.

Part of this work has been accepted for publication in

1. **S. A. Kalam**, N. L. Murthy, J. R. Krishna, V. Srikanth, and Venugopal Rao Soma, "Nanoparticle Enhanced Laser Induced Breakdown Spectroscopy with Femtosecond Pulses," in 13th *International Conference on Fiber Optics and Photonics* (2016), p. Th3A.89."
2. **S.A. Kalam**, and S. Venugopal Rao, "Nanoparticle enhanced LIBS (NE-LIBS) studies towards trace detection of energetic materials", Manuscript to be submitted, 2018.

5.1 Introduction

The ability to detect explosives in bulk or even in traces in both near-field as well as from standoff distances is quintessential for military and homeland security applications so as to avoid illegal transportation, disband the terrorist activities and safeguard the denizens. Detection of different energetic materials at trace levels is a tedious job owing to their low vapor pressures. Mokalled et al. [1] have recently reviewed various electronic/chemical sensors, optical sensors and bio-sensors for vapor detection and highlighted the advantages and disadvantages of each technique. Improvised explosive devices (IEDs) can further complicate this situation as the commercial and military grade explosives that are used in manufacturing are replaced by homemade explosives (HMEs) [1–3]. The presence of numerous varieties of explosives such as organic and inorganic explosives, composites (RDX & TNT, RDX & HMX, etc.), fuel explosives, fuel-air explosives, explosives mixed with reactive metal nanoparticles [4–6] etc. increases the hardships in identifying or discriminating them [1,7]. Mass spectrometry and infra-red absorption techniques are extensively developed for analyzing the explosive traces. Ion mobility spectrometry (IMS) has been used at airport for screening explosives and hazardous chemicals at airports [8]. Further chromatography techniques such as high-performance liquid chromatography (HPLC), capillary electrophoresis (CE), chemiluminescence, and fluorescence quenching are some of the proven potential techniques for detection of trace explosives at laboratory level. Although these techniques are sensitive enough for detecting trace amounts of explosives they are not practical to detect all explosive molecules owing to inherent issues that are associated with the molecular structure, specificity to a particular bond or moiety, low vapor pressure and volatility of explosives. Moreover, in most of the cases, a direct or close contact with the energetic material is required for identification. Thus, the safety of operator as well as device is at stake. Therefore, detection of these substances from a safe distance either in remote mode or in standoff mode has gained consideration [9,10].

LIBS technique has evolved as a potential analytical tool with the capability of qualitative as well as quantitative elemental analysis with several analytical and industrial applications owing to its simple experimental setup, non-invasive or minimal damage on the sample (especially in the single shot mode), robust in-situ measurements [11,12]. LIBS technique has been successfully utilized in analyzing pharmaceutical tablets [13],

soil nutrients, biological tissues and medical samples (such as teeth, bones and nails) [14]. LIBS technique has also been performed for investigating (a) trace elements present in geological samples (ores and rocks, bimetallic and alloy targets, meteorites) [15–17] (b) trace heavy elements present in contaminated water [18–20] and (c) especially explosive residues on various substrates even in standoff mode [21–23] owing to the simplicity of the focusing laser pulses on to a distant target and generate laser spark. However, the analytical figures of merit of LIBS technique such as limit of detection, accuracy and precision are still inferior when compared to the potential mass spectrometry or gas chromatography techniques as the selectivity (or specificity) and sensitivity (detection power) of LIBS towards any analyte (organic explosives or inorganic substance) is poor with limit of detection (LOD) of LIBS is in the order of few ppm (1 ppm =1mg/ lit) for many analyte in most of the cases [24]. Precision refers to the repetitiveness of a measurement, here, the spectral intensity of the analyte and accuracy refers to the close agreement of predicted concentration with actual concentration of the analyte. Sensitivity denotes the potential of a technique to detect as low as concentrations of analyte in proximal as well as from far distances with good signal to noise ratio (SNR). Therefore, several improvisations in LIBS methodology have been implemented to mitigate this problem and conversely improve the performance of LIBS in terms of analytical figure of merits enabling to detect trace elements. These include (a) utilization of two pulses from powerful laser systems in the form of double pulse LIBS technique (DP-LIBS) [25] (b) confinement of plasma by cavities or magnetic fields [26,27] (c) controlled environmental parameters such as using vacuum or buffer gases at various pressures and (d) development of hyphenated systems such as Raman-LIBS, LIBS-LIF (LIF; laser induced fluorescence) and TA-BLASER (trace analyzer based on laser ablation and selectively excited radiation) etc. [12].

A recent review on the enhancement of LIBS signal by Li et al. [28] summarizes different approaches employed to achieve enhancement in LIBS emission to improve sensitivity by lowering the LOD. In orthogonal DP-LIBS configurations, the first laser pulse is used to pre-spark above the sample and then ablate with second pulse or ablate with first pulse and re-heat the generated plasma with second pulse. The enhancements of LIBS signal achieved in DP-LIBS technique was due to the relatively hotter and longer-lived plasmas produced in DP scheme composed with the simultaneous increase in density of emitting species. A 2-30 factor enhancement was achieved in the fs DP-LIBS

Chapter 5

signal of Cu by optimizing the inter-pulse delay between the two pulses [29]. Limit of detection of Cr in industrial soil was improved to 8 times from 18.2 mg/kg to 7.7 mg/kg using confinement of the plasma by a magnetic field [30]. The LIBS signal enhancement of Cr and Si was investigated using plasma confinement with hemispherical cavity along with magnetic field and a factor of 24 and 10 was obtained, respectively, for Cr and Si [31]. The enhancement of LIBS signal in the presence of magnetic field could not attract much attention as large permanent magnets are required and a small Zeeman effect can shift the peaks and alter the analyte information [32]. Employing LIBS and LIF together has certain limitations owing to (i) the much delayed resonance excitation of plasma (about 5 ms) when the ground state is populated to the maximum and (ii) resonance excitation of only one particular element delaying the rapid multi-elemental capability of LIBS [26]. Nevertheless, a collinear DP-LIBS configuration with optimum time delay between the two pulses is more susceptible for many practical real-time applications especially for standoff detection of explosives. Lucia et al. demonstrated that the oxygen and nitrogen interference from the atmosphere has been minimized when DP-LIBS technique was utilized to interrogate explosive residues [33]. Though two different lasers and two different laser pulses (different wavelengths) can be utilized in DP-LIBS to achieve enhancements [34], utilizing two lasers or instrumentation for confining plasma can (a) increase the cost (b) experimental setup size and (c) induce difficulty in operation. Further, it might also concurrently hinder real-time investigations. Additionally, alignment of these two laser focus spots on distant targets is critical and challenging requires sophisticated and customized beam delivery optics.

5.1.1 Nanoparticle Enhanced Laser Induced Breakdown Spectroscopy (NE-LIBS)

Recently nanoparticle enhanced LIBS (NE-LIBS) technique, where enhancement in analyte signal was achieved using nanoparticles, has received lot of attention from various researchers after the successful demonstration of 1–2 orders of enhancement in the LIBS signal of various metallic samples by Giacomo et al. [35]. This technique is being widely investigated owing to its simplicity, imparting no modifications in the LIBS setup, and availability of various plasmonic metallic NPs. NE-LIBS evolved as a potential technique for analyzing various analyte from the first report on enhancement in LIBS signal of nutrients of leaves (*Citrus unshiu* and *Rhododendron obtusum*) using Ag NPs as

demonstrated by Ohta et al. [36] to a small enhancement in analyte signal even using green Ag NPs (stabilized in coffee extract) as demonstrated by Poggialini et al. [37]. The fascinating physical [38] and chemical [39] properties of nanoparticles (NPs), from their micro or bulk counterparts especially because of their high surface to volume ratio, has attracted enormous attention from many researchers and utilized in various applications [40,41]. Plasmonic metal NPs (Ag, Au, and Cu) have been used as potential substrates in surface enhanced Raman spectroscopy (SERS) owing to superior and tunable plasmonic properties [42] in the visible range especially in detecting explosive traces [43–45]. Localized surface plasmon (LSP), a coherent and collective oscillation of the conduction electrons in the metallic NPs, is excited in the presence of external electromagnetic field and in turn amplifies the incident electromagnetic field near the particle surface and as well in the gap between the NPs. Several researchers have investigated the effect of various properties of NPs (size, shape, inter-particle distance) on ablation as these directly interact with the incident laser and can affect the coupling of electromagnetic field with the irradiated target. Eversole et al. [46] utilized this enhanced plasmonic scattering to fabricate well defined nanocraters using gold nanoparticles (~150 nm). Ropers et al. [47] demonstrated immense multi-photon electron emission from sharp metallic nano-tips (~20 nm) when a weak 100-pJ, 7-fs light pulses is incident on these. LSP resonance (LSPR) increases exponentially with a decrease in the inter-particle separation between the NPs [48]. Furthermore, the refractive index or dielectric nature of the medium, particle size, agglomeration of NPs also influences the LSP resonance [49,50]. Ashraf et al. [51] have reported the linear decrease in threshold fluence with decrease in the size of ZnO NPs. NE-LIBS also eases the elemental analysis of transparent materials such as glass and gemstones [52]. Sherbini et al. [53] reported that targets formed by pressing NPs revealed enhanced LIBS emission compared to their bulky counterparts. Sanchez-Ake et al. investigated the effect of an Au thin film on the glass surface for improving the LIBS emission signal using ns pulses [54]. Moreover, NE-LIBS technique has been utilized in enhancing AIO molecular bands during LIBS of Al-based alloys in the presence of NPs [55]. Furthermore, Giacomo et al. had reported an absolute LOD of few pico-grams for Pb and 0.2 pg for Ag using NE-LIBS technique, enabling to quantify sub ppm levels and decreasing the LOD of the technique [56]. Though fs pulses were utilized to understand the ablation mechanism, to investigate surface damage threshold of various materials [57–60], to fabricate nanostructures, the studies on achieving enhancement in

Chapter 5

LIBS signal is restricted to only DP-LIBS [61,62]. Only a few studies have been reported thus far which use fs pulses for achieving the enhancement in LIBS signal using different NPs combined with other enhancement techniques. We have recently reported a two factor enhancement of Cu LIBS signal using Ag NPs with fs pulses [63]. The results are discussed in detail in section 5.5.1.a. Yang et al. [64] combined the double pulse LIBS (DP-LIBS) and NE-LIBS techniques to obtain enhancement on SiO₂ crystal using fs laser pulses. Au NPs of various sizes were used and the best enhancement was observed for 7.5 nm NPs and a fluence of 4.4 Jcm⁻² and the achieved enhancement factors were 13 for NE-LIBS and 30 for DP-NE-LIBS at an optimized delay of 120 ps. Furthermore, Yang et al. [65] proposed a new approach for LIBS with gold nano-film (NF) deposited on various samples prior to investigation with fs pulses. Anoop et al. [66] reported a two factor enhancement in optical emission of Si plasma was also achieved by fs laser induced periodic surface structuring. Dell'Aglio et al. [67] have recently summarized various results demonstrating the enhancements in LIBS signal using NE-LIBS technique. Few important works aimed at trace detection of heavy elements in liquids and metals using NE-LIBS technique are summarized in **table 5-1**. However, sparse literature is available on employing NE-LIBS technique (either with fs or ns pulses) towards detecting or achieving enhancements with HEMs. Gottfried et al. studied the effect of trace elements present in various metallic targets on the emission of RDX traces from plasma chemistry perspective using ns pulses. It was found that the presence of trace elements with high oxidation potential such as Mg can influence in the depletion of C and C₂ species [68]. Nevertheless, increasing the sensitivity of LIBS technique towards detection of HEMs by obtaining the enhancements to achieve higher LOD is interesting as well as challenging. In this chapter, the results from initial NE-LIBS using fs pulses in proximal as well as standoff mode towards the trace detection of explosives has been presented.

5.1.2 Units used for trace detection and their conversions

While reporting the traces of heavy elements or chemicals present in the contaminated soils or polluted water and air, the amount of these elements is routinely described in units such as parts per million (ppm) to parts per trillion (ppt) and mg/liter to pg/liter.

Table 5-1 Recent results from various group utilizing nanoparticles for achieving enhancements in LIBS signal from NE-LIBS technique

Sl. No	Fs/ns NE-LIBS	Material/ Targets	Analyte	NPs	Enhancements achieved	References
1	Ns pulses	Titanium	Titanium	Ag NPs (0.02 mg/ml, NanoComposix, Inc.) Au laser ablated NPs.	$E_f > 100$	[35]
		Certified steel based alloys	Fe	Ag NPs from NanoComposix, Inc.)	$E_f = 5$	
		Certified Cu based alloys (L3, B21, SN1, SN2, SN3)	Cu	Au NPs, Ag NPs, Platinum NPs, Cu/ CuO NPs	$E_f \sim 50$	
2	Ns pulses	Al-based alloy targets (NIST: SRM 1255b)	Ti (0.1477%), Fe (0.1170% mass), AlO molecular bands	Au NPs	$E_f \sim 10$	[55]
3	Ns pulses	CuSO ₄ (aq) and cadmium nitrate solution (Cd(NO ₃) ₂) (aq) liquid on super-hydrophobic glass substrate	Cu and Cd	Au NPs	100 ppt of Cu and 150 ppt of Cr in the presence of magnetic field	[69]
4	Ns pulses (1064 nm)	CuSO ₄ (aq), NaF(aq)	Cu, F	Au SERS substrate (RAM-SERS-Au-3, Ocean Optics, Dunedin, FL)	$E_f = 3.5$ For F LOD~0.1% ppm in 20 μ l	[70]
5	Ns pulses	AgNO ₃ (aq) PbCl ₂ (aq), PbSO ₄ (aq)	Ag, Pb	Au NPs	LOD < 2 ppb in 2 μ l, $E_f > 10$	[56]
6	Ns pulses	Pure Al target with laser pre-treatment	Ni, Cr and Cd heavy elements	Pre-treatment surface	22, 19, and 184 μ g/L (ppb) for Ni, Cr, and Cd	[71]

Chapter 5

7	Ns pulses	CuSO ₄ (aq),Cr (NO ₃) ₂ (aq) Pb (NO ₃) ₂ (aq)	Cu, Cr, Pb	Au NPs loaded on to the electro spun ultrafine fibers	E _f ~4 , LODs of Cr, Pb and Cu 0.5 ppm, 0.5ppm, 1.1 ppm	[72]
8	Ns pulses (1064 nm)	Nutrients in leaves (<i>Citrus unshiu</i> and <i>Rhododendron obtusum</i>)	Fe, Mn, K, Ca, Mo	Au NPs , Ag NPs	E _f = 5	[36]
9	Fs DP-LIBS	SiO ₂ crystal	Si	Au NPs	E _f = 30	[64]
10	Ns pulses	ZnO pressed pellets of NPs	Zn	ZnO	2 < E _f < 120	[51]
11	Ns pulses	Tourmaline; Pyrex glass	Mn, Fe	Au NPs	E _f ~10	[52]

Routinely the units such as mg/Kg or $\mu\text{g}/\text{lit}$ have been used when the analyte is mixed or dispersed in solid or liquid. So, this section gives a small attention to the units which are used for trace elemental analysis and their usage and conversion for better understanding. In soil, the chemical concentration is typically reported as units of mass of analyte (mg or μg) per the mass of soil (Kg). For an analyte dispersed in soil, 1 ppm = 1 mg/kg of analyte in soil, and 1 ppb = 1 $\mu\text{g}/\text{kg}$. Likewise, in water analyte concentrations are typically measured in mass of analyte (milligrams, mg or micrograms, μg) dispersed or dissolved per volume of water (liter, L) and 1 ppm = approximately 1 mg/L of analyte in water, and 1 ppb = 1 $\mu\text{g}/\text{L}$. Further, grams per cubic meter (g/m^3) can be written as mg/L as m^3 is equal to the 1000 liters volume. Thus, $1 \text{ g}/\text{m}^3 = 1 \text{ mg}/\text{L} = 1 \text{ ppm}$.

$$1 \text{ mg}/\text{L} = 1 \mu\text{g}/\text{ml} = 1 \text{ ppm}.$$

$$1 \mu\text{g}/\text{L} = 1 \text{ ng}/\text{ml} = 1 \text{ ppb}.$$

$$1 \text{ ng}/\text{L} = 1 \text{ pg}/\text{ml} = 1 \text{ ppt}.$$

5.2 Experimental details

An ultrafast Ti: Sapphire laser system (LIBRA, $\sim 4 \text{ mJ}$, 1 kHz) delivering $\sim 50 \text{ fs}$ laser pulses and operating at 800 nm was employed to perform NE-LIBS (in proximal setup) and nanoparticle enhanced filament induced breakdown spectroscopy (NE-FIBS, in standoff configuration) experiments in ambient air. **Figure 5.1(a)** depicts the schematic of fs proximal LIBS/NE-LIBS setup and **figure 5.1(b)** depicts the fs ST-FIBS/ST-NE-FIBS setup at ($\sim 6.5 \text{ m}/ \sim 8 \text{ m}$) used for investigating explosives in bulk and traces. In the first case, a plano-convex lens of 10 cm focal length was used to focus fs pulses on to the metal target/bulk explosive pellet (150 mg) to generate plasma. The emissions from plasma were collected by Andor ME-OPT-0007 collector/collimator at 15 cm away. LIBS as well as NE-LIBS spectra in proximal setup were recorded in accumulation mode (2 accumulations) at a gate delay of 20 ns, gate width of 2 μs and ICCD gain at 3000 (0-4000) and the exposure time of ICCD is 1 s. The laser was operated at 2 Hz by varying the delay outputs in synchronized delay generator (SDG). Thus one spectrum is the collection of plasma emissions from 4 shots. In the latter case, a fs filament of $\sim 30 \text{ cm}$ length, obtained using a two-lens configuration (L1 a plano-concave lens (PCV) $f = -50 \text{ cm}$, and L2 a plano-convex lens (PCX) of $f = 100 \text{ cm}$) was utilized to interrogate HEMs in bulk (pellet 150 mg) as well as explosive traces.

Chapter 5

A Schmidt–Cassegrain telescope [see section 4.2.1 in chapter 4] collects the plasma emissions at a distance of ~ 8 m away from the plasma. The optical emissions were coupled to Andor Mechelle (ME 5000) + Andor iStar ICCD system (resolution of 0.05 nm @ 500 nm) via an optical fiber of 600 μ m diameter. The FIBS and NE-FIBS spectra in standoff configuration were recorded in accumulation mode (6 accumulations) at a gate delay of 20 ns, gate width of 2 μ s and ICCD gain at 3000 (0 – 4000) and the exposure time of ICCD is 1.5 s. Each spectrum is the result of signal accumulated from 9000 interactions. Silver and gold NPs were utilized to carry out NE-LIBS and NE-FIBS experiments. The NPs were characterized using UV-Visible spectroscopy and transmission electron microscopy (TEM) to observe their shape and distribution. The details are concise in materials section. Pellets or targets with NPs/explosive residue/ or both were placed on a translation stage and controlled by Newport ESP 300 motion controller to expose fresh surface.

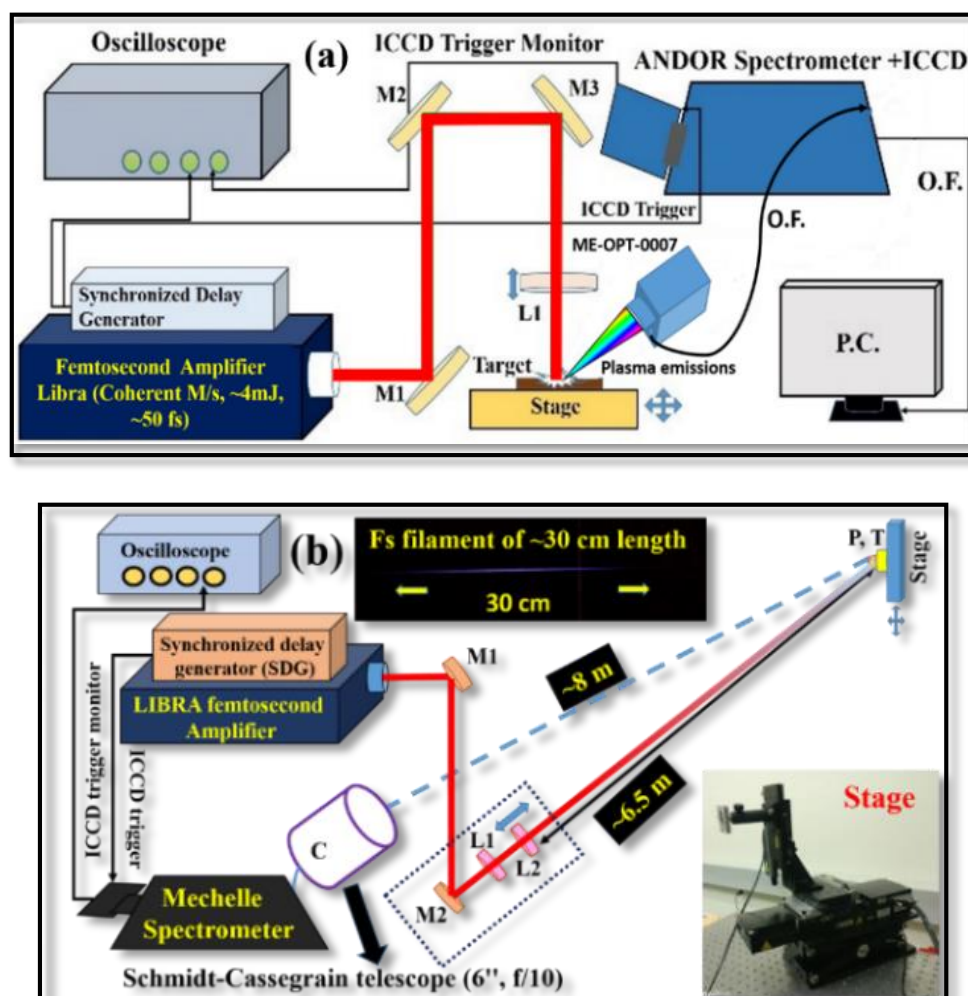


Figure 5.1 Experimental schematic of (a) proximal LIBS (or NE-LIBS) setup and (b) ST FIBS (or ST NE-FIBS) setup. In figure P-plasma; T-target; M-Mirror; L-lens, C: Schmidt-Cassegrain telescope.

5.2.1 Materials

Three types of NPs (a) chemically synthesized silver NPs by sonochemical method (AgDSR) and (b) standard silver NPs (Ag60nm) purchased from M/s NanoComposix (U.S.A.) and (c) gold NPs fabricated through ultrafast laser ablation (AuLAL) in acetone were utilized to perform NE-LIBS experiments. Synthesis and characterizations of these NPs are discussed in this section. Enhancement in the LIBS spectra of pure copper and silver targets was investigated in the proximal fs LIBS setup with Ag DSR NPs and AuLAL NPs respectively. In proximal setup nitroamino (NHNO_2) substituted aryl-tetrazole ($\text{C}_7\text{H}_4\text{N}_8\text{O}_6$) was investigated in the form of a bulk pellet. In standoff mode TNT (bulk) and CL-20 residue were investigated using femtosecond filament induced breakdown spectroscopy (fs ST FIBS). **Figures 5.2(a)-5.2(c)** depicts the molecular structure of these explosive molecules.

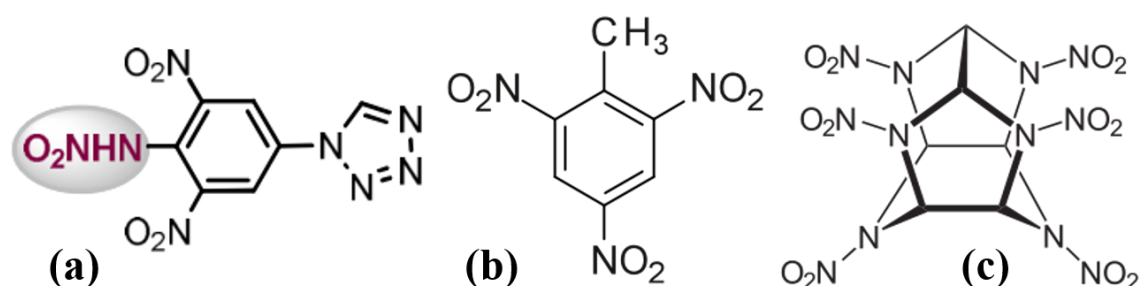


Figure 5.2 Molecular structure of (a) NHNO_2 substituted aryl-tetrazole (b) TNT and (c) CL-20.

5.2.2 NPs characterization techniques

The below characterization techniques (a) Ultraviolet-visible absorption spectroscopy and transmission electron microscopy were utilized to study the NPs.

5.2.2.a Ultraviolet-visible spectroscopy

A Perkin Elmer Lambda 750 absorption spectrometer was utilized to perform the absorption measurements of colloidal NPs solutions in the ultraviolet visible (UV-Vis) range i.e. 200-1000 nm including a small near infrared region. The spectrometer contains Tungsten-halogen (300-2500 nm) and Deuterium lamps (200-400 nm) as broadband light sources, and a monochromator to separate a single wavelength from these continuous sources and mirrors to direct the light on to the sample. The photomultipliers and diode arrays are used to detect the signal. The UV-Visible spectroscopy works on the principle of Beer lamberts law. In these studies, the UV-Visible absorption spectra of NPs were

Chapter 5

recorded using a cuvette of ~10 mm path length carrying out the base line correction. The observed SPR peak position of the metal NPs is a characteristic of the average sizes and shapes of the NPs in the solution [73,74].

5.2.2.b Transmission Electron Microscope

FEI Tecnai G² 20 [75] twin transmission electron microscope (TEM) was used for studying the shape and morphology of NPs as it offers an high point resolution imaging (0.27 nm). From the images, the NPs size distribution, morphology, and crystallinity of the NPs can be studied. It uses an electron source LaB6 with flexible transmission between 20 and 200 kV. To obtain images with high contrast, two objective lenses were used. All the essential microscopic components such as electron gun, optical components, vacuum system, and sample are digitally controlled. The instrument can provide images with high magnification in the range of 25X to 700X with line resolution 0.14 nm. Several other analysis such as SAED which study the crystal structure of material using electron diffraction, EDX can also be obtained using this. In our studies, the samples for TEM analysis were prepared by drop costing 10 μ l colloidal solution on a carbon coated copper grid. The samples were ensured to be dry before carrying out the TEM analysis.

5.2.3 Characterization of various NPs

5.2.3.a Synthesis of Silver NPs by sonochemical method

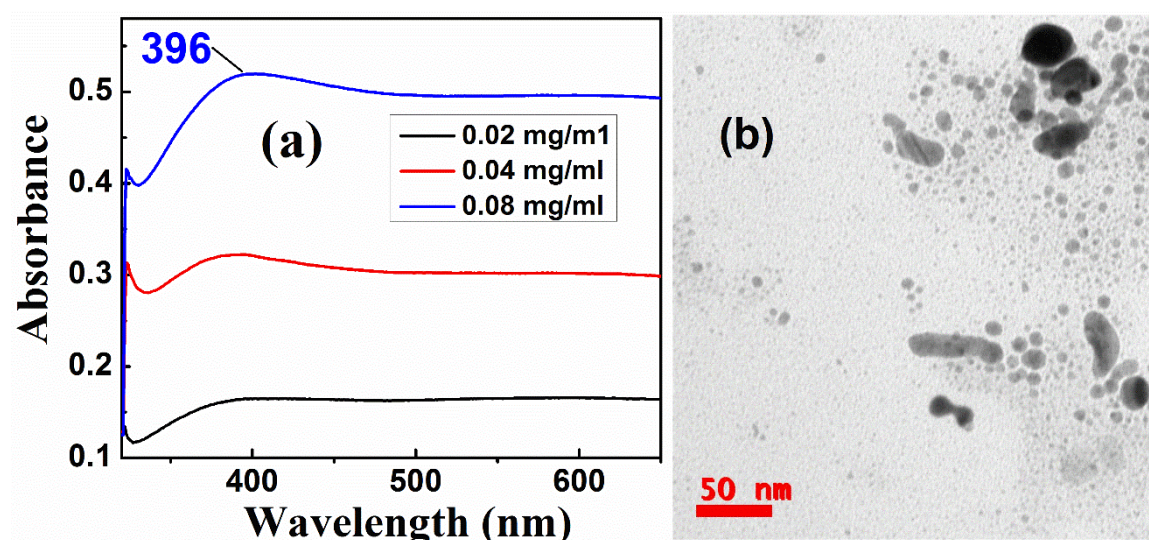


Figure 5.3 (a) Absorption spectra of AgDSR NPs in the wavelength region 320-650 nm and (b) TEM morphology of AgDSR NPs.

Silver NPs were synthesized by the sonochemical method [76]. 2 g of silver acetate ($\text{AgC}_2\text{H}_3\text{O}_2$) dissolved in ethanol was ultrasonicated for two hours. The precipitate collected after evaporating ethanol was heated in a furnace to obtain silver oxide (Ag_2O) NPs and then reduced by chemical methods. The obtained Ag NPs are labeled as AgDSR NPs. **Figure 5.3(a)** depicts the absorption spectra of AgDSR NPs in the wavelength region 320-650 nm and **figure 5.3(b)** illustrates the TEM morphology of AgDSR NPs. Solutions of different concentrations viz. 0.4, 0.16, 0.08, 0.04, and 0.02 mg/ml were made by dispersing 0.4 mg of Ag NPs in 1, 2.5, 5, 10 and 20 ml of acetone respectively. Standard micropipettes were used to measure and place a drop of 5 μl colloidal solution on targets to investigate the enhancement in LIBS signals.

5.2.3.b Fabrication of gold NPs in acetone using ULAL method

Gold NPs were fabricated through Ultrafast Laser Ablation in Liquids (ULAL) technique by immersing a gold target ($10\text{ mm} \times 10\text{ mm} \times 2\text{ mm}$) in acetone. Au NPs fabricated at different input energies of 200 μJ , 300 μJ , 400 μJ , and 500 μJ were labeled as AuLAL0, AuLAL1, AuLAL2, and AuLAL3, respectively. **Figure 5.4 (a)** illustrates the absorption spectra of AuLAL NPs in 320-650 nm wavelength regions and **figure 5.4(b)** depicts their dispersed size distribution obtained through TEM data. The size distribution and other characteristics of these NPs are reported elsewhere [45].

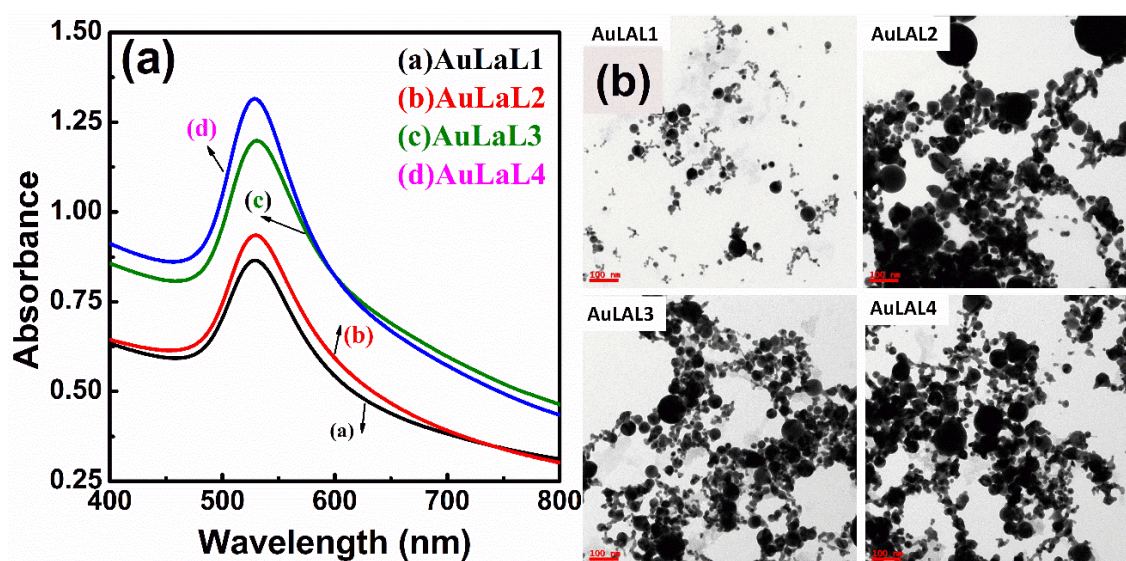


Figure 5.4 (a) UV-Visible absorption spectra and (b) TEM micrographs depicting the ploy dispersed nature of gold NPs synthesized using ULAL method. AuLAL1/2/3/4 represents the Au NPs synthesized using 200 μJ , 300 μJ , 400 μJ , and 500 μJ energy.

5.2.3.c Characterization of standard silver nanospheres (nanoXact, 0.02 mg/ml)

Silver nanospheres stabilized in citrate solution were purchased from nanoComposix (U.S.A.). **Figure 5.5(a)** Shows the UV-Visible extinction spectra of these Ag NPs in 300-750 nm spectral regions. **Figure 5.5(b)** depicts the TEM micrograph of standard Ag NPs.

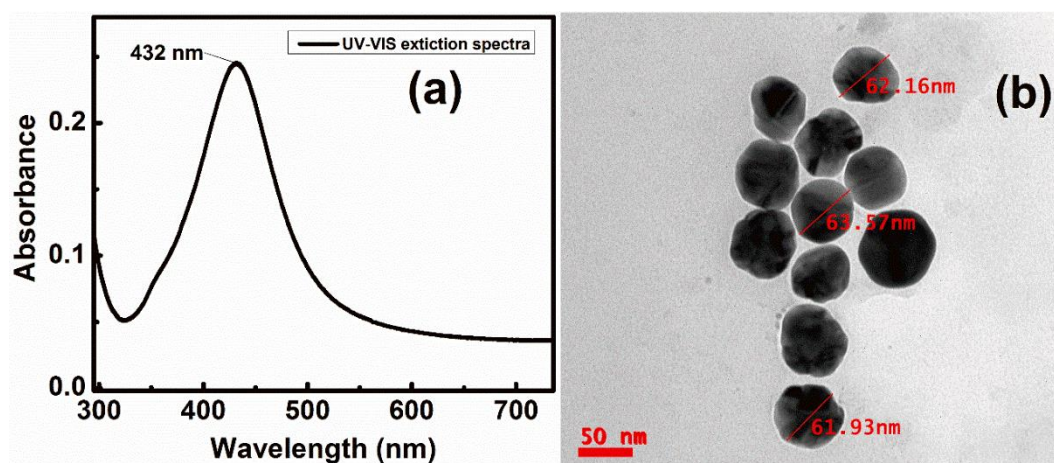


Figure 5.5 (a) UV-Vis extinction spectra and (b) TEM micrograph of standard 60 nm Ag nanospheres (NanoXact, 0.02 mg/ml) purchased from nanoComposix. (U.S.A.)

5.3 Theory

The enhancements achieved in NE-LIBS technique could be attributed to the effect of NPs on the laser ablation process as well as to the target properties (such as conducting or insulating). In this technique, the energy of the pulse should be of the order of ablation threshold of the material. In the first report of NE-LIBS, Ohta et al. [36] employed ns laser pulses with pulse energy (< 1 mJ) near to the ablation threshold. At laser irradiances higher than ablation threshold, the breakdown will be initiated through the ejection of electrons by multiphoton ionization and it is intrinsically difficult to control. Furthermore, at higher laser fluence the NPs could be fragmented to smaller particles. Thus the increase in surface area of the NPs leads to lower laser light penetration [53]. Metal NPs exhibited the reduction in breakdown or ablation threshold by generating the seed electrons leading to more efficient plasma initiation in various metallic targets, a DC discharge and in liquids as well [35,70,77]. The enhancement in the local electric field is due to the excitation of plasmons in noble metallic NPs in the presence of external electric field. Accordingly, the electric field in the proximity of NPs is manifested and, in turn,

effectively extracts electrons in the form of seed electrons. These seed electrons efficaciously participate in accelerating the breakdown process by lowering the breakdown threshold of analyte. Thus, these NPs serve as ignition centers and can lead to the very high enhancements in the LIBS signal. In the present work, we have performed all the NE-LIBS experiments with fs pulses at a wavelength of 800 nm. The use of Nd:YAG pulses at 532 nm could have led to the resonant excitations of surface plasmon of the metallic NPs, particularly in case of Au NPs, deposited on the sample. This could lead to the absorption of most of the laser energy by the NPs and an immediate efficient excitation of the plasma [78]. Nevertheless, the reproducibility and the performance of NE-LIBS technique depends on size, shape, concentration of NPs and their distribution on the target [65,78,79].

5.4 Results and Discussions

All the NE-LIBS results were obtained in proximal setup i.e. (a) enhancement of Cu LIBS signal in the presence of AgDSR NPs (b) enhancement in Ag LIBS signal using AuLAL NPs (c) enhancement in C, CN emissions in the presence of standard AgNPs and the NE-FIBS results (d) demonstrating the CN enhancement in TNT and (e) trace detection of CL-20 on brass target in standoff mode are summarized in separate sections.

5.4.1 Investigation of enhancement in the proximal LIBS setup

NE-LIBS results of various metallic targets (Cu, Ag) and a high energy material in the proximal setup are discussed in this section.

5.4.1.a LIBS and NE-LIBS experiments on Cu target using AgDSR NPs

The LIBS and NE-LIBS experiments (in the presence of AgDSR NPs) on Cu were performed at two focusing positions viz., (i) 2 mm and (ii) 4 mm above the geometrical focus. The experiments were carried at two different positions, slightly above the focus, to increase the area of interaction of pulse on the target and thereby increasing the concentration of NPs in the interaction zone. The theoretically estimated spot-size on the target is 70 μm and 100 μm at respective positions. **Figure 5.6(a)** shows a typical copper LIBS spectrum with persistent atomic and ionic peaks labeled in 250-820 nm range at 2 mm above the focal point. NE-LIBS experiments were performed by drop casting a 5 μl solution of 0.4 mg/ml AgDSR NPs solution on Cu target. A thin layer of NPs was left over after the evaporation of acetone. **Figure 5.6(b)** shows a typical LIBS spectrum of the

copper target in the spectral region of 505-580 nm with (red color) and without AgDSR NPs (0.4 mg/ml; black color). The spectral acquisition conditions for LIBS and NE-LIBS are already described in the section 5.2.

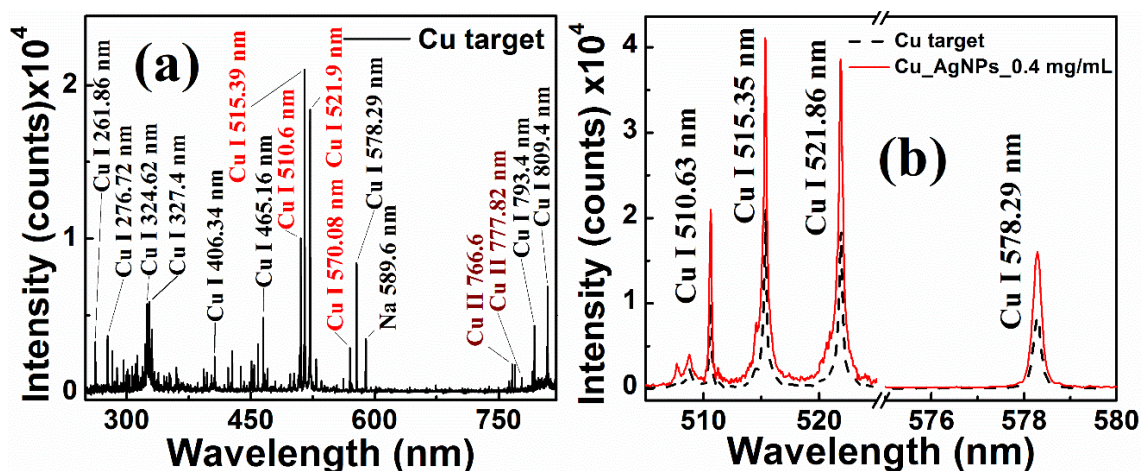


Figure 5.6 (a) Typical LIBS spectrum of Cu target in 220-820 nm (b) LIBS (dash/black) and NE-LIBS (solid/red) spectra of Cu in the region 505nm to 580 nm showing the enhancement of persistent Cu peaks with AgDSR NPs at 2 mm above focal point.

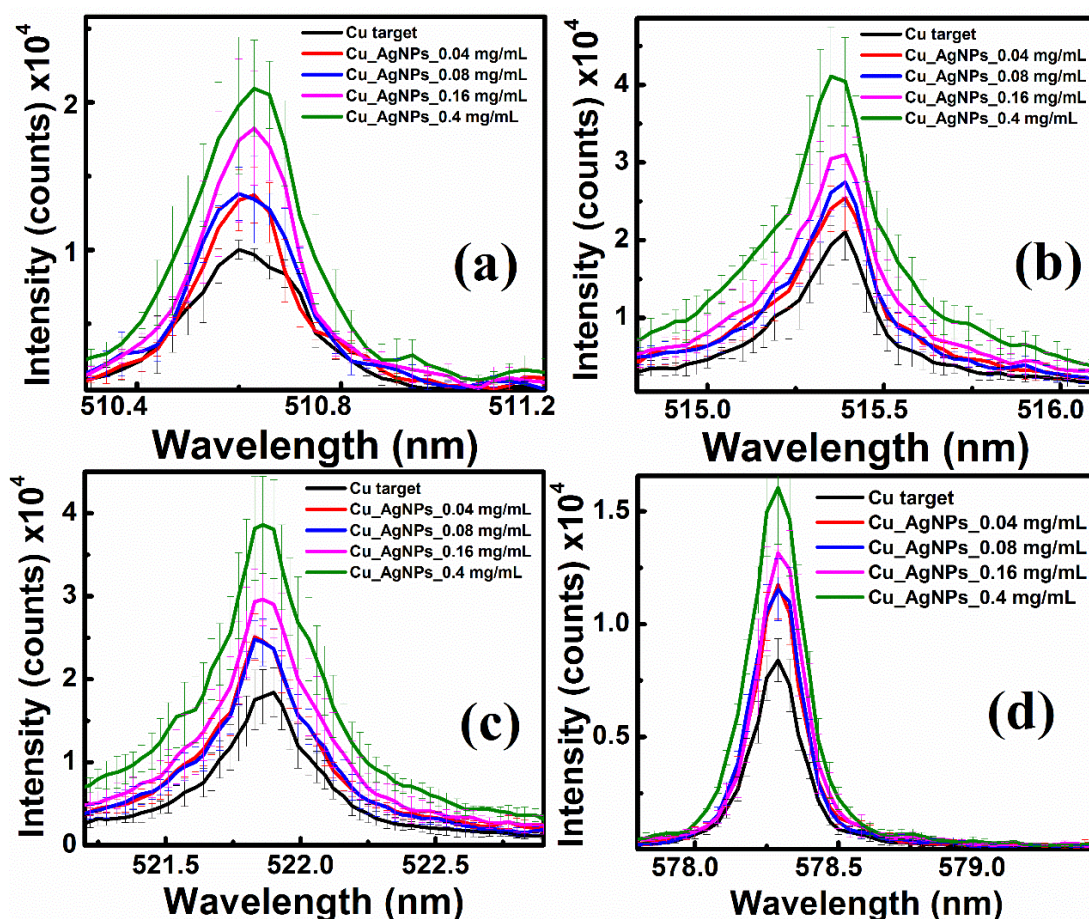


Figure 5.7 Enhancement in Copper persistent atomic transitions (a) Cu I 510.6 nm (b) Cu I 515.32 nm (c) 521.8 nm (d) Cu I 578.21 nm with increasing concentration of AgDSR NPs at 2 mm above the focal point.

A two-fold ($2\times$) enhancement was observed in the presence of AgDSR NPs (0.4 mg/ml). Further the effect of concentration of NPs on the LIBS intensity was examined by drop casting 5 μl colloidal solutions of AgDSR NPs of different concentrations (dispersed in acetone) on Cu at different places. **Figures 5.7(a)-5.7(d)** illustrate a gradual increase in the intensity of three persistent copper atomic peaks viz., Cu I at 510.55 nm, Cu I at 515.32 nm, Cu I at 521.82 nm and Cu I 570.02 nm with the increase in the concentration of Ag NPs. The enhancement in the LIBS signal can be ascribed to the coupling between the laser electromagnetic field and the surface plasmons of NPs in contact with the target surface, which has been demonstrated theoretically and experimentally. Similarly, the LIBS and NE-LIBS experiments were performed at 4 mm above the focal point in order to increase the effective interaction zone. **Figure 5.8** depicts a clear two-fold ($2\times$) enhancement in a typical LIBS spectrum of the copper target in the spectral region of 505-580 nm with (red color) and without AgDSR NPs (0.4 mg/ml; black color) at 4 mm above the focal point. However, the intensity of LIBS as well as NE-LIBS signal decreased as the target is moved above the focal point. The reduction in intensity could be attributed to decrease in fluence (energy/ interaction area). Nevertheless, a gradual increase in intensity of three persistent copper atomic peaks viz., Cu I at 510.55 nm, Cu I at 515.32 nm and Cu I at 521.82 nm and Cu I 578.21 nm with the increase in the concentration of Ag NPs was even observed at this position as seen from **figures 5.9(a)-5.9(d)**.

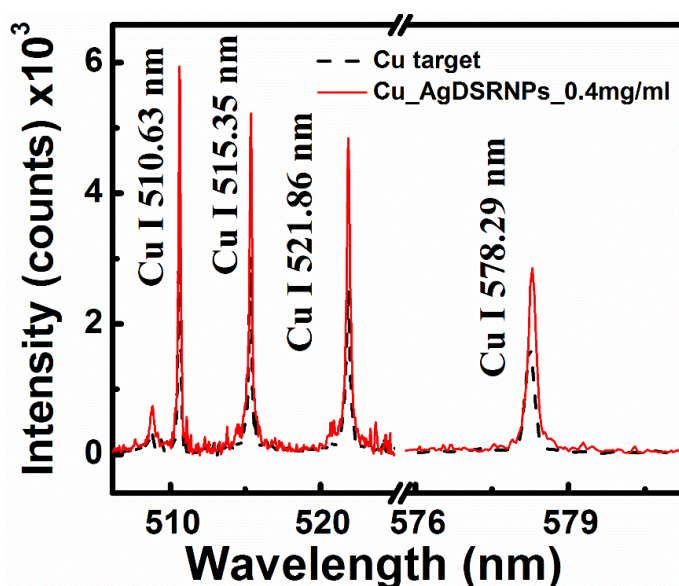


Figure 5.8 LIBS (dashed/black) and NE-LIBS (solid/red) spectra of Cu target in the wavelength region of 505-525 and 576-582 nm showing the enhancement in persistent Cu peaks in the presence of AgDSR NPs at 4 mm above from the focal point.

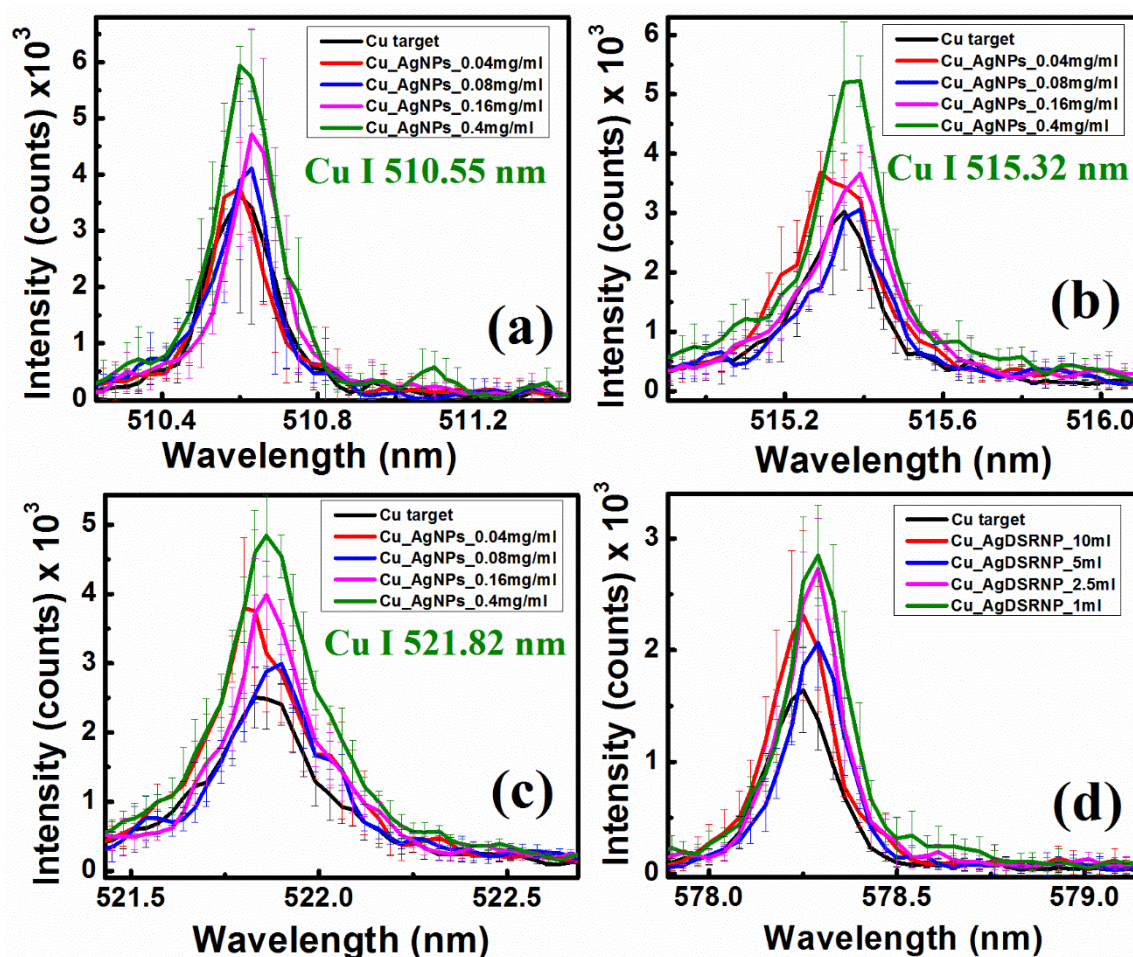


Figure 5.9 Enhancement in Copper persistent atomic transitions (a) Cu I 510.55 nm (b) Cu I 515.32 nm (c) 521.82 nm and (d) Cu I 578.21 nm with increasing concentration of the AgDSR NPs at 4 mm above from the focal point. Labels for graphs in (b), (c), and (d) are same as represented in (a).

5.4.1.b LIBS and NE-LIBS experiments on Ag target using AuLAL NPs

Gold colloidal NPs fabricated through ultrafast laser ablation of Au target in acetone were utilized to investigate the enhancement in the LIBS signal of silver target. The experiments were performed at 6 mm and 8 mm above the geometrical focus of the lens.

Figure 5.10 (a)-(b) depicts the enhancement in silver for the persistent atomic transitions of Ag I 520.90 nm and Ag I 546.54 nm with different concentrations of the AuLAL NPs at (a) 6 mm and (b) 8 mm above the focal point. From the data presented in **figure 5.10** it is evident that the enhancement in the silver peaks is neither uniform nor linear. Moreover, not all the AuLAL NPs have resulted in enhancements except NPs fabricated at 400 μ J (AuLAL2). This could be attributed to the random poly-dispersed nature of NPs [as seen from **figure 5.4(b)**] produced in the ULAL technique. However, these NPs cannot be ruled out as AuLAL2 NPs have resulted in enhancements in both the cases.

Giacomo et al. have also reported significant enhancement using laser ablated Ag and Cu NPs [35] on Al based alloy target.

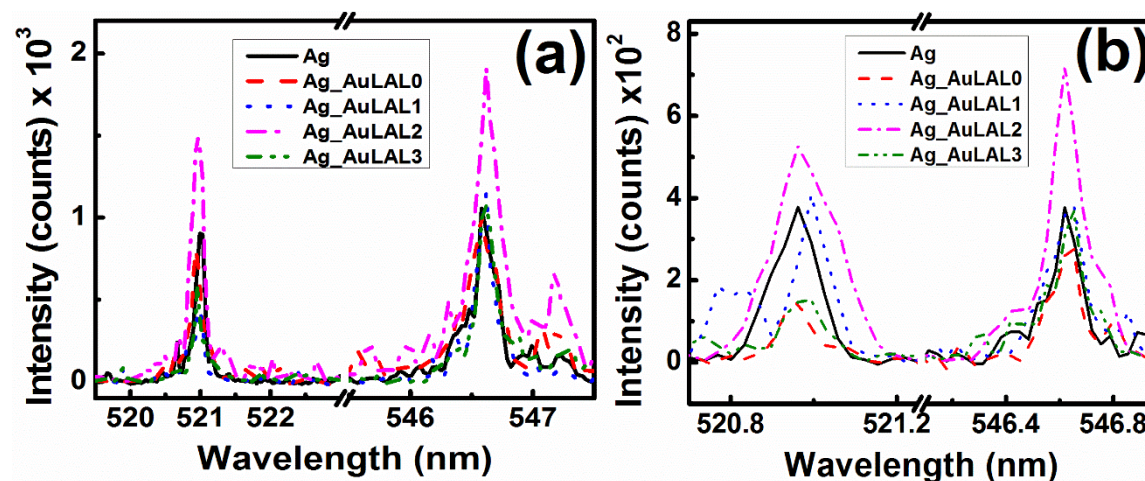


Figure 5.10. Enhancement in silver persistent atomic transitions Ag I 520.90 nm and Ag I 546.54 nm with different concentrations of the AuLAL NPs at (a) 6 mm and (b) 8 mm above the focal point.

5.4.1.c LIBS and NE-LIBS experiments on HEM pellet using standard Ag NPs

NE-LIBS experiments of nitroamino (NHNO_2) substituted aryl-tetrazole (a high energy material) in the form of a bulk pellet (150 mg, 12 mm diameter, and 2 mm thick) were performed using the standard Ag NPs (60 nm). The synthesis and energetic parameters of nitroamino (NHNO_2) substituted aryl tetrazole are reported by Kommu et al. [80]. Due to the ambiguous result in obtained enhancements while using laser ablated NPs on silver target, these AuLAL NPs were not used further. Though LIBS is a multi-elemental analysis technique the molecular bands observed in LIBS spectra (i) owing to fragmentation during the ablation and (ii) due to the various recombination reactions within the plasma constituents as well as between plasma and ambient constituents are useful in analysing organic samples such as plastics, energetic materials. Specific to organic explosives, owing to their similar constituents of C, H, N and O; the LIBS spectra look similar with predominant CN violet band ($\text{B}^2\Sigma^+ \rightarrow \text{X}^2\Sigma^+$) [in the spectral region 358-360 nm, 386-390 nm, 410-422 nm corresponding to Δv values of 1, 0, -1 respectively with $\Delta v=0$ band having maximum intensity], C_2 swan band ($\text{d}^3\Pi_g \rightarrow \text{a}^3\Pi_u$) [in the spectral range of 465-475 nm, 510-518 nm, 555-565 nm with maximum intensity at $\Delta v=0$] molecular emission bands along with C, H, N and O atomic emissions. The molecular bands and atomic peaks were identified and labeled from Gaydon and Pearse molecular database (handbook) [81] and NIST database [82], respectively. The LIBS and NE-LIBS spectra were acquired with a gate delay of 50 ns, gate width of 1 μs , ICCD gain of 3000,

Chapter 5

an exposure time of 1 s, and 2 accumulations at a repetition rate of 2 Hz. Carbon atomic emission (C I 247.8 nm) and CN $\Delta v=0$ (only) band were observed in proximal case owing to few accumulations (4 only). **Figures 5.11(a) and 5.11(b)** depicts the enhancement in carbon atomic transition (C I 247.8 nm) and in CN $\Delta v=0$ band respectively of nitroamino (NHNO₂) substituted aryl-tetrazole in the presence of Ag NPs. In NE-LIBS experiments 10 μ l of Ag NPs were drop casted onto the pellet of NHNO₂ pellet (150 mg). A two factor (2 \times) enhancement was observed in both carbon atomic transition at 247.8 nm and CN ($\Delta v=0$) molecular band.

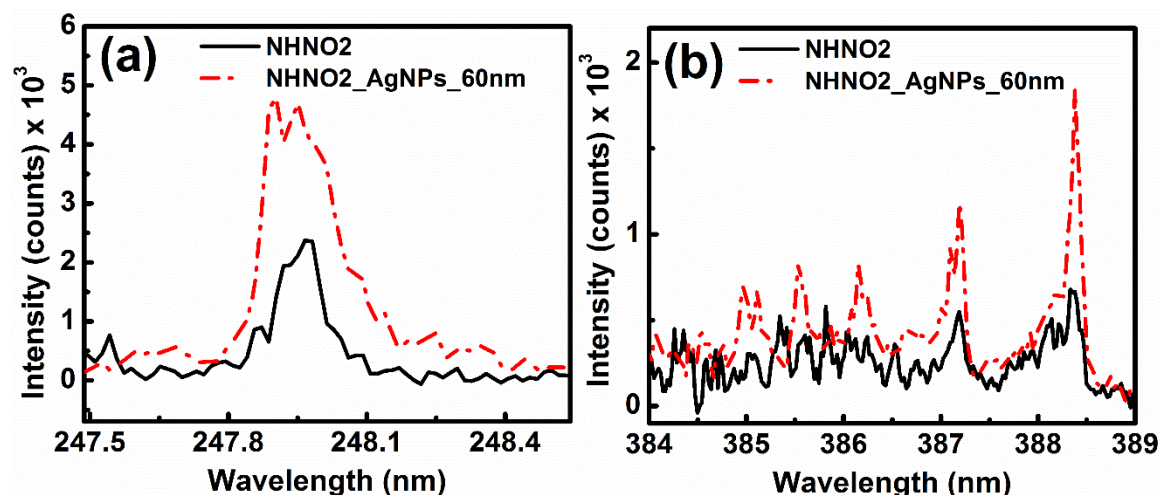


Figure 5.11 Enhancement in the intensity of (a) carbon atomic transition, C I 247.80 nm and (b) CN ($\Delta v=0$) molecular band of nitroamino (NHNO₂) substituted aryl tetrazole in the presence of standard Ag NPs (60 nm) [M/s NanoComposix] in proximal LIBS setup.

5.4.2 Investigation of enhancement in the LIBS signal of high energy materials in standoff configuration

5.4.2.a FIBS and NE-FIBS experiments on bulk TNT standoff mode

Several researchers have investigated the detection and class labeling of explosive molecules. In the existing fs ST-FIBS setup [see **figure 5.1(b)**], the enhancement of FIBS signal from TNT in the form of a bulk pellet (150 mg) was examined. TNT pellet was mounted on pure Si target prior to the experiments. ST-FIBS and ST-NEFIBS spectra of TNT were recorded in the absence/presence of standard Ag NPs. **Figure 5.12(a)** illustrates the ST FIBS and ST NE-FIBS spectra of TNT (in bulk) which was placed on a pure Si target. A silicon atomic peak is seen at Si I 390.55 nm. **Figure 5.12(b)** shows a clear two factor enhancement in two molecular band transitions of CN $\Delta v=0$ molecular band at 388.34 nm and 387.14 nm. In standoff mode, C I 247.8 nm could not be observed as the effective transmission range of the telescope is in visible and NIR region only.

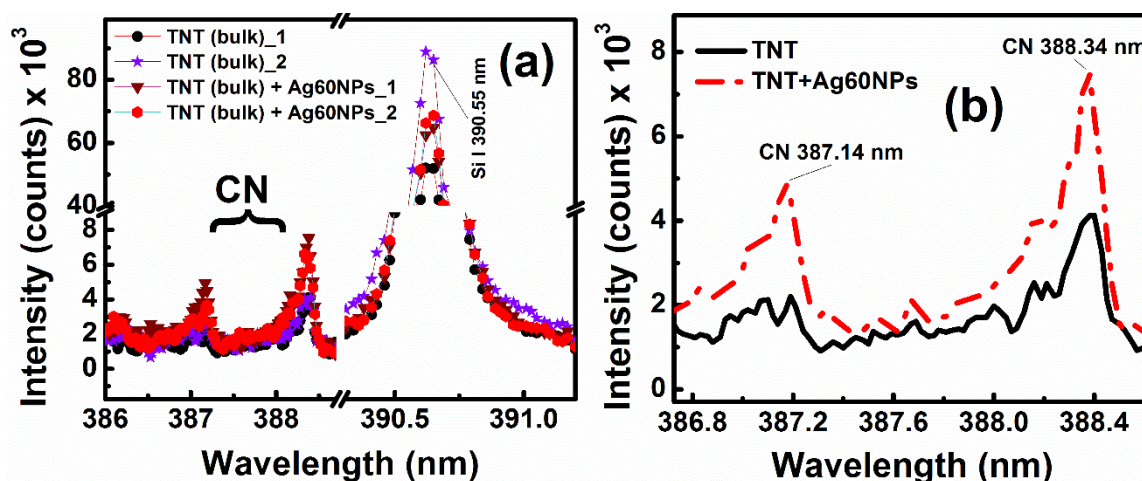


Figure 5.12. Enhancement in intensity of (a) CN molecular band transitions in comparison to Si I atomic peak at 390.55 nm (b) CN molecular transitions shown explicitly of TNT in standoff mode.

5.4.2.b NE-FIBS experiments for trace detection of energetic molecule in standoff mode

Similarly, in STFIBS setup a residue of CL-20 on brass target was examined for the capability of fs filaments for the standoff residue analysis. 22 mg of CL-20 was dissolved in 1 ml of acetone to make 50 mM solution. 50 μ l (1 mg) of CL-20 solution was drop casted on brass target over 1 cm^2 area. After five minutes a layer of CL-20 residue was formed after the evaporation of acetone at room temperature. **Figure 5.13** illustrates the enhancement in CN 338.34 nm in the presence of standard Ag NPs. However, in the absence of NPs no CN band (signature of organic energetic molecule) was observed.

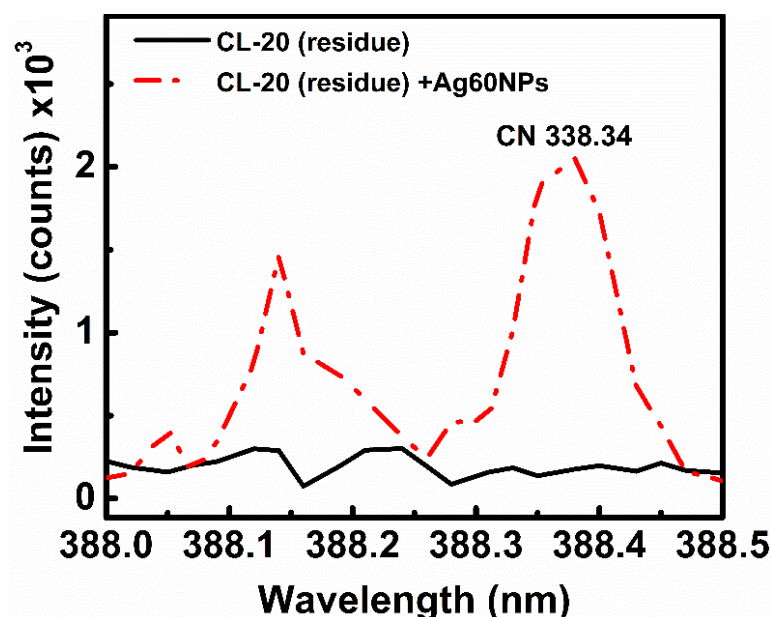


Figure 5.13. Enhancement in intensity of CN molecular band transition at 388.34 nm in the LIBS data of CL-20 and in the presence of Ag NPs.

5.5 Conclusions

Nanoparticle enhanced LIBS (NE-LIBS) in the proximal configuration and Nanoparticle enhanced FIBS in (NEFIBS) at a standoff distance of ~6.5 m is demonstrated using femtosecond pulses for increasing the sensitivity of LIBS technique. The enhancements achieved for various analyte in the presence of NPs shows the increase in sensitivity of LIBS. Chemically synthesized Ag NPs, Au NPs (obtained from ULAL technique) and standard Ag NPs (60 nm) were utilized to investigate the enhancement in LIBS signal of Cu, Ag metallic targets and an explosive pellet (TNT). A two factor (2×) enhancement was observed in all the cases. The enhancements in the LIBS signal in the presence of NPs could be attributed to the electromagnetic field enhancement which can essentially increase the LIBS emission signal up to two/three orders of magnitude with respect to the signal of a sample ablated under normal conditions [35]. The NPs act as impurities over the surface thereby decreasing the breakdown threshold. Furthermore, they act as ignition centers and provide more seed electrons which improves the ablation efficiency and thus resulting in the increased signal [83]. The enhancements in the LIBS spectra of energetic molecules, in the presence of NPs has been witnessed in all the cases even with different molecules viz., tetrazole (proximal), TNT (bulk in standoff), CL-20 (trace in standoff). Thus NE-LIBS could be considered as a promising variant of LIBS for several applications especially in trace detection of explosives in both proximal and standoff detection. Nevertheless, Tang et al. [84] demonstrated enhancement in LIBS signal by combining Au NPs and magnetic field confinement on copper and Sladkova et al. [85] investigated the trace detection of Pb in brass target using ns pulses at various low pressure conditions and achieved a four factor enhancement. Though there are several ways being investigated and reported for achieving enhancements, further systematic studies are mandated to (a) obtain more reliable and satisfactory enhancements and remarkable conclusions because NE-LIBS technique can be influenced by various laser parameters, NPs characteristics and their distribution on the sample surface (b) address few questions regarding optimization of sample preparation, duration of the field enhancement effect, NPs breakdown etc. in NE-LIBS.

5.6 References

1. L. Mokalled, M. Al-husseini, K. Y. Kabalan, and A. El-hajj, "Sensor Review for Trace Detection of Explosives," *Int. J. Sci. Eng. Res.* **5**(6), 337–350 (2014).
2. M. J. Lefferts and M. R. Castell, "Vapour sensing of explosive materials," *Anal. Methods* **7**(21), 9005–9017 (2015).
3. D. S. Moore, "Instrumentation for trace detection of high explosives," *Rev. Sci. Instrum.* **75**(8), 2499–2512 (2004).
4. J. L. Gottfried, D. K. Smith, C. Wu, and M. L. Pantoya, "Improving the Explosive Performance of Aluminum Nanoparticles with Aluminum Iodate Hexahydrate (AIH)," *Sci. Rep.* **8**(1), 8036 (2018).
5. L. Türker, "Thermobaric and enhanced blast explosives (TBX and EBX)," *Def. Technol.* **12**(6), 423–445 (2016).
6. R. Bogue, "Detecting explosives and chemical weapons: a review of recent developments," *Sens. Rev.* **35**(3), 237–243 (2015).
7. J. I. Steinfeld and J. Wormhoudt, "EXPLOSIVES DETECTION: A Challenge for Physical Chemistry," *Annu. Rev. Phys. Chem.* **49**(1), 203–232 (1998).
8. S. Singh and M. Singh, "Explosives detection systems (EDS) for aviation security," *Signal Processing* **83**(1), 31–55 (2003).
9. S. Wallin, A. Pettersson, H. Östmark, and A. Hobro, "Laser-based standoff detection of explosives: a critical review," *Anal. Bioanal. Chem.* **395**(2), 259–274 (2009).
10. J. B. Johnson, S. D. Allen, J. Merten, L. Johnson, D. Pinkham, and S. W. Reeve, "Standoff Methods for the Detection of Threat Agents: A Review of Several Promising Laser-Based Techniques," *J. Spectrosc.* **2014**(Article ID 613435), 13 (2014).
11. D. W. Hahn and N. Omenetto, "Laser-induced breakdown spectroscopy (LIBS), part I: review of basic diagnostics and plasma-particle interactions: still-challenging issues within the analytical plasma community.," *Appl. Spectrosc.* **64**(12), 335–66 (2010).
12. D. W. Hahn and N. Omenetto, "Laser-induced breakdown spectroscopy (LIBS), part II: Review of instrumental and methodological approaches to material analysis and applications to different fields," *Appl. Spectrosc.* **66**(4), 347–419 (2012).
13. A. K. Myakalwar, S. Sreedhar, I. Barman, N. C. Dingari, S. Venugopal Rao, P. Prem Kiran, S. P. Tewari, and G. Manoj Kumar, "Laser-induced breakdown spectroscopy-based investigation and classification of pharmaceutical tablets using multivariate chemometric analysis," *Talanta* **87**, 53–59 (2011).
14. S. J. Rehse, H. Salimnia, and A. W. Miziolek, "Laser-induced breakdown spectroscopy (LIBS): An overview of recent progress and future potential for biomedical applications," *J. Med. Eng. Technol.* **36**(2), 77–89 (2012).
15. R. S. Harmon, R. E. Russo, and R. R. Hark, "Applications of laser-induced breakdown spectroscopy for geochemical and environmental analysis: A comprehensive review," *Spectrochim. Acta B* **87**, 11–26 (2013).
16. G. S. Senesi, "Laser-Induced Breakdown Spectroscopy (LIBS) applied to terrestrial and extraterrestrial analogue geomaterials with emphasis to minerals and rocks," *Earth Sci. Rev.* **139**, 231–267 (2014).
17. R. Wainner and R. S. Harmon, "Analysis of environmental lead contamination : Comparison of LIBS field and laboratory instruments Analysis of environmental lead contamination : comparison of LIBS field and laboratory instruments," *Spectrochim. Acta B* **56**, 777–793 (2001).

Chapter 5

18. Y. Tian, B. Xue, J. Song, Y. Lu, and R. Zheng, "Non-gated laser-induced breakdown spectroscopy in bulk water by position-selective detection," *Appl. Phys. Lett.* **107**, 111107 (2015).
19. V. Lazic and S. Jovi, "Laser induced breakdown spectroscopy inside liquids: Processes and analytical aspects," *Spectrochim. Acta Part B* **101**, 288–311 (2014).
20. G. Arca, A. Ciucci, V. Palleschi, S. Rastelli, and E. Tognoni, "Trace Element Analysis in Water by the Laser-Induced Breakdown Spectroscopy Technique," *Appl. Spectrosc.* **51**(8), 1102–1105 (1997).
21. V. Lazic, A. Palucci, S. Jovicevic, and M. Carpanese, "Detection of explosives in traces by laser induced breakdown spectroscopy: Differences from organic interferences and conditions for a correct classification," *Spectrochim. Acta Part B At. Spectrosc.* **66**(8), 644–655 (2011).
22. I. Gaona, J. Serrano, J. Moros, and J. J. Laserna, "Range-Adaptive Standoff Recognition of Explosive Fingerprints on Solid Surfaces using a Supervised Learning Method and Laser- Induced Breakdown Spectroscopy," *Anal. Chem.* **86**(10), 5045–5052 (2014).
23. C. López-Moreno, S. Palanco, J. J. Laserna, F. DeLucia, A. W. Miziolek, J. Rose, R. A. Walters, and A. I. Whitehouse, "Test of a stand-off laser-induced breakdown spectroscopy sensor for the detection of explosive residues on solid surfaces," *J. Anal. At. Spectrom.* **21**(1), 55–60 (2006).
24. F. J. Fortes and J. J. Laserna, "The development of fieldable laser-induced breakdown spectrometer: No limits on the horizon," *Spectrochim. Acta B* **65**(12), 975–990 (2010).
25. L. B. Guo, B. Y. Zhang, X. N. He, C. M. Li, Y. S. Zhou, T. Wu, J. B. Park, X. Y. Zeng, and Y. F. Lu, "Optimally enhanced optical emission in laser- induced breakdown spectroscopy by combining spatial confinement and dual-pulse irradiation," *Opt. Express* **20**(2), 1436–1443 (2012).
26. A. M. Popov, F. Colao, and R. Fantoni, "Spatial confinement of laser-induced plasma to enhance LIBS sensitivity for trace elements determination in soils," *J. Anal. At. Spectrom.* **25**(6), 837–848 (2010).
27. Q. Wang, A. Chen, D. Zhang, Y. Wang, L. Sui, S. Li, Y. Jiang, and M. Jin, "The role of cavity shape on spatially confined laser-induced breakdown spectroscopy," *Phys. Plasmas* **25**, 073301 (2018).
28. Y. Li, D. Tian, Y. Ding, G. Yang, K. Liu, C. Wang, and X. Han, "A review of laser-induced breakdown spectroscopy signal enhancement," *Appl. Spectrosc. Rev.* **53**(1), 1–35 (2018).
29. C. M. Ahamer and J. D. Pedarnig, "Femtosecond double pulse laser-induced breakdown spectroscopy: Investigation of the intensity enhancement," *Spectrochim. Acta B* **148**, 23–30 (2018).
30. M. Akhtar, A. Jabbar, S. Mehmood, N. Ahmed, R. Ahmed, and M. A. Baig, "Magnetic field enhanced detection of heavy metals in soil using laser induced breakdown spectroscopy," *Spectrochim. Acta B* **148**, 143–151 (2018).
31. L. B. Guo, X. N. He, B. Y. Zhang, C. M. Li, W. Hu, Y. S. Zhou, W. Xiong, X. Y. Zeng, and Y. F. Lu, "Enhancement of laser-induced breakdown spectroscopy signals using both hemispherical cavity and a magnetic field," in *Laser-Based Micro- and Nanopackaging and Assembly VI* (SPIE, 2012), **8244**, p. 82440I.
32. N. B. Zorov, A. M. Popov, S. M. Zaytsev, and T. A. Labutin, "Qualitative and quantitative analysis of environmental samples by laser-induced breakdown spectrometry," *Russ. Chem. Rev.* **84**(10), 1021–1050 (2015).

33. F. C. De Lucia, J. L. Gottfried, C. A. Munson, and A. W. Miziolek, "Double pulse laser-induced breakdown spectroscopy of explosives: Initial study towards improved discrimination," *Spectrochim. Acta B* **62**(12), 1399–1404 (2007).
34. D. K. Killinger, S. D. Allen, R. D. Waterbury, C. Stefano, and E. L. Dottery, "Enhancement of Nd: YAG LIBS emission of a remote target using a simultaneous CO₂ laser pulse," *Opt. Express* **15**(20), 12905–12915 (2007).
35. A. De Giacomo, R. Gaudiuso, C. Koral, M. Dell'Aglio, and O. De Pascale, "Nanoparticle-enhanced laser-induced breakdown spectroscopy of metallic samples," *Anal. Chem.* **85**(21), 10180–10187 (2013).
36. T. Ohta, M. Ito, T. Kotani, and T. Hattori, "Emission Enhancement of Laser-Induced Breakdown Spectroscopy by Localized Surface Plasmon Resonance for Analyzing Plant Nutrients," *Appl. Spectrosc.* **63**(5), 555–558 (2009).
37. F. Poggialini, B. Campanella, S. Giannarelli, E. Grifoni, S. Legnaioli, G. Lorenzetti, S. Pagnotta, A. Safi, and V. Palleschi, "Green-synthesized silver nanoparticles for Nanoparticle- Enhanced Laser Induced Breakdown Spectroscopy (NELIBS) using a mobile instrument," *Spectrochim. Acta B* **141**, 53–58 (2018).
38. P. Buffat and J. P. Borel, "Size effect on the melting temperature of gold particles," *Phys. Rev. A* **13**(6), 2287–2298 (1976).
39. K. Park, D. Lee, A. Rai, D. Mukherjee, and M. Zachariah, "Size-resolved kinetic measurements of aluminum nanoparticle oxidation with single particle mass spectrometry," *J. Phys. Chem. B* **109**(15), 7290–7299 (2005).
40. D. L. Fedlheim and C. A. Foss, *Metal Nanoparticles: Synthesis, Characterization, and Applications* (CRC Press, 2001).
41. W. H. De Jong and P. J. a Borm, "Drug delivery and nanoparticles: applications and hazards.," *Int. J. Nanomedicine* **3**(2), 133–149 (2008).
42. V. Amendola, R. Pilot, M. Frascioni, O. M. Maragò, and M. A. Iatì, "Surface plasmon resonance in gold nanoparticles: A review," *J. Phys. Condens. Matter* **29**(20), p.203002 (2017).
43. A. Chou, E. Jaatinen, R. Buividas, G. Seniutinas, S. Juodkazis, E. L. Izake, and P. M. Fredericks, "SERS substrate for detection of explosives," *Nanoscale* **4**(23), 7419–7424 (2012).
44. V. R. Soma, G. K. Podagatlapalli, and H. Syed, "Femtomolar Detection of Explosive Molecules using Laser Ablated Targets and SERS," in *13th International Conference on Fiber Optics and Photonics* (OSA, 2016), p. Th4D.2.
45. C. Byram, S. S. B. Moram, A. K. Shaik, and V. R. Soma, "Versatile gold based SERS substrates fabricated by ultrafast laser ablation for sensing picric acid and ammonium nitrate," *Chem. Phys. Lett.* **685**, 103–107 (2017).
46. D. Eversole, B. Lukyanchuk, and A. Benyakar, "Plasmonic laser nanoablation of silicon by the scattering of femtosecond pulses near gold nanospheres," *Appl. Phys. A* **89**, 283–291 (2007).
47. C. Ropers, D. R. Solli, C. P. Schulz, C. Lienau, and T. Elsaesser, "Localized Multiphoton Emission of Femtosecond Electron Pulses from Metal Nanotips," *Phys. Res. Lett.* **98**, 043907 (2007).
48. P. K. Jain and M. A. El-Sayed, "Noble metal nanoparticle Pairs: Effect of medium for enhanced nanosensing," *Nano Lett.* **8**(12), 4347–4352 (2008).
49. M. K. Kinnan, S. Kachan, C. K. Simmons, and G. Chumanov, "Plasmon Coupling in Two-Dimensional Arrays of Silver Nanoparticles: I. Effect of the Dielectric Medium," *J. Phys. Chem. C* **113**, 7079–7084 (2009).
50. M. K. Kinnan and G. Chumanov, "Plasmon Coupling in Two-Dimensional Arrays

- of Silver Nanoparticles : II . Effect of the Particle Size and Interparticle Distance," *J. Phys. Chem. C* **114**, 7496–7501 (2010).
51. M. El Ashraf Sherbini and C. G. Parigger, "Nano-material size dependent laser-plasma thresholds," *Spectrochim. Acta B* **124**, 79–81 (2016).
 52. C. Koral, M. D. Aglio, R. Gaudiuso, R. Alrifai, M. Torelli, and A. De Giacomo, "Nanoparticle-Enhanced Laser Induced Breakdown Spectroscopy for the noninvasive analysis of transparent samples and gemstones," *Talanta* **182**, 253–258 (2018).
 53. M. EL Ashraf Sherbini, A. A. Galil, S. H. Allam, A. Sherbini, and Th M EL Sherbini, "Nanomaterials induced plasma spectroscopy," in *Journal of Physics: Conference Series* (IOP Publishing, 2014), **548**, p. 012031.
 54. C. Sánchez-aké, T. García-fernández, J. L. Benítez, M. B. De Mora, and M. Villagrán-muniz, "Intensity enhancement of LIBS of glass by using Au thin films and nanoparticles," *Spectrochim. Acta B* **146**, 77–83 (2018).
 55. C. Koral, A. De Giacomo, X. Mao, V. Zorba, and R. E. Russo, "Nanoparticle Enhanced Laser Induced Breakdown Spectroscopy for Improving the Detection of Molecular Bands," *Spectrochim. Acta B* **125**, 11–17 (2016).
 56. A. De Giacomo, C. Koral, G. Valenza, R. Gaudiuso, and M. D. Aglio, "Nanoparticle enhanced laser-induced breakdown Spectroscopy for microdrop analysis at subppm level," *Anal. Chem.* **88**(10), 5251–5257 (2016).
 57. E. G. Gamaly, A. V Rode, and V. T. Tikhonchuk, "Ablation of solids by femtosecond lasers : Ablation mechanism and ablation thresholds for metals and dielectrics," *Phys. Plasmas* **9**(3), 949 (2002).
 58. P. Mannion, J. Magee, E. Coyne, and G. M. O. Connor, "Ablation thresholds in ultrafast laser micro-machining of common metals in air," in *Opto-Ireland 2002: Optics and Photonics Technologies and Applications*, T. J. Glynn, ed. (SPIE, 2003), **4876**, pp. 470–478.
 59. D. Ashkenasi, M. Lorenz, R. Stoian, and A. Rosenfeld, "Surface damage threshold and structuring of dielectrics using femtosecond laser pulses: the role of incubation," *Appl. Surf. Sci.* **150**, 101–106 (1999).
 60. A. T. B.N. Chicbkov, C. Momma, S. Nolte, F. von Alvensleben, "Femtosecond, picosecond and nanosecond laser ablation of solids," *Appl. Phys. A* **63**, 109–115 (1996).
 61. C. M. Ahamer and J. D. Pedarnig, "Femtosecond double pulse laser-induced breakdown spectroscopy: Investigation of the intensity enhancement," *Spectrochim. Acta B* **148**, 23–30 (2018).
 62. D. Zhang, A. Chen, X. Wang, S. Li, Y. Wang, L. Sui, Y. Jiang, and M. Jin, "Enhancement mechanism of femtosecond double-pulse laser-induced Cu plasma spectroscopy," *Opt. Laser Technol.* **96**, 117–122 (2017).
 63. S. A. Kalam, N. L. Murthy, J. R. Krishna, V. Sriknath, and S. V Rao, "Nanoparticle Enhanced Laser Induced Breakdown Spectroscopy with Femtosecond Pulses," in *13th International Conference on Fiber Optics and Photonics* (2016), p. Th3A.89.
 64. F. Yang, L. Jiang, S. Wang, Z. Cao, L. Liu, M. Wang, and Y. Lu, "Emission enhancement of femtosecond laser induced breakdown spectroscopy by combining nanoparticle and dual-pulse on crystal SiO₂," *Opt. Laser Technol.* **93**, 194–200 (2017).
 65. F. Yang, Z. Cao, B. Yang, F. Yang, Z. Cao, and B. Yang, "Nanofilm-enhanced Femtosecond Laser-induced Breakdown Spectroscopy," *AIP Conf. Proc.* **1829**,

- 020007 (2017).
66. K. K. Anoop, N. Verma, N. Joy, S. S. Harilal, and R. Philip, "Enhancement of optical emission and ion currents in a laser produced silicon plasma by femtosecond laser-induced periodic surface structuring," *Phys. Plasmas* **25**(6), 63304 (2018).
 67. M. Dell, R. Alrifai, and A. De Giacomo, "Nanoparticle Enhanced Laser Induced Breakdown Spectroscopy (NELIBS), a first review," *Spectrochim. Acta B* **148**, 105–112 (2018).
 68. J. L. Gottfried, "Laser-induced plasma chemistry of the explosive RDX with various metallic nanoparticles," *Appl. Opt.* **51**(7), 13–21 (2012).
 69. D. Dong, L. Jiao, X. Du, and C. Zhao, "Ultrasensitive nanoparticle enhanced laser-induced breakdown spectroscopy using a super-hydrophobic substrate coupled with magnetic confinement," *Chem. Commun.* **53**(33), 4546–4549 (2017).
 70. D. A. Rusak, T. P. Anthony, and Z. T. Bell, "Note: A novel technique for analysis of aqueous solutions by laser-induced breakdown spectroscopy.," *Rev. Sci. Instrum.* **86**(11), 116106 (2015).
 71. S. Niu, L. Zheng, A. Q. Khan, G. Feng, and H. Zeng, "Laser-induced breakdown spectroscopic detection of trace level heavy metal in solutions on a laser-pretreated metallic target," *Talanta* **179**, 312–317 (2018).
 72. X. Wen, Q. Lin, G. Niu, Q. Shi, and Y. Duan, "Emission enhancement of laser-induced breakdown spectroscopy for aqueous sample analysis based on Au nanoparticles and solid-phase substrate," *Appl. Opt.* **55**(24), 6706 (2016).
 73. S. BASET, H. AKBARI, H. ZEYNALI, and M. SHAFIE, "Size measurement of metal and semiconductor nanoparticles via UV-Vis absorption spectra," *Dig. J. Nanomater. Biostructures* **6**(2), 709–716 (2011).
 74. V. Amendola and M. Meneghetti, "Size evaluation of gold nanoparticles by UV-vis spectroscopy," *J. Phys. Chem. C* **113**(11), 4277–4285 (2009).
 75. CNSI/EICN, *TF20: Tecnai G2 200kV TEM (FEI). Operation Manual for Basic TEM* (2008), (November).
 76. J. Zhu, S. Liu, O. Palchik, Y. Koltypin, and A. Gedanken, "Shape-controlled synthesis of silver nanoparticles by pulse sonoelectrochemical methods," *Langmuir* **16**(16), 6396–6399 (2000).
 77. J. Sawyer, J. Abboud, Z. Zhang, and S. F. Adams, "Reduction of breakdown threshold by metal nanoparticle seeding in a DC microdischarge," *Nanoscale Res. Lett.* **10**(1), 1–6 (2015).
 78. A. De Giacomo, M. D. Aglio, R. Gaudioso, C. Koral, and G. Valenza, "Perspective on the use of nanoparticles to improve LIBS analytical performance: nanoparticle enhanced laser induced breakdown spectroscopy (NELIBS)," *J. Anal. At. Spectrom.* **31**, 1566–1573 (2016).
 79. M. Majumder, C. S. Rendall, J. A. Eukel, J. Y. Wang, N. Behabtu, C. L. Pint, T.-Y. Liu, A. W. Orbaek, F. Mirri, and J. Nam, "Overcoming the "coffee-stain" effect by compositional Marangoni-flow-assisted drop-drying," *J. Phys. Chem. B* **116**(22), 6536–6542 (2012).
 80. N. Kommu, M. Balaraju, V. D. Ghule, and A. K. Sahoo, "Synthetic Manifestation of Nitro Substituted Tetrazole-N- (Hetero)Aryl Derivatives and Energetic Studies," *J. Mater. Chem. A* **5**, 7366–7371 (2017).
 81. A. G. Gaydon, *The Identification of Molecular Spectra: RWB Pearse and AG Gaydon* (Chapman and Hall, 1976).
 82. "NIST atomic spectra database," <https://www.nist.gov/pml/atomic-spectra->

Chapter 5

- database.
83. A. De Giacomo, R. Gaudio, C. Koral, M. D. Aglio, and O. De Pascale, "Nanoparticle Enhanced Laser Induced Breakdown Spectroscopy: Effect of nanoparticles deposited on sample surface on laser ablation and plasma emission," *Spectrochim. Acta B* **98**, 19–27 (2014).
 84. H. Tang, X. Hao, and X. Hu, "Spectral Characteristics of Laser-induced Plasma by Combining Au-nanoparticles and Magnetic Field Confinement on Cu," *Optik (Stuttg)*. **171**, 625–631 (2018).
 85. L. Sládková, D. Prochazka, P. Po, Š. Pavlína, M. Reme, K. Novotný, Č. Ladislav, and J. Kaiser, "Improvement of the Laser-Induced Breakdown Spectroscopy method sensitivity by the usage of combination of Ag-nanoparticles and vacuum conditions," *Spectrochim. Acta B* **127**, 48–55 (2017).

Chapter 6

Conclusions and future scope

This chapter comprehends the inferences derived from this thesis work. Conclusions from (a) proximal fs/ns LIBS studies of energetic triazole derivatives (in different atmospheres), (b) fs standoff filament induced breakdown spectroscopic (fs ST-FIBS) studies in various configurations viz., ST-FIBS1 (up to ~2 m), R-LIBS (10 cm/~8.5 m), ST-FIBS2 (~6.5 m/~8 m) and ST-FIBS studies bimetallic targets, metals and alloys and energetic molecules (RDX, TNT, HMX, and nitroimidazoles) (c) nanoparticle enhanced LIBS (NELIBS) studies in proximal as well as standoff mode are summarized. Future scope of the present works includes (a) detailed studies on the types and properties of filaments produced and, consequently, their effects on the LIBS plasma (b) detection and identification of standard HEMs such as RDX, HMX, CL-20 etc. at 15-20 m using ST-FIBS (c) detection of explosives in trace level and enhancing their signal in the presence of nanoparticles using NELIBS technique in table-top setup as well as in ST mode.

6.1 Conclusions

Femtosecond LIBS studies of various energetic/explosive molecules were performed extensively. Subsequently, several statistical techniques were employed to obtain the discrimination of these molecules. Furthering our studies we performed the fs LIBS studies in remote and standoff configurations. We had initially investigated a set of six energetic triazole derivatives (HEMs; high energy materials) in air and argon atmospheres using fs and ns laser induced breakdown spectroscopy (LIBS) technique in the proximal setup to understand the (a) influence of various functional groups and their positions on the spectral variations in LIBS spectra (b) effect of pulse duration and ambiance on the formation of atomic and molecular species (c) various feasible mechanisms of the formation and depletion of molecular (d) correlation between the molecular structure and plasma emission by examining the correlation between the percentages of atomic and bond types with atomic and molecular emission intensities, and (e) correlate the detonation parameters with the LIBS spectral features. The molecular emissions are more prominent in fs excitation, while the atomic emissions are dominant in the ns excitation. CN/C₂ ratio i.e. atomization-to-fragmentation ratio was utilized to explain the influence of functional groups and their positions on the recorded LIBS spectral features. Further, for the first time ever, we have proposed and demonstrated the standoff discrimination of high energy materials (HEMs) using fs filament induced breakdown spectroscopy (fs FIBS) technique at a distance of ~6.5m/ ~8 m. Apart from HEMs, metals, bimetallic targets and geological rocks were also investigated in the standoff configuration. The batch-wise discrimination results of all these samples using principal component analysis (PCA) are summarized. Nanoparticle enhanced laser induced breakdown spectroscopy (NE-LIBS) technique was utilized to obtain the enhancements in LIBS signal of metallic targets. Further, the enhancement in LIBS intensity of HEMs was investigated in proximal as well as standoff configurations with the aim of demonstrating the standoff detection of explosive traces.

Highlights from the present thesis work

1. A set of six novel high energy materials which are functional and structural isomers of triazole-substituted nitroarene derivatives with Me (CH₃), OMe (OCH₃), and amino (NH₂) functional groups at para and ortho positions were investigated by fs and ns-

LIBS techniques with an intention to elucidate the role played by substituent functional groups on the spectral emission signatures in LIBS. CN, C₂, and NH molecular bands were identified along with atomic lines corresponding to C, H, N, and O. Molecular signatures were prominent in femtosecond LIB spectra whereas atomic emission lines dominated the ns-LIB spectra.

2. The correlation studies of emission intensities with C–C, C=C, C–N, and C=N bonds and % O revealed that in case of ablation with fs pulses, CN species were formed mostly from native CN bonds while C₂ species were formed mostly from fragmentation of C–C, C=C bonds. This shows the advantage of fs pulses towards identification and discrimination of organic molecules, as the mitigated plasma-ambient interaction. However, in the case of ablation with ns pulses, CN and C₂ are formed from other secondary sources as well.
3. The possible pathways for formation and depletion of CN and C₂ species were accounted by evaluating the thermodynamic parameters such as standard enthalpy change (ΔH_r), Gibbs free energy change (ΔG_r), and equilibrium constant (K_{eq}) of various reactions by considering the transient LPP as a thermodynamic system. The reaction of C and C₂ with atmospheric nitrogen N₂ to form CN seems to be in equilibrium. The formation of CN is more favorable via the reaction of C and C₂ with N.
4. The significant impact of the type and position of substituents on the spectral emission signatures was evaluated using atomization to fragmentation ratio (CN/C₂ ratio). The substituents, Me, OMe, and NH₂, in the order of increasing electron releasing tendency, served to increase the electron density in the ring thus limiting the extent of delocalization of the pi-electron cloud in the aromatic ring. On the other hand, the electronegative 'O' atom (in OMe) and N atom (in NH₂) pull away the electrons leading to a reduction in electron density in the aromatic ring, thus facilitating the delocalization of π -electrons and increasing the chances of atomization (i.e. higher CN/C₂ ratio). Furthermore, we concluded that the position of the –NH₂ group played a crucial role in the stability of the aromatic ring. When the –NH₂ group was in the para position, the extensive H-bonding (intramolecular) with –NO₂ groups on either side prevented the lone pair electrons on N from coupling with the p-electron cloud of the aromatic ring thus promoting p-electron delocalization and increasing the probability of atomization.

Chapter 6

5. The molecular sum to atomic sum (MSAS) ratio $(\text{CN} + \text{C}_2)/(\text{C} + \text{H} + \text{N} + \text{O})$ obtained with fs excitation in air correlated very well with various energetic parameters i.e. oxygen balance, velocity of detonation, detonation pressure, heat of detonation for both the ortho and para substituted triazole derivatives. The MSAS ratio can, therefore, be a reliable performance metric for energetic compounds.
6. The fs and ns LIBS spectra of these HEMs were discriminated using principal component analysis (PCA). The PCA results demonstrate a very good classification of these HEMs with both fs and ns excitations.
7. For the first time, to the best of our knowledge, we have demonstrated the classification of HEMs in true standoff distances up to ~ 2 m and at ~ 6.5 m/ ~ 8 m using fs filament induced breakdown technique (fs ST-FIBS) in laboratory conditions. These studies were carried out systematically in three configurations (i) ST-FIBS1 studies up to 2m (configuration 1), (ii) Remote-LIBS studies (configuration 2) (iii) ST-FIBS2 studies at ~ 6.5 m/ ~ 8 m (configuration 3). Two collection systems i.e. ME-OPT-0007 (ANDOR) and Schmidt-Cassegrain telescope of different sizes, aperture window (2" and 6") and transmission capabilities (200-900 nm and 370-900 nm) were used in configuration 1 and configuration 2 and 3, respectively.
8. Our studies from configuration 1 and configuration 2 revealed that (a) the filament generating conditions can significantly affect the generated plasma (b) the signal (or photons) entering collection system decreases due to the decrease in solid angle ($1/R^2$) as sample distance (R) increases and evidently resulting in decreased SNR. As the standoff distance increased, the variance accounted by first three PCs together has decreased from 99% to 52%, which is related to the decrease in intensity of essential spectral features. However, when the PCA was performed on R-LIBS spectra of HEMs, the first three PCs accounted for 88% of the variance, which is similar to the result obtained at 50 cm standoff distance. Thus, employing big collection optics such as telescopes is essential for remote/standoff experiments.
9. Difference between the ablation efficiency of tightly focused fs pulses to the fs filaments has been understood from R-LIBS (10 cm/ ~ 8.5 m) and ST-FIBS (~ 6.5 m/ ~ 8 m) studies of metals. The fluence at the interaction zone is much higher in case of tightly focused fs pulses compared to the loosely focused filaments. The reduced ablation efficiency of fs filaments lead to the small ablation crater and as well in cooler plasma (with less atomic, ionic and electron density) conditions and decreased

SNR. Further, we have also demonstrated that ICCDs which offer high gain can be utilized to examine in such cases for better results in standoff experiments.

10. Metals and alloys (Al, Cu, brass, and stainless steel), bimetallic (Ag@Au and Ag@Cu) targets with varying concentration were successfully analyzed using fs ST-FIBS technique at ~6.5 m in configuration 3. The variation in characteristic intensities of constituent transitions in bimetallic targets with respect to their weight percentages demonstrated the promise of femtosecond filaments for ST analytical applications. The results obtained from PCA analysis (batch wise and all together) clearly demonstrated that the ST-FIBS technique is adept in classifying targets with similar composition.
11. A good classification of ST-FIBS spectra (in 375-390 nm spectral region) of nitroimidazoles was obtained using PCA, where first three PCs together accounted for 87% (84%, 2%, and 1%) of variance present in the multivariate data. Only CN molecular band region (375-390 nm) was considered for PCA analysis as there are no other important spectral features present in it. Likewise, the normalized ST-FIBS spectra in the 375-390 nm were analyzed through PCA. First three PCs together accounted for 92% (90%, 1%, and 1%) of variance present in the multivariate data. Though slight high variance was accounted in the normalized spectral analysis, the classification was not much clear. Hence, normalization of data may not lead to better classification in all times and supervised classifications techniques will be potential in such situations.
12. Several researchers have utilized NELIBS technique to enhance the LIBS signal of analyte in the presence of nanoparticles [1]. A two-factor enhancement in LIBS signal of Cu and Ag targets was achieved using AgNPS and AuLAL NPs respectively. Enhancement in Cu LIBS signal (a) increased as the concentration of AgNPs drop-casted increased (b) decreased as the fluence delivered on the target is decreased by moving the target above from the geometrical focus.
13. LIBS and NELIBS spectra of nitroamino (NHNO_2) substituted aryl-tetrazole (an energetic molecule) was recorded in the absence and presence of the Ag NPs. A two factor enhancement was obtained in both C and CN molecular bands. Enhancement of LIBS signal from HEMs in the presence of Ag NPs was investigated in standoff mode. Likewise, a two-factor enhancement in CN molecular band of TNT (in bulk) was observed in presence of NPs in comparison to ST FIBS and ST NE-FIBS.

Chapter 6

Furthermore, potential of NEFIBS technique was demonstrated by recording the trace of CL-20 deposited on Cu target, 50 μl (1 mg) of CL-20 solution (50 mM solution, 22 mg dissolved in 1 ml of acetone) was drop casted on Cu target over 1 cm^2 area.

6.2 Future scope

Through the substantial results accomplished from this thesis work, there is a lot of scope and necessity to perform several other systematical studies to demonstrate the advantage of fs LIBS/FIBS for explosive detection in proximal as well as standoff mode.

- LIBS studies of several other energetic materials are required to critically analyze the formation of molecular radicals and species since the pressure, vacuum or surrounding gas [2], pulse duration [3] and shock wave produced in the laser ablation process [4] can affect their formation.
- The general proximal LIBS studies to understand the molecular formation in organic materials can be combined (or correlated/or extended) with other techniques such as selected ion flow tube mass spectrometry (SIFT-MS) [5], time of flight mass spectroscopy (TOF-MS) [6] to gather more insight on stability, sensitivity, and the reactive mechanism of explosives [7].
- Standard energetic materials such as HMX, RDX, CL-20, and TNT etc. should be investigated thoroughly with ns/ fs excitations. The obtained LIBS spectral signatures will be then correlated with their detonation parameters to corroborate the results that we achieved in case of triazole derivatives. This can establish LIBS as a potential laboratory scale technique to measurement or approximate or evaluate the detonation parameters.
- The fs ST-FIBS experiments (in this thesis) were mainly focused at:
 - Delivering of fs pulses to standoff distances in the form of filaments
 - Collection of optical emissions from the distant target materials
 - Qualitative elemental analysis (especially in the case of bimetallic targets and geological rocks) and

- Discrimination of HEMs and other materials (metals, bimetallic targets, geographical rocks) using PCA.
- In continuation of these studies, the next standoff FIBS experiments will focus on:
 - Optimization of ST-FIBS acquisition parameters such as gate delay, gate width and gain of ICCD for various materials especially for explosives to achieve good SNR.
 - Acquiring the fs ST-LIBS spectra of all common/standard explosives.
 - Develop superior supervised algorithms such as PLS-DA, ANN, etc. for exemplary and unambiguous detection.
 - Extending the ST-FIBS detection studies to 15-20 m using advanced telescopes with optimized collection efficiency and throughput to the spectrometer.
 - Investigation of a few hybrid techniques such as LIBS-Raman technique to embrace the advantages of both the methodologies for effective explosives detection.
 - Perform detailed studies on the types and properties of filaments produced and, consequently, their effects on the LIBS plasma will enable the development of an efficient technique for ST trace analysis of any material.
- Further, systematic NE-LIBS (proximal) and NE-FIBS (in standoff mode) experiments are warranted for the trace detection of HEMs. The primary focus in these set of experiments is to
 - (a) Optimize the laser energy and the NE-LIBS spectral acquisition parameters.
 - (b) Utilize plasmonic nanoparticles (Ag, Au and Cu NPs) of different shape and size.
 - (c) Use plasmonic thin film coated substrates to overcome the limitations in the drop casting of NPs.
 - (d) to record NE-FIBS spectra of traces of standard high energy materials such as HMX, RDX, CL-20, and TNT, etc. and classify them using supervised algorithms.

Chapter 6

Finally, we believe that with the latest developments in the sources (of fs pulses) and the detectors it will not be a difficult task to make compact (portable) LIBS systems for field deployment. A combination of two or three lenses can be used to focus fs pulses at the desired standoff position and thus the working distance can be changed by adjusting the distance between lenses. However, it is crucial to understand the complex focusing dynamics of fs pulses [8] and optimize the pulse energy as they affect LIBS signal strength. Recently, it has also been demonstrated that either part of the LIBS spectra [9] or part of the echellograms [10] itself can be utilized effectively in discrimination/classification studies implying the reduction in algorithm time, complexity and increase in the sampling rate. Further, ultrashort pulse fiber lasers can also be used for portable applications owing to their compact size, minimized background emission [11]. Thus, in conclusion, fs laser pulses can be potentially deployed in field for standoff detection due to their appealing features such as (i) lesser intrusion of air, stoichiometric ablation with fs pulses [12] (ii) minimized contribution from the substrate (crater depth attained in fs filament ablation is smaller in comparison with those obtained using fs/ns pulses) [3] (iii) formation of intense long propagating filaments and when augmented with telescopes of large f-number, efficient pulse delivery with an easy user interface assisted with superior multivariate analysis algorithm will result in efficient trace detection of hazardous materials of interest [13].

6.3 References

1. M. Dell, R. Alrifai, and A. De Giacomo, "Nanoparticle Enhanced Laser Induced Breakdown Spectroscopy (NELIBS), a fi rst review," *Spectrochim. Acta Part B* **148**, 105–112 (2018).
2. T. Delgado, J. M. Vadillo, and J. J. Laserna, "Primary and recombined emitting species in laser-induced plasmas of organic explosives in controlled atmospheres," *J. Anal. At. Spectrom.* **29**, 1675–1685 (2014).
3. S. S. Harilal, J. Yeak, B. E. Brumfield, J. D. Suter, and M. C. Phillips, "Dynamics of molecular emission features from nanosecond, femtosecond laser and filament ablation plasmas," *J. Anal. At. Spectrom.* **31**, 1192–1197 (2016).
4. S. S. Harilal, B. E. Brumfield, B. D. Cannon, and M. C. and Phillips, "Shock wave mediated plasma chemistry of AlO formation in laser ablation plumes," *Anal. Chem.* **88**, 2296–2302 (2016).
5. M. Civi and M. Kyncl, "Laser Ablation of FOX-7 : Proposed Mechanism of Decomposition," *Anal. Chem.* **83**, 1069–1077 (2011).
6. W. Zhang, S. Ruiqi, and Y. H. Ye, "Identification and formation mechanism of the transient ion fragments produced in laser- induced dissociation of 1 , 1-diamino-2,2-dinitroethylene," *Laser Part. Beams* 1–5 (2018).
7. J. L. Gottfried, D. K. Smith, C. Wu, and M. L. Pantoya, "Improving the Explosive Performance of Aluminum Nanoparticles with Aluminum Iodate Hexahydrate (AIH)," *Sci. Rep.* **8**, 8036 (2018).
8. C. A. Zuhlke, J. Bruce III, T. P. Anderson, D. R. Alexander, and C. G. Parigger, "A fundamental understanding of the dependence of the laser-induced breakdown spectroscopy (LIBS) signal strength on the complex focusing dynamics of femtosecond laser pulses on either side of the focus," *Appl. Spectrosc.* **68**, 1021–1029 (2014).
9. A. K. Myakalwar, N. Spegazzini, C. Zhang, S. Kumar Anubham, R. R. Dasari, I. Barman, and M. Kumar Gundawar, "Less is more: Avoiding the LIBS dimensionality curse through judicious feature selection for explosive detection," *Sci. Rep.* **5**, 13169 (2015).
10. P. Pořízka, J. Klus, J. Mašek, M. Rajnoha, D. Prochazka, P. Modlitbová, J. Novotný, R. Burget, K. Novotný, and J. Kaiser, "Multivariate classification of echellograms: a new perspective in Laser-Induced Breakdown Spectroscopy analysis," *Sci. Rep.* **7**, 3160 (2017).
11. A. W. Schill, D. A. Heaps, D. N. Stratis-Cullum, B. R. Arnold, and P. M. Pellegrino, "Characterization of near-infrared low energy ultra-short laser pulses for portable applications of laser induced breakdown spectroscopy," *Opt. Express* **15**, 14044–14056 (2007).
12. T. A. Labutin, V. N. Lednev, A. A. Ilyin, and A. M. Popov, "Femtosecond laser-induced breakdown spectroscopy," *J. Anal. At. Spectrom.* **31**, 90–118 (2016).
13. P. M. Pellegrino, E. L. Holthoff, and M. E. Farrell, *Laser-Based Optical Detection of Explosives* (CRC Press, 2015), Vol. 40.

Intentional blank page

Femtosecond LIBS Studies of Energetic Molecules in the Near and Standoff Regimes

by Abdul Kalam S

Submission date: 26-Oct-2018 04:42PM (UTC+0530)

Submission ID: 1027266302

File name: Abdul_Kalam_S_ACRHEM_13ACPA02_for_similarity_check.pdf (15.35M)

Word count: 49542

Character count: 251715

Femtosecond LIBS Studies of Energetic Molecules in the Near and Standoff Regimes

ORIGINALITY REPORT

29%

SIMILARITY INDEX

2%

INTERNET SOURCES

28%

PUBLICATIONS

2%

STUDENT PAPERS

PRIMARY SOURCES

- 1** S. Abdul Kalam, N. Linga Murthy, P. Mathi, N. Kommu, Ajay K. Singh, S. Venugopal Rao. "Correlation of molecular, atomic emissions with detonation parameters in femtosecond and nanosecond LIBS plasma of high energy materials", J. Anal. At. Spectrom., 2017
Publication **11%**
 - 2** Abdul Kalam Shaik, Nageswara Rao Epuru, Hamad Syed, Chandu Byram, Venugopal Rao Soma. "Femtosecond laser induced breakdown spectroscopy based standoff detection of explosives and discrimination using principal component analysis", Optics Express, 2018
Publication **8%**
 - 3** Abdul Kalam Shaik, Ajmathulla, Venugopal Rao Soma. "Discrimination of bimetallic alloy targets using femtosecond filament-induced breakdown spectroscopy in standoff mode", Optics Letters, 2018
Publication **3%**
-

4

Abdul Kalam, Linga Murthy N, Rama Krishna J, Srikanth VVSS, Venugopal Rao Soma.

"Nanoparticle Enhanced Laser Induced Breakdown Spectroscopy with Femtosecond Pulses

", 13th International Conference on Fiber Optics and Photonics, 2016

Publication

1%

5

Submitted to University of Hyderabad, Hyderabad

Student Paper

1%

6

Labutin, Timur A., Vasily N. Lednev, Alexey A. Ilyin, and Andrey M. Popov. "Femtosecond laser-induced breakdown spectroscopy", Journal of Analytical Atomic Spectrometry, 2016.

Publication

<1%

7

Marcella Dell'Aglio, Rim Alrifai, Alessandro De Giacomo. "Nanoparticle Enhanced Laser Induced Breakdown Spectroscopy (NELIBS), a first review", Spectrochimica Acta Part B: Atomic Spectroscopy, 2018

Publication

<1%

8

Francisco J. Fortes, Javier Moros, Patricia Lucena, Luisa M. Cabalín, J. Javier Laserna. "Laser-Induced Breakdown Spectroscopy", Analytical Chemistry, 2012

<1%

Spectrochimica Acta Part B: Atomic Spectroscopy, 200805

Publication

96

micro.magnet.fsu.edu

Internet Source

<1%

97

Luo, Liang, and Jigang Wang. "Terahertz spectroscopy of low-dimensional nanomaterials: nonlinear emission and ultrafast electrodynamics", *Ultrafast Nonlinear Imaging and Spectroscopy III*, 2015.

Publication

<1%

Exclude quotes On
Exclude bibliography Off

Exclude matches < 10 words

Femtosecond LIBS Studies of Energetic Molecules in the Near and Standoff Regimes

ORIGINALITY REPORT

20%

SIMILARITY INDEX

2%

INTERNET SOURCES

17%

PUBLICATIONS

5%

STUDENT PAPERS

PRIMARY SOURCES

- 1** S. Abdul Kalam, N. Linga Murthy, P. Mathi, N. Kommu, Ajay K. Singh, S. Venugopal Rao. "Correlation of molecular, atomic emissions with detonation parameters in femtosecond and nanosecond LIBS plasma of high energy materials", J. Anal. At. Spectrom., 2017
Publication **8%**

- 2** Submitted to University of Hyderabad, Hyderabad
Student Paper **3%**

- 3** Labutin, Timur A., Vasily N. Lednev, Alexey A. Ilyin, and Andrey M. Popov. "Femtosecond laser-induced breakdown spectroscopy", Journal of Analytical Atomic Spectrometry, 2016.
Publication **1%**

- 4** Eshita Mal, Alika Khare. "Studies on Laser produced Tungsten Plasma using LIBS", 13th International Conference on Fiber Optics and Photonics, 2016 **<1%**

5

V.N. Rai, S.N. Thakur. "Physics of Plasma in Laser-Induced Breakdown Spectroscopy", Elsevier BV, 2007

Publication

<1%

6

Abdul Kalam Shaik, Ajmathulla, Venugopal Rao Soma. "Discrimination of bimetallic alloy targets using femtosecond filament-induced breakdown spectroscopy in standoff mode", Optics Letters, 2018

Publication

<1%

7

Abdul Kalam Shaik, Nageswara Rao Epuru, Hamad Syed, Chandu Byram, Venugopal Rao Soma. "Femtosecond laser induced breakdown spectroscopy based standoff detection of explosives and discrimination using principal component analysis", Optics Express, 2018

Publication

<1%

8

Frank C. De Lucia, Jr.. "Multivariate analysis of standoff laser-induced breakdown spectroscopy spectra for classification of explosive-containing residues", Applied Optics, 11/01/2008

Publication

<1%

9

Rao, K. S., and A. K. Chaudhary. "Investigation of the thermal decomposition and stability of energetic 1,2,4-triazole derivatives using a UV

<1%

Spectrochimica Acta Part B: Atomic Spectroscopy, 200805

Publication

61

micro.magnet.fsu.edu

Internet Source

<1%

62

Luo, Liang, and Jigang Wang. "Terahertz spectroscopy of low-dimensional nanomaterials: nonlinear emission and ultrafast electrodynamics", *Ultrafast Nonlinear Imaging and Spectroscopy III*, 2015.

Publication

<1%

63

www.science.gov

Internet Source

<1%

Exclude quotes On

Exclude matches < 10 words

Exclude bibliography On

<p>PERSONAL INFORMATION</p> 	<p>Abdul Kalam S</p> <p>📍 Advanced Centre of Research in High Energy Materials (ACRHEM), University of Hyderabad, Gachibowli, Hyderabad-500046, Telangana, India.</p> <p>☎ +91 8500 86 8147</p> <p>✉ chand.gaffur@gmail.com, abdulkalam89@uohyd.ac.in</p> <p>🌐 https://www.researchgate.net/profile/Abdul_Kalam6 https://scholar.google.co.in/citations?user=YLHCZRwAAAAJ&hl=en&oi=ao</p> <p>Sex: Male Date of birth: 08/06/1989 Nationality: Indian Marital Status: Unmarried</p>
<p>CAREER OBJECTIVE</p>	<p>Seeking a suitable <i>research or scientific position</i> in an active group to join hands in the journey of discovering unknown from known through contributing my skills and abilities towards a bright research career.</p>
<p>EDUCATION</p>	
<p>2013 – till date</p>	<p>Ph.D. in Physics (Submission due in October 2018), Advance Centre of Research in High Energy Materials (ACRHEM), School of Physics, University of Hyderabad (HCU), India.</p> <p>Thesis “Femtosecond LIBS Studies of Energetic Molecules in the Near and Standoff Regimes”</p>
<p>2010 – 2012</p>	<p>M.Sc. Physics with specialization in “Condensed matter Physics”, University of Hyderabad, Hyderabad, Telangana (state), India.</p>
<p>2006 – 2010</p>	<p>B.Sc.Ed. (Bachelor in Science and Education) with subjects Mathematics, Physics and Chemistry. Regional Institute of Education, Mysore, University of Mysore, Karnataka (state), India.</p>
<p>RESEARCH INTERESTS</p>	<ul style="list-style-type: none"> ◆ Standoff detection and discrimination of hazardous CBRNE materials (chemical, biological, radiological, nuclear and explosive) using ultrafast pulses through femtosecond filament induced breakdown spectroscopy (fs FIBS). ◆ Understand the femtosecond filaments and investigate their applications for remote sensing of aerosols, minerals and ores. ◆ Exploring laser matter interaction of fast/ultrafast pulses through laser induced breakdown spectroscopy (LIBS) and laser direct writing (LDW) ◆ Imparting or developing chemometric data analysis techniques such as principal component analysis (PCA), partial least square regression (PLSR) etc. to LIBS and Raman spectroscopy using MATLAB. ◆ In a nutshell “Standoff Raman-LIBS, femtosecond filament LIBS or FIBS, SERS and analysing spectra with multivariate techniques (PCA, PLSR, PLSDA, etc.)”.
<p>RESEARCH EXPERTISE</p>	<ul style="list-style-type: none"> ◆ Handling fast and ultra-fast lasers.

	<ul style="list-style-type: none"> ◆ Broad knowledge and experience in acquiring and analysing LIBS spectra of various materials in near and standoff regime (metals, alloys, geological samples and high energy materials). ◆ Knowledge in fundamentals of laser-matter interactions and plasma spectroscopy. ◆ Experience in laser technology and optics. ◆ Developing chemometric algorithms for multivariate data analysis such as principal component analysis (PCA). ◆ Single-step fabrication of plasmonic nanomaterial through laser ablation using ultrafast laser pulses.
<p>AWARDS</p>	<ul style="list-style-type: none"> ◆ <u>PSSI Best oral presentation Award</u> at 32nd National Symposium on Plasma Science and Technology, IPR, Ahmedabad, India. (November 07-10, 2017). ◆ Qualified Joint Exam and Screening Test in 2015 (All India Rank 172). ◆ Qualified SET examination (Andhra Pradesh State Eligibility test) for lectureship in 2012 (It's a life time qualification). ◆ Bagged second position in university level quiz competition held at University of Mysore in 2008, 2009 consecutively (Undergraduate level).
<p>In this endeavor of earning my Ph.D., I have worked closely with a team of researchers, professors and learned the values of good lab practices. I have learned to respect time of others as well as time of myself. We often engage in scientific discussions which has improved our understanding of concepts. We helped each other in setting up the lab, establishing experimental setups and even in manuscript writing and editing. We appreciated every effort of others, either it could be an experimental demonstration in lab or acceptance of work in any peer reviewed journals. We always believe that this mutual help and mutual understanding has lead us in progressive directions. Thus, I can firmly say that, I can work well as a team member, team leader and always willing to learn and update myself with ongoing research as well as contributing to it.</p> <p>This experience can help me</p> <ul style="list-style-type: none"> ○ To perform an active role in teaching and establishment of lab. ○ To assist in writing manuscripts for the publication, and conference presentation of the results of the research ○ To contribute to the supervision of Ph.D., Masters students, and undergraduate students at your Institution. <p>My resume highlights my background and qualifications, my enthusiasm and determination can be revealed during a personal meeting.</p>	

PUBLICATIONS (in peer reviewed journals; online)

1. **Abdul Kalam Shaik**, Ajmathulla, Venugopal Rao Soma, “Discrimination of bimetallic alloy targets using femtosecond filament-induced breakdown spectroscopy in standoff mode”, (**Optics Letters**, <https://doi.org/10.1364/OL.43.003465>)
 2. **Abdul Kalam Shaik**, Nageswara Rao E, Syed Hamad, Byram Chandu, and Venugopal Rao Soma, “Femtosecond laser induced breakdown spectroscopy based standoff detection of explosives and discrimination using principal component analysis”, (**Optic Express**, <https://doi.org/10.1364/OE.26.008069>)
 3. **S. Abdul Kalam**, N. Linga Murthy, P. Mathi, N. Kommu, Ajay K. Singh, S. Venugopal Rao*, “Correlation of molecular, atomic emissions in femtosecond and nanosecond LIBS plasma of novel high energy materials with detonation parameters,” (**Journal of Analytical Atomic Spectrometry**, DOI: 10.1039/C7JA00136C).
 4. **S. Abdul Kalam**, Epuru Nageswara rao, S. Venugopal Rao, “Standoff LIBS for explosives detection: Challenges and status”, **Laser Focus World magazine**, April 2017 pp. 24-28.
 5. **S. Abdul Kalam**, N. Linga Murthy, J. Ramakrishna, V.V.S.S. Srikanth, S. Venugopal Rao, “Nanoparticle Enhanced Laser Induced Breakdown Spectroscopy with Femtosecond Pulses,” International Conference on Fiber Optics and Photonics, Photonics 2016, IIT Kanpur, December 04-08, 2016. (**OSA proceedings**, <https://doi.org/10.1364/PHOTONICS.2016.Th3A.89>).
 6. **Abdul Kalam Shaik** and Venugopal Rao Soma, “Standoff Detection of RDX, TNT, and HMX Using Femtosecond Filament Induced Breakdown Spectroscopy”, OSA Light, Energy and the Environment Congress meeting 2018, Nov 5th to 8th. Singapore (**OSA proceedings Dec 2018**).
 7. E. Nageswara Rao, P. Mathi, **S. Abdul Kalam**, S. Sreedhar, Ajay K. Singh, B. N. Jagatap and S. Venugopal Rao, “Femtosecond and nanosecond LIBS studies of nitroimidazoles: correlation between molecular structure and LIBS data” (**Journal of Analytical Atomic Spectrometry**, 10.1039/C5JA00445D).
 8. E. Nageswara Rao, **S. Abdul Kalam**, and S. Venugopal Rao, “Femtosecond LIBS Studies of Aluminum target in Standoff Configuration”, Photonics 2018, (**OSA proceedings, Dec 2018**).
- Publications in other areas of interests**
9. Byram Chandu, Moram Sri Sathya Bharati, **Shaik Abdul Kalam**, Soma Venugopal Rao, “Versatile gold based SERS substrates fabricated by ultrafast laser ablation for sensing picric acid and ammonium nitrite,” (**Chemical Physical Letters**, DOI:10.1016/j.cplett.2017.07.043)
 10. P. Karuppasamy, T. Kamalesh, V. Mohankumar, **S. Abdul Kalam**, Muthu Senthil Pandian, P. Ramasamy, Sunil Verma, S. Venugopal Rao, “Synthesis, growth, structural, optical, thermal, laser damage threshold and computational perspectives of 4-nitrophenol 4-aminobenzoic acid monohydrate (4NPABA) single crystal”, (**Journal of molecular structure**, <https://doi.org/10.1016/j.molstruc.2018.08.074>).
 11. P. Karuppasamy, T. Kamalesh, K. Anitha, **S. Abdul Kalam**, Muthu Senthil Pandian, P. Ramasamy, Sunil Verma, S. Venugopal Rao, “Synthesis, crystal growth, structure and characterization of a novel third order nonlinear optical organic single crystal: 2-Amino 4,6-Dimethyl Pyrimidine 4-nitrophenol”, (**Optical Materials**, <https://doi.org/10.1016/j.optmat.2018.07.039>).

Presentations at national and International Conferences/Workshops

1. **S. Abdul Kalam**, E. Nageswara Rao and S. Venugopal Rao, “Femtosecond standoff detection of high energy materials”, (MMISLIBS) International symposium on Laser Induced Breakdown Spectroscopy, Feb19-21, 2018, BARC, Mumbai (Oral Presentation)
2. **S. Abdul Kalam**, E. Nageswara Rao and S. Venugopal Rao, “Femtosecond standoff detection of high energy materials”, DAE-BRNS National Laser Symposium (NLS-26), December 20 - 23, 2017, BARC, Mumbai (Poster).
3. **S. Abdul Kalam**, E. Nageswara Rao, B. Chandu, and S. Venugopal Rao, “Femtosecond standoff detection of high energy materials”, 11th International High Energy Materials Conference & Exhibits (HEMCE), Pune, November 23-25, 2017. (Oral presentation).
4. **S. Abdul Kalam**, E. Nageswara Rao and S. Venugopal Rao, “Femtosecond LIBS based Standoff Detection of Explosive Molecules”, 32nd National Symposium on Plasma Science and Technology, IPR, Ahmedabad, November 07-10, 2017 (Oral presentation, awarded with best oral presentation).
5. **S. Abdul Kalam**, E. Nageswara Rao and S. Venugopal Rao, “Femtosecond LIBS based Standoff Detection of Explosive Molecules”, DAE-BRNS Theme Meeting on Ultrafast Science 2017 (UFS-2017), University of Hyderabad, Hyderabad, November 02-04, 2017. (Poster)
6. **S. Abdul Kalam**, N. Linga Murthy, J. Ramakrishna, V.V.S.S. Srikanth, S. Venugopal Rao, “Nanoparticle Enhanced Laser Induced Breakdown Spectroscopy with Femtosecond Pulses,” International Conference on Fiber Optics and Photonics, Photonics 2016, IIT Kanpur, December 04-08, 2016. (Poster)
7. **S. Abdul Kalam**, N. Lingamurthy, P. Mathi, S. Venugopal Rao, “Femtosecond and Nanosecond LIBS studies of functional and structural isomers of Triazole-Substituted Nitroarene Derivatives,” LIBS2016-France, 12-16 September 2016, Chamonix-MontBlanc, France. (selected for Oral presentation)
8. E. Nageswara Rao, **S. Abdul Kalam**, S. Venugopal Rao, “Femtosecond LIBS studies of Nitropyrazoles in air and argon atmospheres: Correlation between molecular structure,” National Laser Symposium (NLS-25, 2016), Department of Physics, School of Applied Sciences, KIIT University, Bhubaneswar, Odisha, India. (Poster)
9. **S. Abdul Kalam**, N. Linga Murthy, K Nagarjuna, P. Mathi, Ajay K. Singh, S. Venugopal Rao, “Nanosecond LIBS Studies for Classification of Triazole-substituted Nitroarene Derivatives,” National Laser Symposium (NLS-25, 2016), Department of Physics, School of Applied Sciences, KIIT University, Bhubaneswar, Odisha, India. (Poster)
10. B. Chandu, **S.A. Kalam**, S. Venugopal Rao, “Gold nanoparticles and nanostructures fabricated by femtosecond ablation towards explosives detection,” Recent Advances in Optical Sciences– 2 (RAOS 2, 2016), May 6-7, University of Hyderabad, Hyderabad, India. (Poster).
11. **S. Abdul Kalam**, and S. Venugopal Rao, “single shot trace detection of heavy elements in water”, IC-IMPACTS summer school, June 20-24, 2015, University of Toronto, Canada. (Oral presentation).

References

Prof. Soma Venugopal Rao
(Thesis supervisor)
Advanced Centre of Research in
High Energy Materials (ACRHEM)
South Campus,
University of Hyderabad,
Prof. C.R. Road, Gachibowli
Hyderabad-500046, Telangana,
India.
Email: soma_venu@yahoo.com
Email: soma_venu@uohyd.ac.in
PHONE:+91-040-2313-4406/07

Dr. K. Venkateswara Rao,
Ex-Director,
Advanced Centre of Research in
High Energy Materials
(ACRHEM)
University of Hyderabad,
Prof. C.R. Road, Gachibowli,
Hyderabad-500046, Telangana,
India
Email: drkadiyam@gmail.com

Prof. Anil K Bhatnagar,
INSA senior scientist,
Visiting professor
School of Physics,
University of Hyderabad
Prof. C.R. Road, Gachibowli,
Hyderabad-500046, Telangana, India.
Email: anilb42@gmail.com